Al-Si interdiffusion under lower mantle conditions

Analytical TEM study of Al-bearing bridgmanite

DISSERTATION

zur Erlangung des akademischen Grades einer Doktorin
der Naturwissenschaften (Dr. rer. nat.)
in der Bayreuther Graduiertenschule für Mathematik und Naturwissenschaften

(BayNAT)

der Universität Bayreuth

vorgelegt von

Laura Czekay

aus Bonn

Bayreuth, 2023

Die vorliegende Arbeit wurde in der Zeit von September 2019 bis März 2023 unter Betreuung von PD Dr. Catherine McCammon und Dr. Nobuyoshi Miyajima angefertigt.

Vollständiger Abdruck der vvon der Bayreuther Graduiertenschule für Mathematik und Naturwissenschaften (BayNAT) der Universität Bayreuth genehmigten Dissertation zur Erlangung des akademischen Grades einer Doktorin der Naturwissenschaften (Dr. rer. nat.).

Dissertation eingereicht am 21.03.2023

Zulassung durch das Leistungsgremium am 21.03.2023

Wissenschaftliches Kolloquium am 10.05.2023

Amtierender Direktor: Prof. Dr. Hans Keppler

Prüfungsausschuss:

PD. Dr. Catherine McCammon (Gutachterin)

Prof Dr. Daniel Frost (Gutachter)

PD. Dr. Gerd Steinle-Neumann (Vorsitz)

Dr. habil. Marcel Thielmann

Abstract

Experimental investigation of diffusion in minerals is a fundamental tool for understanding the rheological properties of the Earth's mantle. Bridgmanite is the major component in the Earth's lower mantle (Irifune, 1994). Previous theoretical studies on deformation rates show that the crucial mechanism for the deformation of bridgmanite (Brg) is the diffusion-driven creep of the slowest element, silicon (Si) (Reali *et al.*, 2019 a). Bridgmanite is a magnesium silicate which crystallises in a perovskite structure with end-member formula $MgSiO_3$ and can contain significant amounts of iron (Fe) and aluminium (Al) (Irifune, 1994). Al can be incorporated by substitution of Si, with charge balancing occurring through the formation of oxygen vacancies (OV) or charge-coupled (CC) substitution of magnesium (Mg) and Si by 2 Al (Navrotsky, 1999). Understanding the interdiffusion of Al and Si in bridgmanite is, therefore, essential for understanding the geodynamics of the mantle.

This study aimed to investigate Al-Si interdiffusion in Brg experimentally. Therefore, Brg diffusion couples were synthesised from 0 – 5 mol % Al_2O_3-bearing $MgSiO_3$ enstatite and glass samples and from Mg-excess glass with 2.7 wt. % Al_2O_3 at 24 GPa and 1,750 – 2,000 °C using conventional high-pressure and high-temperature multi-anvil presses. The synthesised samples could be further made into diffusion couples with a total volume of 1 mm^3 by careful sample preparation and well-polished diffusion surfaces. The diffusion couples were run in a conventional multi-anvil press under the same pressure and temperature conditions as during synthesis (24 GPa and 1,750 – 2,100 °C). The diffusion couples were analysed after the experiments with a scanning transmission electron microscope (STEM) and an energy-dispersive X-ray spectrometer (EDXS). STEM-EDXS was used to evaluate elemental composition at the nanometer scale and to determine Al concentrations. During chemical analysis, the element concentration was measured along a line perpendicular to the diffusion interface determined from two-dimensional elemental distribution maps. The resulting ASCII data were converted into diffusion profiles and used to determine the diffusion rate using the semi-infinite diffusion model (Crank, 1975).

The diffusion coefficients were determined from ten of the 15 diffusion experiments that were carried out at different temperatures and for different annealing times. The number of experiments may appear to be small, but they include a large investment in analytical effort to establish a high degree of confidence in the dataset. The Al-Si interdiffusion was calculated to be $D_{Al\text{-}Si} = 4.2 \pm 0.9 \times 10^{-11} \exp[-400\ [kJ\ mol^{-1}]/RT]\ m^2/s$. Results differ profoundly from previous measurements, indicating a 1 to 2 orders of magnitude slower diffusion rate in bridgmanite than previously experimentally determined Si and Mg self-diffusion measured at similar pressures and temperatures(Yamazaki *et al.*, 2000; Dobson *et al.*,2008; Xu *et al.*, 2011) as well as Fe-Mg interdiffusion in bridgmanite (Holzapfel, 2004). Potential factors leading to differences with previous data are discussed, as well as the effect of sample surface preparation, diffusing species, and mineral structure.

Following models that suggest diffusion-controlled creep can be assumed in magnesium silicate bridgmanite (Yamazaki *et al.*, 2000), the obtained diffusion rates provide insight into deformation rates of bridgmanite in the lower mantle. For this purpose, the temperature dependence of the Al-Si diffusion rate of bridgmanite was examined. This enabled rheology of the lower mantle to be approximated and implications for mantle rheology to be considered.

Zusammenfassung

Die Berechnung der Diffusion in Mineralien ist ein grundlegendes Instrument zum Verständnis der rheologischen Eigenschaften des Erdmantels. Bridgmanit ist der Hauptbestandteil des unteren Erdmantels (Irifune, 1994). Frühere theoretische Studien über Verformungsraten zeigen, dass der entscheidende Mechanismus für die Verformung von Bridgmanit (Brg) das diffusionsgetriebene Kriechen des langsamsten Elements, Silizium (Si), ist (Reali *et al.*, 2019 a). Bridgmanit ist ein Magnesiumsilikat, das in einer Perowskitstruktur mit der Endgliedformel $MgSiO_3$ kristallisiert und erhebliche Mengen an Eisen (Fe) und Aluminium (Al) enthalten kann (Irifune, 1994). Al kann durch Substitution von Si eingebaut werden, wobei der Ladungsausgleich durch die Bildung von Sauerstoffleerstellen (OV) oder durch ladungsgekoppelte (CC) Substitution von Magnesium (Mg) und Si durch 2 Al erfolgt (Navrotsky, 1999). Das Verständnis der Interdiffusion von Al und Si in Bridgmanit ist daher für das Verständnis der Geodynamik des Mantels unerlässlich.

Diese Studie zielte darauf ab, die Interdiffusion von Al und Si in Brg experimentell zu untersuchen. Die Brg-Diffusionspaare für die Interdiffusionsexperimente wurden aus 0 – 5 mol % Al_2O_3-haltigem $MgSiO_3$-Enstatit und Glasproben bei 24 GPa und 1.750 – 2.000 °C unter Verwendung konventioneller Hochdruck- und Hochtemperatur-Vielstempel-Pressen synthetisiert. Die synthestisierten Proben konnten durch sorgfältige Probenvorbereitung und gut polierte Diffusionsoberflächen zu Diffusionsexperimente mit einem Gesamtvolumen von 1 mm^3 weiterverarbeitet werden und in einer konventionellen Vielstempel-Presse bei den selben Druck- und Temperaturbedingnungen wie während der Synthese (24 GPa und 1.750 – 2.000 °C) durchgeführt werden. Der 7/3-Versuchsaufbau für die Diffusionsexperimente wurde hierfür noch weiterentwickelt und die Temperaturmessung stabilisiert. Die gewonnenen Diffusionsproben wurden mit einem Rastertransmissionselektronenmikroskop (RTEM) und einem energiedispersiven Röntgenspektrometer (EDXS) analysiert. Mit dem RTEM-EDXS wurden Element-Zusammensetzungen im Nanometerbereich bewertet und zur Untersuchung der Al-Konzentrationen entlang einer Linie senkrecht zur Diffusionsgrenzfläche verwendet. Die Elementkonzentration wurde während der chemischen Analysen aus zweidimensionalen Elementverteilungskarten abgelesen. Die daraus resultierenden ASCII-Daten wurden in Diffusionsprofile umgewandelt und zur Bestimmung der Diffusionsrate mit Hilfe der Crank-Gleichung (Crank & Gupta, 1975) verwendet.

Die Diffusionskoeffizienten wurden aus zehn der 15 Diffusionsexperimente ermittelt, die bei verschiedenen Temperaturen und für unterschiedliche Glühzeiten durchgeführt wurden. Die Anzahl der Experimente mag gering erscheinen, aber sie beinhalten einen hohen analytischen Aufwand, um ein hohes Maß an Vertrauen in den Datensatz zu schaffen. Die analytischen Ergebnisse ergaben eine Al-Si - Interdiffusion von $D_{Al\text{-}Si} = 4{,}2 \pm 0{,}9 \times 10^{-11}$ exp[- 400 [kJ mol^{-1}]/RT] m^2/s. Die Ergebnisse unterscheiden sich erheblich von früheren Messungen und weisen auf eine um 1 bis 2 Größenordnungen langsamere Diffusionsrate in Bridgmanit hin, als die zuvor experimentell ermittelte Si- und Mg-Selbstdiffusion, die bei ähnlichen Drücken und Temperaturen gemessen wurden (Dobson *et al.*, 2008; Xu *et al*., 2011; Yamazaki *et al*., 2000), sowie die Fe-Mg-Interdiffusion in Bridgmanit (Holzapfel, 2004). Mögliche Faktoren, die zu Unterschieden zu früheren Daten führen können, werden ebenso diskutiert wie die Auswirkungen der Probenvorbereitung, der diffundierenden Spezies und der Mineralstruktur.

In Anlehnung an Modelle, die ein diffusionsgesteuertes Kriechen in Magnesiumsilikat-Bridgmanit vermuten lassen (Yamazaki *et al.,* 2000), geben die erhaltenen Diffusionsraten Aufschluss über die Verformungsraten von Bridgmanit im unteren Erdmantel. Zu diesem Zweck wurde die Temperaturabhängigkeit der diffusionsgesteuerten Kriechrate von Bridgmanit bestimmt. Dies ermöglichte eine Annäherung an die Viskosität des unteren Erdmantels und eine Betrachtung der Auswirkungen auf die Rheologie des Erdmantels.

Table of contents

Abstract I

Zusammenfassung III

Table of contents VI

1. Introduction 1

1.1. Problem statement 1

1.2. Bridgmanite in the lower mantle 3

1.3. Diffusion in bridgmanite 5

1.3.1. Solution to Fick's equation 6

1.3.2. Substitution mechanism in Al-bearing bridgmanite 8

1.3.3. Defects in bridgmanite 11

1.3.4. Temperature dependence of diffusion coefficients 14

1.4. Creep mechanism in bridgmanite 16

1.4.1. Diffusion creep 17

1.4.2. Dislocation Creep 19

1.5. Viscosity in the lower mantle 20

1.6. State of analytical methods research 23

1.7. Aim of this study 24

2. Experimental and analytical methods 27

2.1. Starting material preparation 27

2.2. High-pressure – high-temperature experiments 28

2.2.1. Pre-synthesis of pyroxene and pyrope 28

2.2.2. Synthesis of diffusion couples and diffusion experiments 29

2.2.3. Diffusion capsule preparation 34

2.3. Sample characterisation 35

2.3.1. Powder and micro-X-ray diffraction 35

2.3.2. Raman spectroscopy 40

2.3.3. Scanning electron microscopy 42
2.3.4. Focused ion beam: TEM lamella preparation 45
2.3.5. Transmission electron microscopy 49
3. Results 68
3.1. TEM characterisation of the samples 69
3.1.1. Experimentally determined k-factors 69
3.1.2. TEM characterisation of surfaces and defects/dislocations 76
3.1.3. Ternary diagrams of bridgmanite in the Mg-Al-Si system 78
3.2. Al-Si interdiffusion in bridgmanite 83
3.2.1. SEM investigations of bridgmanite diffusion experiments 83
3.2.2. Diffusion profiles and coefficients 88
3.2.3. Comparison of diffusion coefficients 94
3.2.4. Temperature dependence of Al-Si interdiffusion at 24 GPa 101
3.3. Evaluation of the diffusion experiments S7766 and H5548 104
3.4. Stishovite observations 110
4. Discussion 113
4.1. Evaluation of data reliability 113
4.2. Magnitude of Al-Si interdiffusion in the Earth's lower mantle 116
4.2.1. Effect of grain size and contribution of grain boundary diffusion 118
4.2.2. Comparison of other diffusing species in bridgmanite 120
4.2.3. Effect of mineral structure on diffusion 122
4.2.4. Effect of Al^{3+} substitution and point defects on bridgmanite properties 124
4.2.5. Effect of sample surface treatment and convolution 126
4.3. Effect of temperature 128
4.4. Rheology of the lower mantle 130
4.5. Potential geothermometer 132
5. Conclusion and Perspectives 134

Acknowledgements 138
List of Figures 140
List of Tables 152
List of References 154
Appendix A: Tables 168
Appendix B: Figures 174
(Eidesstattliche) Versicherungen und Erklärungen 176

1. Introduction

1.1. Problem statement

Bridgmanite is the most abundant mineral in the lower mantle, so it is essential to study the different properties of this mineral under the pressure and temperature conditions of the lower mantle. However, not all influences on the lower mantle have been studied. It is generally accepted that the mantle is divided into two parts. The high-pressure transition to the magnesium silicate mineral ringwoodite represents the mantle transition zone at a depth of about 660 km. The transition into $MgSiO_3$ bridgmanite marks the upper boundary of the lower mantle. To date, theoretical models show that bridgmanite remains stable down to the lowest part of the mantle, known as the D″ layer, at a depth of about 2,700 km to 2,900 km.

It is commonly agreed that bridgmanite contains a significant amount of ferric iron (Fe^{3+}) (McCammon, 1997) and a significant amount of aluminium (Al^{3+}). Aluminium seems to have emerged from lower-pressure Al-bearing minerals such as majorite (Shimojuku *et al.*, 2009; Van Mierlo *et al.*, 2013), which break down after the transition zone. Al can affect the viscosity of bridgmanite in the lower mantle and, consequently, the heat transfer from the core to the upper mantle and the Earth's thermal profile. It is widely accepted that the lower mantle is highly viscous and mainly flows influenced by diffusion-driven mechanisms (Reali *et al.*, 2019 a; Reali *et al.*, 2019 b). In general, diffusion rates depend on many factors, such as the grain size of the rock aggregate, the diffusing species, the crystallographic structure of the lattice, the presence and type of defects in the lattice, the pressure and temperature conditions. Many researchers have already studied diffusion in mantle minerals like wadsleyite, ringwoodite and majorite (Holzapfel *et al.*, 2009; Shimojuku *et al.*, 2009; Chakraborty, 2010). While diffusion studies in bridgmanite have been limited to Si and Mg self-diffusion (e.g. Yamazaki *et al.*, 2000; Xu *et al.*, 2011) and Fe-Mg interdiffusion (Holzapfel *et al.*, 2005), the effect of Al has not yet been investigated.

An analysis of the literature on diffusion in mantle minerals shows that there are discrepancies in the order of 1 to 2 in laboratory diffusion experiments. Even when the diffusion mechanisms are similar, it is clear that a large amount of information needs to be included to make a conclusive statement about rheological issues in the lower mantle. One possible reason for the discrepancies in the literature is the contribution of the much faster grain boundary diffusion, which becomes significant under laboratory conditions due to the small grain size. In contrast, in the Earth's mantle, volume diffusion conditions determine the effective diffusion coefficients. Until a few years ago, it was difficult to synthesise mineral grain sizes of more than a few microns under laboratory conditions. As conventional methods do not provide sufficient resolution to exclude grain boundary diffusion at a grain size of less than 2 - 3 µm, grain boundary diffusion may affect the effective diffusion coefficients differently from study to study. An appropriate technique is necessary to determine the volume diffusion coefficient correctly. In this work, we used high-temperature, high-pressure machines, which are designed to maintain Earth's mantle conditions for long periods of time, thus providing the opportunity to synthesise Earth's mantle minerals with large grain sizes. To determine the volume diffusion of Al and Si under natural conditions, mineral grains up to 20 µm in size were synthesised and investigated using a high-resolution analytical technique. Transmission electron microscopy (TEM) was found to be an excellent technique to determinate short diffusion profiles < 200 nm. Since Fe-Mg interdiffusion in bridgmanite has already been addressed in the literature (Holzapfel *et al.*, 2005), we focussed our study on Al-Si interdiffusion in iron-free bridgmanite to be able to consider volume diffusion independently of other diffusing species.

1.2. **Bridgmanite in the lower mantle**

Bridgmanite ($MgSiO_3$) occurs over a wide range of depths from 660 km to several hundred kilometres above the core-mantle boundary (~ 2,700 km) as an orthorhombic ABO_3 perovskite structure and has two cation positions: Si^{4+} in octahedral coordination (B-site substitution; shown in blue in Figure 1.1) and Mg^{2+} occupying a larger dodecahedral site (A-site substitution, a distorted bicapped prism; shown in orange in Figure 1.1). Al^{3+} is the most abundant trivalent cation substituting into bridgmanite, followed by Fe^{3+} (McCammon, 1997; Lauterbach *et al.*, 2000), and can be incorporated either by substitution for Si, with charge balance provided by the formation of oxygen vacancies (OVs) or by the charge-coupled (CC) substitution of Mg and Si by 2 Al (Liu *et al.*, 2019). See section 1.3.2. Furthermore, bridgmanite occurs in the space group *Pbnm* (Horiuchi *et al.*,1987) and is distorted with the a- and b-axes deviating by 45° from the cubic type-structure (space group $Pm\bar{3}m$) with tilted corner-linked SiO_6 octahedra (B-site). Mg-occupied cavities form bicapped trigonal prisms (A-site) (Glazer, 1972; Howard & Stokes, 1998, 2004). After the discovery of $MgSiO_3$ perovskite in meteorite samples (Tschauner *et al.*, 2014), it was named bridgmanite. Bridgmanite honours the 1946 Nobel laureate in Physics, Percy W. Bridgman (1882 – 1961). He received his Nobel Prize for his fundamental contributions to high-pressure mineralogy and high-pressure research in general.

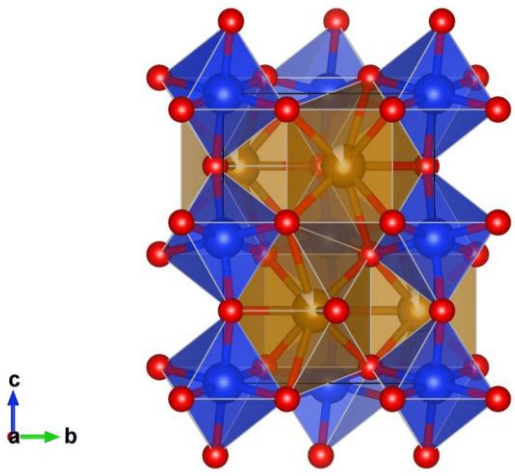

Figure 1.1: Crystal structure of bridgmanite (Mg, Fe)SiO_3 (space group Pbnm, #62). Red spheres represent oxygen (O) atoms, orange spheres represent magnesium (Mg) or iron (Fe) atoms, and blue spheres correspond to silicon (Si) atoms. The two cation positions of bridgmanite can be seen: the dodecahedral A-site substitution of Mg and the octahedral B-site substitution of Si. Figure by Merkel (2023).

The Earth's lower mantle is considered to consist of ~ 80 % $MgSiO_3$ bridgmanite (Irifune, 1994; Tschauner *et al.*, 2014), ~ 20 % ferropericlase and a small amount of $CaSiO_3$ perovskite by volume. Bridgmanite is omnipresent in the lower mantle, accounting for 38 vol.-% of the total Earth (Stixrude & Lithgow-Bertelloni, 2011). Various lines of evidence show that it formed by the breakdown of $(Mg, Fe)_2SiO_4$ olivine into (Mg, Fe)O periclase and $(Mg, Fe)SiO_3$ bridgmanite below 660 km depth, and extends nearly down to the core-mantle boundary region at a depth of 2,900 km (Ito & Matsui, 1978; Ito *et al.*, 1984; Ringwood, 1991; Hemley, 1992; Murakami *et al.*, 2005; Stixrude & Lithgow-Bertelloni, 2012). Mantle viscosity is a key parameter in all model calculations and estimates of mantle convection (Bunge *et al.*, 1996; Tackley, 1996) and the thermal state of the Earth (Reali *et al.*, 2019). It is now well accepted that the mantle flows by solid-state creep (Maurice *et al.*, 2017) and, consequently, that its viscosity depends on temperature (through activation energy) and pressure (through activation volume) (Poirier & Liebermann, 1984). Understanding diffusion creep in the major silicate, bridgmanite, at relevant high pressures and high temperatures is essential for constraining the viscosity of the lower mantle. This will be introduced in section 1.5 and discussed in section 4.3.

1.3. **Diffusion in bridgmanite**

Diffusion is a fundamental physical process in which atoms migrate through matter by following the gradients from a highly concentrated region to a less concentrated region, leading to the homogenisation of materials. If this motion of material becomes undirected, it leads to a random flux. The mathematics of the random-walk problem allows us to go back and forth between the diffusion coefficient defined in Fick's laws (Fick, 1855b, 1855a). The first law describes the flux of material *J* in response to a concentration gradient:

$$J = -D\nabla C \qquad (1.1)$$

where ∇C is the concentration gradient and *D* is called the diffusion coefficient. For non-cubic minerals, the measuring diffusion coefficients are direction-dependent and must be considered. Bridgmanite has an orthorhombic crystal structure and consists of three independent components: D_{11}, D_{22}, and D_{33} for the normal convention of the crystal-physical coordination system (Nye, 1985). For direction-dependence, the flux J_i shows in the i-direction, and the first Fick's law from Equation 1.1 changed to:

$$J_i = -D_{ij}\nabla C_j \qquad (1.2)$$

where ∇C_j is the concentration gradient derivative in the j-direction and D_{ij} is the diffusion tensor's corresponding component, forming a symmetric second-rank tensor (Lane & Ganguly, 1980). Diffusion anisotropy in bridgmanite has been shown to be weak through the lattice (Wentzcovitch *et al.*, 2004; Karki *et al.*, 2000). Therefore, the directional dependence of diffusion for orthorhombic bridgmanite has been neglected in this study. In diffusion couple experiments, the diffusion is usually in the non-steady state where the flux is a function of time. Taking this into account, Fick's second law can be obtained:

$$\frac{\partial C}{\partial t} = \nabla \cdot (D\nabla C) \qquad (1.3)$$

1.3.1. Solution to Fick's equation

This section will outline a form of the solution of Fick's equation for an important case, which forms the basis for most experimental determinations of the diffusion coefficient *D*. This consists of setting up a diffusion couple in which a specimen with a specific element concentration C_1 is physically connected to another sample with the element concentration C_2. In this experimental setup, it is essential to distinguish the concentration and composition between the diffusion couples to estimate the diffusion direction of specific specimens. In this case, it is the Al-Si interdiffusion, where Al diffuses into the $MgSiO_3$ endmember, and Si diffuses into the Al-bearing diffusion companion. Neither Al nor Si can move independently of the other, and the movement of both contributes to the rate of homogenisation and hence to the value of *D* obtained from Fick's second law. This equation is useful to describe the diffusion equation under experimental conditions:

$$C(x,t) = \frac{C_1 + C_2}{2} + \frac{C_1 - C_2}{2}\,\mathrm{erf}\left(\frac{x}{2\sqrt{Dt}}\right) \qquad (1.4)$$

In general, the concentration is a function of time *t* and distance *x*, and the diffusion coefficient is calculated using the mathematical error function (*erf*) (Putnis, 1992). Interdiffusion is characterised by diffusion from lattice to lattice and is referred to as lattice diffusion. In some literature, lattice diffusion is also referred to as volume diffusion. For the sake of clarity, only the term "volume diffusion" is used in this document. Volume diffusion can be either isotropic or anisotropic, depending on the diffusion medium. As can be seen in Figure 1.2, there are several diffusion pathways in the lower mantle. Volume diffusion is just one of them. As mentioned at the beginning, this study aims to contribute to the rheological questions of the Earth's lower mantle under natural conditions. Since grain boundary diffusion is negligible in the lower mantle, this study focuses exclusively on volume diffusion. On long geological time scales, diffusion processes can reach the macroscopic scale, making it one of the most important processes in geophysics, which also controls the viscosity of the minerals.

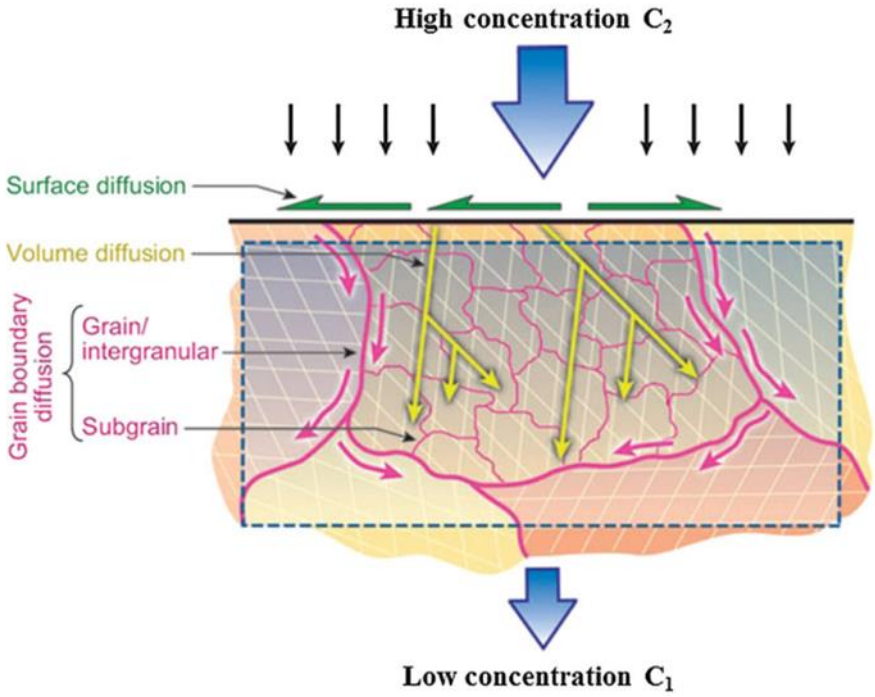

Figure 1.2: Schematic drawing of three types of diffusion paths in polycrystalline materials. Surface diffusion is the motion of atoms or molecules on the solid surface matter. Volume diffusion is diffusion through the crystal lattices and is also called lattice diffusion. Grain boundary diffusion is relatively faster than bulk diffusion along individual grain boundaries. This is due to the gradient, as less energy must be expended to diffuse along a grain boundary than through the crystal lattice. Figure by Zhang (2017).

1.3.2. Substitution mechanism in Al-bearing bridgmanite

Bridgmanite is the main host phase of aluminium (Al) in the Earth's lower mantle (Irifune, 1994), and Al, therefore, produces significant effects on the chemical and physical properties of bridgmanite, including elasticity (Walter *et al.,* 2004) and electrical conductivity (Yoshino *et al.,* 2016). Decisive here is the relevant components $AlAlO_3$ and $MgAlO_{2.5}$, referred to as the charge-coupled (CC) component and oxygen-vacancy (OV) component (Hirsch & Shankland, 1991; Richmond & Brodholt, 1998; Navrotsky, 1999; Navrotsky *et al.,* 2003a; Andrault *et al.,* 2007). In the CC component, Al^{3+} ions occupy only Mg^{2+} A-sites and Si^{4+} B-sites in the orthorhombic perovskite structure along the $MgSiO_3 – M_2O_3$ join:

$$Mg_{Mg}^{X} + Si_{Si}^{X} \rightarrow M_{Mg}^{\cdot} + M_{Si}^{\prime} \qquad (1.5)$$

This achieves electrical neutrality without forming vacancies. Here the superscript $(\cdot)$ represents a positive and $(')$ a negative net charge on the site, and (X) indicates a neutral charge (Kröger & Vink, 1956). This aluminium substitution can refer to a stoichiometric or Tschermakitic substitution (Navrotsky *et al.,* 2003a) and can be written as a $MgSiO_3 – AlAlO_3$ join. The OV substitution takes place along the $MgSiO_3 – MgMO_{2.5}$ join (Liu *et al.,* 2019):

$$2\, Si_{Si}^{X} \rightarrow V_{O}^{\cdot\cdot} + 2\, M_{Si}^{\prime} \qquad (1.6)$$

An oxygen vacancy is created to provide charge balance by replacing Si^{4+} on the B-site. This mechanism forms defects (see section 1.3.3) and can be written as $MgSiO_3 – MgAlO_{2.5}$ (red dashed line in Figure 1.3). The mechanism is an analogue to the $CaTiO_3$ perovskite – $CaFeO_{2.5}$ brownmillerite join (Becerro *et al.,* 1999) and leads to the incorporation of trivalent cations in most low-pressure ceramic perovskites (Navrotsky, 1999). Considering the coexistence of ferropericlase and bridgmanite in the lower mantle, this mechanism may also have a significant impact on the lower mantle. The low SiO_2 activity favours Mg/Si > 1, and the resulting oxygen vacancies provide an opportunity to influence mantle diffusivity, conductivity, compressibility, and creep rate and to incorporate water into the dense structure of bridgmanite (Navrotsky *et al.,* 2003a; Murakami *et al.,* 2005). Sample compositions along the $MgSiO_3 – AlAlO_3$ join (blue dashed line in Figure 1.3) produce Brg samples that fall along the charge-coupled substitution (CCS) trend line. On the other hand, sample compositions with Mg > Si result in Brg compositions (red dashed line in Figure 1.3) between the CCS and oxygen-vacancy substitution (OVS) trend lines.

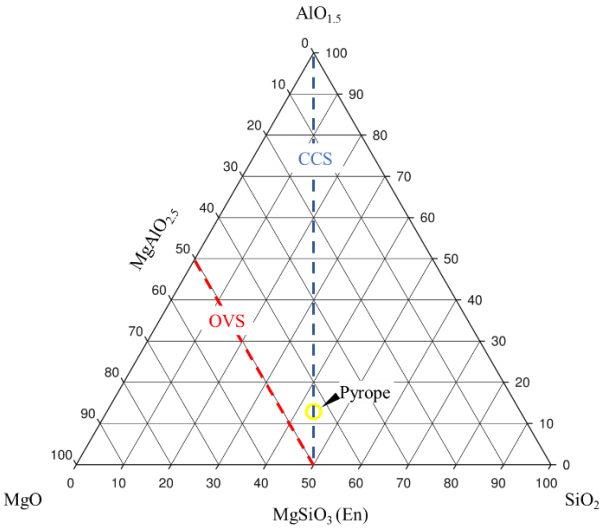

Figure 1.3: Substitution mechanism in ternary systems. Sample compositions along the $MgSiO_3$ – $AlAlO_3$ join (blue dashed line) produce bridgmanite samples that fall along the CCS trend line. Sample compositions with Mg > Si result in bridgmanite compositions (red dashed line) between the CCS and OVS trend lines. Figure modified after Liu et al. (2019, Figure 1).

Previous results suggest that CCS dominates in aluminous bridgmanite, as shown by the cation ratio between Mg and Si (Mg/Si) as a function of the Al per formula unit (pfu) in aluminous bridgmanite (Kubo & Akaogi, 2000; Stebbins, Kroeker & Andrault, 2001; Navrotsky *et al.*, 2003 a; Walter *et al.*, 2006; Liu *et al.*, 2017 a, 2019; Liu *et al.*, 2019). However, the XRD patterns in the study of Liu *et al.* (2017 b) and in this study show that trace amounts of stishovite can coexist with bridgmanite, suggesting that trace amounts of oxygen vacancy substitution may also occur in aluminous bridgmanite. The literature review by Huang (2020) shows an OVS dominance at low Al pfu (< 0.10 pfu), as shown in Figure 1.4 a. Further supporting this, it can be seen in Figure 1.4 b that the $MgAlO_{2.5}$ OVS component initially increases to a maximum at Al = ~ 0.1 atoms pfu and then decreases with further increase in Al. This is due to interaction parameters indicating less than ideal mixing of oxygen vacancies and the mixing of Mg and Al at the A-site. This means that much larger interaction parameters for cation mixing are required than are common in other mantle silicates to significantly affect speciation with a small change in total Al content. The exchange of the $AlAlO_3$ and $MgAlO_{2.5}$ components in Brg has been described in the literature (Panero *et al.*, 2006; Huang, 2020).

The OV component has also been shown to reduce the creep strength of bridgmanite, which may account for the increase in the mid-mantle viscosity (Liu *et al.*, 2017 a). Bridgmanites with oxygen vacancies have significantly higher compressibility than those without such vacancies. These oxygen vacancies become unfavourable at high pressures and therefore affect the physical properties of the shallow lower mantle mainly through Al (Brodholt, 2000). The vacancy concentration limit in nominally pure $MgSiO_3$ bridgmanite appears to be on the order of 10^{-2} (Reali et al., 2019 b) and is associated with a preferential substitution site. When trivalent cations such as Al partition onto the Si site, extrinsic oxygen vacancies will increase, suppressing the concentration of cation vacancies. If Al is partitioned onto the Mg site, this would enhance the cation vacancy concentrations but create a disorder and depress the oxygen vacancy concentrations to an intrinsic level. This type of disorder would affect the diffusion of oxygen to a rate-limiting mechanism for the climb with vacancy concentrations many orders of magnitude lower than 10^{-2} (Reali *et al.*, 2019 a).

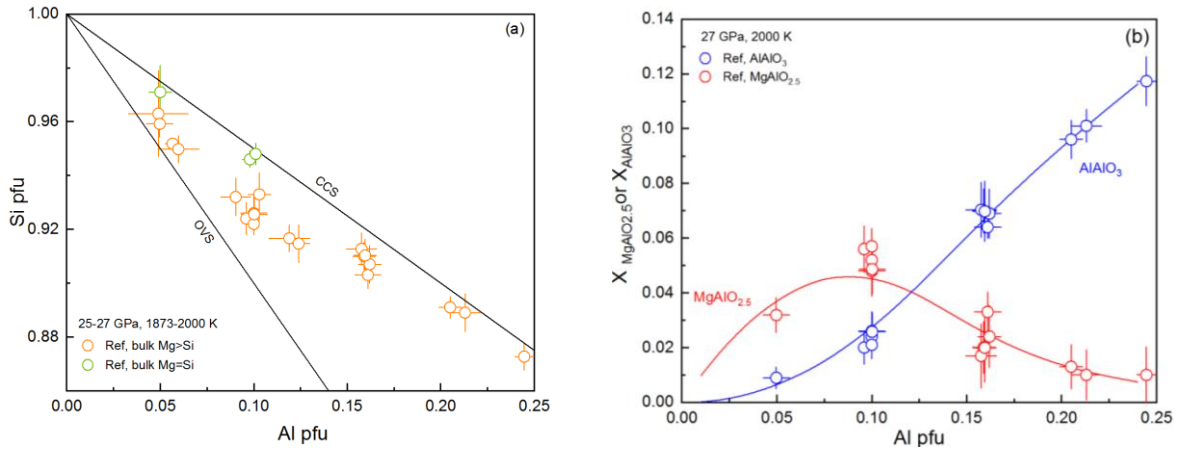

Figure 1.4: (a) Si cation number of Brg versus the Al per formula unit based on three oxygens at 25 – 27 GPa and 1,600 – 1,727 °C. The CCS and OVS lines indicate the trend expected for trivalent cation substitution by charge-coupled or oxygen vacancies substitution mechanisms. Different starting bulk compositions were studied: Mg > Si for the orange circles and Mg = Si for the green ones. The data comes from Navrotsky et al. (2003b); Kojitani et al. (2007); Liu et al. (2017 a), and Liu et al. (2019 a, b). (b) Mole fraction of $MgAlO_{2.5}$ (red) and $AlAlO_3$ (blue) versus the Al per formula unit at 27 GPa and 1,727 °C. The data come from Liu et al. (2019 a, b). The lines were calculated based on the thermodynamic models. Figures by Huang (2020).

1.3.3. Defects in bridgmanite

One way that diffusion allows minerals to change their chemical composition and crystal structure is through point defects. In general, there are two types of crystal defects: point defects and line defects. Some defects are acquired during the growth of the crystals when they are first formed, and others develop in the crystals during deformation. These defects determine the strength of crystals, minerals and rocks. The motion of these defects accommodates the strain of the crystals. Point defects are defined as zero-dimensional atomic disorders in a perfect atomic lattice, such as missing ions, also called vacancy defects, impurities and interstitial ions (Figure 1.5).

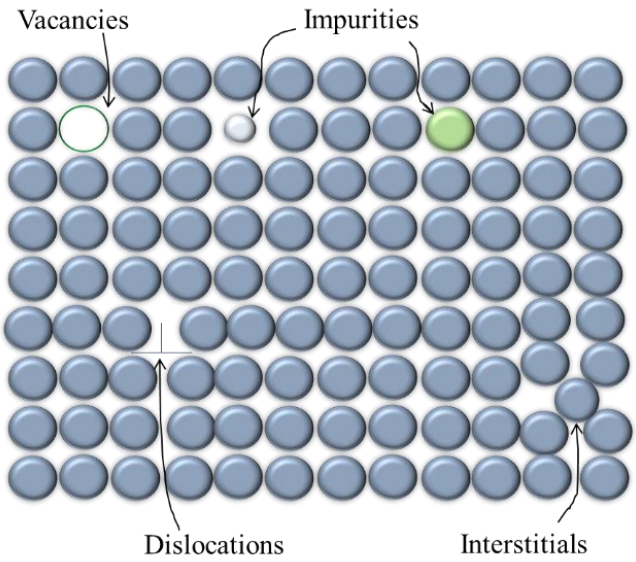

Figure 1.5: Point defect species in crystals. Vacancy defects are lattice sites in a crystal that would otherwise be occupied by a regular atom or ion. Interstitial defects are atoms such as the ones the crystal is made of that sit 'in the gap' between the regular atoms. Impurity atoms (green) or ions (light grey) are often incorporated into a crystal. These are neither vacant sites nor regular atoms on an interstitial site. The diffusion of impurity atoms does not require vacancies. Here the atoms jump directly from one interstitial site to the next. Interstitial impurity atoms, therefore, often diffuse faster than substitutional atoms.

Line defects, on the other hand, are called dislocations and occur as additional one-dimensional planes of atoms in the crystal lattice. Their motion accounts for much of the strain in crystals and weakens the crystal structure. Furthermore, the motion is controlled by the slowest diffusing species in minerals (e.g. Kirby & Raleigh, 1973), which means that the rate-controlling process is a dislocation climb, (e.g. Kohlstedt, 2006). Si is the rate-limiting element in most silicate minerals in the Earth's lower mantle (Costa & Chakraborty, 2008; Dobson *et al.*, 2008; Shimojuku *et al.*, 2009). Deformation occurs through dislocation motions, including dislocation glide on a given glide plane and dislocation climb out of its glide plane. The theoretical model of Weertman (1968) shows that the plastic strain is mainly produced by dislocation glide. In total, there are two types of dislocations: edge dislocations and screw dislocations (Figure 1.6). An edge dislocation is the edge of an extra half-lattice plane that extends part way across the crystal lattice structure and glides through the whole crystal by strain and annihilation of the dislocation. Furthermore, edge dislocations can also rise by adding or removing vacancies. Screw dislocations, however, are more complex; they are the edge of a zone along which the crystal has been translated parallel to the dislocation line. Screw dislocations can also glide through the lattice. The movement of the planes by any translation vector of the lattice is called Burger's vector *b*. For edge dislocations, the Burger's vector is perpendicular to the dislocation line (Figure 1.6 a) and, for screw dislocations, *b* is parallel to the line (Figure 1.6 b). If there were no dislocations in crystals, all crystals would be brittle.

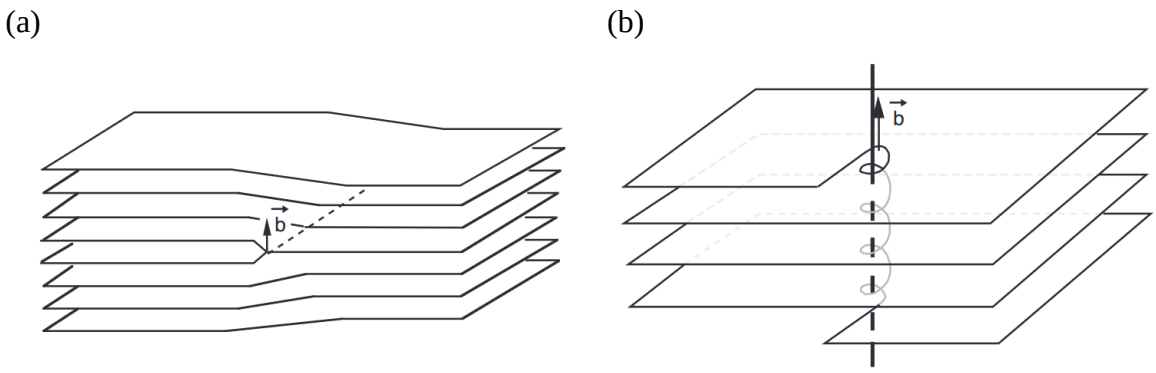

Figure 1.6: Scheme of (a) edge dislocation and (b) screw dislocation. (a) Edge dislocation: The Burger's vector b (the movement of the planes through any translation vector of the grid) is perpendicular to the dislocation line. (b) Screw dislocation: The Burger's vector b is parallel to the dislocation line. Figure by Oswald (2019).

The point defects depend on thermal vibrations and occur with increasing temperature in many materials, such as metal, ionic and molecular crystals (Chadwick & Terenzi, 1985). The mobility of atoms in the crystal lattice increases and solid-state diffusion is enhanced. So, for example, neighbouring atoms will jump in a vacancy. This site occupancy only works when the neighbouring site is vacant or when the jump of an interstitial atom is considered. Therefore, the mobility V and the number of point defects affecting the diffusion coefficient D are as follows:

$$D = [V] * D_v \tag{1.7}$$

where [V] includes all defect types and D_v is the diffusion rate of V. The dependence of the defect concentration can be calculated similarly to the temperature dependence (section 1.3.4). For this, a thermodynamic view is helpful. For a given temperature T ($T > 0$ K), the Gibbs free energy of a crystal $G(T)$, is,

$$G(T) = G^0(T) + N_V \Delta E_f - T\Delta S_{conf} \tag{1.8}$$

where $G^0(T)$ is the Gibbs free energy of a perfect crystal at temperature T, plus the number of defects N_V and the energy required to form a single defect ΔE_f minus the temperature-dependent crystal entropy $\Delta S_{conf} \approx -kN_V \times ln$, assuming the equilibrium state where N_V and $G(T)$ are constant (Borg & Dienes, 1988; Schmalzried & Frick, 1995). Using the configured entropy S of the defects in the lattice, the following formula is obtained:

$$N_V = A_0 N \exp(-\Delta E_f kT); \qquad C_V = \frac{N_V}{N} = A_0 exp\left(-\frac{\Delta E_f}{kT}\right) \tag{1.9}$$

With constant A_0 and the concentration of defects C_V, Equation 1.9 relates to the Arrhenius relationship. If the Boltzmann constant k is converted into the ideal gas constant R and ΔE_f relates to the energy required to form 1 mole of defects ΔE_{mol}, the concentration of defects is therefore a function of temperature:

$$\frac{N_V}{N} = A_0 \exp\left(-\frac{\Delta E_{mol}}{RT}\right) \tag{1.10}$$

For deeper detailed insights, literature such as Borg & Dienes (1988) and Schmalzried & Frick (1995) is recommended. Most dislocations in crystals have both edge and screw components and form complex geometrical shapes.

1.3.4. Temperature dependence of diffusion coefficients

Not only is defect propagation thermally dependent, but diffusion as a separate mechanism is also a thermally controlled process in which activated atoms are transported along a distance *x* as a result of random molecular motion (Crank & Gupta, 1975). This process is mainly affected by atomic jumps and increases significantly with temperature. These atomic jumps strongly depend on point defects and temperature. Therefore, the diffusion coefficient *D* depends strongly on temperature and defect concentration (section 1.3.3). The temperature dependence of the diffusion coefficient often follows an Arrhenius relationship:

$$D = D_0 \exp\left(-\frac{E_A}{RT}\right) \qquad (1.11)$$

where E_A is the sum of activation energies $\Delta E_{mol} + \Delta E_i$, with ΔE_i representing extrinsic diffusion and ΔE_{mol} representing intrinsic diffusion affected by defect motion. D_0 is the pre-exponential factor that, among other things, can be related to the increase in entropy due to diffusion, geometric factors and jump frequency of the atom (Mehrer, 2005), *R* is the universal molar gas constant, and *T* is temperature. Equation 1.11 implies a linear relationship of *ln D* versus inverse temperature where the slope gives the activation energy (Figure 1.7).

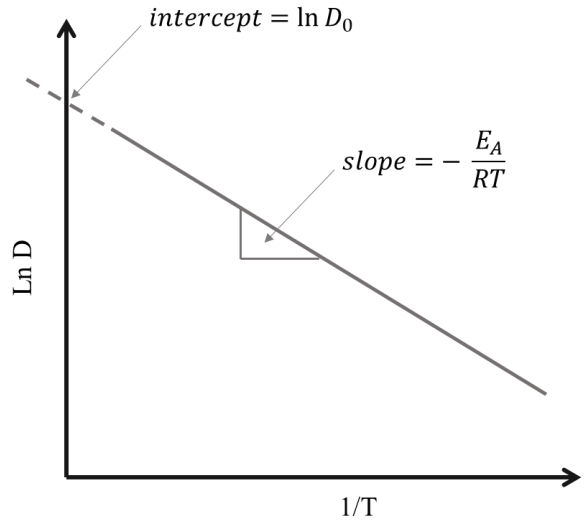

Figure 1.7: The Arrhenius plot is obtained by the linear relationship of ln D versus inverse temperature. The line helps find the missing variables of the Arrhenius equation. The slope gives the activation energy divided by the gas constant R, and the extrapolation of the line back to the y-intercept yields the value for ln D_0.

Thermal intrinsically and extrinsically activated mechanisms control diffusion. Intrinsic temperature dependence has been understood as the increase in the concentration of vacancies or interstitials with temperature. At the same time, extrinsic diffusion depends on changes in the impurities that control the defect concentrations. Since the activation energy for extrinsic diffusion (ΔE_i) is usually weaker than that for intrinsic diffusion (ΔE_{mol}), the temperature

dependence of diffusion is mainly influenced by intrinsically activated mechanisms (Chakraborty, 1997). In conclusion, the Arrhenius relation depends on many factors (such as impurities or microstructural irregularities and vacancies) and should be taken into account in calculations. When vacancies start to migrate, this process is called Nabarro-Herring creep and is part of the diffusion creep mechanism, which will be explained in the following section 1.4.1. Furthermore, the diffusion coefficients along a mantle geotherm can be calculated (Stacey & Davis, 2004) to provide an overview of the relation between diffusion, pressure and temperature conditions through the depths of the Earth's interior.

1.4. Creep mechanism in bridgmanite

Plastic deformation, including dislocation and diffusion creep in deformed minerals, is controlled by the dislocation density and the rate of dislocation motion (Xu, 2017). Therefore, the slowest diffusing atom controls the rate of plastic deformation. Due to the high lattice friction that inhibits sliding in bridgmanite, climb should also be considered (Kraych *et al.*, 2016; Kraych *et al.*, 2016). Dislocations move through climb by absorbing or emitting point defects (e.g. vacancies) and generating strain through them. Diffusion is mediated by a vacancy-exchange mechanism (see section 1.3.2) and occurs only through the bulk of the lattice (Herring's model). This mechanism is driven by the gradient of the vacancy potential μ_v and the difference between the chemical potentials of the relevant atoms μ_A (Brassart & Delannay, 2019). Under high-pressure – high-temperature conditions, vacancies can diffuse through the lattice, as considered in the Nabarro-Herring creep mechanism (Herring, 1950; Nabarro, 1967) which will be introduced in the following section.

Either dislocation creep or diffusion creep dominates the deformation mechanism in the lower mantle. The dislocation creep is independent of grain size *d*. Recent experimental studies have challenged the conventional view of dislocation creep and shown that diffusion processes influence creep and grain growth in forsterite (Nakakoji & Hiraga, 2018). This aggregate serves as an analogue for the upper mantle. These studies show that large parts of the Earth are likely to be deformed by diffusive creep under the superplastic Earth hypothesis (Maruyama & Hiraga, 2017; Okamoto & Hiraga, 2022).

On the other hand, diffusion creep is inversely proportional to d^2 (Nabarro-Herring creep) or d^3 (Coble creep), where *d* is the average grain size. Additionally, thermally activated atomic transport drives the deformation mechanism in diffusion creep. The grain size of bridgmanite in the lower mantle is estimated to be less than 1 mm even after 1 billion years (Solomatov *et al.*, 2002; Solomatov & Reese, 2008; Glišovic *et al.*, 2015). Fei *et al.* (2021) show that the grain size of bridgmanite will be 30 – 45 μm. This leads to the assumption that the D_{eff} depends mainly on volume diffusion, which is one of the main focal points of our study.

1.4.1. Diffusion creep

Creep is the slow plastic deformation of a material under constant stress. When the stress is low and the high temperature is constant, polycrystalline materials deform by diffusion creep (Cocks, 1996). This stress is balanced in diffusion creep by atoms moving from areas of high stress to low-stress areas. In contrast, vacancies move from low-stress to higher-stress regions in the crystal lattice. Vacancies at grain boundaries that are under tension in the direction of the grain boundary typically diffuse to grain boundaries at which compressive stresses usually prevail at the grain boundaries (Figure 1.8). This is achieved either by volume diffusion or by grain boundary diffusion. This process of vacancy migration is called Nabarro-Herring creep. Higher chemical potentials prevail at the highly stressed surface and matter can flux down the chemical gradient. This mechanism is described by the Nabarro-Herring equation (Herring, 1950) for pure shear:

$$\dot{\varepsilon} = A\,\sigma\frac{D_{eff}\Omega}{d^2RT} \qquad (1.12)$$

where d is the characteristic grain size, A is a geometrical factor (40/3 or 16/3 with or without grain boundary sliding, respectively), Ω is the molecular volume and the effective diffusion coefficient was given by Stocker & Ashby (1973) and further developed by Frost & Ashby (1982)

$$D_{eff} = D_v + \frac{\pi\delta}{d}D_{gb} \qquad (1.13)$$

Here, δ is the effective grain boundary width, d is the grain size and D_{gb} is the grain boundary diffusion coefficient. Previous studies show for Si self-diffusion approximately 4 orders of magnitude faster grain boundary diffusion than volume diffusion (Yamazaki *et al.*, 2000). For Al-Si interdiffusion in bridgmanite no experimental data on grain boundary diffusion exist. Still, assuming that the grain boundary width in the lower mantle is 1 nm (Holzapfel *et al.*, 2005) and the grain size is larger than 100 µm (Solomatov & Reese, 2008; Shimojuku *et al.*, 2014), a quantitative estimation shows the effective diffusion coefficient becomes $\approx D_v$.

This is supported by the current assumption that the volume diffusion D_V becomes dominant (Ammann et al., 2010). D_{eff} can be used to estimate the strain rate, which is described as follows (Nabarro, 1948; Herring, 1950; Coble, 1963; Frost & Ashby, 1982):

$$\dot{\varepsilon}_{diff} \approx \alpha\sigma \frac{D_{eff}}{d^2} \frac{\Omega}{RT} \quad (d > 0.1\,mm) \tag{1.14}$$

with tension σ and the constant α. However, grain boundary diffusion may be significant in other systems, called Coble creep (Poirier, 1985). In the Nabarro-Herring creep, the flow of material occurs by diffusion through the lattice (Figure 1.8).

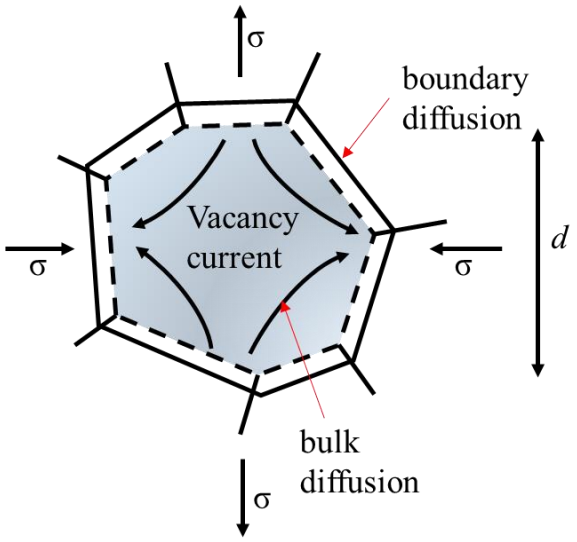

Figure 1.8: Creep by a diffusion mechanism modified after Bhadeshia (2003). Grain boundaries are sinks and sources of vacancies. Vacancies move in the crystal lattice from regions with low tension σ to regions with higher tension.

To measure the pure volume diffusion it is important to estimate the viscosity of the upper part of the lower mantle by the Nabarro-Herring creep (NH).

1.4.2. Dislocation Creep

In contrast to diffusion creep, dislocation creep is a deformation mechanism independent of grain size. Here, the crystals are deformed by the movement of dislocations through the crystal lattice. Under lower mantle conditions, the dislocation migrates by climb assistance, where the rate-limiting step is the transport of matter. Each time a dislocation moves, the movement is limited by the absorption and emission of point defects into or out of dislocations, which is controlled by the diffusion of atoms or vacancies (Hirth & Lothe, 1983.; Hull & Bacon, 2011). The part of the crystal thus shifts by one lattice point along a plane, relative to the rest of the crystal. The dislocation-climb process is in turn rate-limited by the fastest diffusion direction of the slowest diffusing species. The dislocation creep is a power law function of shear stress and is also believed to be controlled by the self-diffusion of the atoms in the lattice. Therefore, the activation energy for dislocation creep is identical to that for volume diffusion and leads to a strong lattice-preferred orientation at large strain:

$$\dot{\varepsilon}_{dis} \approx \alpha \sigma^n exp\left(-\frac{Q}{RT}\right) \tag{1.15}$$

where Q is the activation energy and n (= 3 – 5) is a dimensionless constant of strain, which describes the degree of stress dependence (Figure 1.9). So, to be able to make a meaningful assumption about the activation energy, it is of great interest to measure the diffusion coefficient experimentally and to be able to determine the activation energy via the Arrhenius connection.

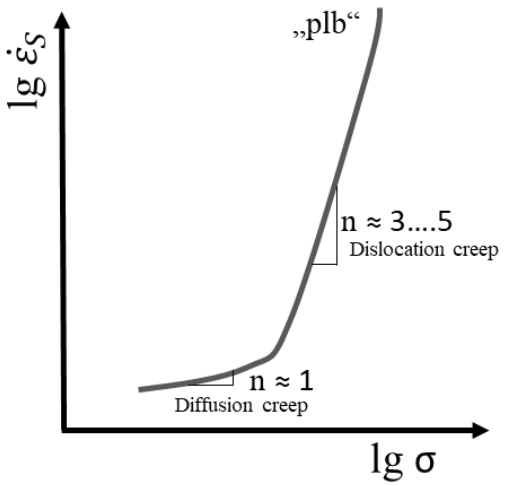

Figure 1.9: A second range of the creeping stage: range of constant/minimal strain rate with a dynamic equilibrium of strain hardening and softening (overcoming obstacles due to increased temperatures). Creep rate is an exponential function of temperature T and depends on external stress σ via a power law (see Equation 1.15). Creep exponent modified after Bürgel et al. (1998).

1.5. **Viscosity in the lower mantle**

Viscosity is arguably the most important parameter for understanding the thermochemical evolution of the Earth. The viscosity of the mineral aggregate of the Earth's mantle controls the strength of convection that transports heat from the core to the Earth's surface (Figure 1.10).

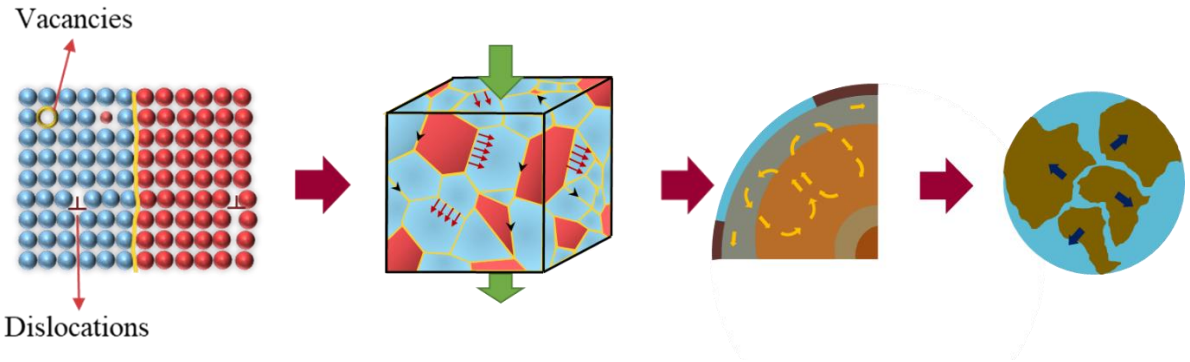

Figure 1.10: The mantle can flow like a viscous fluid at the geological time scale. This is influenced by the creep mechanism, which involves the motion of the atoms between crystals and their defects. This work focuses on elemental diffusion at the nanometre scale. It could, in the future, contribute to the modelling of bulk diffusion in the lower mantle, allowing the consequences for different Earth models to be considered.

This heat flow and the ratio of the viscosities of the upper and lower mantle determines plate tectonics (Höink *et al.*, 2012) and whether plates can penetrate the lower mantle and reach the core-mantle boundary. The viscosity of the mantle also determines the topology of the core-mantle boundary (Lay *et al.*, 2008) and its physical coupling with the core. The multitude of geophysical phenomena controlled by viscosity and its changes requires a better understanding of this quantity. However, our current knowledge of the viscosity of the Earth's mantle is very limited, as it is impossible to measure it directly.

The lack of seismic anisotropy in the lower mantle (e.g. Karato & Wu, 1993), the grain size (Solomatov, 2007) and the low stresses suggest that diffusion creep is the dominant creep mechanism in the lower mantle (Karato *et al.*, 1995). Additionally, the high viscosity and small grain size associated with small grain growth rates reported in previous studies (Yamazaki *et al.*, 1996; Imamura, 2018) suggest that the lower mantle is isolated from the convecting mantle as a primordial reservoir and is strongly affected by diffusive creep. Moreover, the viscosity can be linked to geophysical determinations of post-glacial rebound, geoid anomalies and convection (Mitrovica & Forte, 2004; Figure 1.11).

Bridgmanite with orthorhombic perovskite structure is the major component of the lower mantle, along with (Mg,Fe)O-ferropericlase and $CaSiO_3$-perovskite. The viscosity of the lower mantle results from the rheological behaviour of its two main constituents, the aluminous $(Mg,Fe)(Si,Al)O_3$ bridgmanite and (Mg,Fe)O-ferropericlase. Modelling of the long-wavelength non-hydrostatic geoid (Rudolph *et al.*, 2015) suggests an increasing viscosity in the region between 800 and 1,200 km depth. One possible explanation could be the experimentally determined deformation behaviour of ferropericlase (Marquardt & Miyagi, 2015). Tsujino *et al.* (2022) attempted to confirm the observed viscosity by using deformation mechanism maps of bridgmanite to explain the estimated viscosity of bridgmanite at lower mantle conditions.

Further understanding of mantle viscosity requires a detailed study of lower mantle mineral chemistry and defect structures. For example, an experimental study of oxygen vacancies in bridgmanite with increasing pressure shows that the fraction of oxygen vacancies in bridgmanite decreases continuously from 25 to 40 GPa, reaching almost zero at 40 GPa (Huang, 2020). This supports an increase in lower mantle viscosity towards 1,000 km on the assumption that oxygen vacancies affect the diffusion rate.

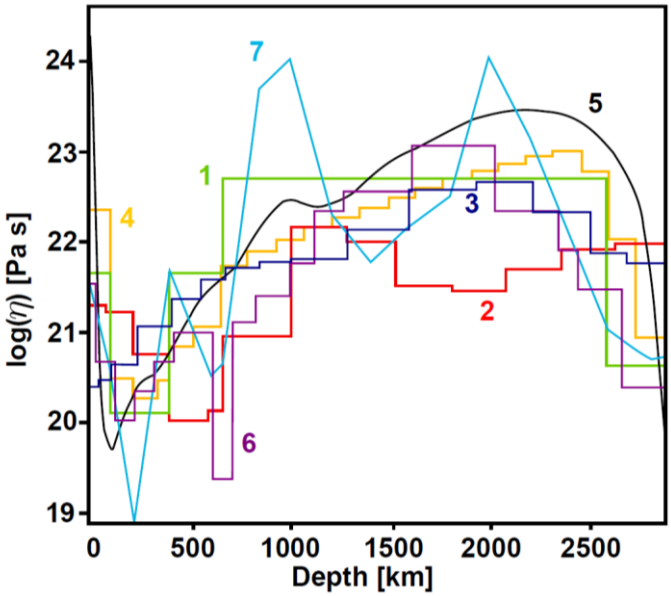

Figure 1.11: Viscosity models with depth from Amman (2011). Models were derived by inversion of geophysical data and involve different datasets, inversion techniques and observables: (1) (Hager & Richards, 1989), (2) (Forte & Mitrovica, 1996), (3) (Ricard & Wuming, 1991) (4) (Steinberger & Calderwood, 2001), (5) (McNamara et al., 2003) (6) (Mitrovica & Forte, 2004) and (7) (Forte & Mitrovica, 2001).

The experiments can provide insight into viscosity along the geotherm. Compared to models (Figure 1.11), a common trend emerges, starting with a stiff uppermost mantle, followed by a narrow region of low viscosity near the transition zone and a viscosity peak in the second half of the lower mantle. Moreover, Ammann (2011) experimentally limited the viscosity of the Earth's lower mantle to 10^{21-24} Pa and pointed out that the effects of impurities such as Fe and Al on diffusion need to be studied since the presence of impurities increases the number of vacancies, which should lead to a decrease in viscosity. He superimposed his diffusion data by a viscosity model from Mitrovica & Forte (2004) (Figure 1.12) and recognised the connection among viscosity, the geotherm and the absolute diffusion data by this time.

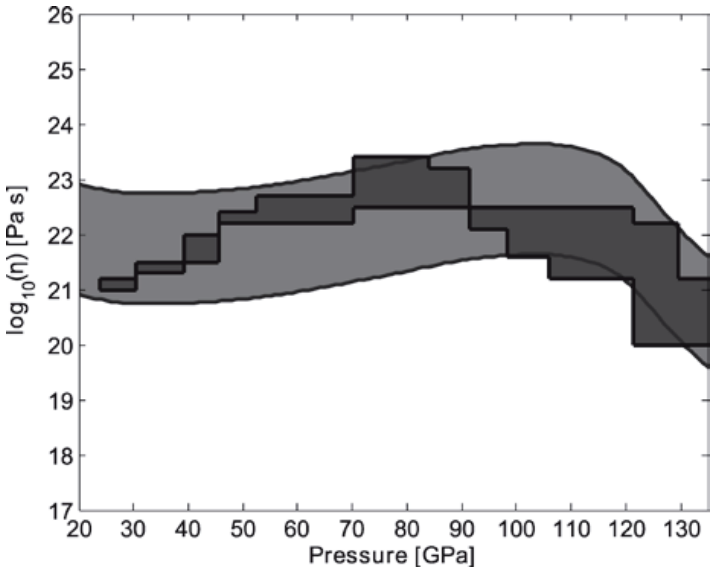

Figure 1.12: Calculated viscosity of perovskite in the lower mantle by Ammann (2011) based on his absolute diffusion results. The viscosity profile was calculated for the lower mantle using 100 % $MgSiO_3$ perovskites (curved) composition. Regarding upper bounds, he assumed the vacancy concentration $N_V = 2 \times 10^{-5} mm^{-1}$ for a grain size of 1 mm and for a grain size (G) of 0.1 mm a vacancy concentration of 2×10^{-7} mm^{-1}. The lower bound corresponds to $N_V = 2 \times 10^{-3}$ mm^{-1} (G = 1 mm) and $N_V = 2 \times 10^{-5}$ mm^{-1} (G = 0.1 mm), which is two orders of magnitude greater than the upper bound (for the same grain size). The geotherm was derived from Stacey (1995) and Stacey & Davis (2008). *Superimposed on his predicted viscosity profile is that obtained by Mitrovica & Forte (2004) from a join inversion of convection and glacial rebound data.*

1.6. State of analytical methods research

The diffusion coefficients reported in the literature were determined either by ab initio atomistic simulation (e.g. Wright & Price, 1993) or by experimental analysis of the diffusion profiles of diffusion elements obtained from high-pressure, high-temperature diffusion experiments. One widely used experimental method is secondary ion mass spectrometry (SIMS) (e.g. Xu *et al.*, 2017; Shimojuku *et al.*, 2009). SIMS is an analytical method with a detection limit of 10^{16} atoms/cm^3. This device analysis ejected secondary ions after sputtering the surface of the specimen with a focused primary ion beam. Other methods are Rutherford backscattering spectrometry (RBS) and Nuclear Reaction Analysis (NRA) (e.g. Cherniak & Watson 2019). The RBS is weakly sensitive to light elements, which often requires combining this method with NRA. These methods help to detect trace elements and to analyse elemental composition with depth. However, these methods are difficult to apply to diffusion pair experiments performed at high temperatures and pressures. This is because the sample must be polished to ¾ of the depth of the in epoxy mounted diffusion couple after the multi-anvil experiments. This means that the diffusion has to be analysed laterally, and the lateral resolution (greater than ~ 2 µm) of the analytical techniques mentioned above makes them unsuitable. Instead, an analytical method with sufficient accuracy and lateral resolution is required. Holzapfel (2004) suggested electron microprobe analysis (EPMA) and TEM as the most suitable methods for samples that can't be investigated in depth mode and need to be studied parallel to the surface. TEM provides significantly higher resolution and has been shown to be more efficient than EPMA for very short diffusion profiles (Meißner et al., 1998; Holzapfel, 2004). Based on existing data we expect diffusion profiles to be shorter than the resolution limit of EPMA, hence we used TEM for all analytical determinations.

1.7. Aim of this study

Mantle models provide a detailed picture of the viscosity that prevails in the lower mantle. However, most data for example magnesium, silicon and oxygen have been calculated without considering other major elements such as aluminium. Since it is known that the lower mantle contains a large amount of aluminium, this motivates experimental work to examine the data on which this is based. In this study, the activation energies of the diffusivity of Al in 6 coordinated Si-bearing high-pressure orthorhombic perovskite phases (bridgmanite) were determined and the influence of impurities such as trivalent atoms on the silicon diffusivity was examined. As previous studies have shown (Van Mierlo *et al.*, 2013), slow diffusion rates are to be expected for Al-Si interdiffusion experiments, which is why high-resolution methods are essential. Volume diffusion is also assumed to be dominant in the lower mantle, so the grains in the sample synthesis were grown to grain sizes larger than 2 µm to exclude grain boundary diffusion and to reproduce realistic mantle conditions.

Conventional methods for measuring short-concentration profiles mainly provide point micro analysis. The method here offers a complete quantitative chemical characterisation along a line-scan perpendicular to the diffusion interface. Therefore, a TEM method is used in the present work to demonstrate the possibility of measuring short concentration profiles (a few 100 nm) with high accuracy using Al-Si interdiffusion in experimentally prepared bridgmanite diffusion couples. This method is suitable both for small diffusion coefficients and for the direct determination of interdiffusion coefficients from experiments.

To perform the experiments, diffusion couples were prepared to study Al and Si interdiffusion rates. For this purpose, the minerals were synthesised at pressures of 24 GPa and temperatures of 1,750 – 2,000 °C using conventional tungsten carbide anvils in a multi-anvil apparatus.

After the high-pressure experiments, the diffusion couples were measured with an analytical transmission electron microscope (ATEM) equipped with an energy-dispersive X-ray spectrometer (EDXS) to determine, among other things, the Al concentration of coexisting phases with a resolution in the order of nanometres. By analysing diffusion profiles, accurate diffusion coefficients can be obtained. The diffusion coefficients obtained for different temperatures can be used to model the temperature dependence of the viscosity of bridgmanite in the lower mantle, which can be calculated via the diffusion activation energy, assuming diffusion-controlled creep in the bridgmanite. The aim of this project was to obtain diffusion coefficients for Al-Si interdiffusion at different temperatures of the lower mantle, which can be used in further projects for modelling the temperature dependence of the diffusion-controlled creep rate of bridgmanite to constrain the viscosity of the lower mantle and its variation with depth.

2. Experimental and analytical methods

2.1. Starting material preparation

To perform interdiffusion experiments, diffusion couples were first synthesised in appropriate compositions (Table 2-1). For this purpose, the dry and weighed oxides MgO, SiO_2, and Al_2O_3 were crushed to a homogeneous 1 g powder in an agate mortar using ethanol as suspension. Subsequently, two different preparation methods were chosen:

(1) For the Al-free samples, pyroxene was fabricated by a solid annealing. In this process, the powder for the endmember was pressed three times into pellets and annealed. This process converted the starting material into orthopyroxene at 1,650 °C in a solid-state reaction.

(2) In a platinum crucible, $Mg_{0.93}Al_{0.06}Si_{0.97}O_3$ (stoichiometric), $MgAl_{0.1}Si_{0.9}O_3$ (stoichiometric, higher Al content) and $MgAl_{0.05}Si_{0.95}O_3$ (Mg excess) homogeneous 1 g powder samples were fused at 1,650 °C and rapidly quenched into ice water to transform into a glass.

Method 2 was repeated three times by grinding the glass into powders under ethanol till the ethanol was fully evaporated. Powder X-ray diffraction and optical microscopy were performed on all samples to ensure that no crystallisation occurred during quenching for the glass samples. The recovered Al-free samples consisted of ortho- and clinoenstatite and were free of secondary phases like quartz, also confirmed through X-ray diffractometry (section 2.3.1). The Al content in Al-bearing glasses was examined in the TEM by EDXS analysis for the powder samples. These enstatite and glass powders were prepared for further piston-cylinder and multi-anvil experiments.

The following powders were produced:

- Stoichiometric ortho-enstatite with different Al content,
- Al-bearing $MgSiO_3$ glasses, and
- pyrope.

Table 2-1: Chemical compositions of the diffusion couples before the experiment, analysed by TEM and calculated from the absolute element concentrations. The detailed data are given in Appendix A, Table 3.

	Phases	MgO (wt%)	Al_2O_3 (wt%)	SiO_2 (wt%)	total	Mg	Al	Si	O	Mg/Si
En97Cor3	Brg (n=8)	38.5 (7)	3.0 (4)	56.5 (12)	100	0.98 (2)	0.06 (1)	0.96 (1)	2.92 (4)	1.02 (3)
En90Brm10	Brg (n=6)	38.2 (11)	5.1 (19)	56.6 (24)	100	0.95 (1)	0.10 (4)	0.95 (2)	2.98 (5)	1.01 (1)
En95Brm5	Brg (n=8)	39.1 (2)	2.7 (1)	56.8 (6)	100	0.99 (1)	0.05 (0)	0.96 (1)	2.94 (2)	1.03 (1)

2.2. High-pressure – high-temperature experiments

2.2.1. Pre-synthesis of pyroxene and pyrope

The starting material powders were stored in a desiccator to prevent contamination by H_2O. The synthesis experiments were carried out at the target pressure and temperature using the piston cylinder and the Zwick multi-anvil press at BGI (Table 2-2). Pt capsules with a diameter of 5 mm and a length of 10 mm were used for the ½“ piston-cylinder experiments. The capsules were filled with the ortho-pyroxene powder starting material to produce enstatite polycrystalline samples by solid-state reaction at over 2 GPa and 1,200 °C for up to 45 h (Figure 2.1). The temperature was monitored using an S-type thermocouple (Pt – Pt90Rh10) connected to a temperature controller (Eurotherm). For the pyrope synthesis, the glass starting material was filled into platinum capsules with a diameter of 5 mm and a length of 10 mm and annealed at 3.5 GPa for 4 h at 1,650 °C in a 25/17 graphite assembly in the 500 t Zwick press. For the used 25/17 assemblies, the pressure calibration was based on the Qtz-Coe transition obtained from previous experiments. The pyrope is later used as a k-factor standard for bridgmanite composition analysis in TEM measurements.

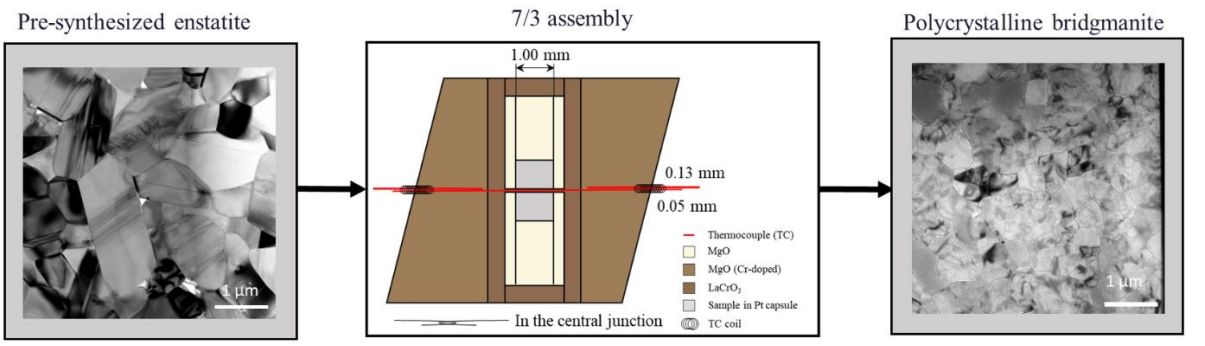

Figure 2.1: Synthesis of polycrystalline bridgmanite from pre-synthesized enstatite. The Brg diffusion couples for the interdiffusion experiments were synthesised from 1 – 5 mol % Al_2O_3-bearing $MgSiO_3$ enstatite at 24 GPa and 1,750 – 2,000 °C, using conventional multi-anvil apparatuses. See section 2.2.2.

2.2.2. Synthesis of diffusion couples and diffusion experiments

The mineral grains must have an average size of at least 1 – 2 µm to ensure interdiffusion so that the effect of grain boundary diffusion can be neglected. The pre-synthesised enstatites and glasses were ground to a coarse powder and then converted into bridgmanite using conventional tungsten cubes in a large-volume, high-pressure multi-anvil (MA) apparatus (Figure 2.1). Initially, a few syntheses with 0, 3 and 5 mol % Al_2O_3-bearing silicate bridgmanites were synthesised at 24 GPa at temperatures between 1,750 °C and 2,000 °C (Appendix A, Table 1). With a success rate of 64 %, 32 out of 50 multi-anvil experiments were successful. Due to the high pressures and temperatures, both the cubes and the material can be destroyed under the experimental load, invalidating the experiment. Furthermore, the tungsten cubes can only be used up to six times before they break. However, as the frequency of use is not reliable, it is difficult to estimate when the cubes will break under load. This introduces uncertainty into the planning and can lead to failed experiments. The typical uncertainty in the pressure measurement could be in the order of 0.5 GPa. These synthesised polycrystalline samples were observed under the scanning electron microscope to find the best position for cutting out the diffusion pair. The samples were then polished with colloidal silicon and cut into 250 × 250 µm disks. See also section 2.2.3. These prepared disks were brought into contact to form a diffusion couple (see section 2.2.3). Then, the diffusion couple was kept at temperatures between 1,750 and 2,000 °C and 24 GPa within the bridgmanite-single phase region for long run durations of 3 to 21 h (Table 2-3) before being rapidly quenched by switching off the power (Figure 2.2). In the ongoing series of experiments, two capsules were running simultaneously. One capsule contained the diffusion experiment, and the other held a new synthesis for diffusion experiments — saving time and material.

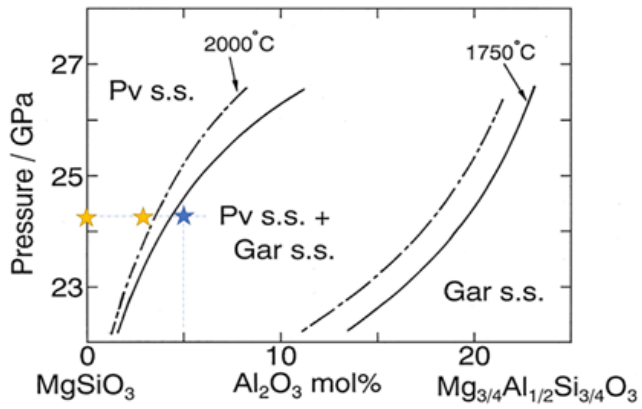

Figure 2.2: Experimental conditions for 0, 3 and 5 mol % Al_2O_3 bridgmanite at MA high-pressure experiments. Blue star: 95 mol % $MgSiO_3$ + 5 mol % Al_2O_3 (En95Cor5) starting material; Yellow stars: En100 and En97Cor3 starting materials. Figure by Akaogi & Ito (1999).

Most of the diffusion experiments were performed using the Sumitomo 1,200 t Kawai-type large-volume press with a 7/3 assembly. The 7/3 assembly consists of a 7 mm edge length of the Cr_2O_3-doped (5 wt. %) MgO octahedron and a 3 mm truncation edge length (TEL) of the tungsten carbide anvils from Hawedia grade ha6 with 6 % Co binder (Akaogi, 2022).

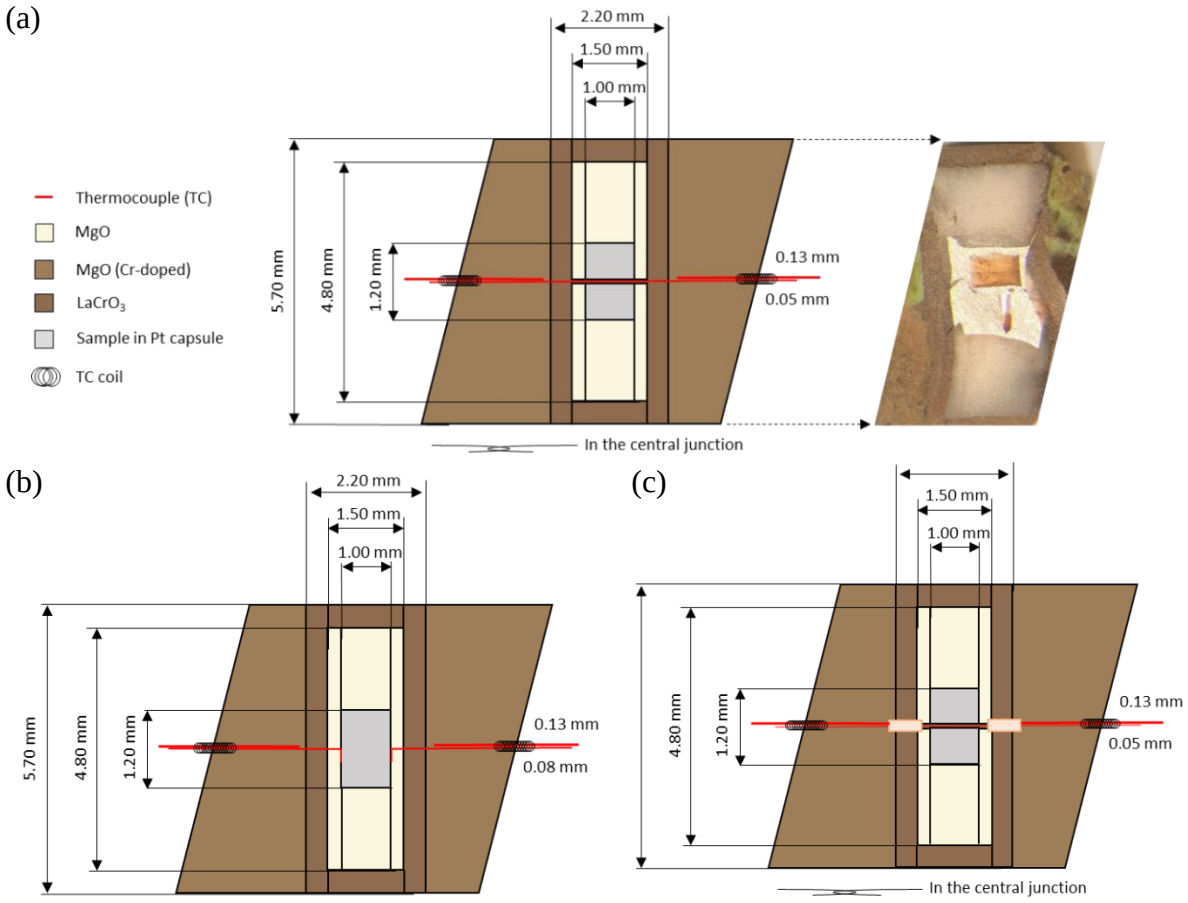

Figure 2.3: Schematic setups/Cross-section of the 7/3 assembly types used for diffusion experiments and polycrystalline sample syntheses. The 7/3 assembly (a) has been used for most experiments. D-type thermocouples were inserted into all assemblies but mostly failed at reading the temperature at assembly method (b). (a) the right side shows the recovered sample after the S7791 run. (c) shows the same layout as (a) except for the fused Si capillaries in the heater to isolate the TC from the heater.

The starting materials were encapsulated by 1 × 1 mm Re-foil or Pt tube capsules (outer diameter OD = 0.8 mm and inner diameter ID = 0.6 mm) and were then inserted into a MgO sleeve and placed in the central portion of a cylindrical lanthanum chromite ($LaCrO_3$) furnace. The Re capsules were mechanically closed, and the Pt capsules were welded under oxygen-free conditions using argon gas.

MgO spacers filled the MgO sleeves, and to ensure good electrical contact with the anvils, the furnace was closed by $LaCrO_3$ lids located at the top and bottom (Figure 2.3). The temperature was monitored using a D-type thermocouple (W97%Re3% – W75%Re25%) that was inserted through pre-drilled holes in the centre of the octahedron and connected in different ways, as shown in Figure 2.3 a – c.

In this study, several thermocouple (TC) assembly methods were tested to find the best one for the diffusion experiments. The best method is shown in Figure 2.3 a. The first method was a single-capsule experiment with a bent TC touching the capsule material (Figure 2.3 b). The problem was that the MgO sleeve material squeezed into the space between the capsule and the TC. This caused the TC to lose contact, and the temperature could no longer be read. The second method was tested with a central junction (Figure 2.3 a) in the centre and two capsules of 2 mm total length *d*. The central junction ensures stable contact between the sensing elements located in the centre of the assembly between the sample capsules. Consequently, the heater remained stable, and the TC became more reliable.

The last method (Figure 2.3 c) was tried towards the end of the series of experiments to determine the usability of the temperature determined via the TC. The TC was isolated from the heater by fused Si capillaries. However, this made no significant difference to the temperature measurement, and the very high additional effort made additional insulation unprofitable. At the same time, the uncertainty of the temperature measurement depends on the TC position, the capsule size and whether the temperature measurements were successful. In the case of non-working TC, the temperatures were estimated from the correlation between the power applied and the previous experimental runs with working TC (Table 2-3 - TC worked: yes "y", no "n" or partly worked "y/n"). Therefore, all temperatures T_{exp} were recalculated from the power-temperature correlation (Figure 2.4) of 23 experiments with a working thermocouple up to the start of the decompression process. These calculated temperatures have an uncertainty of ± 80 °C. As shown in section 3.2.3 ("Temperature estimation"), the results were recalculated with the new temperature T_{calc} (Table 3-1).

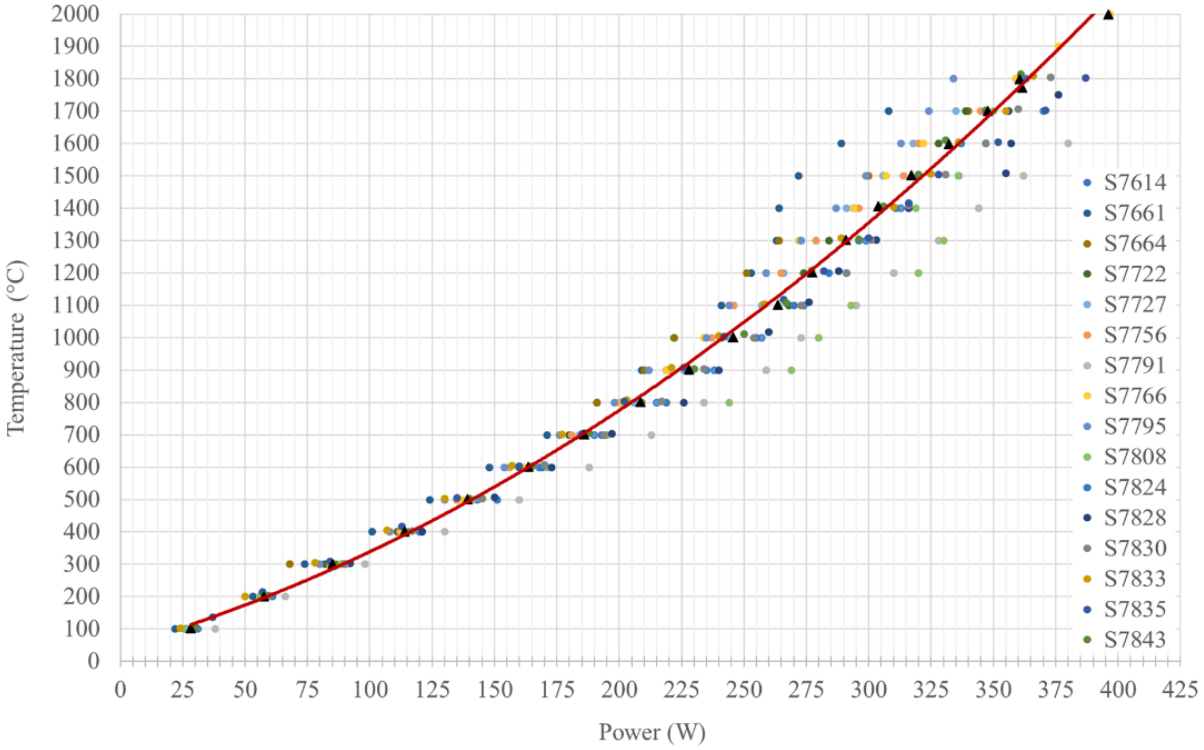

Figure 2.4: Power-temperature correlation calculated via consistently stable and readable temperatures through the TC of 16 multi-anvil experiments from this study and 7 multi-anvil experiments from Greta Rustioni (pers. comm.) at the same PT conditions and assembly size. The red fitting curve of the second- order polynomial equation was calculated by least-squares fitting ($y = 0.0071\ x^2 + 2.226\ x + 44.803$).

Table 2-2: Overview of the pre-synthesis conditions, including the experimental conditions and source material pyrope (Prp), enstatite (En) and corundum (Cor) in different mixture volumes. For these experiments the thermocouple (TC) worked in every synthesis.

Name	Material	Press	Assembly	TC	P [GPa]	T [°C]	Heating – time [h]
V1158	Prp	500t Zwick	25/17	y	5	1650	5
S7380	En100	Sumitomo	7/3	y	24	1650	3.5
B1288	En95Cor5	Piston cylinder B	1/2 "	y	2	1200	24
B1338	En97Cor3	Piston cylinder B	1/2 "	y	2	1200	26

Table 2-3: Multi-anvil diffusion experiments in 7/3 assemblies at 24 GPa. Listed with experimental conditions and source material pyrope (Prp), enstatite (En), brownmillerite (Brm) and corundum (Cor) in different mixture volumes. The thermocouple (TC) did not work in every diffusion experiment. TC worked? – Yes " y" , no " n" or worked partly " y/n" .

Name	Material	Press	TC	P [W]	Annealing time [h]
S7596	En100+En97Cor3	Sumitomo	n	340	3.5
S7614	En100+En97Cor3	Sumitomo	y	370	7
S7830	En100+En97Cor3	Sumitomo	y	381	21
S7835	En100+En97Cor3	Sumitomo	y	387	21
S7766	En100+En97Cor3	Sumitomo	n	397	4
S7808	En100 + En95Brm5	Sumitomo	n	350	3
S7824	En100 + En95Brm5	Sumitomo	y/n[+]	363	6
S7828	En100 + En95Brm5	Sumitomo	y	395	4
S7843	En100 + En95Brm5	Sumitomo	y	361	21
S7751	En100+En90Brm10	Sumitomo	n	370	8
S7791	En100+En90Brm10	Sumitomo	n	380	0.5
H5548	En100+En90Brm10	Hymag	y/n[+]	605	4

[+] The TC was working at the beginning of the experiment. It broke during the test run.

2.2.3. Diffusion capsule preparation

The technicians in the sample preparation laboratory at BGI prepared the diffusion assemblies (Figure 2.5). The synthetic polycrystalline bridgmanite diffusion sample was divided into 1/3 and 2/3 sections. The smaller 1/3 part was kept for surface analysis and used later. The larger piece was cut in half and attached to a sample holder using super glue. Cylindrical cores with a diameter of 250 µm and a height of 250 µm were cut out. Glycerine was used as a grease and coolant to prevent the sample from detaching, while the sample was cut out in rotation using a drill head. Subsequently, platinum capsules were made from a 1 mm diameter Pt rod, into which a 750 µm deep hole was drilled. The bottom of the capsule was ground flat with a ground-off drill head and reworked by hand. After that, the capsule was cleaned in acetone in an ultrasonic bath until no impurities were visible under the optical microscope. The diffusion couples were then inserted, and the position was noted, as shown in Figure 2.5. Finally, the capsule was mechanically closed, and the position of the Al-containing bridgmanite was marked with an "X" on the end of the capsule to ensure the experimental setup was always the same. In this study, the Al-containing bridgmanite sample was always placed on top of the Al-free sample and was also built into the multi-anvil device in this way.

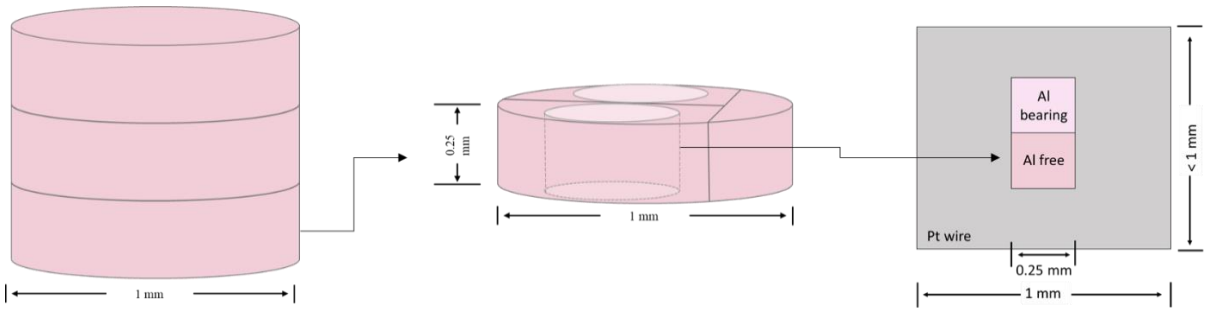

Figure 2.5: Drawing of a diffusion experiment. The bridgmanite sample after synthesis is shown on the left. The sample was cut into three pieces and each piece was polished with colloidal silica. In the middle, the shapes of cylinders with a diameter of 250 µm and a height of 250 µm are indicated for further processing. Two cylinders can be cut from a sample disk. One of these cylinders was inserted into the experimental setup on the right. In this case it was the Al-free bridgmanite sample. The same procedure was followed for the Al-bearing bridgmanite samples.

2.3. Sample characterisation

2.3.1. Powder and micro-X-ray diffraction

Powder X-ray diffraction is a method for phase identification. A diffractometer generally consists of a radiation source (X-ray tube) of a specific wavelength λ, a sequence of slits to adjust the beam shape or an incident X-ray beam passed through a collimator (or mirror lenses) to adjust the beam shape and is directed through a sample holder in which the specimen is located (Figure 2.6). A counter detector (or a 2-dimensional detector) is used to record the diffracted waves. X-ray diffraction has two main analytical purposes, leading to different crystallographic information. Single crystal X-ray diffraction is mainly used for structure elucidation and refinement. In contrast, powder X-ray diffraction is used to determine unit cell parameters and for phase identification. The methods can be distinguished by their respective diffraction patterns: A single crystal pattern consists of discrete spots (Bragg reflections) formed by the scattering of atoms in a particular orientation, reflecting the symmetry of the material under study. In contrast, a typical powder pattern is characterised by spherical concentric *hkl* Debye rings formed by the scattering of randomly oriented grains.

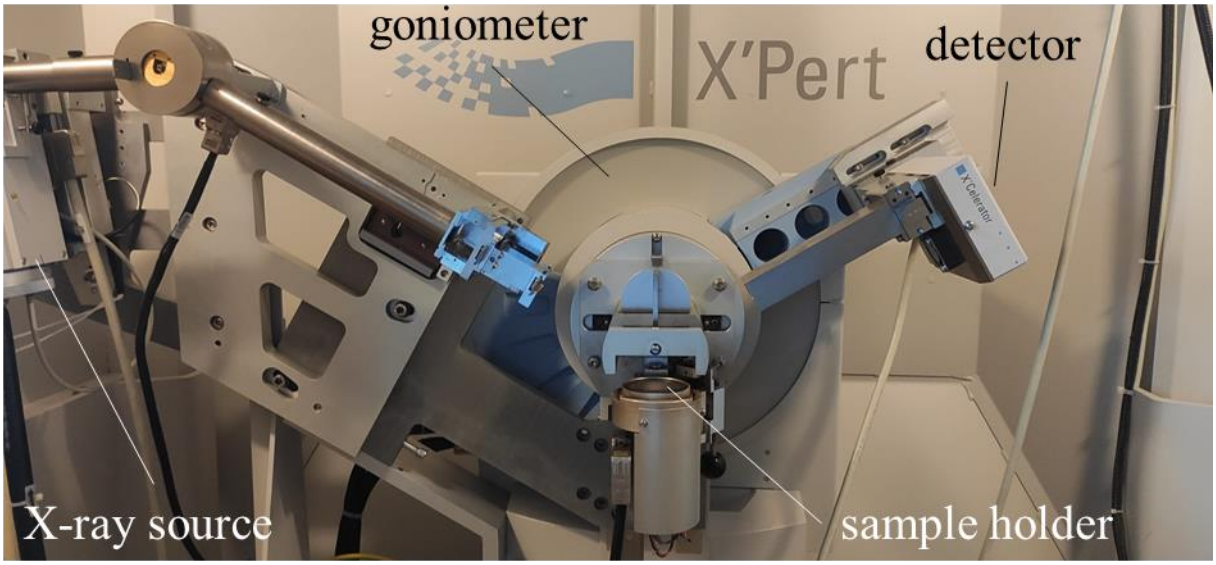

Figure 2.6: Photo of the Philips X'Pert powder diffractometer located in BGI Bayreuth. Equipment with a high-intensity ceramic sealed tube (3 kW) characterised the glass and orthopyroxene starting materials using an energy-dispersive system.

The X-rays are diffracted from crystal planes depending on a particular geometry defined by the relationship between the wavelength of the incident beam and the diffraction angle. Bragg's equation expresses that the angle θ of incidence must be equal to the angle of reflection (Figure 2.7) (Putnis, 1992; Massa, 2015). The interference conditions of Bragg's Equation (2.1) are only fulfilled when all diffracted waves are in phase. Thus, each lattice plane (*hkl*) has a characteristic lattice plane spacing *d* and defined diffraction angle θ.

$$2d_{hkl}\, sin\theta = n\lambda \qquad (2.1)$$

The integer *n* is the reflection "order" (1,2,3…, *n*) and is related to the order of reflection from the planes (*nh,nk,nl*). Bragg's law has to be fulfilled to determine the lattice parameters. The more randomly oriented the crystals are, the higher the probability of obtaining the correct Bragg angle for each (*hkl*) plane. Several different crystal orientations are needed (Figure 2.7).

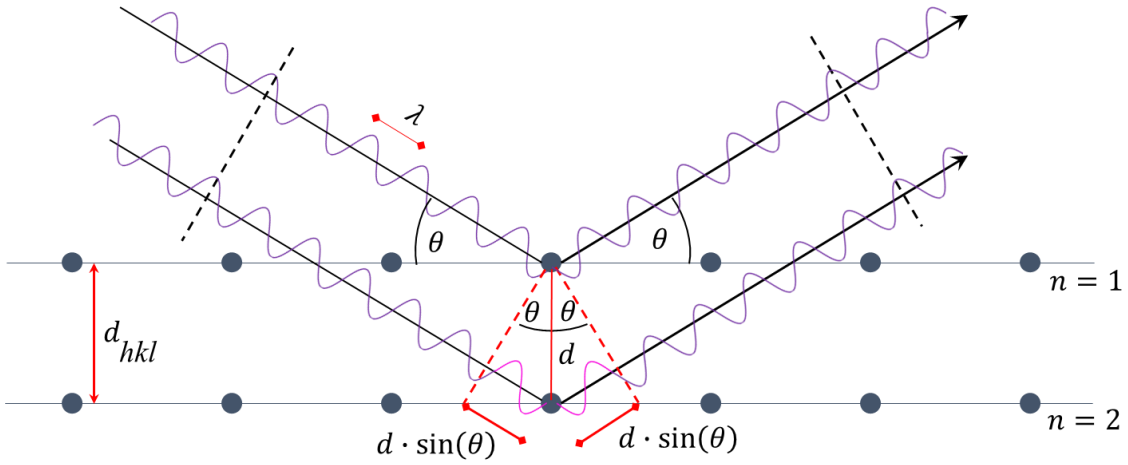

Figure 2.7: To maximally amplify each other (interfere constructively), two waves must be in the same phase. In the case of reflection from a thin crystal lattice with lattice spacing d, this is only the case for two waves arriving in the same phase if the additional distance l that a wave travels because it is reflected only at the second lattice plane is a multiple of the wavelength λ. The difference in path length l between the two waves depends on the angle of incidence θ of the wave and the distance d of the lattice planes. The incident and scattered X-rays in Bragg condition reflected from the plane (hkl) with d spacing d_{hkl} at a scattering angle of θ. This image has been modified from Putnis (1992).

A Philips X'Pert (Figure 2.6) equipped with a high-intensity ceramic sealed tube (3 kW) characterised the glass and enstatite starting materials using an energy-dispersive system with Co-Kα_1 radiation (1.78897 Å). The radiation operated at 40 kV and 40 mA, using a symmetrically cut, curved Johansson Ge (111) crystal-diffracted beam monochromator. The diffractometer is equipped with a Philips X'celerator count detector. The enstatite data collections were performed in a 2 θ range between 15° and 90° for a total measurement time of two hours. For the glass samples after the annealing process at 1650 °C in the Eurotherm oven, the pulverised samples were measured in a 2 θ range between 20° and 90° for a total measurement time of two hours. The collected X-ray patterns (Figure 2.8) are compared with the former pattern from the Crystallography Open Data (COD) database. Due to maintenance work on the Philips, the En100 endmember was examined at Bruker (Figure 2.9), and the phases were also identified. The endmember was found to consist of both orthoenstatite and clinoenstatite.

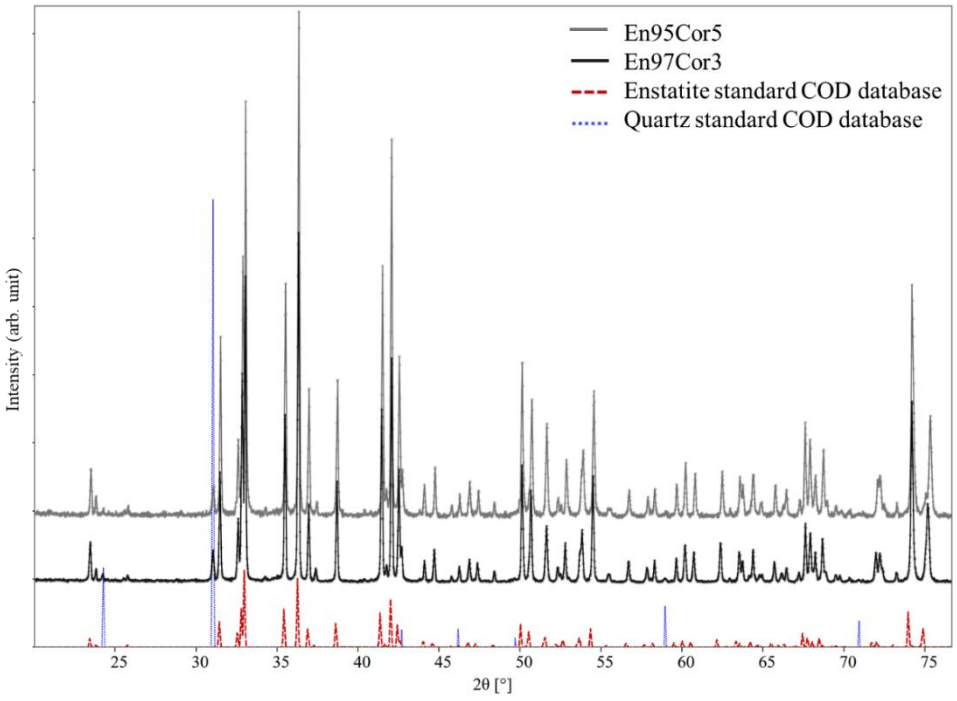

Figure 2.8: Powder diffraction pattern obtained from the different starting materials. Quartz and orthoenstatite are the identified phases by CrystalDiffrac 6.

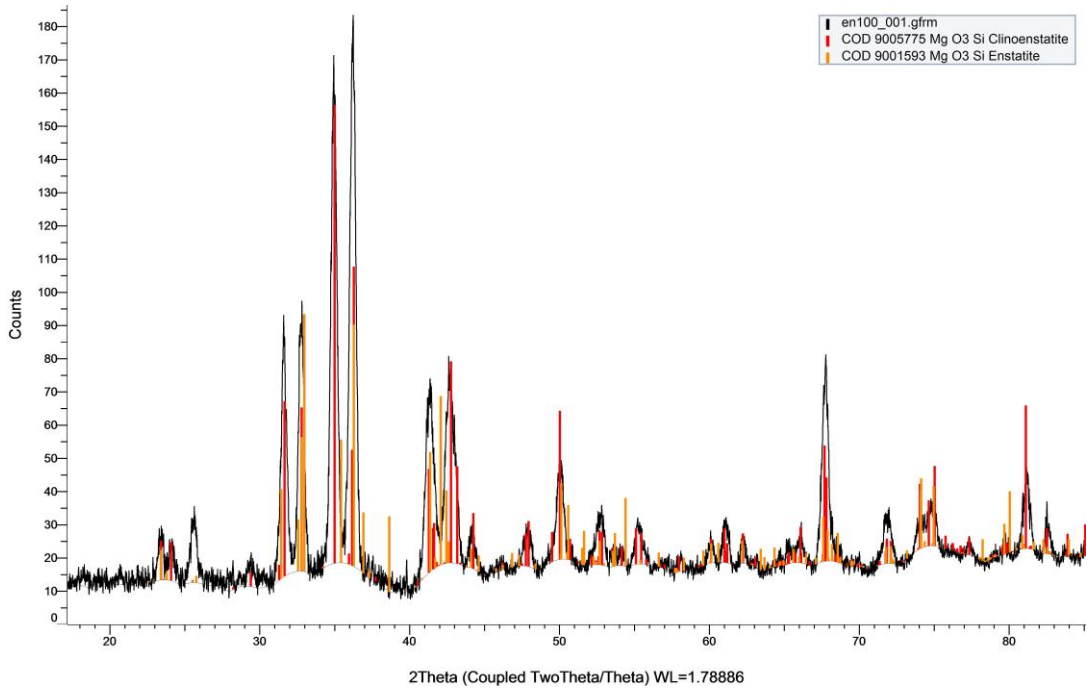

Figure 2.9: Powder diffraction pattern collected by Bruker. The pattern shows the En100 endmember is composed of clino- and orthoenstatite.

The pyrope polycrystalline experimental run products (Figure 2.10) were polished from one side after being recovered from the multi-anvil experiment and analysed using a Bruker Discover diffractometer with a micro-focus source (IμS) of Co-Kα radiation (1.79026 Å) operated at 40 kV and 500 μA with a spot size of less than 100 nm. This diffractometer is equipped with a two-dimensional solid-state detector (VÅNTEC500). Data collections were performed in a 2 θ range between 25° and 85° for a total measurement time between 600 s and 1,000 s per frame for three frames. Measurements were taken at several locations to test homogeneity.

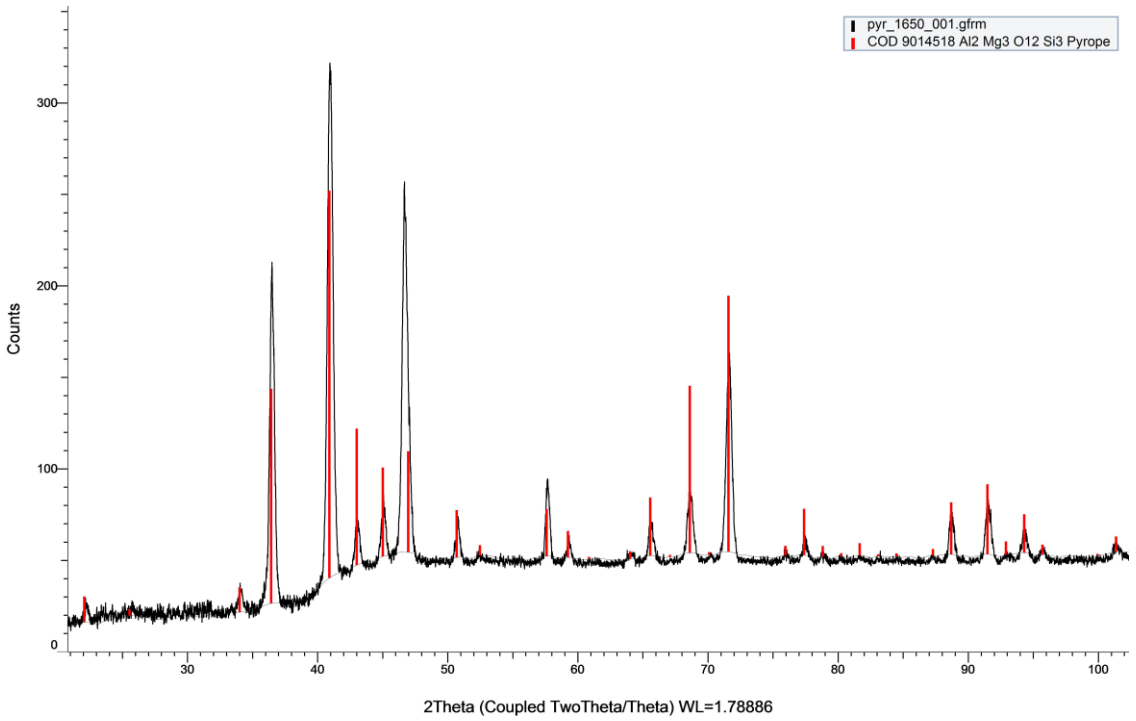

Figure 2.10: Micro X-ray diffraction of Pyrope. Phase identification was made via diffract.eva and compared with the diffraction pattern from the COD database.

For the phase identification the collected X-ray patterns (Figures 2.9 and 2.10) were fitted in the software diffract.eva (Bruker) and (Figure 2.8) CrystalDiffract 6 from CrystalMaker (Philips). The data were compared with the former pattern collected from the "Crystallography Open Data" database (Chateigner *et al.*, 2014), RRUFF Project website (RRUFF, 2016) and Misasa Kanzaki's webpage (www.misasa.okayama-u.ac.jp/eng/; (Kanzaki, 2021)).

2.3.2. Raman spectroscopy

Raman spectroscopy is vibrational spectroscopy based on inelastic light scattering on molecular or lattice vibrations. A sample is analysed chemically by causing the matter to move at the molecular level through a monochromatic light source. Monochromatic light scattered on vibrational modes (also rotational and low-frequency modes) results in a set of peaks in the spectrum. These peaks correspond to the energy of the light source ± the energies of every Raman-active mode. Thus, the Raman spectrum is characteristic of any material and can be used as a "fingerprint" of the material for quick qualitative analysis of the sample. For Raman analysis, a HORIBA Labram-HR and DILOR XY Raman spectrometers irradiated a sample with a HeNe laser operating at 633 nm and an Nd:YAG laser with a wavelength of 532 nm was used. An optical bandpass filter removes the excitation wavelength in both spectrometers. The scattered light diffracted using 1,200 g/mm and 1,800 g/mm gratings corresponding to the Pringston Instruments Peltier-cooled CCD detectors. The resulting Raman spectrum consists of characteristic peaks for the investigated material and can be compared with reference data on the web database rruff.info or directly with previous studies. In this study, the pyroxene starting material was analysed before the synthesis. Furthermore, the recovered multi-anvil and piston-cylinder samples were first embedded in epoxy resin, polished on one side, and analysed between $0 – 1{,}500\ nm^{-1}$. Al-bearing and Al-free bridgmanite (Figure 2.11) was measured between $200 – 700\ cm^{-1}$ and had four prominent peaks at wave numbers near 255, 280, 380 and 500 (Liu *et al.*, 1995; Gillet *et al.*, 2000).

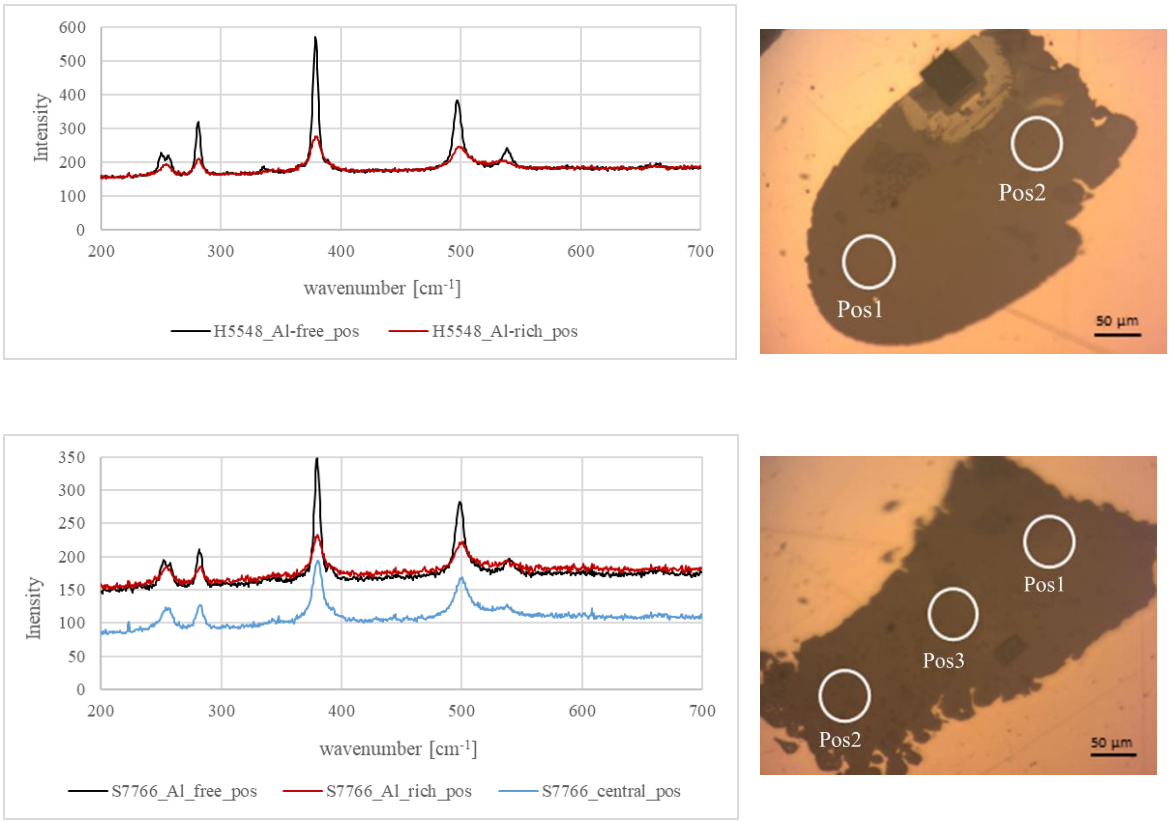

Figure 2.11: Left: Raman spectrum of bridgmanite sample collected from Pos1 (black), Pos2 (red) and Pos3 (blue). Right: Optical image of the collected sample. For all images applies: Pos1 –> Al-free part of the sample. Pos2 –> Al rich part of the sample. Pos3 –> Central position of the sample. Data were compared with data from Liu et al. (1995).

2.3.3. Scanning electron microscopy

The multi-anvil run products were first examined under a light microscope to get an initial overview of the sample, crystal structure and grain size. The samples were then coated with amorphous carbon to prevent electrical charging of the sample under the electron beam. The thickness of the coating was adapted to the intended operation (~ 5 nm for secondary electrons (SE) and 14 nm for backscattered electrons (BSE)). GEMINI LEO 1530 scanning electron microscope (SEM) images were taken to determine the grain size and crystal morphology of the minerals. Inelastic secondary electron, elastic backscattered electron and oriented contrast images were taken. The overview images were later used to find the best locations for the diffusion experiments and to determine the focused ion beam (FIB) sampling position after the diffusion experiments for further sample analysis. An electron gun generates a fine electron beam focused on the sample surface. The beam sweeps across a polished specimen in a raster. Depending on the interaction between the electron beam and the specimen, different signals can be emitted (Prior *et al.*, 1999; Goldstein *et al.*, 2018). One of these signals is inelastically scattered low energy secondary electrons (Figure 2.13). A typical energy range is 5 – 30 keV (Reed, 2005). The SE is emitted from the near-surface regions of the sample and is affected by slight variations in the sample topography by the amount of secondary electrons emitted. The SE is used to image the sample topographic features. On the other side, the BSE is generated by the elastic interaction between the electron beam and the sample and is strongly dependent on the average atomic number. Because of the strong dependence, heavy atoms scatter more strongly, and consequently, heavy elements thus appear brighter than light materials in the resulting image. This relation can be used for the qualitative identification of mineral phases. In principle, the SEM resolution is defined by Ernst Abbe's diffraction limit formula:

$$d = 0.61 \frac{\lambda}{n * \sin \alpha} \qquad (2.2)$$

where λ is the wavelength, n is the refractive index and α the aperture angle (or $n * \sin \alpha$ the numerical aperture). The SEM allows a resolution of up to ~ 0.1 nm, depending on the wave number. The SEM provides a spatial resolution of ~ 10 nm in topographic mode (SE) and up to 100 nm in compositional mode (BSE) (Reed, 2005).

Moreover, the interaction between the electron beam and the sample also produces the emission of X-ray photons when the inner shell electrons are ejected, and the electrons from the outer shell fill the produced vacancies. This process is an elemental energy characteristic and can be detected by energy dispersive measurements (EDX), providing a qualitative chemical composition of the individual phases by relative intensities of major elements (Newbury & Ritchie, 2013). The semi-quantitative EDX has been performed using INCA and Aztec software (Oxford Instruments) at an acceleration voltage of 5 – 15 kV and a working distance of 7.5 – 14 mm.

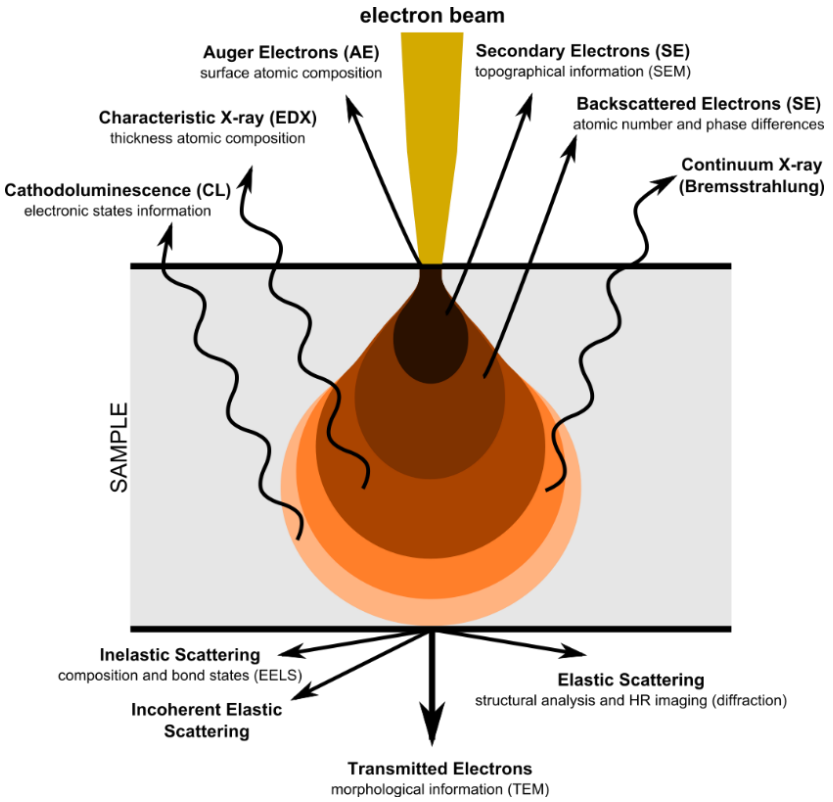

Figure 2.12: Illustration of the phenomena that occur from the interaction of highly energetic electrons with matter. Various types of signals are generated as a result of electron–matter interactions. Also depicted is the pear shape interaction volume, which is typically observed in this type of interaction. Figure by ThermoFisher Scientific, (2022).

At the beginning of this study, oriented contrast (OC) images were taken to determine the grain size via the grain contrasts (Figure 2.13). However, this imaging was abandoned as the effort required was too great and the grain size could be well determined by BSE and optical microscope images. To produce oriented contrast images, the sample must be very well polished. For this purpose, the samples were polished with colloidal silicon and coated with only 3 – 5 nm carbon. The sample stage was then tilted by 70° to the incident beam. The scattered electrons hitting the forescatter diodes (FSD) mounted on the top and bottom parts of the phosphor screen generated OC images to complement quantitative crystallographic data from the electron backscatter patterns (EBSP) (Prior *et al.*, 1996).

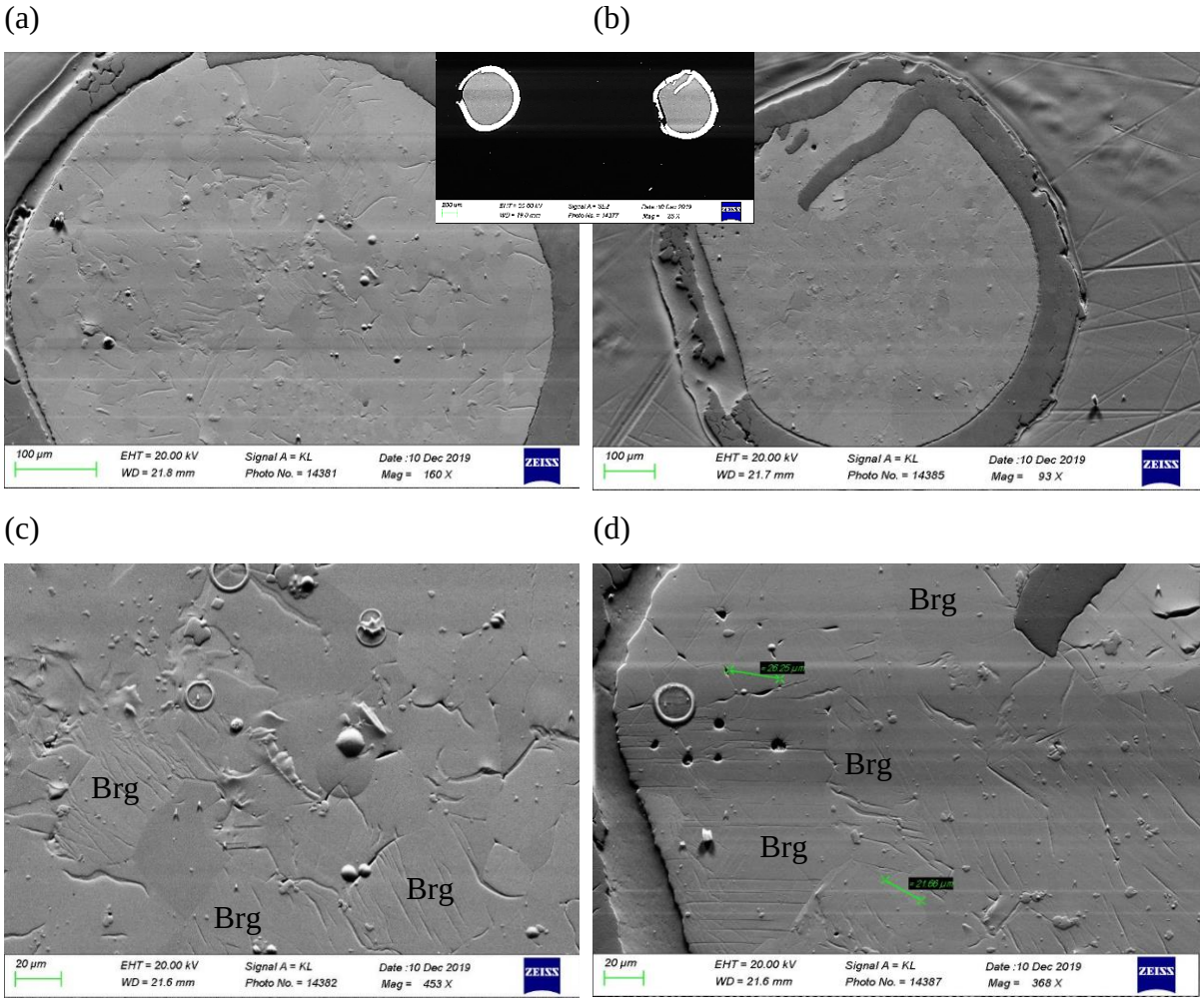

Figure 2.13: SEM images of the Al-free bridgmanite (Brg) sample S7381. (a) and (c) are orientated contrast images of the left-sided sample. (b) and (d) are orientated contrast images of the right-sided sample. The top-middle inset is an overview SE image. Orientated contrast images were made to estimate the grain sizes in the samples.

2.3.4. Focused ion beam: TEM lamella preparation

The focused ion beam device (FIB) method is based on scanning beam microscopy, except that the main beam used is a Ga^+ ion beam (Figure 2.14). This beam allows high precision in removing material from the sample at a nanometre scale (Wirth, 2004; Miyajima *et al.*, 2010; Rigort & Plitzko, 2015). This meant the remnants of the bulk sample could be further used, and, if necessary, another lamella could be cut from the same sample. Moreover, the dual-beam FIB contains an SE beam which permits monitoring of the milling process by high-resolution scanning electron imaging.

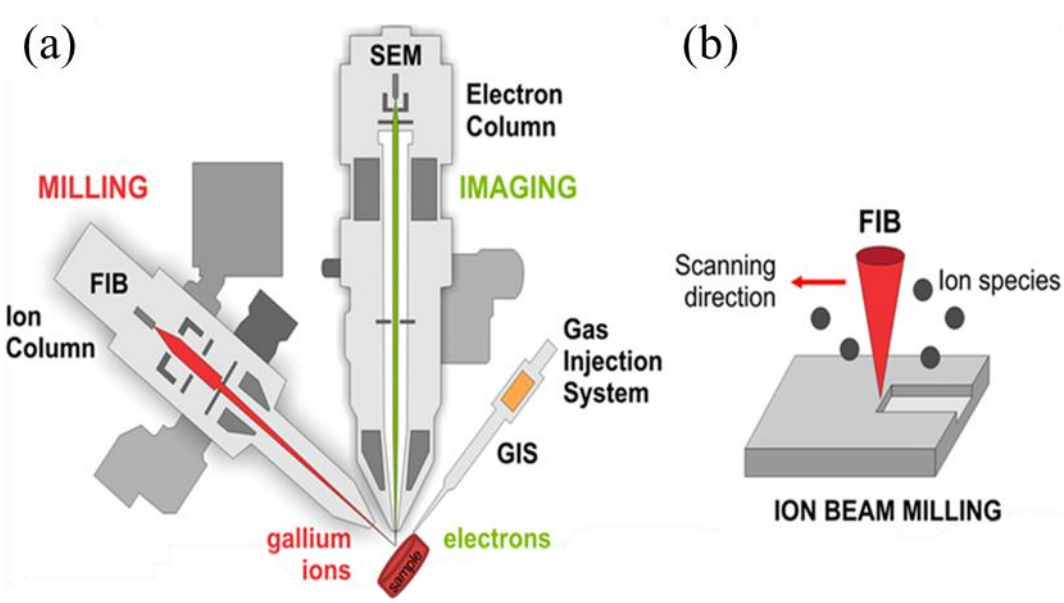

Figure 2.14: Schematic drawing of the commonly found dual beam FIB-SEM instrument. (a) FIB/ SEMs combine an SEM and a FIB in a single device and are often equipped with multiple detectors incl., SE, BSE, EDX, EBSD and in-lens detectors as well as a gas injection system. (b) shows the milling process with the Ga^+ beam. Inspired by Rigort & Plitzko, (2015).

For further sample analysis, a position was found along the diffusion interface with bridgmanite grains in the size of 1 – 3 µm and without a secondary phase (e.g., stishovite). A carbon layer of ~ 20 nm was coated on the sample surface to prevent electrical charging of the specimen surface under the electron beam. After inserting the sample in the FIB, the sample was moved to a working distance of 7 mm, and the sampling position was placed in the center of the monitor. Operations in the SE mode were performed at 20 kV and 13 pA to avoid surface damage. After manually focusing and adjusting the image stigmation and brightness/contrast, a platinum (Pt) layer was deposited perpendicular to the diffusion interface (Figure 2.15 a) by a gas injection system (GIS). This Pt layer functions as a lamella protection layer during the milling process. Subsequently, the Ga^+ beam was used to cut a 14 × 20 μm^2 small lamella with a thickness of 2 µm by excavating trenches with 30 kV and 30 – 3 nA (Figure 2.15 a; Overwijk, (1993). These trenches were placed on both sides of the Pt deposition at a distance of 1 – 5 µm. The higher the current, the greater the distance between the pattern and the Pt deposition. After cleaning the trenches, a J-cut was made at a 7° tilted sample (Figure 2.15 b) to separate the lamella from the sample and then attach it to a copper grid (Figure 2.15 c, "Omniprobe 4 Post Copper Lift-out Grid"). Then the Focused Ion Beam machine (FEI Scios DualBeam) was used with a Ga^+ ion beam at 30 kV and 0.50 – 0.05 nA to thin this lamella to 50 – 100 nm thickness (Figure 2.15 d) for nanoscale analysis with a transmission electron microscope (TEM). This thinning process was done from both sides of the lamella to ensure a parallel shape. Finally, the "ion shower" cleaned the sample to remove the Ga^+ contamination. For this, the Ga^+ beam operated at 5 kV and 48 pA for 30 s at 200 ns/frame.

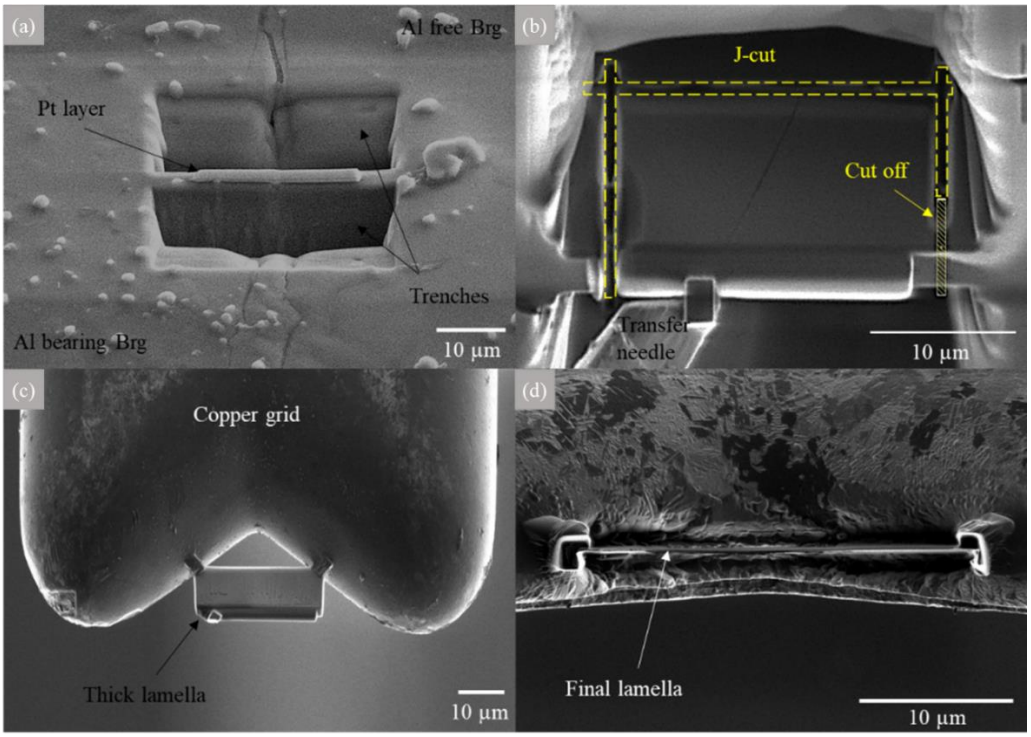

Figure 2.15: Scanning electron microscopy images showing the cutting process on recovered MA samples in the FIB. (a) SE image showing trenches before cutting the lamella. (b) Cut off of the lamella and transfer procedure using a needle micromanipulator. (c) Untreated lamella fixed to the copper grid. (d) Ga^+ beam image showing final lamella before "ion shower".

Another application of the FIB in this study was in producing a cross-sectioning of the surfaces of the synthesised samples before they were used for diffusion experiments. For this purpose, the remnants left over from the production of diffusion couples were embedded, and lamellae were also cut out for TEM observation. This was done to examine the surfaces before and after polishing with colloidal silicon and to determine whether the surface was affected by dislocations and damage after diamond polishing. The crystal defect would make the sample unusable for a diffusion experiment, as these defects would cause the aluminium atoms to diffuse faster, resulting in an erroneous volume diffusion. For more information, see section 4.2.4. ("Effect of sample surface treatment and convolution").

2.3.5. Transmission electron microscopy

The primary analytical device used for obtaining the results presented in this thesis was the FEI Titan G2 80-200 scanning transmission electron microscope (S/TEM) that accelerates a 200 kV electron beam (Figure 2.16). The TEM can be used both as an imaging device, which can image the specimen's microstructure down to the nanometre scale and as a device with a nanometre scale spatial resolution in chemical analysis. This combination of techniques makes it very powerful. When Max Knoll and Ernst Ruska built the first transmission electron microscope in Berlin in 1931, the microscope had a resolution of 50 nm and a magnification of 12,000 ×, operated with three lenses. Since the first electron microscope was constructed, the essential components of the TEM have not changed substantially. The TEM evolved into complex computer-controlled machines, and many manually changeable principles are hidden from the user now. There is still an improvement in the quality and current of the main lenses and the high voltage stability (De Graef, 2003).

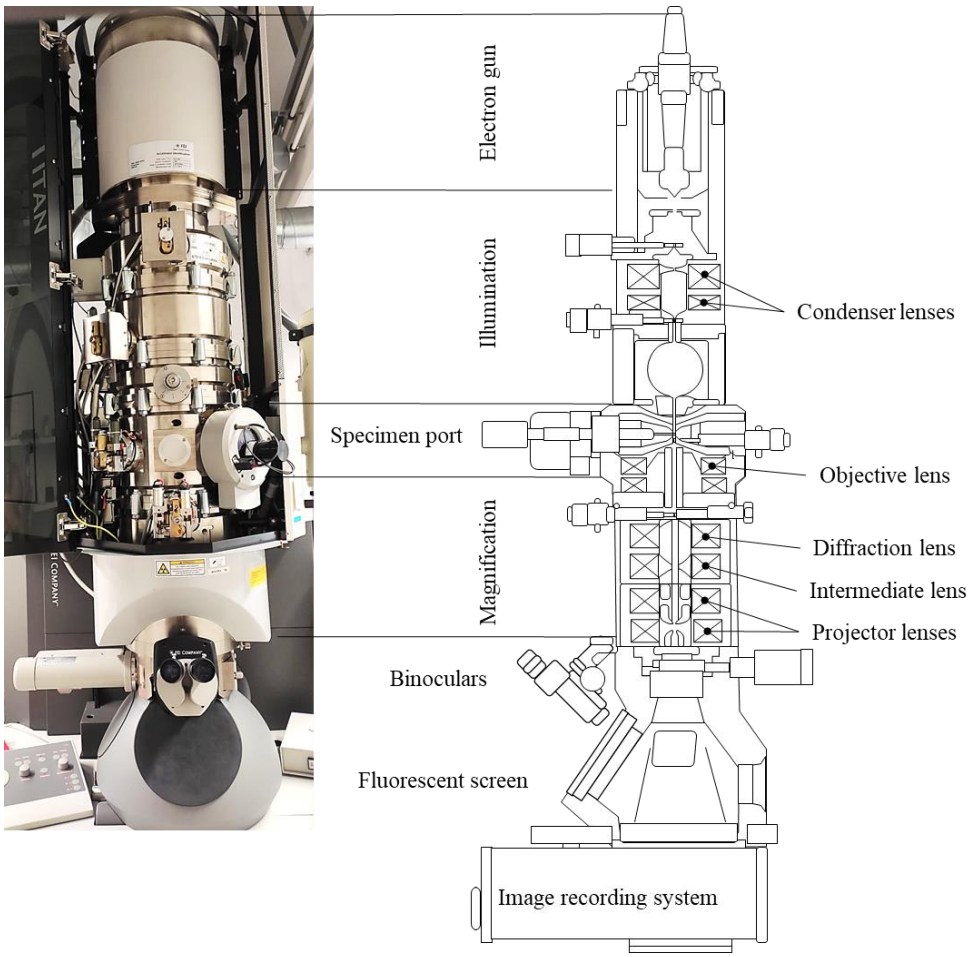

Figure 2.16: Photograph of a transmission electron microscope Titan G2 at BGI with associated sketch modified by © wikipedia.com/Gringer.

Basic principles of the TEM

Typically, the angle of vision must be as large as possible to see an object several centimetres in size clearly with the eye. Since it is impossible to get as close to the object as we would like, physicists consider the optimum viewing distance to be S = 25 cm (Figure 2.17). There is a challenge with tiny things – with a regular optical microscope, we can see small details with a size of 200 nm. To recognise even more minor details, we must get closer to the object (S < 25 cm). Here the problem arises. With a normal optical microscope, we cannot see even smaller things with our eyes because the distance to the object cannot be infinitely small. So we need advanced technology to see structures in the order of nanometres. This technology allows a viewing angle smaller than 10^{-5} mrad ≈ 0.0000006° (Thomas & Gemming, 2013). This is like trying to see a unicorn in focus from a distance of 100,000 km (Figure 2.17). We need an (optical) device that allows us to compensate the angle of vision without having to approach the object. This requires the development of lenses. In this limiting condition, the angle of vision σ is given by the size y of the object:

$$\tan\sigma = \frac{y}{S}\ ; (\sigma \ll 1): \sigma = \frac{y}{S} \qquad (2.3)$$

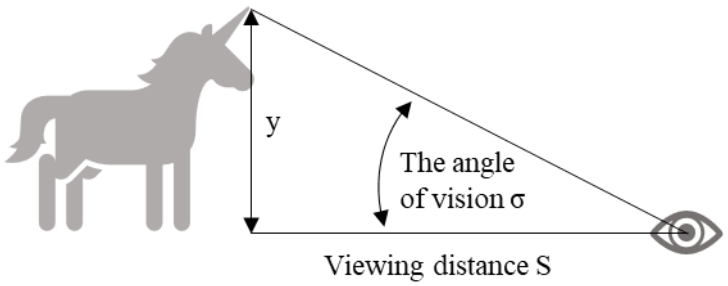

Figure 2.17: Physical relation between the distance to the object S, the size of the object y and the angle of vision σ to see an object in focus and its entirety. Modified after Thomas & Gemming (2013).

The TEM operates similarly to a conventional light microscope but enables us to see structures in the sub-nanometre range. It operates in high vacuum and consists of a condenser and projectors, which are lens systems instead of individual lenses. The electron gun serves as the light source, and the lenses are electric coils with pole pads that generate rotationally symmetric magnetic fields (Williams & Carter, 2009). The electron beam, thus focused by the condenser lenses, hits the electron-transparent > 100 nm thick sample inserted in a precisely adjustable two-axis sample holder. The image is focused and magnified by an objective lens, while the intermediate and projector lenses provide further magnification. The objective lens aperture coincides with the lens back focal plane and is located under the specimen and objective lens. This is followed by the selected-area diffraction (SAD) aperture, which is located in the image plane, while the basic method of TEM operation is to create a diffraction pattern. The developing image is projected onto the fluorescence screen or forwarded to a charge-coupled device (CCD) camera and can be saved as an image or vector file. The TEM can be used for different purposes, such as determining chemical composition and crystal structure of unknown samples and creating nanoscale images. Furthermore, the TEM is equipped with spectroscopy devices. More on this is given in section 2.5.4.

Imaging and diffraction in the TEM

A convenient feature of the TEM is switching between diffraction patterns and bright or dark field images. The sample diffracts the incident electrons, and the objective lens forms the diffraction pattern in the back focal plane (Williams & Carter, 2009). Changing the strength of the intermediate lens allows for a switch from real space (image) to reciprocal space (diffraction pattern). In this thesis, polycrystalline samples were used. This means that the electron beam was diffracted in the crystal planes under Bragg conditions, and a diffraction pattern were formed due to elastic interaction of the electron beam. Each diffraction spot represents a reciprocal lattice point.

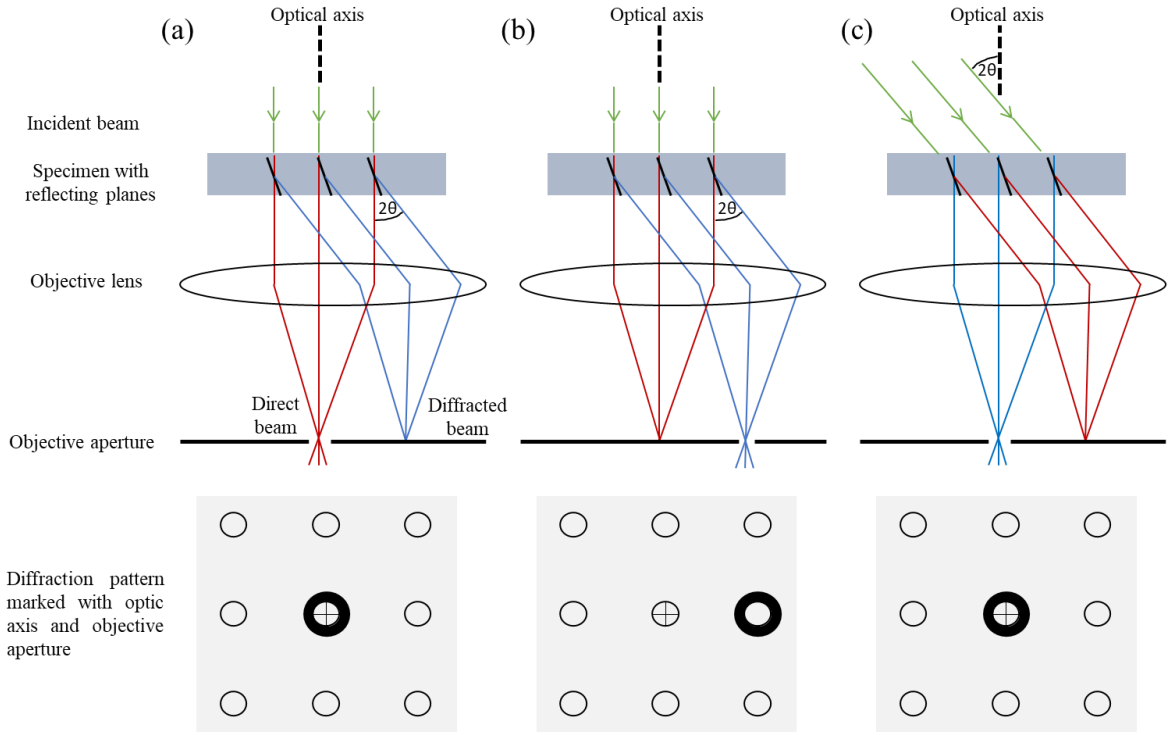

Figure 2.18: Drawing showing how to adjust the objective aperture and lens to produce a BF image (a), a displaced-aperture DF image (b) and a centred dark-field image (c) where the diffracted beam emerges on the optical axis by tilting the incident beam. Figure modified after Williams & Carter (2009), p. 156.

A bright field (BF) image was produced by selecting mainly the direct beam through the objective aperture, which was inserted at the back focal plane of the objective lens (Figure 2.18 a). In this case, strongly scattering areas of the sample appear dark. This was due to the diffraction/scattering contrast and the mass thickness contrast. In thicker areas of the sample or areas with a higher atomic number, the scattering cross-section of the atomic species and the number of scattering atoms along the propagation of the electron beam are higher. Areas without samples or areas with weak scattering appear bright – hence the term "bright field".

For high-resolution phase contrast, the size of the aperture was important to select lattice-spacings (i.e. wave frequencies) of the target materials (a smaller aperture was advantageous for high contrast imaging). The more coherent and parallel the beam, the better the quality of the phase contrast image and the better the diffraction contrast in BF and dark field (DF) images. In the dark field mode, the direct beam was interrupted by moving the objective aperture so that only the diffracted beam contributes to the image formation (Figure 2.18 b). A higher resolution of the dark field can be achieved by tilting the primary beam, and it was possible to quickly switch from bright field mode to dark field mode by flipping a knob (Figure 2.18 c). The bright and dark field images were used to study the grain size and crystal defects, such as stacking faults and dislocations (Figure 2.19).

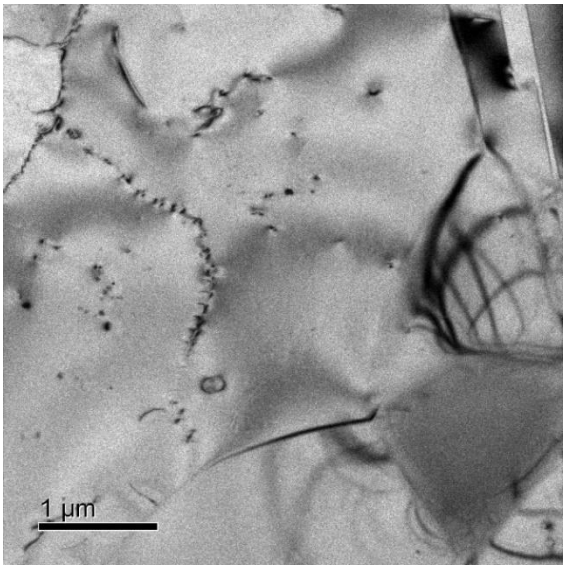

Figure 2.19: Bright field image of sample S7808_L2 with dislocations and bending contours in bridgmanite crystals. Recorded in TEM mode on the Titan G2 at the BGI.

The enstatites show grey to black lines; these could be twin lamellae or stacking faults (Figure 2.20). Twinning can be caused by improper growth or by deformation and results in a misorientation of a crystallographic plane perpendicular to a plane in the crystal lattice. The defect position and the defect type can be determined by orienting the sample to the incident beam. In the BF, the dislocation has a dark contrast because the incident beam is scattered at a local crystal lattice distortion in the vicinity of the dislocation core.

(a) (b)

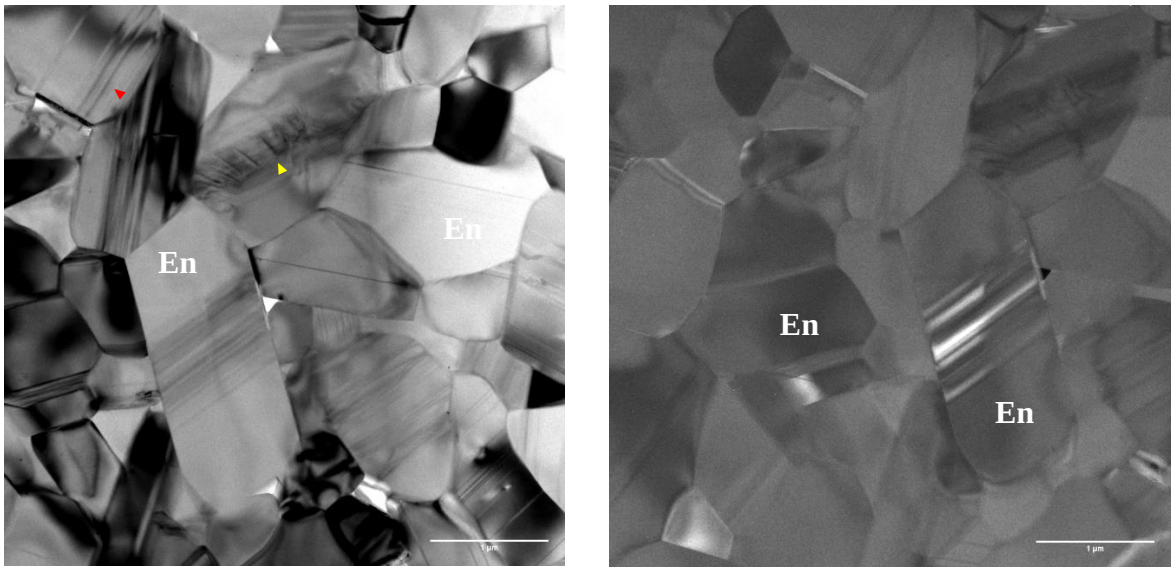

Figure 2.20: (a) Bright field and (b) Dark field of the Al bearing enstatite (En) sample B1288 with stacking faults or twin lamellae (red arrow) and dislocations (yellow arrow).

Another useful TEM mode is diffraction. This is based on the diffraction of the electron beam at certain angles by a crystalline lattice. The electrons, diffracted by the crystal lattice, produce bright spots on the fluorescence plate (visible inversely in Figure 2.21 a; the bright spots are black, and the background is white). The central bright spot represents the direct beam, i.e. the non-diffracted electrons. The distances between the spots represent the lattice spacing of the crystal.

The smaller the lattice spacing, the farther the representative white spot is from the central point. Each crystal and crystal orientation has a specific atomic lattice spacing. This allows unknown crystal symmetries and structures to be distinguished. The ability to tilt the sample holder allows us to determine the crystal orientations relative to the beam. For further technical details, following textbooks are recommend: de Greaf (2003) and Williams & Carter (2009).

(a) (b)

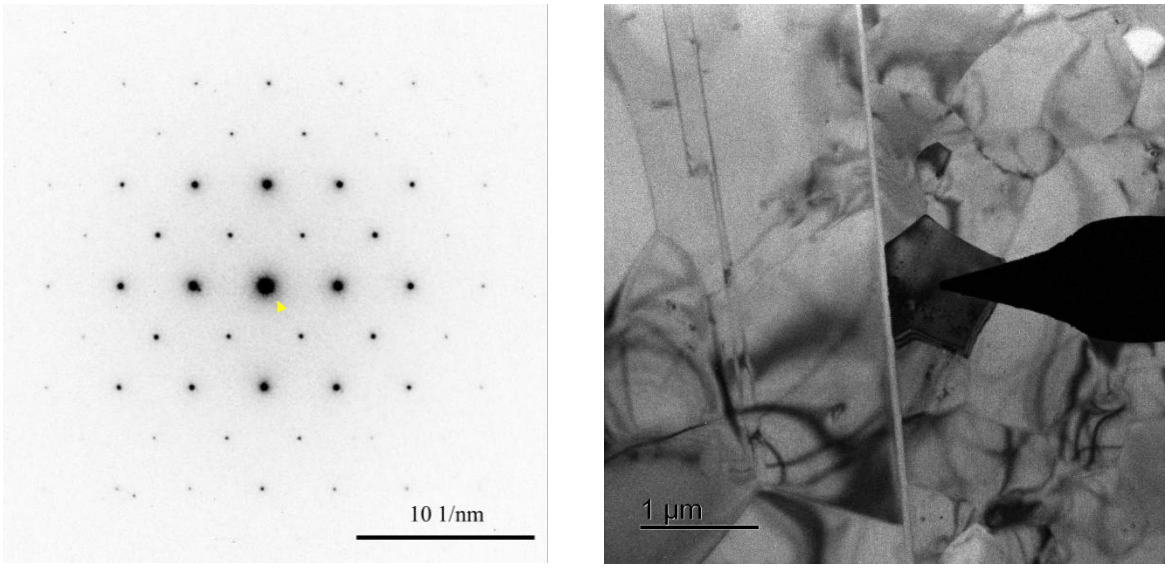

Figure 2.21: (a) Inverse diffraction pattern of the crystal on the right side in the bright field image. The central spot, marked by the yellow arrow, represents the direct beam. The crystal in figure (b) is centred under the beam and marked by a retractable arrow (beam stopper) on the TEM.

k-factor determination in the TEM-EDX analysis

To evaluate a chemical composition precisely, the calibration of the k-factor is essential. A standard with a known composition, e.g. a starting material, is used for the calibration. To calculate the k-factors, the detector-specific factors, such as the applied acceleration voltage, must also be known. Due to the increased volatility of lighter elements, the detector parameters have a much stronger influence on these elements and inevitably lead to a larger error than heavier elements. For higher analytical accuracy, the k-factors are determined experimentally. Since the k-factors calculated from measured characteristic X-ray counts in Equation (2.4) depend on the sample thickness, different spectra-areas were recorded at different sample thicknesses (Figure 2.22). For each pixel, a complete spectrum was stored in the data. Each rectangular spectra area gives the element content per pixel area within the rectangle. To increase the information density, rectangular measurement areas were spanned instead of point analysis to generate a sum spectrum on the whole area. The rectangles were made as large as possible to include as much information as possible with approximately the same size and without irregularities. A better representation of the element ratios could be achieved by using the count rates instead of the atomic percentages of the EDX spectra.

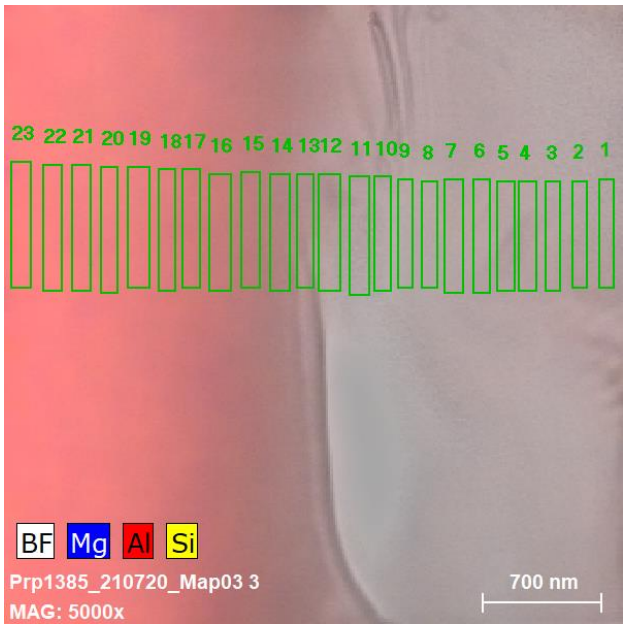

Figure 2.22: EDX-map of the pyrope starting material. Green boxes show the position of the spectra from the chemical map, displaying the thin part of the TEM sample (right side) to the thick part of the TEM sample (reddish left side).

Since k-factors are valid for a sample thickness of t = 0, the measured k-factors for t = 0 were determined by extrapolation towards 0. This method is the PCM method (parameterless correction method; Van Cappellen, (1990); Van Cappellen & Schmitz, (1992)). Meanwhile the thicknesses of the samples can only be determined with an uncertainty of ± 50 nm in the analytical error, so the live time counts are taken instead. Live time counts are counts per second and can be read from the quantification info table in the Bruker software after the quantification map process. These counts are proportional to the thickness and the acceleration voltage. Since silicon is the basis of the silicate materials in this study, the k-factors are given relative to silicon. The results of determining the k-factors are summarised in section 3.1.1. The k-factors are calculated by relating the extrapolated ratios of the element contents at t = 0 to the weight percent ratios of the compositions. This means that the k-factors must be determined separately for each sample-specific element ratio (Mg, Al and O against silicon (Si)) as a function of the accelerating voltage. For infinitely thin samples, absorption and fluorescence should be ignored. The compositions can be calculated as follows (Cliff & Lorimer, 1975):

$$\frac{c_\alpha}{c_\beta} = k_{\alpha\beta} * \frac{i_\alpha}{i_\beta} \qquad (2.4)$$

where c_α and c_β are the element weight percentages; α and β representing elements; i_α and i_β are the intensities of characteristic X-ray, and $k_{\alpha\beta}$ is the Cliff-Lorimer k-factor. In analysing samples, selecting a proper sample thickness ranging from 50 to 400 nm is essential, as the data can deviate significantly from the fitting function chosen in the range of minimal sample thickness. This is usually caused by already amorphised surface layers, which already account for a considerable proportion of the total analysed volume. A similar systematic deviation from the selected regression function is also possible with increasing thickness, which is caused by increasing absorption effects. According to Williams & Carter, (2009), the absorption correction factor k^A can be calculated using the mass absorption coefficient for a specific X-ray concerning each element in the sample. The sample thickness, density, and take-off-angle must be known for the calculation. For more in-depth theoretical explanations, I recommend the following literature: (Waldo *et al.*, 1993; Van Cappellen & Doukhan, 1994; Holzapfel *et al.*, 2005; Williams & Carter, 2009).

Energy dispersive X-ray spectroscopy (EDX)

EDX analysis is performed continuously in STEM mode as a 0.2 nm-focussed electron beam. It scans on the thin TEM sample with a fast scanning time, usually 16 microseconds (µsec) dwell time, so the electron beam irradiation damage is lower due to the fast scanning. In addition, the EDX detection system is more efficient. It requires lower total electron doses due to the high efficiency of X-ray acquisition in the 4 silicon drift detectors, which causes minor damage to the samples. For a spot size on the sample surface between 2 and 5 nm, the spatial resolution of the TEM is 10 and 26 nm in diameter (Meißner, 2000). In combination with fast-mapping electronics with up to 100,000 spectra/second, precise EDXS analysis is possible (Thomas & Gemming, 2013).

The TEM sample is generally 50 to 100 nm thick, so the beam scattering reduces the horizontal resolution. The spatial resolution is defined as the smallest distance (R) between two analysis spots, and for a C_s-corrected 300 kV FEG-TEM, the spatial resolution for small spot sizes of 1 – 2 nm is $R \approx 0.8 – 5$ nm. More detail on spatial resolution is given in section 3.1.1. The TEM image resolution is typically 0.25 nm for non-Cs corrected TEM at 200 kV and < 0.1 nm for Cs corrected TEM at 200 kV (Williams & Carter, 2009). The absorption effect is a significant consideration for sample thicknesses greater than 50 nm. In the TEM software “Bruker Esprit” used at BGI, values for thickness and density can be entered to correct the absorption effect at low atomic numbers and due to specimen thickness. The self-determined values for thickness and density should be similar to or better than the actual values. In general, it can be assumed that both absorption (A) and fluorescence (F) are negligible for a thin TEM sample (e.g., silicates, averaged Z-numbers = 10) less than 50 nm. Also, the atomic number-dependent stopping power and X-ray generation (Z) is approximately constant for electron-transparent samples.

Furthermore, k-factors are included in the analysis. These serve as a standard, and adjusting them before each sample analysis is recommended. For this purpose, a standard or a sample with a known composition is usually measured, and the k-factors are adopted for the unknown sample of similar composition. After the TEM and STEM observation, the EDX map is used to determine the diffusion profile (Figure 2.23) and to calculate the diffusion coefficient. More detail is given in the next section.

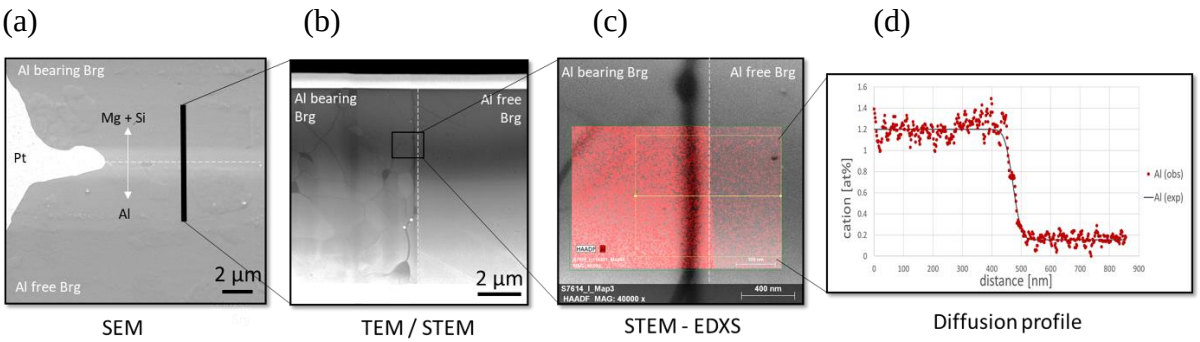

Figure 2.23: Scheme of step-by-step evaluation of a diffusion experiment. In SEM image (a), the diffusion interface is shown as a dashed white line. The black bar represents the sampling position of the FIB sample. The HAADF STEM image (b) shows an overview of a diffusion lamella with the diffusion interface indicated as a white dashed line and the map position in black. In image (c), the EDX map is superimposed on the HAADF image of the sample position. It also shows how the line scan is aligned in the sample (yellow). The last image (d) shows the element concentration of each spectrum (red dots) of the line scan evaluation. It shows the diffusion profile for this sample in an Excel graph.

Determination of diffusion coefficients

The chemical composition of the samples was calculated based on the intensity ratios of the characteristic X-rays using a transmission electron microscope (TEM) equipped with an energy-dispersive X-ray (EDX) detector. The Al content of the samples was then measured at the nanometre scale, and the EDX spectrometry (EDXS) maps were used to evaluate the Al substitution mechanisms in Brg. Some samples were also characterised for crystal orientation and lattice defects using bright and dark field TEM imaging and electron diffraction patterns. Assuming that diffusion anisotropy in bridgmanite is negligible, we used differently oriented samples to determine isotropic diffusion coefficients.

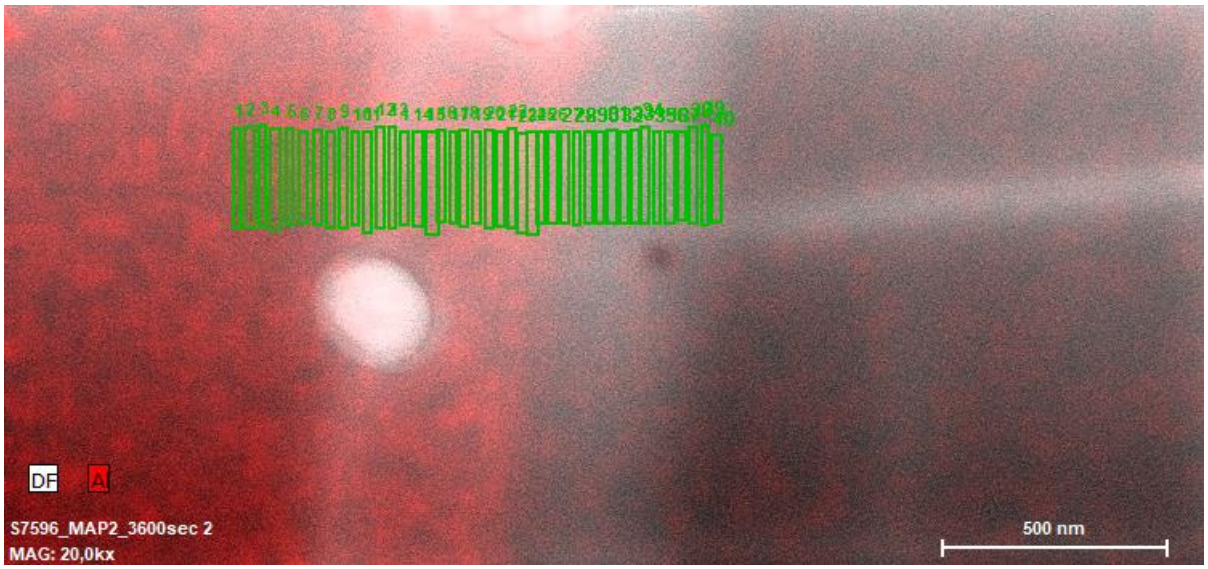

Figure 2.24: Hypermap with 40 spectra to measure the diffusion coefficient manually. For this purpose, individual rectangles of approximately the same size are stretched in a line. Boxes are used instead of points to increase the information density and to generate a representative result.

The EDXS maps were evaluated with the Esprit 1.9 software in the Bruker Quantex detector. For this purpose, the data were acquired as HyperMap in a function of the EDX software (Figure 2.24). These maps can be further evaluated by Cliff-Lorimer (CL) quantification after saving and QuantMaps (QMaps) can be created to quantitatively obtain the element-dependent intensity per pixel from the spectra data. The hypermaps have an average size of 1.6 × 1.6 µm^2 with 490 × 450 measured points (MP), resulting in a pixel density of 2.0 × 10^5 pixels/µm^2 (see Appendix A, Table 5). This makes the data very high-resolution and reliable. Depending on the sample thickness and map size, samples were measured for 3,600 s or 7,200 s.

To achieve sufficient spectral density to maximize the number of individual spectra along the diffusion profile we tried different magnifications and the best results were obtained at a magnification of 14 kx and a QMap resolution of 1.5 × 1.6 µm^2 (400 × 300 MP) with a pixel density of 1.5 × 10^5 pixels/µm^2 and a mapping time of 7,200 s. The QMap was constructed with a map filter of "3" and a QMap filter of "9" to smooth the image. The "rainbow" image (Figure 2.25) view was displayed in atomic percent and adjusted to the sample composition. As a k-factors library, which is filled by the self-created k-factors collected for this study as explained earlier, "k-calib LauraCz_Pry_Map04_new.esl". The QMaps were initially evaluated by lining up many boxes (Figure 2.24); this created some unevaluated pixel areas between the rectangular boxes. In the progress of the work, line scans perpendicular to the diffusion interface were used (Figure 2.25) since they guarantee a seamless and low-error evaluation of the maps. For this purpose, the sample thickness was first evaluated, and then a QMap was generated based on this estimated sample thickness.

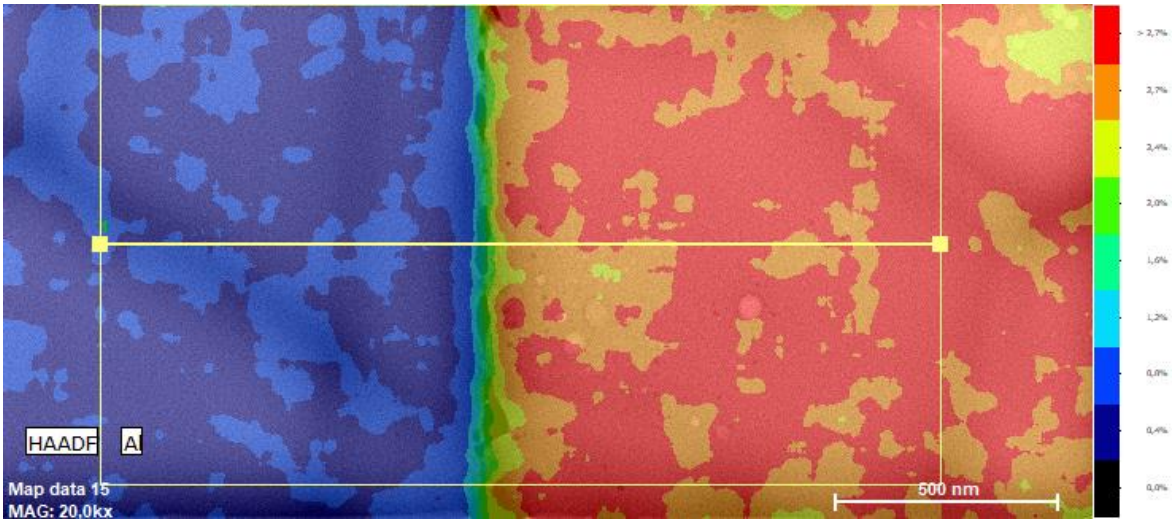

Figure 2.25: QMap of the element Al in atomic percentages. Magnification 20 kx. Line scan covered the whole map height to generate high information depth.

Subsequently, the line scan was adjusted to the mineral grain size to exclude the effect of grain boundary diffusion from the results of target volume diffusion. The resulting data were evaluated in the "line scan" mode of the Bruker software and exported to ASCII data. The ASCII files from the line scan evaluation were further processed with Excel (Figure 2.26). For this purpose, the ASCII files were converted to Excel, and the diffusion coefficient was estimated approximately by the Crank equation. The PACE (the Program for Assessing

Convolution Effects) software was used to determine the diffusion coefficient for a more comprehensive evaluation.

For the approximation, the aluminium content in atomic per cent *(x,t)*, diffusion distance *x*, the minimum C_{min} and maximum aluminium content C_{max} and the diffusion profile centre was entered into the semi-infinite diffusion model, this equation, we call it as "the Crank equation" (Crank 1975):

$$C(x,t) = C_{min} + \frac{1}{2}(C_{max} - C_{min})erfc\left(\frac{x}{2\sqrt{Dt}}\right) \qquad (2.5)$$

Diffusion coefficients tabulated in Excel (Appendix A, Table 2 + 6) were compared with those evaluated by using the PACE diffusion software (Jollands, 2020).

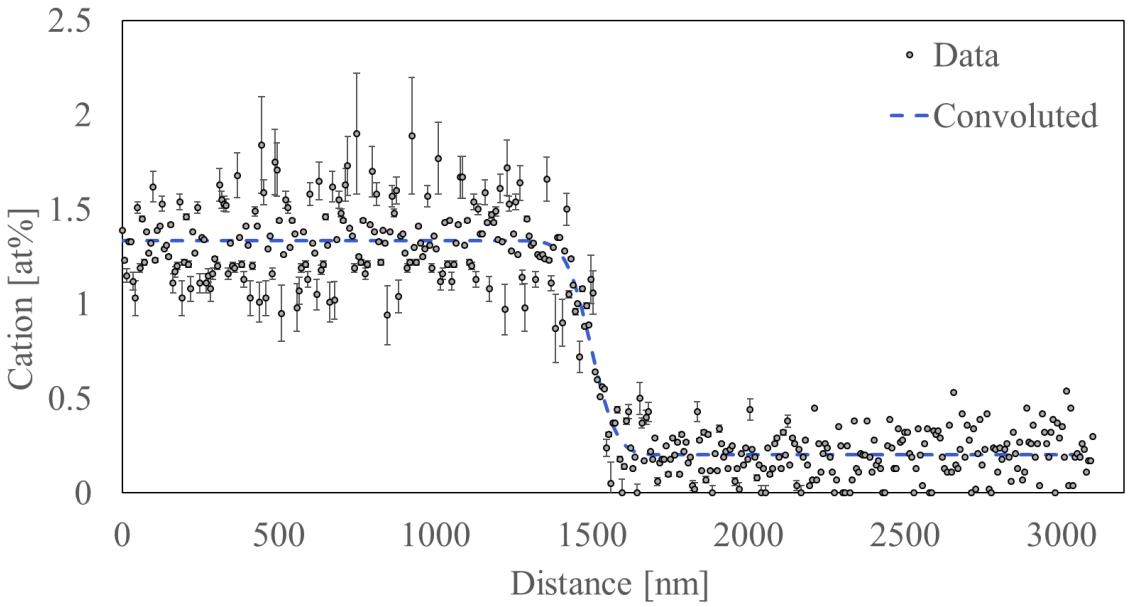

Figure 2.26: The diffusion profile of sample S7835 is fitted by the diffusion Equation (2.5) in an Excel spreadsheet. Cation diffusion of aluminium occurred between endmember bridgmanite and 3 mol % Al_2O_3 bridgmanite at 24 GPa and 1808 °C for 21 h. The black points represent the measured data points. The blue dashed line shows the data calculation by the Crank equation implemented by the Solver function in Excel.

Since the total diffusion length of the diffusion profile is comparable to two to three times lengths of a Gaussian beam profile in the TEM analysis, the profile is likely to have a strong convolution effect. Therefore, the profiles could be significantly overestimated, which is why the profiles were also acquired by deconvolution over the Gaussian interaction volumes using PACE software (Jollands, 2020). PACE is a software developed in MATLAB that allows for extracting deconvoluted diffusion profiles from measured profiles (Figure 2.27 b). To do this

in this study, the Gaussian interaction volumes must be assumed, the beam size must be known, and the geometry of the curve must be specified.

(a)

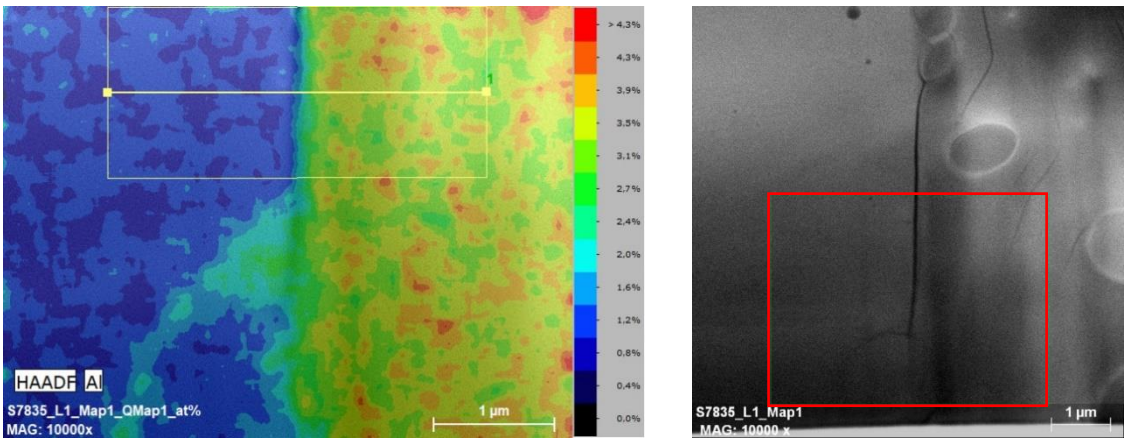

(b)

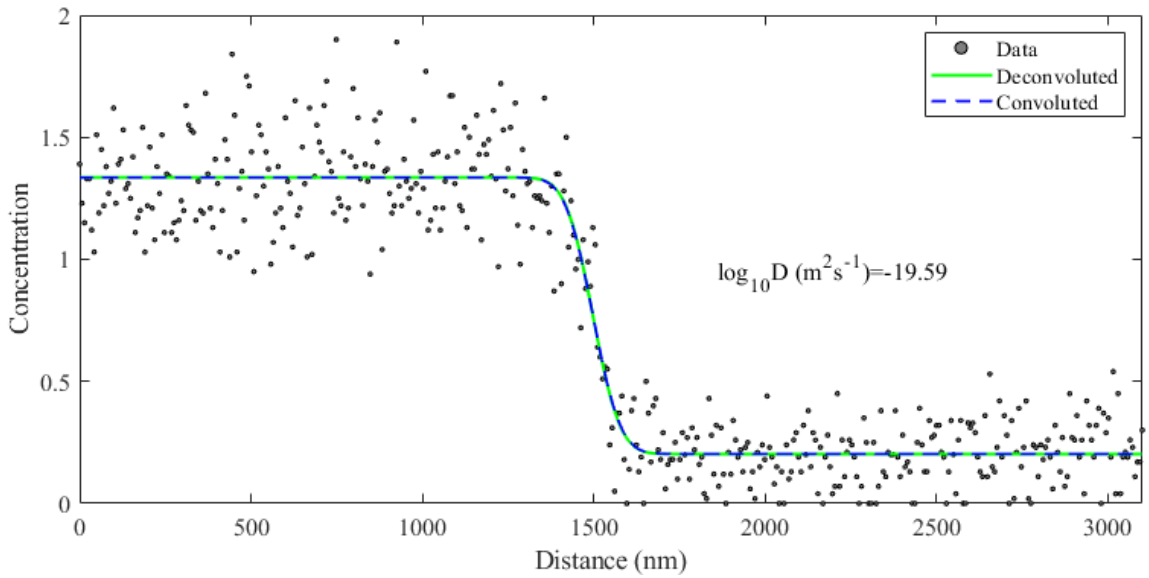

Figure 2.27: Diffusion profiles of Si^{4+} + Mg^{2+} = $2Al^{3+}$. (a) shows the TEM-EDXX map of S7835. The yellowish part is Al-bearing diffusion couple; the bluish part shows the endmember En100. The yellow line with the rectangle represents the line scan area and includes all spectra data in this rectangle. The HAADF images show the map location marked in red. (b) shows sigmoidal diffusion profiles calculated by the PACE software (Jollands, 2020) with FWHM = 26.4 nm and the diffusion coefficient of its profiles. Experimental data: En97Cor3, 24 GPa, 1,808 °C for 21 annealing hours. Both lines coincide within the line thickness and can hardly be distinguished in this plot.

The Gaussian interaction volumes can be estimated using PACE-GD and fitted to the method's boundary conditions. For this purpose, several mechanical interfaces were taken from the diffusion profiles and compared with the sample thickness (Figure 2.27). The full width at half maximum (FWHM) was determined and applied to the diffusion profiles by linear regression. The FWHM describes the beam diameter as the diameter at half height of the intensity distribution and is derived from the Gaussian distribution of electrons in the beam. In the end, three diffusion coefficients were available for each diffusion experiment:

- Unconvoluted diffusion coefficient from Excel calculation,
- Diffusion coefficient with FWHM = 10 nm as the lowest limiting value of the beam diameter and,
- Diffusion coefficient with FWHM = 26.5 nm as the highest limiting value of the beam diameter.

Together they formed the representative diffusion coefficient in the mean with the maximum and minimum errors. For accurate evaluation of analysis with short concentration profiles, it is essential to consider the resolution of the measurement method over the location. This also minimises inaccuracies in the x-axis and measured concentration profiles and avoids the convolution effect mentioned above. The spatial resolution is a function of the interaction volume of the incident electron beam with the sample. This volume depends on parameters such as accelerating voltage, atomic number and sample thickness.

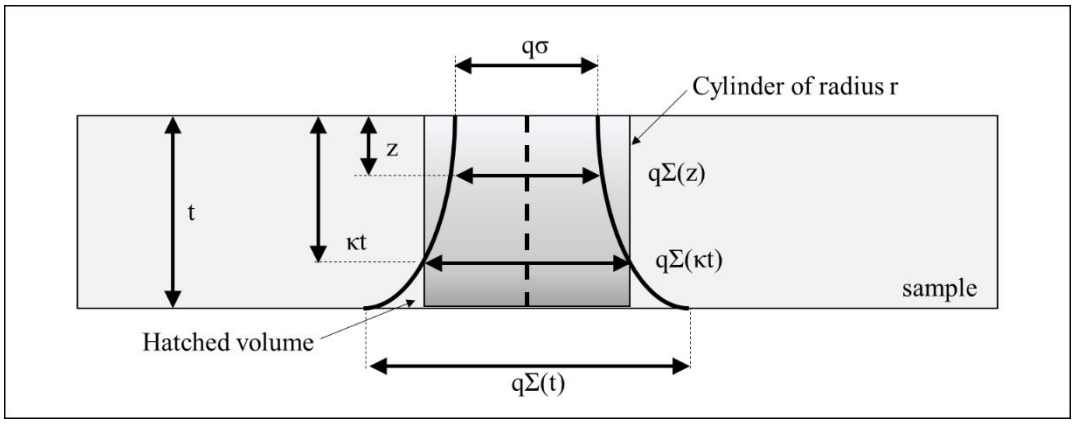

Figure 2.28: Cross-section of an irradiated TEM sample and visualizes beam broadening. With the electron density distribution and hatched volume around the primary beam in the way proposed by (Van Cappellen & Schmitz, 1992) *to define the Spatial resolution of EDXS in the section with z as defining coordinate of the distance from the foils top surface in a direction parallel to the incident beam. The dark grey box contains 50 % of X-ray intensity if q = 2.35 and intersects with the hatched volume at a depth κt.*

Spatial resolution is the smallest distance (*R*) between two points to be analysed that should yield independent chemical analysis (Williams *et al.*, 1992). This considers the shape of the excited volume as the beam passes through the sample. As shown in Figure 2.28, the diameter assumes a concentric, capped cylinder around the primary beam (hard core model) and represents the neck of the excitation bulb. *R* is a function of the sample thickness *t*. The intensity distribution of the electrons in the beam is assumed to be a Gaussian curve (soft core model). The important factor here is how large the proportion of generated electrons is assigned to this volume. According to Van Cappellen & Schmitz (1992), this electron density distribution can be described by a normal distribution with depth-dependent standard deviation. This beam broadening parameter can be used to derive an electron intensity distribution across the foil, assuming the beam broadening is Gaussian. Figure 2.28 show a cross section of an irradiated TEM sample and visualizes this beam broadening. Van Cappellen & Schmitz (1992) recommend a penetration depth $t \cdot \kappa$ with $\kappa = 0.63$. The lateral spatial resolution of EDXS should therefore be defined for a diameter *R* of the cylinder in which 82 % of the generated X-rays are contained. Thus, a detailed description of the spatial resolution is given by:

$$R(82\%) = 3.7 * \sqrt{\left(\sigma^2 + \frac{1}{8}\beta * t^3\right)} \qquad (2.6)$$

σ: Standard deviation of the incident electron beam

t: Sample thickness

β: broadening parameter which depends on accelerating voltage and the foil material:

$$\beta = 500\left(\frac{4Z}{E_0}\right)^2 \frac{\rho}{A} \qquad (2.7)$$

The parameter β describes the scattering of the electrons in the sample, which depends on the average atomic number *Z*, the density ρ and the average atomic weight *A* of the sample material as well as the accelerating voltage in volts E_0. For quantitative measurements in bridgmanite, for a sample thickness of 150 nm, a spatial resolution *R* of 7.5 - 18.5 nm with a spot size *(s)* of 2 - 5 nm can be assumed. The microscope spot sizes are usually given by their FWHM values. The theoretical FWHM are analysed in detail in Van Cappellen & Schmitz 1992 as follows:

$$FWHM = 2.35\sigma \qquad (2.8)$$

For 50 % of the X-ray radiation generated within the activation volume used to define the resolution.

In this study, the spatial resolution and the FWHM were examined experimentally, as the technique has developed over the decades, and the equations need to be adapted. The effect of the limited spatial resolution becomes significant when analysing interfaces where the composition changes in a spatial interval of similar dimensions to the resolution. Suppose a line scan is taken perpendicular to the interface, and the concentration profile is determined from it. In this case, the experimentally determined concentration profile will appear broader than the actual one (Figure 2.29 a-c). To avoid this effect, the mechanical limits were used to eliminate this analytical error. The FWHM values determined experimentally by the mechanical boundaries allowed a deconvolution of the actual diffusion profiles. The sigma value represents the deviation ± σ from the mean value of the Gaussian distribution.

(a) (b) (c)

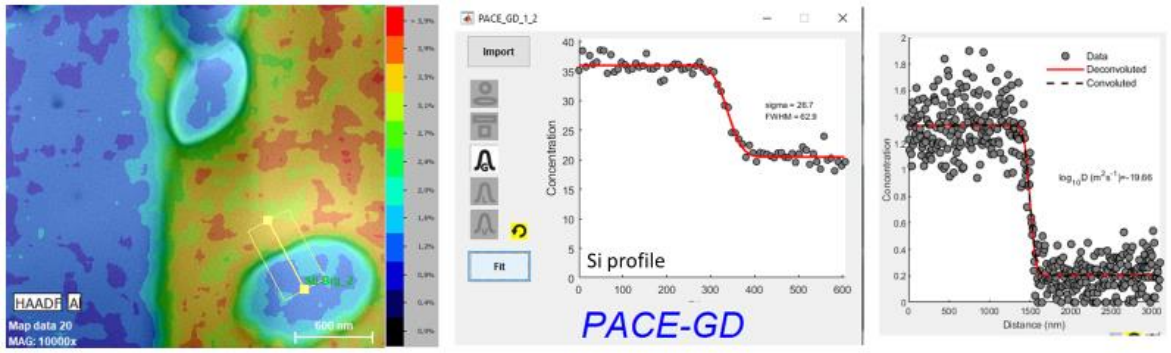

Figure 2.29: Procedure for FWHM determination. First: find a mechanical interface, like the Sti-Brg interface in (a). Second: Determine the beam size from a Gaussian convoluted profile using PACE-GD (b), showing the Si concentration profile with the corresponding sigma and FWHM values, which are extracted the beam size from a Gaussian convoluted profile and used for the third step). Third: Apply to deconvoluted diffusion profiles with calculated diffusion coefficient (c). In this case, S7835_L1 was annealed at 1,808 °C for 21 h.

3. Results

After successful runs, the diffusion experiments were prepared and evaluated for TEM analysis. Table 3-1 shows all the successful diffusion experiments with the corresponding experimental conditions. All diffusion experiments were performed in 7/3 assemblies at 24 GPa at different temperatures and annealing times. This section first adresses the methodological work with the TEM, considering the physical parameters. Subsequently, the suitability of the TEM-EDX method for diffusion coefficient measurements is demonstrated on the basis of the diffusion profiles. The determined diffusion coefficients were then used to estimate the temperature dependence and are presented in section 3.2.4. Furthermore, the results of the MgO-Al_2O_3-SiO_2 ternary diagrams of the bridgmanite samples and the investigation of the Al content in stishovite are presented in sections 3.1.3 and 3.4. The diffusion coefficient data obtained from the present study are compared with previous results and discussed in chapter 4.

Table 3-1 Summary of successful diffusion experiments in 7/3 assembly at 24 GPa. The table indicates if the temperature measurement via the TC worked, what experimental temperature was reached or estimated, and what power was applied. Additionally, the calculated temperature is shown derived from the temperature-power relation. The last column shows the annealing time.

Name	Material	Press	TC	T_{exp} [°C]	T_{calc} [°C]	P [W]	Time [h]
S7596[+]	En100+En97Cor3	Sumitomo	n	1,750	1,800	340	3.5
S7614	En100+En97Cor3	Sumitomo	y	1,750	1,870	370	7
S7830	En100+En97Cor3	Sumitomo	y	1,810	1,910	381	21
S7835	En100+En97Cor3	Sumitomo	y	1,810	1,950	387	21
S7766*	En100+En97Cor3	Sumitomo	n	2,000	2,000	397	4
S7808	En100 + En95Brm5	Sumitomo	n	1,800	1,802	350	3
S7824	En100 + En95Brm5	Sumitomo	y/n	1,800	1,900	363	6
S7828	En100 + En95Brm5	Sumitomo	y	1,750	2,000	395	4
S7843	En100 + En95Brm5	Sumitomo	y	1,800	1,805	361	21
S7751	En100+En90Brm10	Sumitomo	n	1,750	1,850	370	8
S7791	En100+En90Brm10	Sumitomo	n	1,750	1,910	380	0.5
H5548*	En100+En90Brm10	Hymag	y/n	1,750	1,850-2,100 °	605	4

* Diffusion experiments show an unusually long diffusion profile.

° Large variation between temperature measurement by TC (1,750 °C) and temperature determined by power curve (1,850 - 2,100 °C).

[+] 1/3 of the annealing time at 400 W (corresponds to 2,100 °C)

3.1. TEM characterisation of the samples

3.1.1. Experimentally determined k-factors

The k-factors are essential for the accuracy of the EDX analysis in the TEM evaluation and described in detail in section 2.3.5 (subsection "k-factor determination in the TEM-EDX analysis"). They are determined experimentally for an accelerating voltage of 200 kV and silicate minerals using the parameterless correction method (Van Cappellen, 1990) before analysis. The k-factors were determined using synthetic stoichiometric pyrope $Mg_3Al_2Si_3O_{12}$ and tested for their applicability to enstatite samples with unknown chemical composition. The enstatite starting material (B1288) with known composition was chemically analysed by TEM, and an absorption correction was applied. It is assumed that the resulting values correspond to the composition of the pyrope sample (used as a standard) and the sample thickness. In this case, it can be assumed that the k-factor used will give the correct results in the subsequent chemical analysis of unknown mineral compositions of the same starting material. Figure 3.1 shows an example of the determined $k_{Mg,Si}$, $k_{Al,Si}$ and $k_{O,Si}$ in the synthetic pyrope.

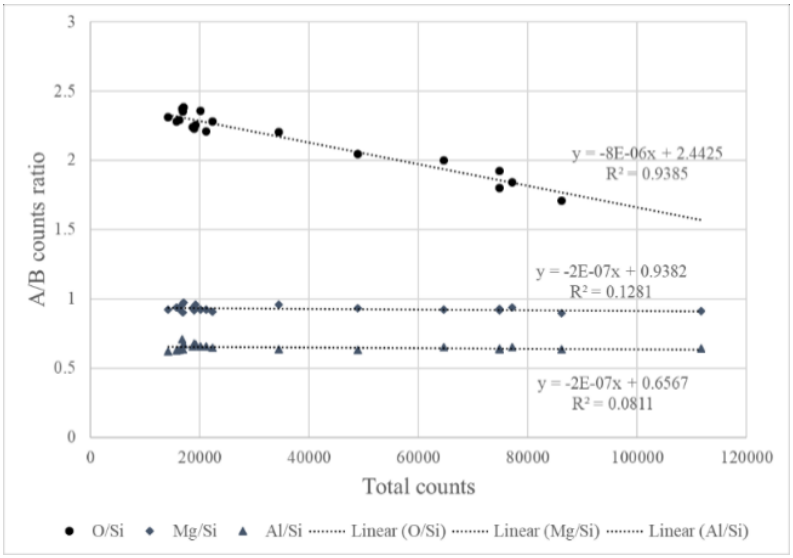

Figure 3.1: Determination of the k-factors $k_{Mg,Si}$, $k_{Al,Si}$ and $k_{O,Si}$ by using a standard of synthetic pyrope. Calculating by

$$\left(\frac{c_\alpha}{c_\beta}/intercept\right) = k_{\alpha\beta},$$

where c_α and c_β are the element's weight percentages.

The regression lines can be used to calculate the intercepts for the elemental ratios at t = 0. Several spectra were recorded and the total counts were used to calculate the k-factors according to Equation 2.4. An optimal spectrum of the standard is shown in Figure 3.2. This spectrum shows a stoichiometric pyrope sample without Mg loss caused by radiation damage.

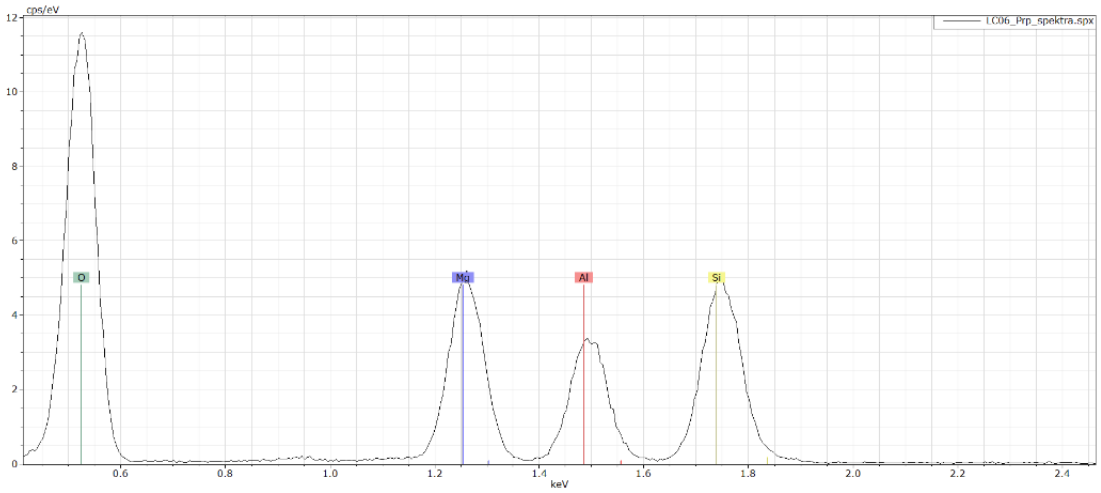

Figure 3.2: Typical EDX spectrum of the stoichiometric standard pyrope sample.

Table 3-2 shows all the measured values of the k-factors from this study and previously evaluated k-factors of pyrope glass and garnet samples. It also shows the means with error, where the errors given are the mean deviations from the statistical mean. The last column of the table shows the averaged k-factors used in this study. The factors for oxygen were adjusted over time (see Table 3-2; "k-factors I used"), and the validity of the experimentally determined k-factors was regularly checked, since the measurements of the O-K_α line, particularly, react very strongly to changes on the detector side. In addition, the effect of Mg loss inevitably occurs in very thin parts of the bridgmanite samples during analysis. See section 3.2.2.

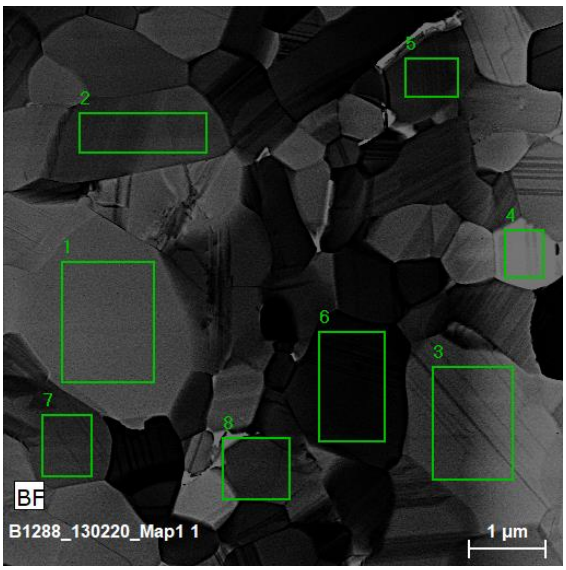

Figure 3.3: EDX spectra were measured in the green squares for the EDX analysis to test the k-factors in the B1288 sample.

Before using the k-factors to evaluate the chemical composition of the diffusion couples, the k-factors were tested on enstatite samples. The sample (Figure 3.3) was previously analysed for its stoichiometric composition by EDX, shown in Table 3-3. It can be seen that the listed atomic composition of the sample matches the expected atomic composition of $Mg_{0.95}Al_{0.1}Si_{0.95}O_3$ enstatite. Likewise, the analytical error is small. Also, when comparing the other enstatite samples, the k-factors were able to give the expected result. Therefore, the k-factors could be used for further evaluation and were deposited in the directory of the Bruker software 1.9 Software, which the programme refers to when evaluating the spectra. This directory serves as a standard library and basis for later evaluating the unknown samples in the $MgSiO_3 – Al_2O_3$ system. The software is part of the EDX evaluation, which is described in more detail in the next section. The standard library fed with the Pyrope k-factors was called "k-calib LauraCz_Prp_Map04_new.esl" in the computer used in the TEM laboratory.

Table 3-2: Summary of the k-factors for Mg, Al, O and their mean values determined on standards, using the FEI Titan G2, BGI, operating at 200 kV, t = 0.

Standard	$k_{Mg,Si}$	$k_{Al,Si}$	$k_{O,Si}$
Pyrope 1	0.89	0.93	0.86
Pyrope 2	0.93	0.98	0.98
Pyrope 3	0.92	0.98	0.93
Pyrope 4	0.92	0.98	0.91
Pyrope glass	0.98	0.99	1.15
C-Garnet	0.93	1.01	0.93
Average	0.93 ± 0.03	0.98 ± 0.03	0.96 ± 0.10
k-factors I used	0.93	0.98	0.94

Table 3-3: Chemical analysis of B1288 corrected by the previously calculated k-factors of the known sample pyrope.

k-calib LauraCz_Prp_Map04_new.esl Density: 3.2 g/cm²

No.	O [at%]	Mg [at%]	Al [at%]	Si [at%]	Mg/Si	$ct_{Al_2O_3}$ [wt%]	sample thickness [µm]
Spectrum 1	60.00	18.77	2.44	18.80	1.00	6.10	0.249
Spectrum 2	60.00	18.94	2.53	18.53	1.02	6.33	0.299
Spectrum 3	60.01	18.54	2.54	18.91	0.98	6.35	0.286
Spectrum 4	60.00	18.81	2.51	18.69	1.01	6.27	0.245
Spectrum 5	60.00	18.71	2.15	19.14	0.98	5.38	0.300
Spectrum 6	60.00	18.52	2.33	19.15	0.97	5.83	0.306
Spectrum 7	60.00	18.38	2.49	19.13	0.96	6.23	0.293
Spectrum 8	59.95	18.56	2.63	18.87	0.98	6.57	0.313
Average	60.00 ± 0.02	18.65 ± 0.18	2.45 ± 0.15	18.90 ± 0.23	0.99 ± 0.02	6.13 ± 0.37	0.29 ± 0.03

Determination of the TEM resolution

The spatial resolution is a function of the interaction volume of the incident electron beam with the sample and has already been described in section 2.3.5 (subsection “Determination of diffusion coefficients”). The half-width of the Gaussian function of the electron beam must be evaluated to determine deconvolution. The resulting values are used as FWHM values for assessing the diffusion coefficients in the PACE software. In the study presented here, the mechanical interfaces were defined analytically to determine the spatial resolution of the chemical analysis on the TEM. For this purpose, grain boundaries between bridgmanites and stishovites were analysed using the same method as the diffusion experiments (Figure 3.4). Since the FWHM strongly depends on the sample thickness, two values were used to determine the diffusion profiles (FWHM = 26.4 & 10 nm; Figure 3.5). A line scan profile was created perpendicular to straight grain boundaries in a TEM-EDX chemical map. To be able to compare the values later to diffusion interface data, efforts were made to ensure that the grain boundary thickness between Brg and Sti was similar to the diffusion interface thickness of the conventional chemical analysis to aim for the same sample thickness. The "grain boundary diffusion profiles" were then fitted into the PACE software to determine the FWHM values. This was done for nine grain boundaries in different samples and sample thicknesses. The resulting FWHM of the "diffusion profiles" were plotted considering the sample thickness. A regression line was used to determine the intercept at $t = 0$ and estimate the spatial resolution (Figure 3.5). The data points define two trends and therefore two regression lines were defined with a goodness of fit by R^2 with almost 1 and thus corresponds to an optimal model with the upper and lower limits of the possible width of the Gaussian function (were determined to be FWHM 10 nm and 26.4 nm). The blue regression line includes all data points and does not describe the data well. This regression line was therfore not used.

(a)

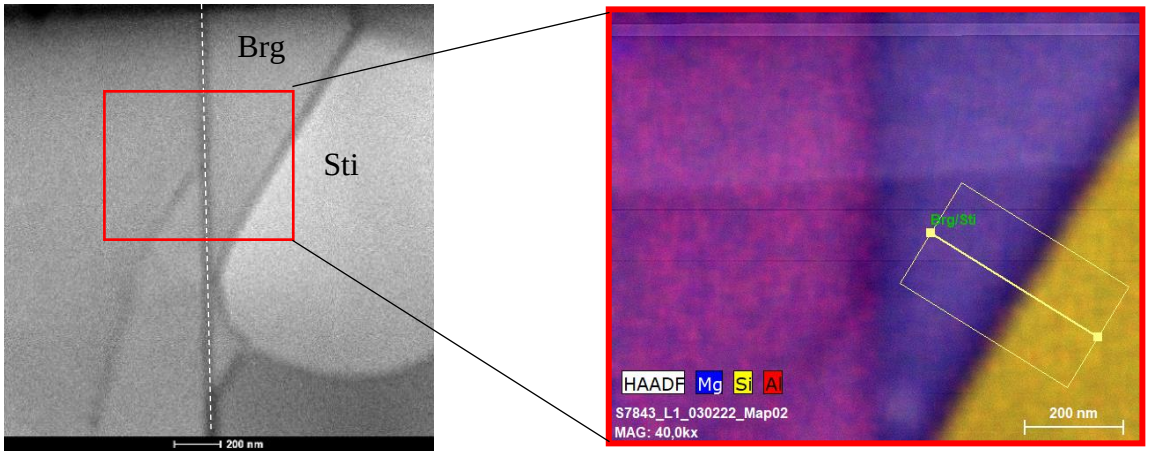

(b)

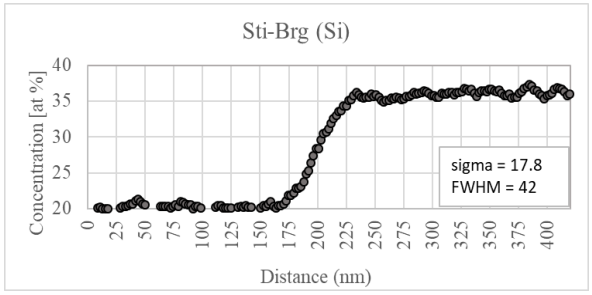

(c)

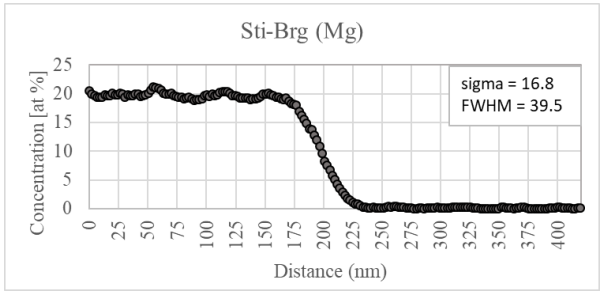

Figure 3.4: Images and graphs intended to show the influence of the amorphous layer/grain boundary effect. This amorphous grain boundary layer has the same width (~ 50 nm) as the one at the diffusion interface of the same sample (white dashed line). (a) shows the EDX map of the sample S7843 and the HAADF image. The yellow box indicates the line scan perpendicular to the grain boundary between Brg and Sti, and the red box shows the EDX map position in the sample. (b) and (c) display the Si and Mg concentration profiles along the line scan. The PACE software calculated the sigma values and FWHM. The FWHM value gave the diameter at half the height of the intensity distribution.

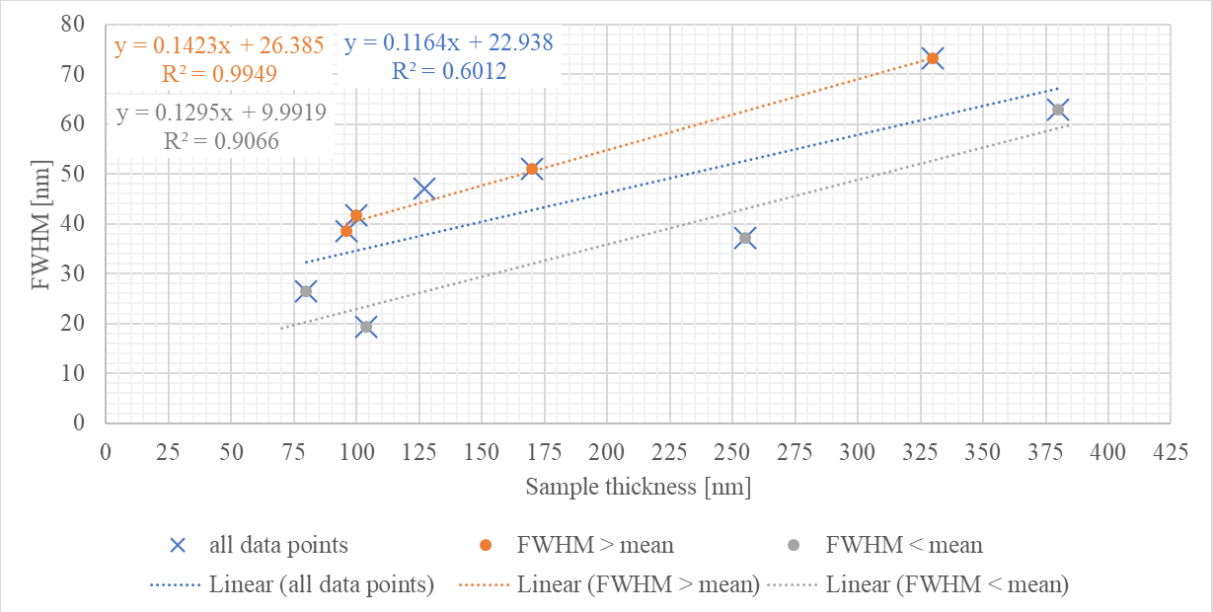

Figure 3.5: Calculated FWHM values related to the sample thickness and determined by the same method as the diffusion profiles. The individual data points are highly scattered and therefore, not uniformly correlated (blue regression line). Therefore, two regression lines were constructed to cover the scattering data points' upper and lower limits.

On the other hand, the FWHM value can be calculated using the equations from section 2.3.5 (subsection "Determination of diffusion coefficients"). This more elaborate method was not used in the present study because some developed physical parameters like the used spot size needed to be included. The spatial resolution depends on the beam current, the sample density and the average atomic number, so comparing the spatial resolutions to calculated spatial resolutions from previous studies is more complex. Meißner (2000) used a similar TEM but measured olivine samples and concluded that the spatial resolution must be between 10.4 and 26.0 ± 0.6 nm diameter for spot sizes of 2 - 5 nm (beam spot on the sample surface; p. 39) for a sample thickness of 200 nm, related to Equation 2.7 in section 2.3.5 (subsection "Determination of diffusion coefficients"). Our theoretical calculations show similar results, meaning that the theoretical considerations must be adapted to the evolution of technology in the last decade. Furthermore, it should be mentioned that Meißner (2000) and Holzapfel (2004) used point spectra to determine the diffusion profiles, and this entails a lower resolution of the diffusion profile. The study presented here used two-dimensional chemical maps superimposed by line scans to acquire the diffusion profile with a spatial resolution of 7 nm/pixel.

3.1.2. TEM characterisation of surfaces and defects/dislocations

Silicate perovskites can be unstable during mechanical preparation, so in this study chemical polishing with a colloidal silica suspension with a particle size of 0.04 µm (OP-U NonDry suspension obtained from Struers) was performed. The suspension was applied to a TexMet C polishing cloth from Buehler. The polishing process was performed for 3 × 15 min to remove defects and dislocations on the sample surface.

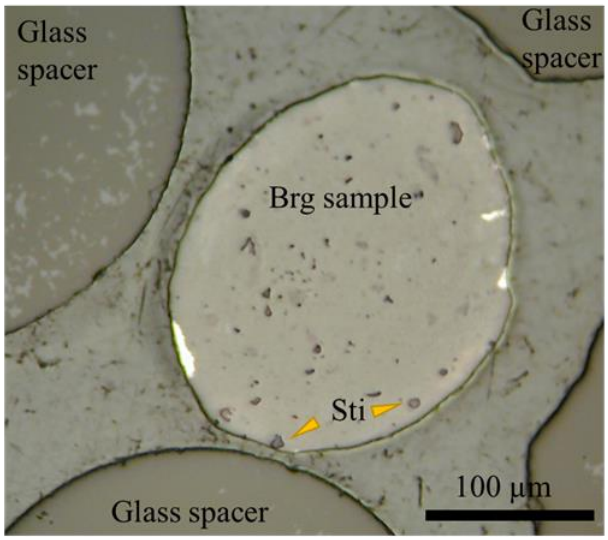

Figure 3.6: Optical microscope image of sample S7761b. Yellow arrows indicate stishovite crystals with a darkish margin. The glass spacers are used to polish the sample evenly during the polishing process and provide stability during polishing. The sample is already 250 µm thick after cutting and is divided into two 250 µm diameter disks after the polishing process.

Under the optical microscope (Figure 3.6), stishovite, unlike bridgmanite, is more resistant to chemical polishing. That is why dark rims can be seen around the stishovite crystal grains. These are to be interpreted as relief and make clear that stishovite grains settle from the surface and form a relief. Since the secondary phase represents only a tiny proportion of the primary phase in the sample, the relief is negligible. The undamaged surface of the bridgmanite is of greater relevance, as seen in the TEM image in Figure 3.7. When the polished surface of the samples was evaluated, it was found that chemical polishing successfully removed the surface defects and dislocations. Therefore, this method was used for all diffusion samples.

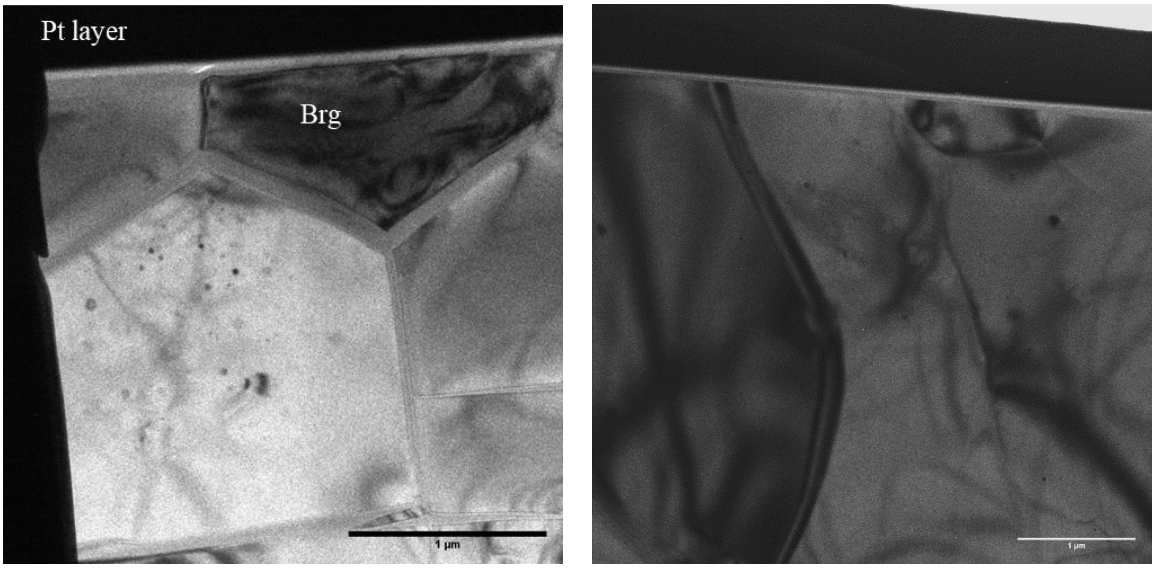

Figure 3.7: Bright-field TEM image of a surface sample. The black part is the Pt protective deposition on top. Directly below the protective film, the amorphous layer of carbon evaporation deposition can be seen. Underneath are crystalline bridgmanite crystals separated by a visible amorphous grain boundary. The radiation of the electron beam forms this amorphous grain boundary. No defects or dislocations are visible.

3.1.3. Ternary diagrams of bridgmanite in the Mg-Al-Si system

Compared to some mantle minerals $MgSiO_3$ bridgmanite (Brg) contains significant amounts of aluminium (Al) (Irifune, 1994). Al can be incorporated by substituting for silicon (Si), with charge balance provided through the formation of oxygen vacancies (OV) or by charge-coupled (CC) substitution of magnesium (Mg) and Si by 2 Al (Kojitani *et al.*, 2007; Liu *et al.*, 2019). To investigate the effect of the substitution mechanisms and the changes in the defects during the experiments, the diffusion profile was first divided into three parts (Figure 3.8).

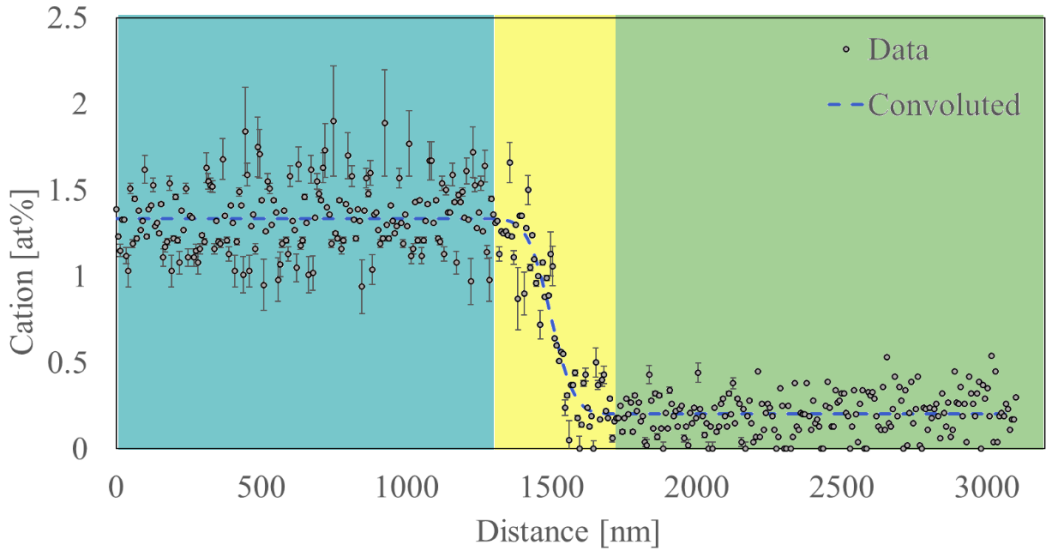

Figure 3.8: Example diffusion profile, divided into three parts. The blue-shaded part represents the Al-bearing bridgmanite before the diffusion experiment. The yellow shaded area shows the actual diffusion profile. The green shaded area corresponds to the Al-free endmember before the diffusion experiment. For the ternary diagram, all data of the diffusion profile were converted to an Al content ≙ 0 of the Al-free endmember.

For this purpose, the end phases of the diffusion couples (blue and green shaded areas) and the actual diffusion profile (yellow shaded area) were considered separately. The data points of the green region do not correspond to zero. This is due to a systematic error and was corrected for in determining compositions for the ternary diagram by adjusting all data points lying in the diffusion profile to an Al content ≙ 0 of the Al-free endmember. An average value was calculated from all differences between the endmember points and zero. This value was calculated to be the mean error of 0.2 at. % aluminium of the Al-free endmember. The resulting data were plotted separately in a ternary diagram (Figure 3.9).

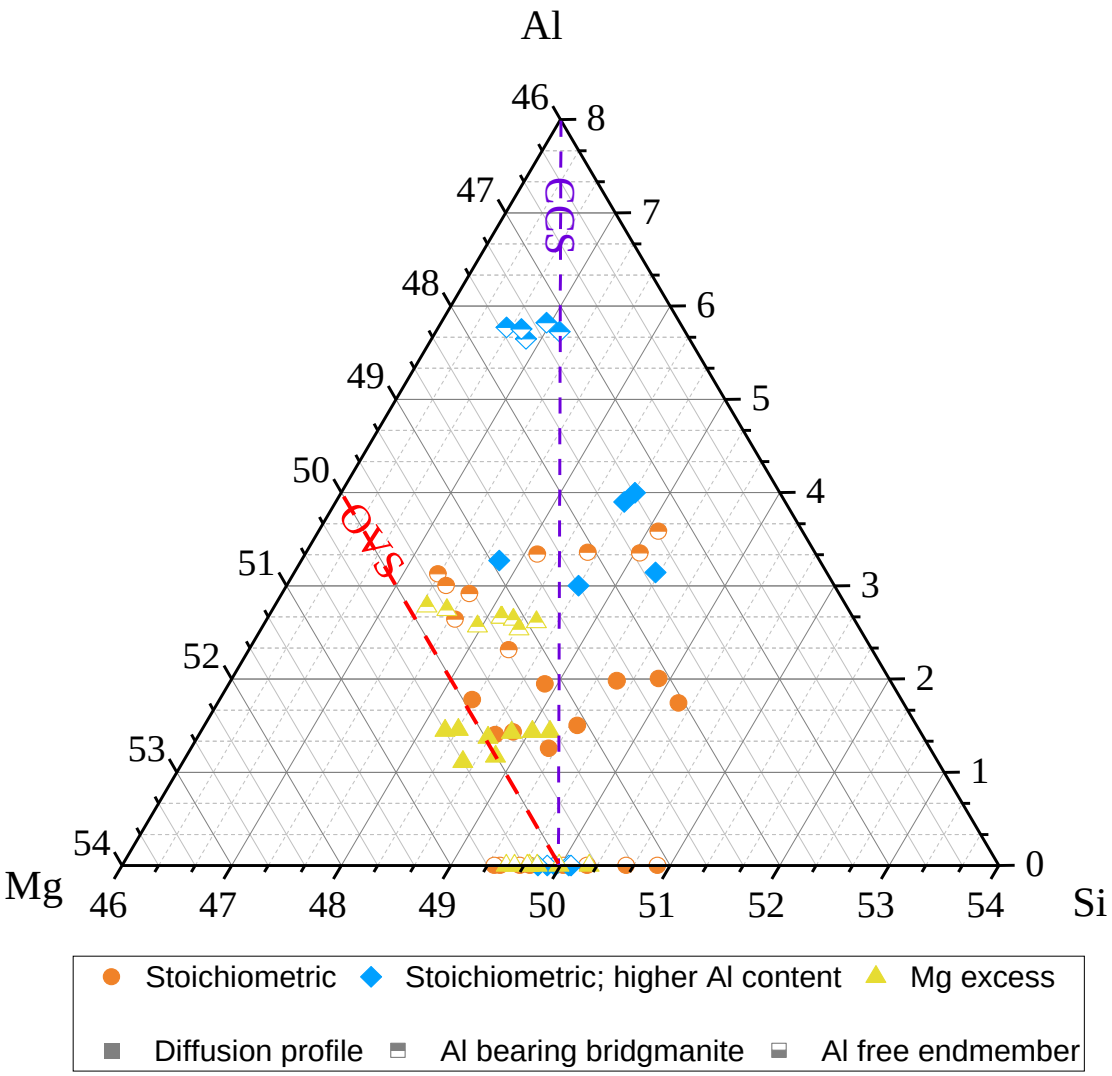

Figure 3.9: Ternary diagram of bridgmanite in the Mg-Al-Si system (at. %) with the separated data of each part in the diffusion profile. CCS: charge-coupled substitution line. OVS: oxygen vacancy substitution line. Composition data are from TEM analysis with the different starting materials. Full symbols relate to data from the diffusion experiment (shown in yellow in Figure 3.8). Symbols with a half-filled upper part represent the Al-bearing bridgmanite samples (blue in Figure 3.8) and symbols with half-filled lower part represents the Al-free endmember (green in Figure 3.8).

In this diagram, it can be seen that the data points of the Al free endmember plot on the Mg-Si line. It can also be observed that they scatter around the stoichiometric point of the Mg-Si line, similar to the data points of the Al-bearing bridgmanite representative for the sample before the diffusion experiment. In comparison, the large yellow triangle data points (those of the actual diffusion profile) are on the Mg-rich side of the ternary plot. At the same time, some orange circle data points are on the Si side of the diagram. Looking at the starting material (before the diffusion experiments were carried out, which is also indicated as the part of the sample that

was not affected by the diffusion, marked in blue in Figure 3.8.), the yellow data points are enriched in Mg, and the orange data points are slightly enriched in Si, caused by the secondary phase stishovite.Thus, as expected, the diagram reflects the composition of these two samples. However, it is also noticeable that the stoichiometric orange data points have a wide range. The large uncertainties are caused by the high analytical error of the absolute chemical values from the EDX analysis. To sum up, they tend to lie (on average) on the stoichiometric line of the $MgSiO_3 - Al_2O_3$ composition (CCS), as expected. The data points of the Al bearing bridgmanite representative for the sample before the diffusion experiment behave differently (marked in the blue area of Figure 3.8). Most of these points lie on the Mg excess and stoichiometric side of the diagram (Figure 3.9). If we look more closely at the composition of the Al bearing data points, we find that they correspond to the starting material (compare Table 2-1) and to the EDX SEM evaluation of those samples. From this table of chemical analysis of the starting material, it can be seen that the stoichiometric samples with higher Al content (blue diamonds) have an Al content of 5.1 wt. %, the Mg excess samples (yellow triangles) have an Al content of 2.7 wt. %, and the stoichiometric samples (orange circles) have an Al content of 3.0 wt. %, which corresponds approximately to the weight per cent taking into account the uncertainty in the ternary diagram. From the EDX SEM analysis it is noticable that the Mg excess samples have coexisting periclase grains (see Appendix B; Figure 1 + 2) and the stoichiometric samples with 5.1 and 3.0 wt. % Al content have a coexisting stishovite phase (see Appendix B; Figure 3 + 4). The irregularities in the endmember and diffusion data may be due to Mg loss during analysis which is explained in detail in section 3.2.2.

Looking at the errors in Figure 3.10, we see that the uncertainties in the Al content of the samples are smaller than those of the Mg/Si ratio. The uncertainties represent the deviation of the individual measurement from the average result. The large uncertainties in the ternary diagrams caused by the high analytical error of the absolute chemical values from the EDX analysis (at. %). They do not affect the relative results of the Al concentration estimation (at. %) and diffusion profile evaluation. More significant deviations can be observed in further analyses. Additional data points from the SEM analysis were added to this diagram (S7766 + H5548), indicated by the open hexagon shape. The experiment H5548, unlike the other experiments, shows a fast diffusion coefficient. Despite the Si and Al excess in the starting material, it is close to the results from the stoichiometric experiments.

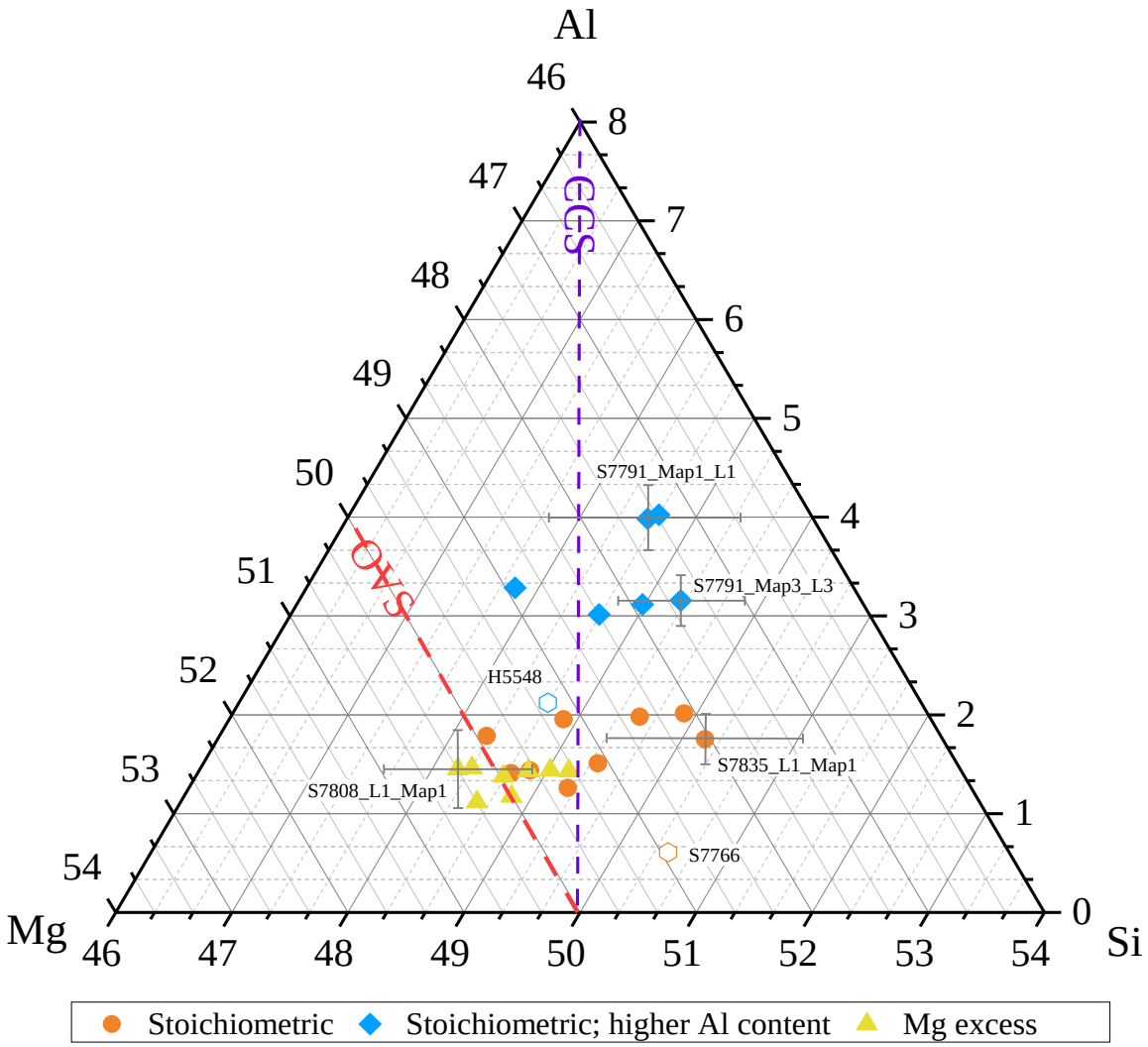

Figure 3.10: Final ternary diagram including estimated uncertainties for four data points. These four data points serve as examples to provide a rough estimation of uncertainties. CCS: charge-coupled substitution line. OVS: oxygen vacancy substitution line. The stoichiometric samples are approximately on the CCS line considering the large uncertainties. Additional data points from the SEM analysis were added to this diagram (S7766 + H5548), indicated by the open hexagon shape. The large uncertainties are caused by the high analytical error of the absolute chemical values from the EDX analysis and do not apply to the relative determination of the Al concentration evaluation.

So far, it has not been possible to establish a relation between the changes in the diffusion coefficient and the substitution mechanism. In general, the yellow data points show a larger compositional scatter. This makes it difficult to reach a final statement about the substitution mechanism of these samples. The same can be said about the other data points. No clear picture emerges that allows a conclusion about the substitution behaviour of the bridgmanite samples.

The yellow triangles on the oxygen vacancy substitution join in Brg indicate Mg-excess conditions. At the same time, orange points and blue diamonds must be at or close to stoichiometric conditions, although with a possible Mg loss due to randomly higher electron doses in some TEM-EDS analysis and higher analytical error for the chemical analysis of absolute element concentrations. However, reliable statements can be made about the relative Al content and the Mg and Si enrichment of the starting material. It can be seen that Al-bearing samples of the Mg excess composition and stoichiometric composition material have an Al content of about 2.7 – 3.5 wt. % and thus contain less Al than the samples with the stoichiometric 5 – 6 wt. % Al_2O_3 bearing starting material. Furthermore, it can be seen that the yellow triangles are enriched in Mg, and the blue and orange data points are enriched in Si.

3.2. Al-Si interdiffusion in bridgmanite

The methodological results show that the TEM-EDX is a suitable method for determining meaningful diffusion coefficients. This section explains the approach from evaluation of the synthesised bridgmanite to the final diffusion coefficient evaluation. The images shown here are examples and the procedure was the same for all experiments.

3.2.1. SEM investigations of bridgmanite diffusion experiments

SEM characterisation was used to determine grain sizes using SE images and chemical composition quickly and easily through point spectra and map analysis of the sample. This was done at 5 kV and 30 µm aperture to protect the surface of the samples. The surface of bridgmanite can be amorphised if the beam current is too high. The method was used after the synthesis and diffusion experiments. In both samples, the grain sizes and chemical composition were of interest. In the case of synthesis, it was essential to determine whether the synthesis was successful and whether the sample was suitable as a diffusion couple. The focus was on the homogeneity of the sample in terms of grain size and chemical composition. The best location for the FIB diffusion specimen sections was then determined from the SE images. The sample needed to have no contamination and a homogeneous grain size distribution. An overview image was first created, which was used to identify more significant impurities and to get an overview of the nature of the sample.

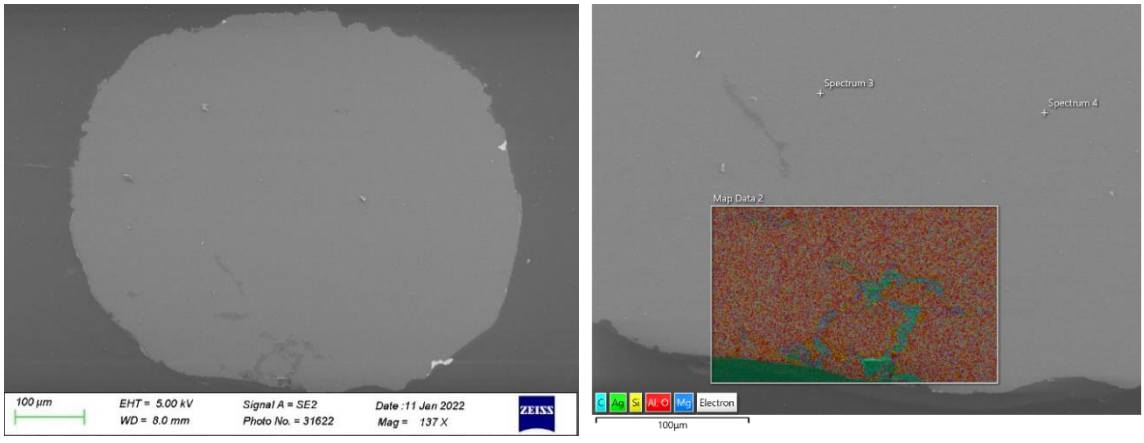

Figure 3.11: SE view of S7828 with associated chemical analysis of the lower sample area. Darker areas can be seen on the left-hand side. These areas were analysed in an EDX measurement to determine the chemical composition of this sample. As can be seen, sample S7828 contains Ag rich impurities which are removed during further sample preparation. In addition, two spectra were carried out to determine the chemical composition of the surrounding material. As expected, it was bridgmanite and the sample could be used for further work.

As seen in Figure 3.11, there is an impurity in the lower part of sample S7828. During chemical analysis, the darker area was found to have an increased Ag content and omitted during further processing of this sample. In general, samples were then enlarged (Figure 3.11 right side + 3.12) to estimate the grain sizes and chemical composition. In this sample, the average grain size is 2 – 3 µm. The grain size in Al-containing bridgmanite is 2 – 4 µm and in Al-free bridgmanite is 7 – 10 µm (Appendix A; Table 4).

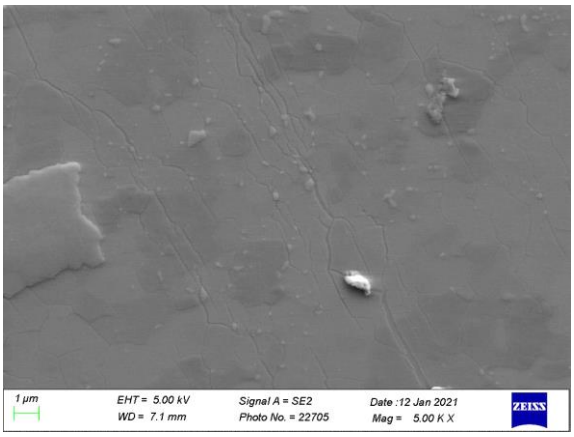

Figure 3.12: Detailed SE image of S7614 to estimate the grain size and wt. % of the secondary phase stishovite. It can be seen that the beam damage has already partially amorphized the grain boundaries and crystal grains, causing them to appear elevated in the image. This happens when radiation is too long and too strong. Since stishovite is more resistant to the beam, the grains show a clear relief.

After successful diffusion experiments, the position of the TEM specimens could be determined using SE images. First, an overview image was taken to determine if the sample was intact (Figure 3.13 a). Then, the image was further magnified to provide an overview of the diffusion interface (Figure 3.13 b). After further magnification, a close-up of the interface of the two diffusion couples provides an impression of the contact between the two samples. It allows for estimating the size of the resulting decompression cracks (Figure 3.13 c).

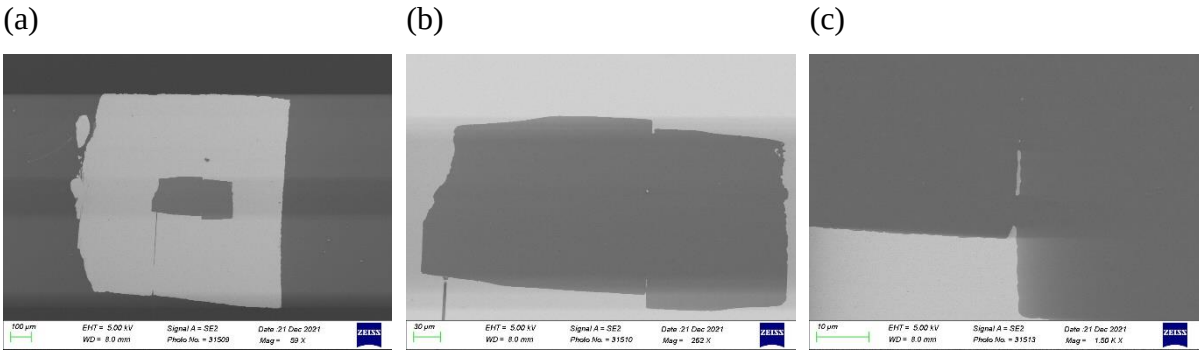

Figure 3.13: Process during SEM observation of diffusion experiment S7828. (a) shows an overview image. This is enlarged as (b) and (c) show. (b) offers a more detailed overview image and provides an overview of the diffusion interface. (c) is a detailed image of the interface of the two diffusion couples and is used to get an impression of the contact between the two samples and to see if decompression cracks have developed.

The diffusion capsules were removed from the multi-anvil sample and then ground longitudinally up to 1/6 of the sample thickness to obtain a good overview of the entire sample. In some cases, the whole run product was embedded in epoxy resin and ground until an overview of the entire experimental setup was visible. This is also illustrated in Figure 3.14. This procedure was carried out in the case of particularly successful experiments or of experiments that went wrong to be able to reconstruct the experimental process. Figure 3.14 shows the complete experimental setup of a successfully performed experiment. The experiment was successful because the temperature reading and the entire compression and decompression run did not present any recognisable failures.

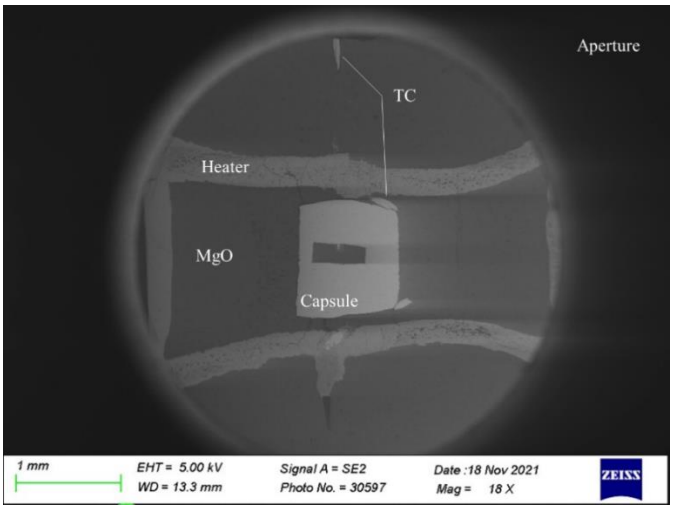

Figure 3.14: SEM image in SE mode at the lowest possible magnification (S7808). The view is through the aperture. The intact sample with heater, filling material (MgO), thermocouple and the Pt case with the sample in the centre can be seen.

After the initial survey, areas were sought where it was critical to find locations that had no decompression cracks and no secondary phases (Figure 3.15). Decompression cracks can cause the TEM samples to break or even to be amorphised too quickly during sample preparation and thus become unusable. Likewise, too many secondary phases, in this case, stishovite, make sample preparation difficult due to their resistance to the Gallium beam. It requires a higher current to cut the stishovite in the FIB processes, and at the same time, the probability increases of destroying the bridgmanite grains by amorphisation.

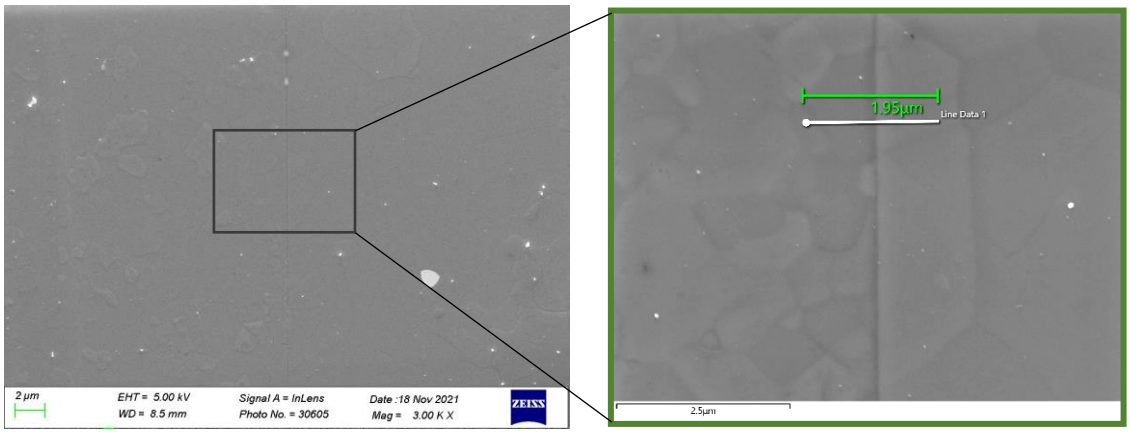

Figure 3.15: Overview of the S7808 sample. Visible are the diffusion interface and Pt surface impurities in the sample, which were created during polishing. In addition, bridgmanite mineral grains are visible in the enlarged image due to the longer exposure time. The enlarged detail image of S7808 shows the perfect placement for a FIB lamella on the right.

In Figure 3.15, the secondary phases can be seen well. An elevated relief characterises them in the left SE image. This is the result of polishing since stishovite is more resistant than bridgmanite. After long exposure times in the SE mode, bridgmanite grains can also exhibit a positively pronounced relief by amorphisation processes on the grain boundaries. Only chemical analysis can provide a reliable determination. In the enlargement of Figure 3.15, the individual grain boundaries and the diffusion interface are visible. This area in the sample is well suited for further processing for TEM observations. In addition, a line scan was taken at this location to check the resolution of the SEM-EDX at 5 kV (Figures 3.15 and 3.16). For this sample, the calculated diffusion coefficient was very similar to the TEM result. A diffusion coefficient of $D = 5.6 \times 10^{-20}$ m^2/s or $\log_{10}D = -19.25$ m^2/s was determined. However, in general the diffusion coefficients were not determined via SEM.

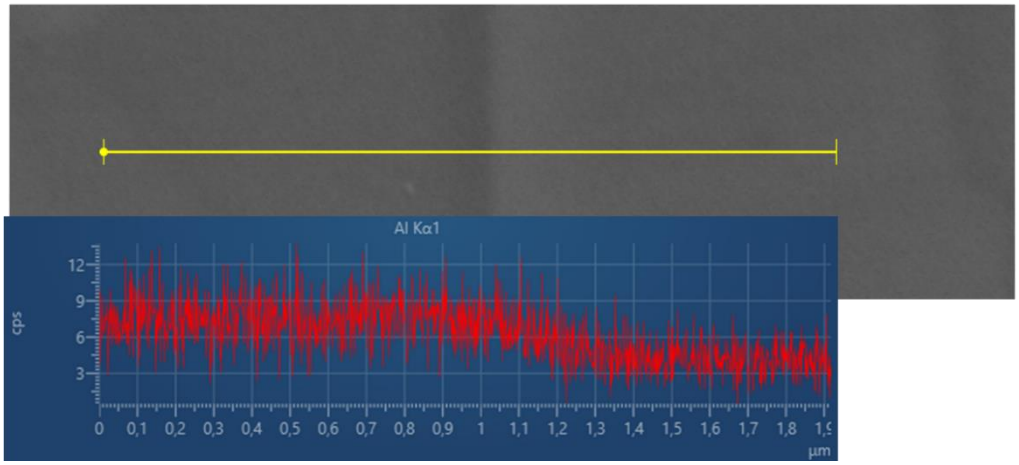

Figure 3.16: Superimposed chemical evaluation of the Al content in sample S7808 for the line scan (yellow), also shown in green in Figure 3.15. The relative Al concentration profile is shown in red.

3.2.2. Diffusion profiles and coefficients

Diffusion profiles and coefficients are obtained by relating the relative aluminium concentration to the diffusion length. The diffusion length, represented by the x-axis, is obtained by graphically determining the measurement endpoints in STEM mode. A profile line is created on an EDX map, which is always perpendicular to the diffusion interface and is defined by grid units. The completed line scan gives the length from one endpoint to another in nanometres. This length is based on the pixel size and the respective magnification and is individual for each measurement. The diffusion data can be compared by determining the diffusion length from the graphical representation. The computer-controlled beam position ensures that the dwell time of the electron beam is the same for all measurement methods. To minimise analytical error, it is essential to consider the shape and position of the mineral grains when aligning and positioning the line scan. Thus, the surface of the line scan is adapted to the nature of the sample. For example, as can be seen in Figure 3.17, the full height and width of the EDX map could not be integrated to obtain individual EDX spectra at each x-positions because of the curvature of the diffusion interface.

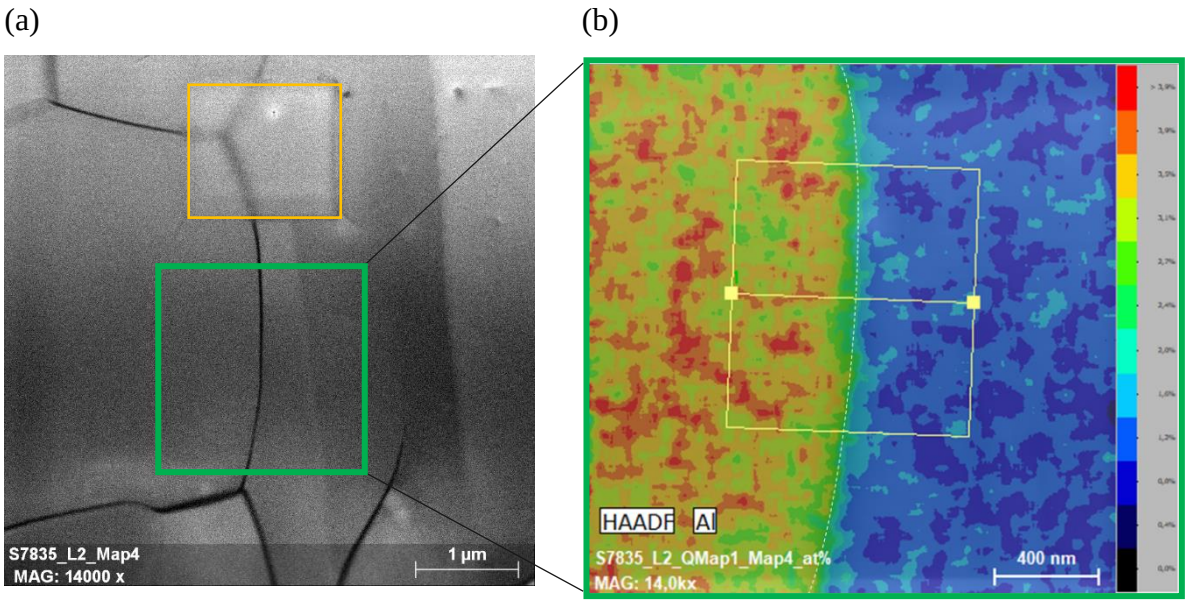

Figure 3.17: (a) HAADF image in which the freshly created EDX map (in the image (b)) is shown as a green box. An EDX analysis has already been carried out, indicated by the measurement spot in the upper middle area (orange box) in the image (a). Cracked carbon deposits cause such measurement spots. (b) QuantMap with line scan of sample S7835. The line scan is perpendicular to the diffusion interface (white dashed line) and is shorter than the map height because the crystal boundary is convex.

In the same image, individual grains can be observed. These can be useful to omit to be able to exclude grain boundary diffusion from the diffusion data. In addition, map positions in the sample have been selected where irregularities are negligible. Another important point when setting the maps is the relation between magnification, map size and electron beam damage. The map must be large enough to allow an optimal diffusion profile length of about 400 – 600 nm. At the same time, the spectral density should be high enough to obtain as many individual spectra as possible along the diffusion profile to ensure a meaningful calculation of the diffusion coefficient (Figure 3.18).

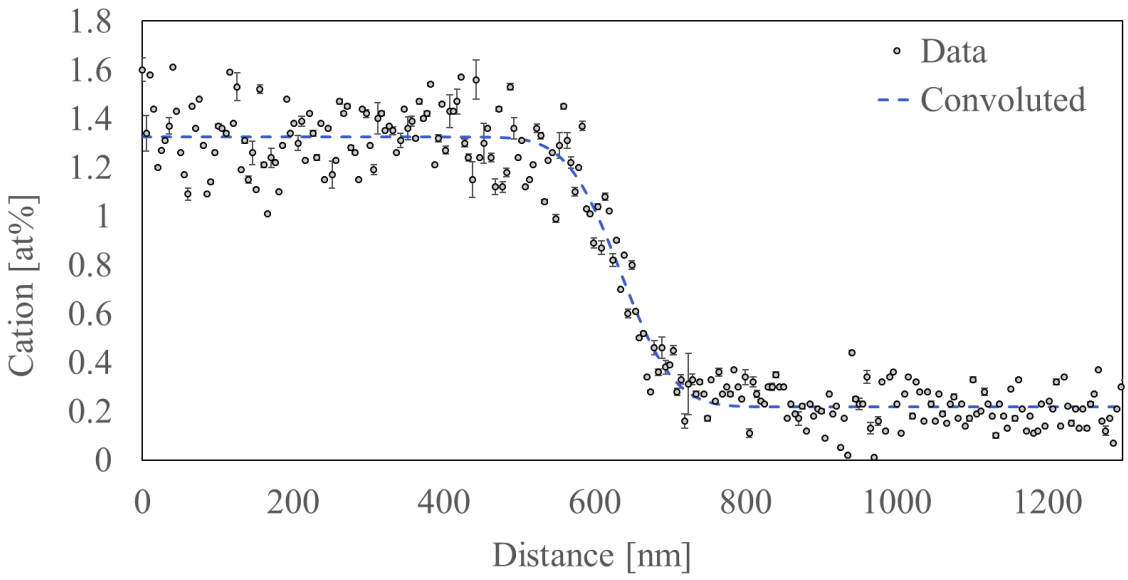

Figure 3.18: Ideal diffusion profile with many data points along the diffusion path (S7835). The data points represent the measured relative aluminium concentration. The dark line shows the data calculation by the Crank equation implemented by the Solver function in Excel.

Furthermore, the dwell time of the beam on the sample and the associated damage to the sample has to be considered. The greater the damage, the more that, the lighter elements, such as Mg, may have been volatilised from the sample surface or diffused from the beam-irradiated area. The resulting Mg loss can distort the chemical analysis and result in an incorrect Mg/Si ratio in the evaluation (Figure 3.8 + 3.9). This effect is mainly evident at very thin parts of the sample or if the electron dose is too high. This effect occurs after analysis due to the amorphisation effect and contamination by the deposition of cracked hydrocarbons. It is observable on the locally heated sample by measurement spots, as seen in the orange box in Figure 3.17.

The extent of Mg loss was further investigated by Holzapfel (2004) with a time series analysis at a single measurement point. A decrease in Mg intensity is observed for live times between 60 and 120 seconds (Figure 3.19). As in his work, mass balance calculations based on the analysis indicate that the component lost during electron bombardment is MgO.

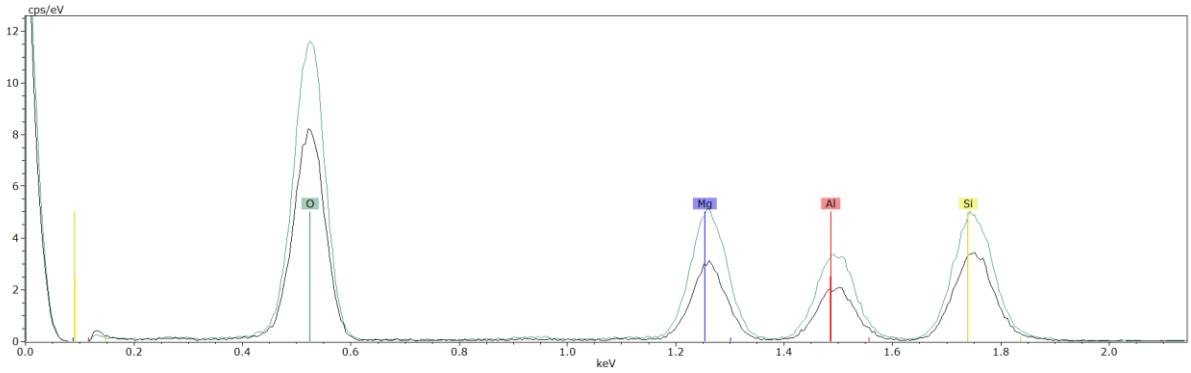

Figure 3.19: Two spectra measured for 0-60 sec and 60-120 sec, respectively, in the same sample. The green spectrum represents an optimal spectrum of the stoichiometric sample. The black spectrum indicates a light Mg-loss.

However, the spectra in this study were all recorded under the same conditions to ensure reproducibility and reliability:

STEM Mode		**TEM Mode**	
Gun lens setting	8	Gun lens setting	3 or 4
Spot size	3	Spot size	10
C1-aperture Ø	50 µm	C1-aperture Ø	30 µm

In STEM mode, the spot size "3" corresponds to roughly 0.2 nm when the beam is properly focused on the sample. In TEM mode, the spot size "10" corresponds to about 0.2-2 µm, depending on the beam size, which is manually adjusted to the grain size. The beam size is changed by changing the beam convergence in the convergent lens 2, C2. Despite the consistent analytical method, some spectra deviate from the optimal spectrum (Figure 3.19). This indicates that different sample thicknesses cause the effects of Mg loss. The thinner the sample, the greater the beam damage and the more that light elements can diffuse.

Meißner (2000) also discussed the optimum conditions for single spectra in her work. She recommended a gun lens setting of 5 or 3 with a spot size of 3 at a C1 aperture diameter of 30 µm. Due to the susceptibility of bridgmanite to radiation and the resulting amorphisation and incorrect analysis, the spot size was set to 10. This reduces the beam intensity and allows bridgmanite to be studied safely over a longer period of time.

In TEM mode, this allows samples to be examined for crystal orientation and mineral structure over several minutes. A smaller spot size (higher probe current) would destroy bridgmanite within a few milliseconds. In order to obtain the correct mole fraction of the Mg component in the perovskite, X_{MgSiO_3}, we did not perform a single spot spectra analysis (i.e. stationary beam irradiation) for a stoichiometric analysis. Instead, we switched to a scanning mode (i.e. continuous scanning beam). Due to the short dwell time (e.g., 16 microseconds in the dwell time) of the electron beam on one point in the sample, beam damage is avoided.

Table 3-4: Diffusion coefficients calculated by the Crank equation in Excel from the raw data from the EDX Maps.

name	$\log_{10}D$ [m^2/s]
S7596	-19.46 ± 0.29
S7614	-20.09 ± 0.29
S7830	-20.04 ± 0.78
S7835	-19.43 ± 0.36
S7751	-20.38 ± 0.45
S7791	-19.19 ± 0.36
S7808	-19.63 ± 0.35
S7824	-19.75 ± 1.06
S7828	-19. 22 ± 0.40
S7843	-20.84 ± 0.12

An average of two TEM lamellae were created for each diffusion experiment, and 2 to 4 EDX maps were produced in each case. For each map, one to two line scan data were extracted. From this data set, an average diffusion coefficient was determines and listed in Table 3-4. The error here represents one standard deviation (=STDEVA), which is calculated using the "n-1" method.The error calculation is used to estimate the degree of uncertainty. The systematic error includes among other things, the measurement deviations resulting from differences between individual devices (device errors), temperature and specific measurement procedures.

If systematic errors cannot be measured or calculated, estimating an upper limit for the systematic error is expected. If a large number of measurements are available, positive and negative errors, i.e. positive and negative deviations from the "true value", will occur in the simplest case, and the most probable value $\bar{x}$ (mean value) will be determined from the available values. The same applies to reliable measurements:

$$\bar{x} = \frac{1}{n}\sum_{i=1}^{n} x_i \qquad (3.1)$$

The most probable value of a measured variable is thus calculated as the arithmetic mean of a series of measurements. In order to be able to assess the quality of the measurement methods used, the scatter of the individual measured values around the mean value is assumed. A measure of the dispersion of the individual is given by the standard deviation *S:*

$$S = \sqrt{\frac{1}{n-1}\sum_{n=1}^{n}(\bar{x} - x_i)^2} \qquad (3.2)$$

The standard deviation of the individual measurements is thus a measure of how far, on average, a measurement point of the measurement series deviates from the mean value, i.e. it represents the mean error of the individual measurement. The greater the number of measurements, the more trustworthy the arithmetic mean. The mean square error is given by:

$$\sigma_m = \sqrt{\frac{1}{n(n-1)}\sum_{n=1}^{n}(\bar{x} - x_i)^2} \qquad (3.3)$$

After optimising the measurement method, the purely analytical error can be considered to be relatively small, while the error in data evaluation can be regarded as relevant. The errors relevant to data evaluation are to be expected in the concentration profiles and in calculating the diffusion coefficients.

On the one hand, analytical errors may already have occurred in preparing the diffusion profile. On the other hand, errors in the diffusion coefficient calculation must be considered due to applying different mathematical methods and models, such as the solver function in the Excel spreadsheets or the evaluation program "PACE". To reduce errors, a line scan was taken as perpendicularly as possible to the interface to determine the concentration profile with a high information density (point density) in order to calculate the diffusion coefficient with little error.

Even with lower point density or non-equivalent measuring points, reasonable accuracy can be achieved, e.g. by using an interpolation method. The scatter of the measurement data alone has a minor influence on the result. In contrast, calculating a difference quotient is very sensitive to the amount of data present in the concentration profile and the statistical scattering of the data, especially for very steep concentration profiles. In geometrical terms, this difference quotient measures the slope of the secant line that passes through the points with the coordinates (a, f(a)) and (b, f(b)) and used as approximations in numerical differentiation.

The calculation of the diffusion coefficient with a suitable function (solver function) usually leads to better results, provided that the selected function describes the measurement data sufficiently accurately. To minimise the error even further, the raw data of the line scans were also used to deconvolute the diffusion profiles. This was done with the help of the PACE software, as described in section 2.3.5 (subsection "Determination of diffusion coefficients") of the methods section. This results in three average values of the respective diffusion coefficients with individual errors per diffusion experiment. These are listed in Table 3-5. Several calculated coefficients per sample are summarised to calculate the diffusion coefficients, and a standard deviation of the individual results is calculated (see Appendix A, Table 2 + 6). The determined diffusion coefficients are used to calculate the temperature dependence and the activation energy. See section 3.2.4.

Table 3-5: Deconvoluted diffusion coefficients calculated by the Crank equation in PACE from the raw data from the EDX Maps. Several estimated coefficients per sample were summarised to calculate the diffusion coefficients, and a standard deviation of the individual results was calculated.

name	$\log_{10}D$ [m^2/s] (FWHM = 26.4)	$\log_{10}D$ [m^2/s] (FWHM = 10)	$\log_{10}D$ [m^2/s] (Average)
S7596	-19.01 ± 0.35	-18.93 ± 0.30	-18.97 ± 0.32
S7614	-20.38 ± 0.30	-20.18 ± 0.18	-20.28 ± 0.24
S7830	-20.14 ± 0.89	-20.05 ± 0.79	-20.10 ± 0.84
S7835	-19.67 ± 0.07	-19.66 ± 0.07	-19.67 ± 0.07
S7751	-20.05 ± 0.81	-19.90 ± 0.67	-19.98 ± 0.74
S7791	-19.14 ± 0.05	-19.29 ± 0.45	-19.22 ± 0.25
S7808	-20.17 ± 0.22	-19.90 ± 0.10	-20.03 ± 0.16
S7824	-19.8 ± 0.85	-20.13 ± 0.57	-19.97 ± 0.57
S7828	-19.61 ± 0.45	-19.53 ± 0.39	-19.57 ± 0.42
S7843	-21.24 ± 0.30	-20.85 ± 0.12	-21.05 ± 0.21

3.2.3. Comparison of diffusion coefficients

This section describes the process of deriving the final results. This includes the evaluation of the experimental temperature and the comparison between the convoluted and deconvoluted diffusion coefficients. Furthermore, the diffusion coefficients are correlated with the Mg/Si ratios, the aluminium content and the substitution mechanisms. This elaboration of the results should contribute to a better understanding of the following results sections and to evaluate the relaibility of the analytical data. Table 3-6 lists all the diffusion experiments and their associated results that are compared in this section. This includes the convoluted and deconvoluted diffusion coefficients, as well as the results for the Mg/Si ratio, the substitution data and the diffusion profile length.

Table 3-6: Summary table of all diffusion experiments and associated results of convoluted diffusion coefficients (Excel), deconvoluted diffusion coefficients calculated by the PACE software, the average of the deconvoluted PACE diffusion coefficients (deconvoluted diffusion coef.) and further analytical results like the Mg/Si ratio and the oxygen vacancy (OV) and charge – couple (CC) substitution data calculated from the absolute data from the EDX measurements at the STEM.

Starting material	Al free	Al rich	**Sample name**	TC	T_{exp} [°C]	P [W]	T_{calc} [°C]	±σ	Heating [h]	FIB Samples	TEM EDX maps	Sample thickness [µm]	Excel $log_{10}(D)$	Avg.	StdDev
Stoichiometric	S7381_a	S7563_2	**S7596**	n	1,750	340	2,100	79	1	#1442	S7596_L1_Map1	0.14	-19.84	-19.46	0.29
											S7596_L1_Map2	0.14	-19.13		
											S7596_L1_Map3	0.13	-19.44		
										#1464	S7596_L2_Map1	0.08	-19.69		
											S7596_L2_Map2	0.08	-19.53		
											S7596_L2_Map3	0.13	-19.14		
	S7596_a	S7563_1	**S7614**	y	1,750	370	1,870	83	7	#1459	S7614_L1_Map1	0.31	-20.12	-20.09	0.29
											S7614_L1_Map2	0.18	-20.11		
											S7614_L1_Map3	0.11	-20.41		
											S7614_L1_Map4	0.38	-19.71		
	S7795_I	S7732_I	**S7830**	y	1,808	381	1,910	84	21	#1571	S7830_L1_Map1	0.16	-20.60	-20.04	0.78
											S7830_L1_Map2	0.08	-19.49		
	S7795_II	S7732_II	**S7835**	y	1,808	387	1,950	87	21	#1574	S7835_L1_Map1	0.38	-19.57	-19.43	0.36
											S7835_L1_Map2	0.25	-19.02		
										#1585	S7835_L2_Map4	0.28	-19.69		
Stoichiometric; higher Al content	S7664_a	S7722	**S7751**	n	1,750	370	1,850	80	8	#1520	S7751_L1_Map1	0.23	-20.19	-20.38	0.45
											S7751_L1_Map2	0.24	-19.99		
										#1532	S7751_L2_Map1	0.22	-20.30		
											S7751_L2_Map3	0.18	-21.04		
	S7664_b	S7722	**S7791**	n	1,750	380	1,910	84	0.5	#1552	S7791_L1_Map1	0.17	-19.01	-19.19	0.36
										#1560	S7791_L2_Map1	0.22	-19.80		
											S7791_L2_Map2	0.23	-19.22		
											S7791_L2_Map3	0.25	-18.98		
											S7791_L2_Map4	0.21	-18.94		
Mg excess	S7664b1_II	S7800_I	**S7808**	n	1,800	350	1,802	79.5	3	#1563	S7808_L1_Map1	0.20	-19.80	-19.63	0.35
											S7808_L1_Map2	0.17	-19.87		
										SEM	S7808_SEM	0.23	-19.23		
	S7664b2_I	S7800_II	**S7824**	y/n	1,800	363	1,900	83.5	6	#1564	S7824_L1_Map1	0.08	-20.50	-19.75	1.06
										#1565	S7824_L2_Map1	0.15	-19.00		
	S7726_III	S7824_I	**S7828**	y	1,750	395	2,000	90	4	#1568	S7828_L1_Map2	0.23	-19.08	-19.22	0.40
										#1570	S7828_L2_Map1	0.20	-19.67		
											S7828_L2_Map2	0.17	-18.90		
	H5562_I	S7830_I	**S7843**	y	1,800	361	1,805	80	21	#1576	S7843_L1_Map1	0.12	-20.96	-20.84	0.12
											S7843_L1_Map2	0.10	-20.72		
										#1578	S7843_L2_Map1	0.08	-20.84		

* Not measurable

As can be seen from the table, there are 10 diffusion experiments with different chemical compositions. The "stoichiometric" composition has an aluminium content of 3 wt% and a Mg/Si ratio of one within the error. For this chemical composition ($Mg_{0.93}Al_{0.06}Si_{0.97}O_3$, stoichiometric), four diffusion experiments were carried out at different temperatures and annealing times. Experiments S7830 and S7835 were carried out under the same conditions to test reproducibility and because S7830 has an amorphous decompression crack up to 500 nm thick. This raised the question of whether the decompression cracks affected the analytical result and the associated diffusion coefficient. When comparing all the data (both with and without decompression cracks), it was assumed that the analytical error caused by the decompression crack is very small and does not need to be included in the weighting of the analytical results. In addition, this data series contains a diffusion experiment where the temperature increased to 2,100 °C (400 W), for about 1/3 of the time. This data point has therefore been recalculated using to the higher temperature and shorter annealing time. For the chemical component with the higher Al content ($MgAl_{0.1}Si_{0.9}O_3$), the experiments were performed for 0.5 and 8 hours of annealing.

PACE $log_{10}(D)$ (FWHM=26.4)	Avg.	StdDev	PACE $log_{10}(D)$ (FWHM=10)	Avg.	StdDev	**Deconv. diffusion coef.**	**StdDev**	Mg/Si	Avg.	StdDev	OV (diff. profile)	Avg.	StdDev	CC (diff. profile)	Avg.	StdDev
-19.50			-19.33					1.03			2.59			0.52		
-18.62			-18.59					1.02			0.76			1.42		
-18.97	-19.01	0.35	-18.92	-18.93	0.30	**-18.97**	**0.32**	1.02	1.02	0.01	1.69	1.62	0.79	1.24	1.28	0.53
-19.27			-19.16					1.01			0.70			1.85		
-19.07			-19.00					1.02			2.38			1.35		
-18.63			-18.60					1.02			1.48			0.51		
-20.29			-20.13					1.04			0.00			4.80		
-20.27	-20.38	0.30	-20.12	-20.18	0.18	**-20.28**	**0.24**	1.01	1.03	0.02	1.11	1.56	1.68	0.95	1.92	2.10
-20.81			-20.43					1.04			3.57			0.00		
-20.14			-20.02					1			0.00			1.32		
-20.77	-20.14	0.89	-20.61	-20.05	0.79	**-20.10**	**0.84**	1.03	1.02	0.01	1.68	1.04	0.91	0.59	0.83	0.33
-19.51			-19.49					1.01			0.40			1.06		
-19.59			-19.58					0.97			0.00			3.91		
-19.71	-19.67	0.07	-19.70	-19.66	0.07	**-19.67**	**0.07**	0.96	0.97	0.01	0.00	0.00	0.00	4.34	3.75	0.68
-19.71			-19.70					0.98			0.00			3.01		
-20.37			-20.21					0.98			0.00			4.00		
-20.64	-20.05	0.81	-20.37	-19.90	0.67	**-19.98**	**0.74**	1	1.00	0.02	0.00	0.56	1.11	2.33	2.86	0.83
-19.13			-19.13					1.02			0.00			2.93		
*			(-21.08)*					1.01			2.22			2.17		
-19.19			-19.02					1.01			0.00			4.60		
*			-19.87					1.01			0.00			1.69		
*	-19.14	0.05	-19.64	-19.29	0.45	**-19.22**	**0.25**	0.99	1.00	0.01	0.00	0.00	0.00	2.51	2.93	1.41
-19.14			-18.98					1.00			0.00			4.44		
-19.10			-18.95					1.00			0.00			1.81		
-19.99			-19.81					1.03			3.41			1.06		
-20.10	-20.17	0.22	-19.88	-19.90	0.10	**-20.03**	**0.16**	1.03	1.03	0.01	2.63	2.81	0.25	0.06	0.37	0.60
-20.41			-20.01					1.02			2.99			0.00		
(-21.5)*	-19.80	*	-20.53	-20.13	0.57	**-19.97**	**0.57**	1.02	1.02	0.01	2.36	2.06	0.42	0.00	0.79	1.11
-19.80			-19.73					1.01			1.76			1.57		
-19.11			-19.09					1.01			1.03			0.93		
-19.77	-19.61	0.45	-19.68	-19.53	0.39	**-19.57**	**0.42**	1.01	1.01	0.01	0.65	1.17	0.61	0.31	0.74	0.37
-19.96			-19.82					1.02			1.84			0.97		
-21.56			-20.98					1.04			3.37			0.00		
-20.97	-21.24	0.30	-20.74	-20.85	0.12	**-21.05**	**0.21**	1.01	1.03	0.02	1.09	2.62	1.32	1.66	0.55	0.96
-21.18			-20.84					1.04			3.39			0.00		

The short annealing time was accidental and it was probably not possible to reach equilibrium in such a short time. However, as the experiment performed excellently during the heating period and all measured values remained stable, it was decided to include it in the results calculations. The last data set corresponds to the Mg excess component ($MgAl_{0.05}Si_{0.95}O_3$), which includes four experiments at different temperatures and different annealing times. It is the only data set with a temperature at 2,000°C.

For higher reliability and lower statistical error, two FIB samples were made for each diffusion experiment and from each FIB sample one to four EDX measurements were made (the number of EDX measurements depends on the habit and behaviour of the FIB sample against the TEM beam). For each EDX measurement the substitution mechanism was determined and can be found in the last columns of Table 3-6. Throughout the table, all data points related to the specific EDX measurements have been combined into an average value with a standard deviation.

Temperature estimation

As can be seen in Figure 3.20 a, 5 of 10 diffusion experiments could not be carried out with a consistently functioning thermocouple (in Table 3-5, column "TC" is marked with "n" for consistently no working thermocouple or "y/n" for partially functioning thermocouple). Due to this, a power-temperature relation (Figure 2.4) was created on the basis of 23 experiments in which the thermocouple functioned without fluctuation during the entire heating phase, which is used to calculate the temperature for Figure 3.20 b. It can be seen that this results in a higher range of temperatures, taking into account the deviations of ± 80 °C. Due to the high number of experminets without a consistently working thermocouple, it was decided to use the calculated temperature (T_{calc}) as a more meaningful and reliable parameter and to use this in the following results evaluation.

a)

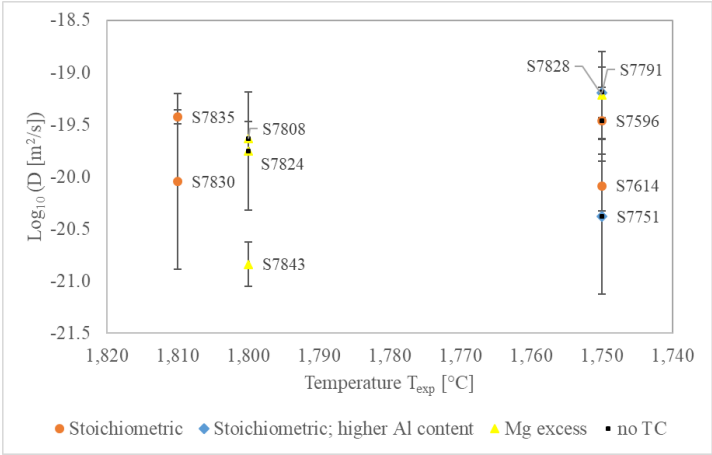

b)

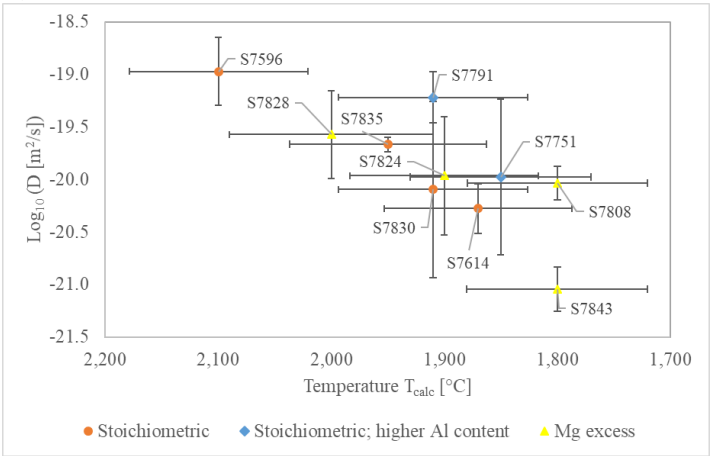

Figure 3.20: The relationship between the diffusion coefficients and the temperature read during the experiment (Temperature T_{exp}) and the temperature calculated from the power-temperature relationship (Temperature T_{calc}). a) shows the diffusion coefficient (Excel $log_{10}(D)$) versus the temperature read from the working TC or estimated temperature (from previous experiments at same PT conditions). The black dot indicates the 5 experiments that did not have a fully functional thermocouple and where the temperature was estimated. b) shows the diffusion coefficient vs. the calculated temperature from 23 successfully performed experiments with a fully functional thermocouple.

Deconvoluted diffusion coefficients

The diffusion coefficients can now be compared by using the calculated temperature. For this purpose, the crude and convoluted diffusion coefficients (larger markers in Figure 3.21) were compared with the deconvoluted diffusion coefficients determined using PACE (subsection “Determination of diffusion coefficients” in section 2.3.5.) for FWHM = 26.4 nm (smaller markers in Figure 3.21) and FWHM = 10 nm (small dark markers in Figure 3.21). In addition, the deconvoluted diffusion coefficients have been averaged and plotted against temperature as "Deconvoluted diffusion coef." (small bright markers with a red border in Figure 3.21). As described in section 2.3.5 (subsection “Determination of diffusion coefficients”), the Gaussian beam width of the STEM was determined experimentally to determine the spatial resolution and to avoid overestimation of the diffusion profiles. It was found that there was a lot of scatter in the data, so an upper and lower regression line was determined to include all possible data in the calculation of the diffusion coefficient. In the following, only the average data of the deconvoluted diffusion coefficients are used, as these data already take into account the convolvtion effect and also integrate the scatter of the deconvoluted data. These data are considered to be reliable.

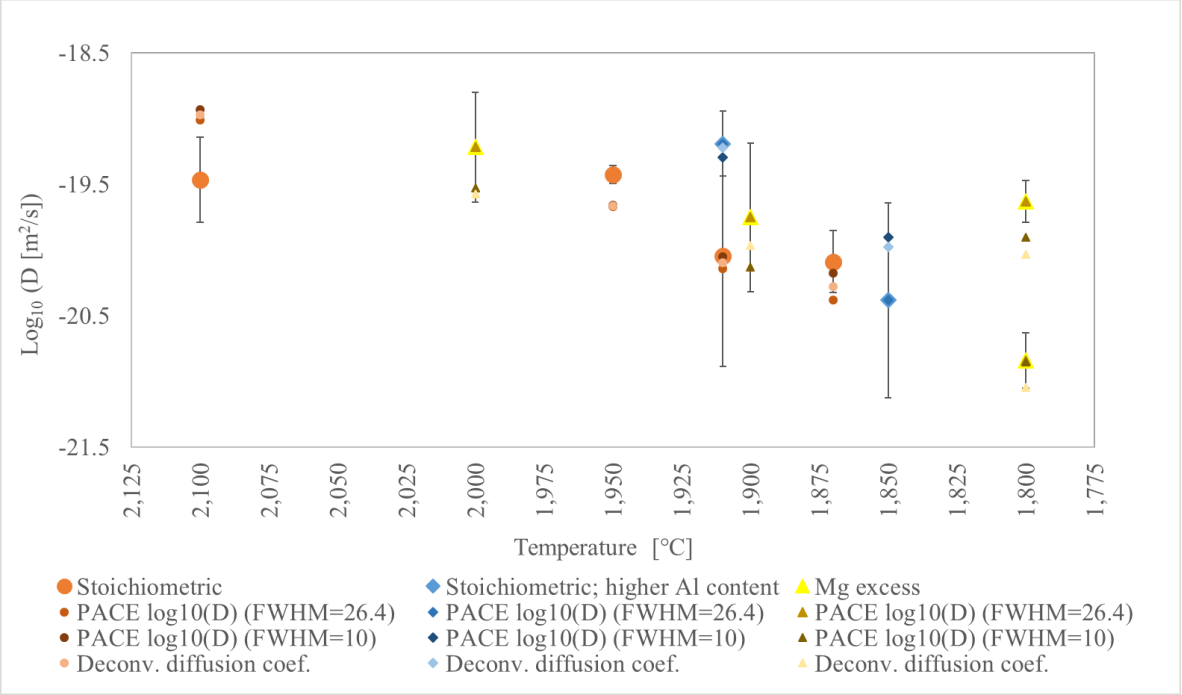

Figure 3.21: Correlation between diffusion coefficients and temperature. To do this, all four calculated diffusion coefficients were plotted against temperature. The largest markers represent the convolute diffusion coefficients calculated using the Crank equation and the solver function of Excel. The smaller markers represent the deconvoluted diffusion coefficients determined using the software PACE, considering the different Gaussian beam widths during the chemical analysis using the STEM. These deconvoluted diffusion coefficients have been averaged for simplicity and are shown as bright small markers.

Comparing diffusion coefficient and Al content

The correlations of the averaged deconvoluted diffusion coefficient (ADDC) and the aluminium content are shown in Figure 3.22. For this purpose the ADDC is related to the Al content, the chemical composition and the temperature in order to understand its correlation and effects to classify the results better. The comparison of diffusion rates and Al concentration shows no compositional relation between the data sets. In addition, the compared data were generated at different temperatures and different annealing times. This makes it difficult to make a quantitative statement about the relation between Al content and diffusion rate. In addition, the differences in Al content are very small and further Al concentrations are required to obtain a complete picture of the correlation between Al content and diffusion rate.

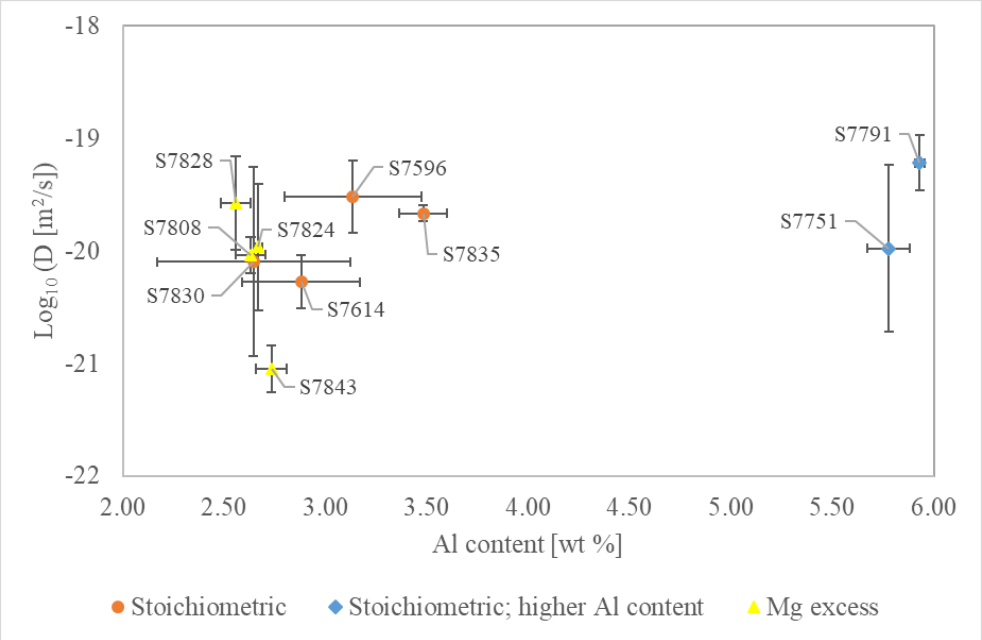

Figure 3.22: Comparison of the deconvoluted diffusion coefficient and aluminium content. Diffusion coefficients were calculated from deconvoluted average data shown in Table 3-6.

3.2.4. Temperature dependence of Al-Si interdiffusion at 24 GPa

In order to compare diffusion coefficients obtained at different temperatures, an Arrhenius plot was used. The diffusion coefficient *D* depends on the temperature *T* and can be described by the following expression:

$$\ln D = \ln D_0 + \ln\left[exp\left(\frac{-E_A}{RT}\right)\right] = \ln D_0 - \frac{E_A}{RT}\ ;\ (y = c + mx) \qquad (3.4)$$

D_0 is the diffusion coefficient at infinite temperature, and *R* is the ideal gas constant (= 8.135 J × mol^{-1} × K^{-1}). When plotting the diffusion coefficient in an Arrhenius plot, concentration-independent *D* values of a given material system for different temperatures lie on a straight line with the slope:

$$m = -\frac{E_A}{R};\quad x=10^4/T \qquad (3.5)$$

$$intercept = \ln D_0 \qquad (3.6)$$

The activation energy for the diffusion process can therefore be read directly from the slope. For simplicity, only the average between 2 deconvoluted data sets is shown in Figure 3.23 (see subsection "Deconvoluted diffusion coefficients" in section 3.2.3). Three datasets of diffusion coefficients were measured for three different compositions as a function of temperature. Yellow-coloured points correspond to the Mg excess samples ($MgAl_{0.05}Si_{0.95}O_3$; ***b***), orange ones to stoichiometric samples ($Mg_{0.93}Al_{0.06}Si_{0.97}O_3$; ***a***), and blue ones to stoichiometric samples with higher Al content ($MgAl_{0.1}Si_{0.9}O_3$; ***c***). It can be seen that data sets ***a*** (stoichiometric) and ***b*** (Mg excess) are indistinguishable within the experimental error, so ***a*** and ***b*** were fitted as one data set. This means that sample differences cannot be distinguished based on different amounts of oxygen vacancies (see Table 3-6). Data set ***c*** plots systematically higher, although it only has two data points. There are respectively 4 and 5 different data points at different temperatures for the other two chemical components (***a*** and ***b***).

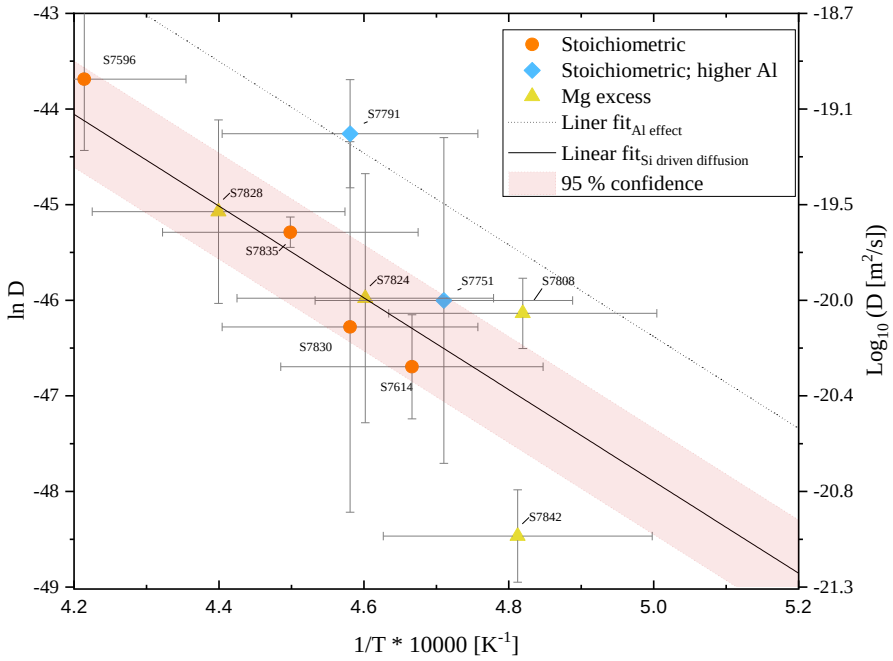

Figure 3.23: Comparison of diffusion coefficients and temperature as a function of chemical composition. The slope was fixed at - 4.8, corresponding to E_A=400 kJ/mol. No clear statement can be made about the differences due to chemistry. Data points S7596 and S7808 were excluded from the fit as the experiments were performed at the lowest temperature and times of 1 h and 3 h, respectively, making them unreliable as equilibrium was most likely not reached. Experiment S7842 was included in the fit as the diffusion time was increased to 21 hours for the lowest temperature. The dashed linear regression (Al effect) was calculated from the blue data set with the same slope as for the other linear regression (Si driven diffusion). It is assumed that an increased Al content influences the diffusion behaviour in bridgmanite and therefore the data with increased Al content are considered separately in this plot.

It can be seen that there is a large scatter in the data at the lowest temperature, for example, the two Mg excess samples, S7842 and S7808, which were synthesised at the same conditions, differ by more than two natural log units. The only difference between the two syntheses is that S7808 was kept at temperatures for 3 hours, whereas S7842 was equilibrated for 21 hours (Table 3-1). This suggests that longer runs are necessary to reach equilibrium, at least at 1,700 °C. For this reason, the data points S7808 and S7596 run only for 3 and 1 hours, respectively, were considered for further analysis, due to a lack of equilibrium. Furthermore, data point S7596 shows another irregularity, as the power increased to 400 W during the experiment, corresponding to a temperature of approximately 2,100 °C.

It can also be seen that each data set does not have a large enough temperature range (1,700 - 2,100 °C) to constrain a linear fit. This results in a high correlation between the pre-exponential coefficient D_0 and the activation energy E_A (slope and intercept), and the uncertainties become large.

When plotting the linear regression line, the E_A value becomes very high (796 kJ/mol), making comparing with literature data difficult. Due to the high correlation between E_A and $D_{0,}$ we decided to keep E_A fixed for further discussion. For the fit of the Arrhenius equation, we set the slope (activation energy E_A) to - 4.8, corresponding to E_A=400 kJ/mol, which is the averaged and rounded value reported in previous data for mantle minerals (see Figure 4.1; Holzapfel *et al.*, 2005; Xu *et al.*, 2017). Furthermore, this slope is consistent with the calculations for a slope calculated from all available data points. If a similar fit is performed for the Al-rich concentration (~ 5 wt.- %, data set ***c***), an order of magnitude faster diffusion rate is obtained. Given that only two data points exist for this Al concentration, the dotted line reported in Figure 3.23 is not intended to be taken quantitatively. Despite the uncertainties, it is still possible to speculate that for the ***a*** and ***b*** data, Al-Si substitution at the octahedral side is the major factor influencing the diffusion mechanism, at least for low Al concentrations. As the coupled substitution mechanism becomes dominant (Al-rich samples, c data), there is increasing incorporation of Al into the bridgmanite structure A-site, and the diffusion rate appears to increase.

The D_0 parameters obtained for the Al-Si interdiffusion are $4.2 \pm 1 \times 10^{-11}$ m^2/s ($\ln D_0 = - 23.9 \pm 0.2$ m^2/s) for fixed E_A parameters of 400 kJ/mol. The diffusion rate at higher Al content can be taken to be $1.9 \pm 1 \times 10^{-10}$ m^2/s ($\ln D_0 = - 22.4 \pm 0.3$ m^2/s). Both diffusion coefficients are lower than the Si self-diffusion rate in other high-pressure phases (Yamazaki *et al.*, 2000; Shimojuku *et al.*, 2009, 2014).

3.3. Evaluation of the diffusion experiments S7766 and H5548

When the S7766 diffusion experiment was opened, both the sample material and the capsule appeared brittle and crumbled easily (Figure 3.24 a). This differed from the other experiments where the sample material is robust and typically deforms only slightly. This diffusion experiment was heated in the Sumitomo press at 24 GPa, 2,000 °C and 397 W for four hours. Both the thermocouple and the power were constant throughout the experiments. The experimental compression, annealing and decompression process appeared to be as expected.

(a) (b)

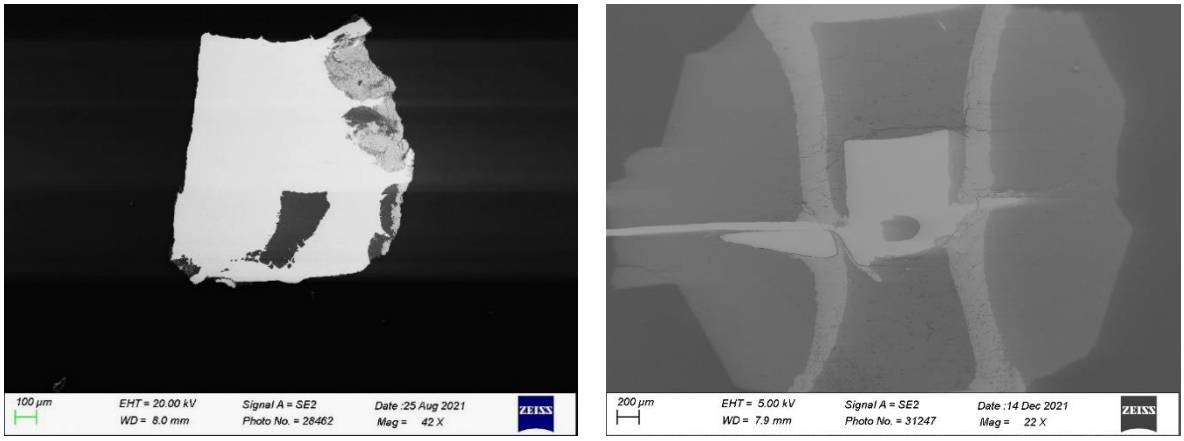

Figure 3.24: Overview of the whole capsule of diffusion experiments S7766 and H5548. The capsule from S7766 (a) no longer has a rectangular shape and looks pitted. This is unusual compared to the other experiments. Compared to this, the capsule from diffusion experiment H5548 (b) indicates a typical shape. In this SE image, the whole experiment setup is shown, with TC, heater and MgO spacers.

In comparison, the H5548 sample shows a conventional shape (Figure 3.24 b). The sample was neither deformed nor did it crumble when opened. This experiment was heated in the Hymag multi-anvil apparatus at 24 GPa, 1,850 - 2,100 °C (605 watts) for 4 hours (Table 3 - 1). The temperature range refers to the difference between the TC measurement and the temperature calculated from the power. The TC may have been partially contaminated, or the position of the TC may have changed due to capsule deformation, giving an incorrect reading. When the capsules were opened, it was found that the samples were no longer rectangular and looked 'melted' (Figure 3.25 a + b). These experiments are therefore fundamentally different from the others. The first hypothesis about these experiments is that melting took place and caused a change in the geometry of the sample capsule.

(a) (b)

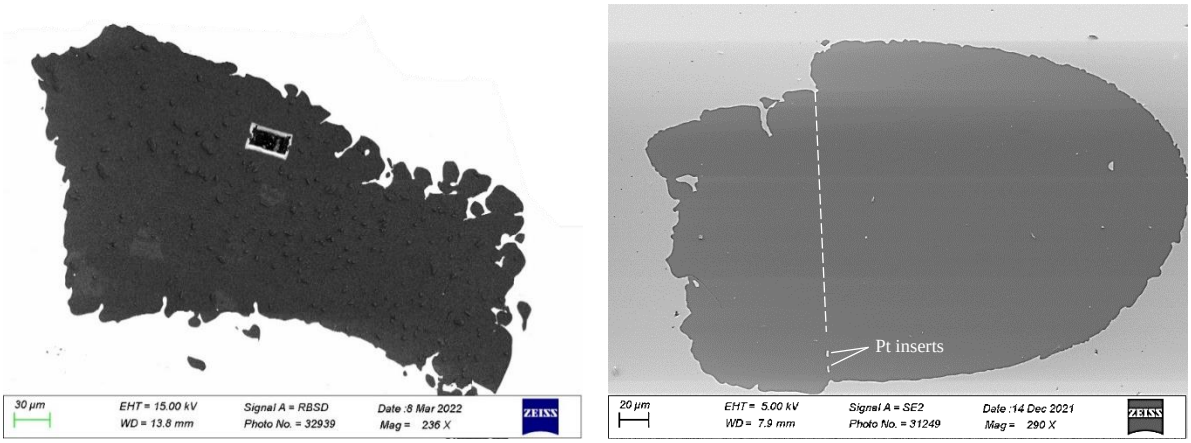

Figure 3.25: Overview images of diffusion experiments S7766 (a) and H5548 (b). Both samples look partially melted. In sample S7766, the original diffusion couples are no longer visible. In sample H5548, the diffusion interface can still be guessed at, marked here by the white dashed line.

A pressure drop due to damaged cubes can be excluded after the experiment. Furthermore, analysis of the pressure record shows no significant reduction in the applied pressure. It may be that the capsule material melted or flowed extensively and the capsule and sample geometry changed during the diffusion experiment. As can be seen in Figure 3.24, the diffusion couples are at the edge of the capsule after the experiment. Partial melting of the bridgmanite sample can be ruled out in both cases as no quench crystals are visible in the sample and the TEM images show crystalline material (Figure 3.26).

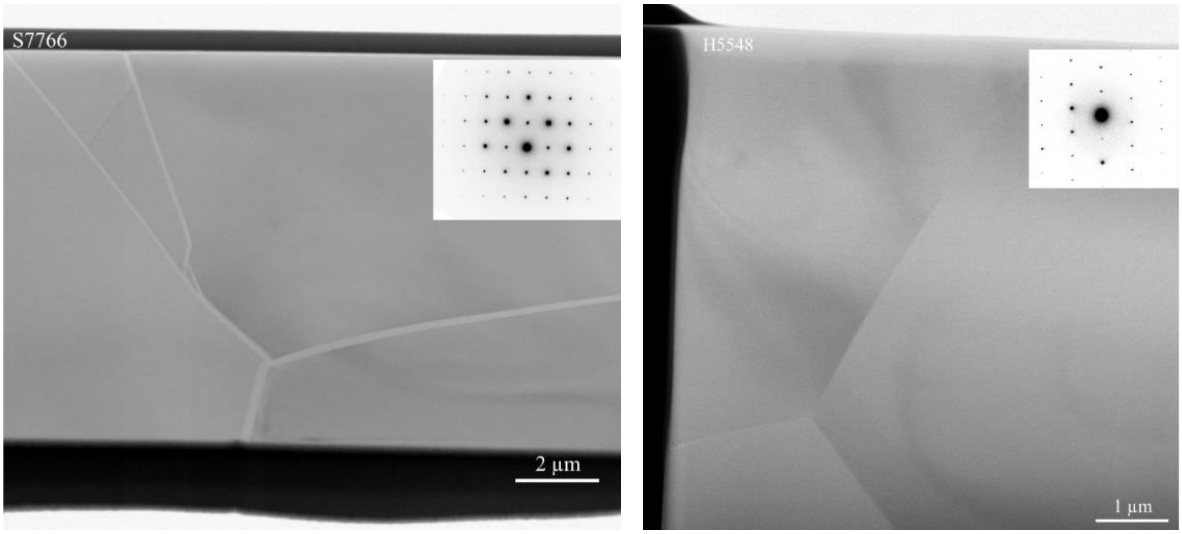

Figure 3.26: Parts of the TEM lamella from samples S7766 and H5548 with associated diffraction pattern. This shows that the bridgmanite sample is crystalline with ~ 5 – 10 times bigger crystal sizes than in the other diffusion experiments.

Figure 3.26 also shows large grain sizes after the diffusion experiments compared to other diffusion experiments. Typically, the approximate average grain size after diffusion experiments is between 2 and 5 µm for Al bearing and 5 - 10 µm for Al-free bridgmanite (Appendix A, Table 4). The grain sizes before these diffusion experiments were not different from the others. The grain sizes are up to 10 times larger at the end of these rapid experiments. It is possible that the temperature rose for a few minutes during the experiments and then fell again before decompression, leading to crystal formation rather than melting or partial melting.

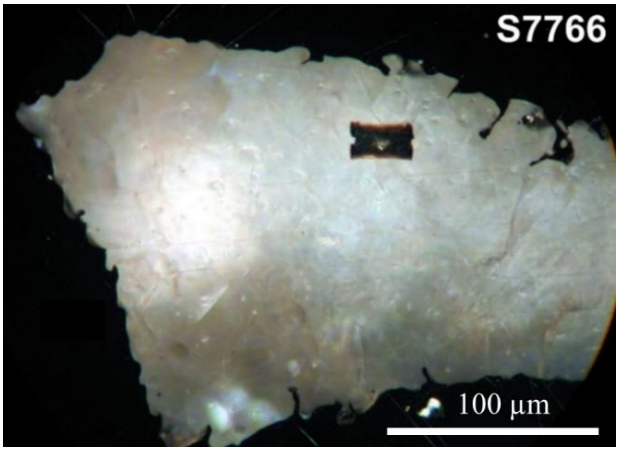

Figure 3.27: Optical microscope image of S7766. It suggests that the sample lies tilted in the Pt capsule and was polished at an angle, which is why the diffusion profile became longer. Because En100 measured in the EDX is on the far-left edge. This sample was ground to 5/8 to expose the diffusion pair fully. The dark rectangular region in the sample represents the FIB sample. This was taken on the side containing aluminium, as it was initially thought that the diffusion interface would be in the middle of the diffusion pair, as in all other diffusion experiments. It was decided not to take another sample because the Al profile was longer than the length of a FIB lamella.

For sample S7766 it is noticeable (Figure 3.27) that the Al-free part of the experiment is smaller than the Al-containing part. The EDX analysis of the whole sample also shows that the Al-free part is a small part of the sample. This raises the possibility that the sample may have been cut in a tilted position. However, optical light microscopy (Figure 3.27) shows that the Al-free sample is no larger than the already exposed sample. In addition, the sample would have to have been highly tilted to favour a diffusion profile 600 times longer in the chemical analysis (Figure 3.28). Thus, a tilted sample can be mainly excluded.

This raises the question of what happened to the remaining Al-free diffusion sample. The original thickness of the samples was 140 µm for the Al-free end member and 250 µm for the Al-rich sample. After the diffusion experiment, the Al-free end member is 50 µm thick and the Al-containing sample is 135 µm thick. Under the optical light microscope, no more material can be seen inside the capsule, indicating that there is no unopened material left in the capsule. Focusing on the capsule through the optical microscope along the diffusion interface also shows that the sample is not tilted.

Extensive TEM and SEM observations were made on both samples. The TEM examinations did not give any useful results for sample S7766. The EDX maps showed a fully equilibrated sample. After further investigation using single spectra, no Al gradient could be detected in this sample. This indicates a diffusion profile larger than the 20 µm TEM lamella sample. For this reason, a chemical SEM analysis of sample S7766 was carried out along the entire sample length (Figure 3.28). The SEM studies showed an average diffusion coefficient of $D = 3.9 \pm 1.6 \times 10^{-14}$ m^2/s.

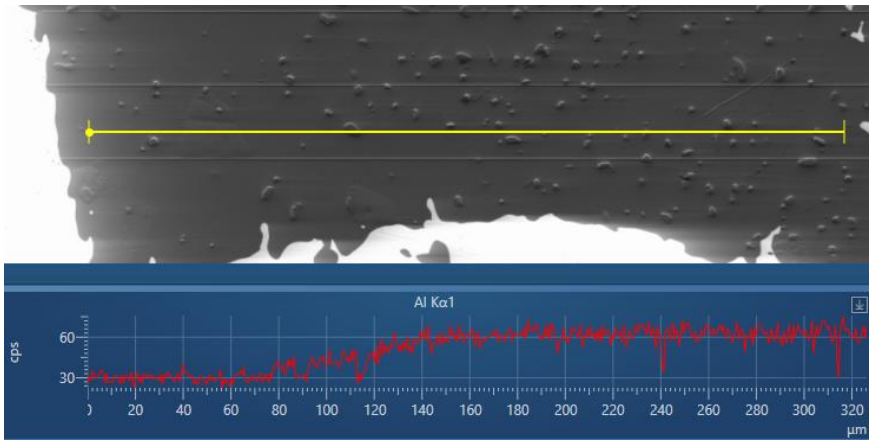

Figure 3.28: Example of a chemical analysis of sample S7766 along the whole sample using a line scan. The upper image shows the SE image together with the line scan. The lower graph shows the Al profile in counts per second vs distance. A clear Al gradient can be seen. The peaks correspond to places where the line scan was placed over stishovite (SiO_2) or corundum (Al_2O_3) and thus contains either a little or a lot of Al.

For sample H5548, a diffusion coefficient of $D = 8.33 \times 10^{-17}$ m^2/s could be determined by TEM-EDX measurements. The calculated diffusion coefficient obtained from the SEM-EDX evaluation was $D = 3.82 \pm 5 \times 10^{-15}$ m^2/s. The fact that a diffusion profile could be generated on the TEM for H5548 but not for S7766 may be due to the fact that the temperature and device were different during the experiment. It is unclear whether the difference in diffusion profiles is due to grain boundary diffusion or simply the use of a different multi-anvil device. Therefore, no significant conclusions can be drawn as to the exact diffusion coefficient for this sample.

The SEM was also used to determine the Al content in stishovite. Further details are given in section 3.4. Since partial melting has already been excluded, this could be predominantly grain boundary-controlled diffusion. Since this tends to be faster than volume diffusion (Joesten, 1991; Farber, Williams & Ryerson, 2000; Herzig & Mishin, 2005), this could be the reason why the EDX profile is longer than in the other diffusion experiments.

(a) (b)

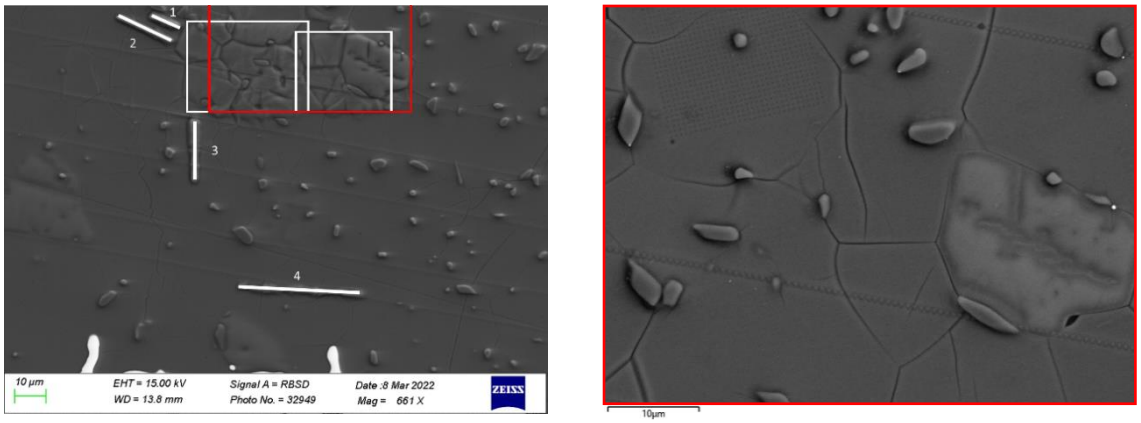

Figure 3.29: (a) Overview image of the EDX analysis of experiment S7766. Line scans (white lines) perpendicular to the grain boundary were measured to assess the Al content along the grain boundary. A gradient can be seen from the interior of the mineral grain to the mineral boundary. Additionally, maps (white and red boxes) were taken for the same purpose. (b) Enlargement to assess the SEM resolution. Each point in the line scan and the map has measured a spectrum. This corresponds to a resolution of 0.7 µm (10 µm = 14 spectra) for the line scan and 0.55 µm (10 µm = 18 spectra) for the map in the picture above left.

Therefore, an EDX analysis across the grain boundaries was performed (Figures 3.29 and 3.30). Three out of four line scans found that the Al content hardly changes from the mineral centre over the grain boundary to the adjoining mineral grain centre. Consequently, the SEM cannot measure diffusion driven mainly by grain boundaries. The spatial resolution of the SEM-EDX analysis would need to be higher to get reliable results because it cannot detect Al enrichment at the grain boundaries.

Finally, it can be assumed that grain boundary diffusion was predominant in these two experiments. However, no valid statement can be made about what led to this. This requires further investigation, such as determining the water content of the sample.

1) 2)

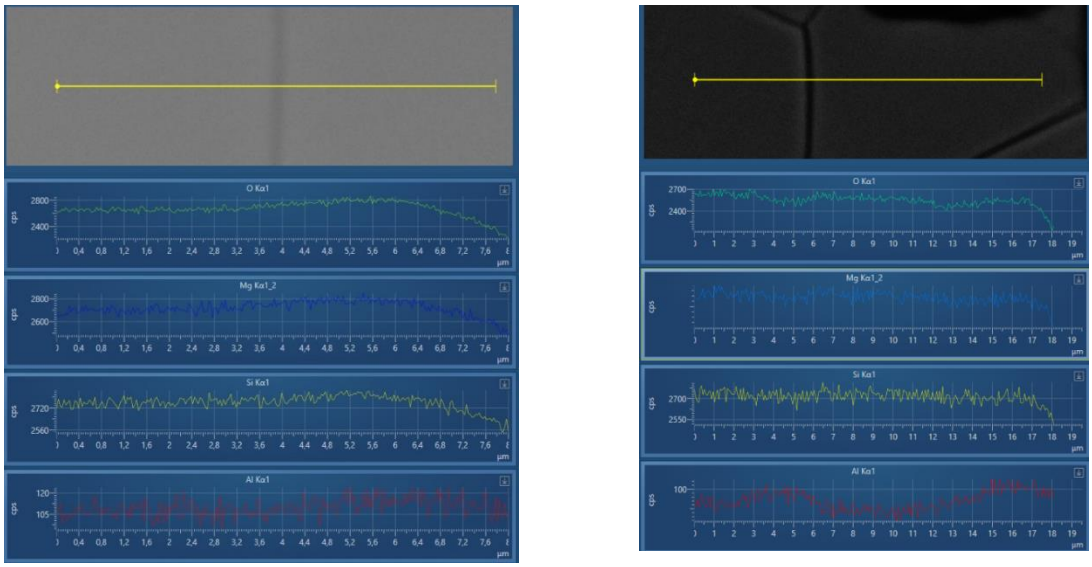

Figure 3.30: Line scans 1 and 2 marked in yellow corresponding to the white lines 2 and 3 in Figure 3.29 of sample S7766. Underneath the SE images, the element concentrations can be seen for oxygen (green), magnesium (blue), silicon (yellow) and aluminium (red).

3.4. **Stishovite observations**

Stishovite occurs commonly as a secondary phase in the Al rich and Al free bridgmanite samples in this study. The average grain size of the stishovite minerals is 2 to 5 µm. Upward and downward size variations are present. The samples prior to diffusion experiments already show homogeneously distributed quartz grains, and stishovite grains are visible as well in the synthesised bridgmanite samples. The grains do not grow significantly during the diffusion experiments. The stishovite minerals observed here are from the synthesis and diffusion experiments.

The Al content in stishovite can provide information about the prevailing temperature during an experiment (Liu *et al.*, 2006). To determine the temperature during the diffusion experiments more precisely, the Al content in stishovite was measured in TEM EDX maps of the diffusion and synthesis samples previously made. Subsequently, the synthesis and diffusion experiments were also examined using the SEM. For this purpose, 4 to 20 individual EDX spectra and chemical maps per sample were measured in the SEM to evaluate the composition of the stishovite mineral grains (Figure 3.31). In addition, spectra of bridgmanite were also recorded. Since there should be no Mg in stishovite, the Al concentration was normalised to Mg = 0, which did not give a significant improvement.

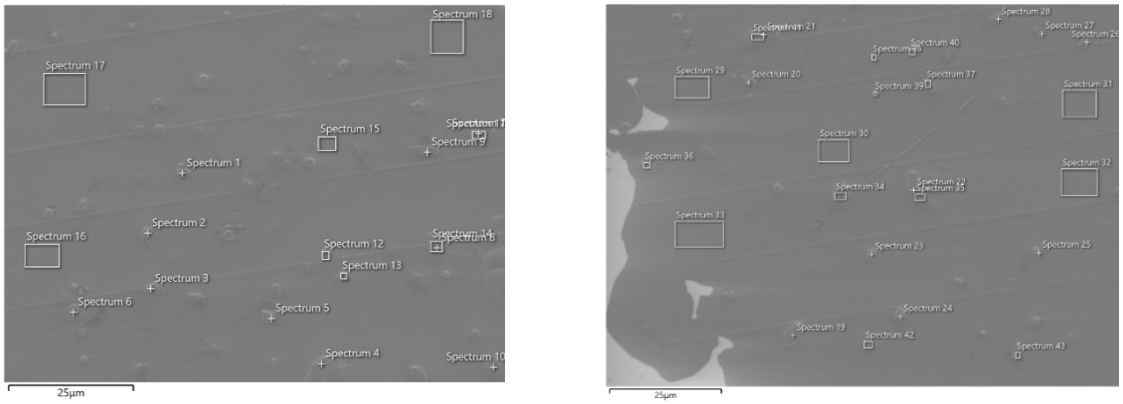

Figure 3.31: Al content measurements of stishovite and bridgmanite in S7766. Individual spectra, as well as maps in different areas of the sample are indicated by crosses and boxes. Only the stishovite grains were used for evaluation.

The data were then plotted against temperature (Figure 3.32). It can be seen that the samples analysed by TEM tend to have higher Al contents than those analysed by SEM. This could be related to the resolution of the methods and will be discussed in section 4.4. There is an apparent negative trend in the TEM data. Higher temperatures roughly correspond to lower the Al contents. The data are compared with previous data (Figure 4.6) in section 4.4.

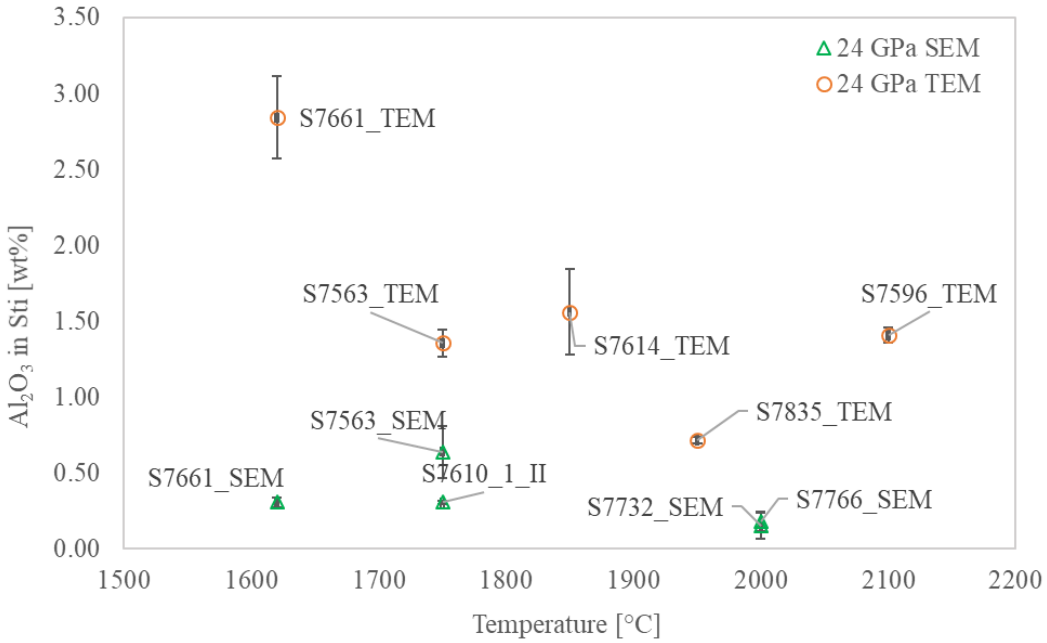

Figure 3.32: Plot of Al content in the stishovite grains against the calculated temperature. Data were collected with TEM and SEM often in the same samples. It is noticeable that the analytical data for the same samples are sometimes different.

4. Discussion

4.1. Evaluation of data reliability

We repeated most of the experiments several times at similar conditions to test reproducibility of our diffusion data. By having diffusion profiles as short as in this study, it is crucial to minimise experimental uncertainty and to understand outliers. By varying diffusion annealing times that range over at least an order of magnitude, profile lengths that extend by a factor of ~ 3 could be obtained, enhancing the precision of the diffusion data. Through the successful analysis of very short diffusion profiles, the interdiffusion coefficients in Al-bearing bridgmanite can now be compared with previously reported data on diffusion coefficients of different diffusing species in bridgmanite and other Earth's mantle-relevant minerals.

As shown in section 3.1.3 and in Figure 3.9, samples with an Al content of 2.7 - 3 wt. % show oxygen vacancies and charge-coupled substitution, irrespective of whether they belong to the Mg-excess or the stoichiometric samples. The samples containing 5 wt. % Al_2O_3, on the other hand, show predominantly charge-coupled substitution (Figure 3.9), with some of them lying in the Si-rich part of the diagram, probably due to Mg loss during EDX measurement and the weakness of bridgmanite against the electron beam. As reported in section 3.2.4, diffusion coefficients of samples containing 5 wt. % Al_2O_3 appear to be slightly faster than those of the samples with lower Al content, although it is difficult at present to draw any quantitative conclusions due to the uncertainties. For this reason, data are presented together in the following section and shown in the same colour (dark red) to increase the visibility of the data. However, the data are displayed by different markers depending on their chemical composition to allow differentiation.

As already mentioned in section 3.2.4 the activation energy in the Arrhenius plot was fixed to 400 kJ/mol based on earlier results from previous studies (i.e. Holzapfel *et al.*, 2005; Xu *et al.,* 2017). In this way, in spite of the relatively small temperature range (~300 K) and the limited number of experimental points, our data can be meaningfully compared with other data in the pressure-temperature range relevant to Earth's mantle. For example, the average Al-Si interdiffusion coefficient for bridgmanite from our study becomes $3 \pm 1 \times 10^{-21}$ m^2 /sec at 1,800 °C for a pre-exponential factor of $D_0 = 4.2 \pm 1 \times 10^{-11}$ m^2/s.

The Al-Si interdiffusion coefficients obtained in this study are ~ 2 orders of magnitude lower than the previous results listed in Table 4-1. Such previous results include the Fe-Mg interdiffusion coefficients in bridgmanite (Holzapfel *et al.*, 2014; $D_0 = 4.0 \pm 0.7 \times 10^{-9}$ m^2/sec (under IW-3) and $D_0 = 7.9 \pm 1.4 \times 10^{-8}$ m^2/sec (under IW+3) at $E_{(A, 24)} = 414$ kJ/mol). The Al-Si interdiffusion coefficients obtained in this study are also 1.5 to 2 orders of magnitude lower than Al-Si interdiffusion in majoritic garnets (Nishi *et al.*, 2013; $D_0 = 2 \times 10^{-10}$ m^2/s and $E_{(A, 17)} = 364 \pm 47$ kJ/mol and Van Mierlo *et al.*, 2013; $D_0 = 2.3 \times 10^{-11}$ m^2/s and $E_{(A,15)} = 291 \pm 51$ kJ/mol) (Figure 4.1). This finding implies that both atomic (ionic) sizes and mineral lattice (matrix) structures of the diffusing species play a significant role in the diffusion rate in Earth's mantle-related minerals. This effect will be discussed in the following subsection. Furthermore, our data show ~ 2 orders of magnitude lower diffusion rates than Si and Mg self-diffusion obtained by Yamazaki *et al.* (2000) ($D_0 = 2.7 \times 10^{-10}$ m^2/sec and H = 336 kJ/mol), Dobson *et al.* (2008) ($D_0 = 8.3 \times 10^{-10}$ m^2/sec and $E_{(A, 25)} = 347 \pm 73$ kJ/mol) and Xu *et al.* (2011) ($D_0 = 5 \times 10^{-11}$ m^2/sec and $E_{(A, 25)} = 308$ kJ/mol). The Si self-diffusion in stishovite (Xu *et al.*, 2017; $D_0 = 2.4 \times 10^{-12}$ m^2/s and $E_{(A, 25)} = 387 \pm 90$ kJ/mol) shows a significantly slower diffusion rate than previous results for bridgmanite samples under the same pressure and temperature conditions.

Table 4-1: Comparison of pre-exponential factors and activation energies from this study and previous studies of different mantle minerals at comparable pressures.

Study	**D_0 [m^2/s]**	**E_A [kJ/mol]**	**P [GPa]**	**Analytical method**
Bridgmanite				
This study	4.2×10^{-11}	400[+]	24	TEM
Yamazaki *et al.* (2000)	2.7×10^{-10}	336	25	SIMS
Holzapfel *et al.* (2005) (IW-3)	4.0×10^{-09}	414	24	TEM
Holzapfel *et al.* (2005) (IW+3)*	7.9×10^{-08}	414	26	TEM
Dobson *et al.* (2008)	8.3×10^{-10}	347	25	SIMS
Xu *et al.* (2011)	5.0×10^{-11}	308	25	SIMS
Majoritic garnet				
Nishi *et al.* (2013)	2.0×10^{-10}	364	17	TEM
Van Mierlo *et al.* (2013)	2.3×10^{-11}	291	15	TEM
Stishovite				
Xu *et al.* (2017)	2.4×10^{-12}	387	25	SIMS

* Not in included in the Figures

[+] Fixed

To date, there do not appear to be any experimental diffusion studies on bridgmanite that demonstrate a resolvable change in the length of the profiles with time, and the time period varies only by a factor of ~ 2. Thus, it is not clear from the previous studies that are plotted in Figure 4.1 whether the concentration profiles of cation species presented are actual volume diffusion profiles. None of the studies reports time-series diffusion experiments at the same temperature, and their diffusion profiles might have convolution effects from the surface-roughness of their diffusion samples and in their short diffusion profiles. In this study, experiments were performed at 24 GPa and different temperatures with annealing times of 3, 6, and 21 h, thus contributiong to the reliability of the data.

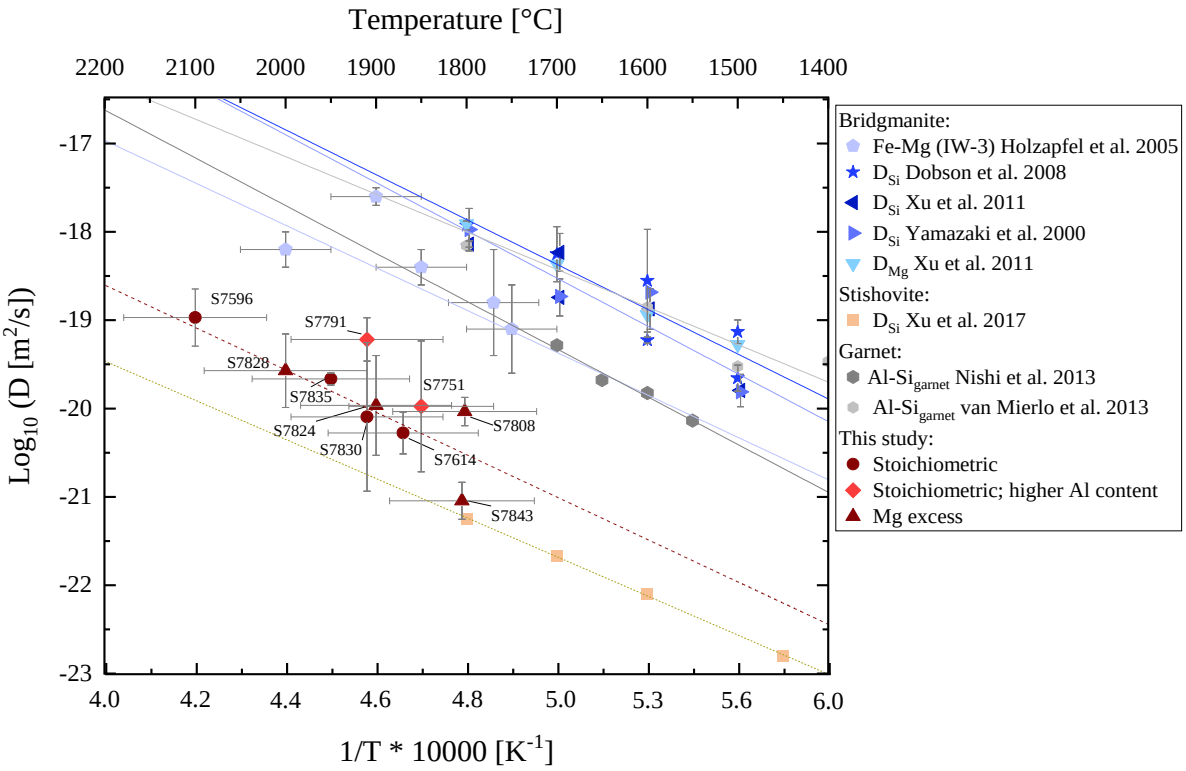

Figure 4.1: Overview of the data that were compared in the discussion. The Arrhenius plot includes all data points of the averaged deconvoluted diffusion coefficients and shows the Al-Si interdiffusion data from this study in dark red at 24 GPa. The blue scale coloured data points represent all diffusion data from bridgmanite studies (excluding our data) at 25 GPa, and greyscale indicates Mg and Si self-diffusion coefficients in majoritic garnet from previous studies at 15 and 17 GPa. The red line shows Si self-diffusion in stishovite at 25 GPa. The lines of corresponding colours represent the linear fits of the literature data, in order to highlight the difference at any temperature in the range of interest.

4.2. **Magnitude of Al-Si interdiffusion in the Earth's lower mantle**

As mentioned in the introduction, diffusion depends on many factors, including the grain size of the rock aggregate, diffusing species, crystallographic structure of the lattice, presence and type of defects, and pressure and temperature conditions. Here, the results will be compared to the available literature data, separately considering the factors listed above. As it was already mentioned in the introduction and result chapters, in order to compare the diffusion data obtained at different temperatures, both activation energy E_A and pre-exponential factor D_0 are required. However, usually these parameters are highly correlated and can not be compared independently. Figure 4.2 shows the plot of the activation energy E_A against the $\log_{10}$ of the pre-exponential factor D_0, incorporating new and some previously published data (Table 4-1) for majoritic garnet at lower mantle transition zone pressures (15 - 17 GPa) and Sti and Brg at lower mantle pressures (24 and 25 GPa). It can be seen that the similar data sets of Si self-diffusion studied in Brg by Yamazaki *et al*. (2000), Dobson *et al*. (2008) and Xu *et al*. (2011) as well as the data of majoritic garnet by Van Mierlo *et al.* (2013) plot on one line in Figure 4.1 + 4.2. Data of Nishi *et al*. (2013) and Holzapfel (2005) would plot as a parallel line shifted towards slower diffusion. To compare our data and the data of Xu *et al.* (2017) with the other data, one needs to imagine a line going through the point parallel to the other lines. This plot is called a compensation plot (described in Lowry *et al.,* 1982; Béjina & Jaoul 1997) and is used to compare reported couples of E_A and D_0, which are usually correlated. The noticeable differences in the plot will be discussed in section 4.2.5. The effect of the diffusing species and the mineral structure will be addressed in the corresponding section (4.2.2 + 4.2.3).

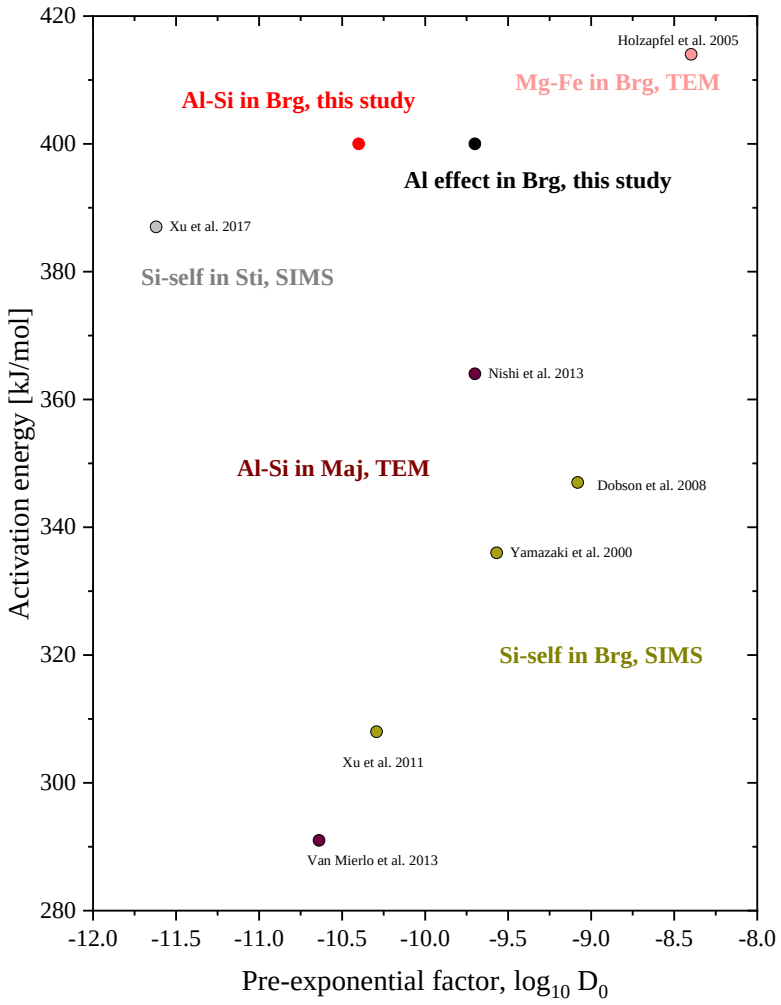

Figure 4.2: Plot (log D_0 vs E_A) for atomic diffusion in lower mantle silicate minerals including bridgmanite (Brg), stishovite (Sti) and majoritic garnet (Maj). The diffusion data from this study are compared with previously published data in the context of their analytical methods such as TEM and SIMS. Majoritic garnet (dark red) was experimentally investigated at 15 and 17 GPa and Sti and Brg at 24 and 25 GPa. It is assumed that an increased Al content influences the diffusion behaviour in bridgmanite and therefore the data with increased Al content are denoted as "Al effect in Brg" on the plot. Details on determination of D_0 for dataset with increased Al content are given in 3.2.4.

4.2.1. Effect of grain size and contribution of grain boundary diffusion

This study is focused on volume diffusion as the dominant diffusion mechanism at the Earth's mantle conditions (see Introduction 1.4.1). However, in laboratory experiments with much smaller characteristic grain sizes, it is not easy to ensure that the measured concentration of diffusing species in the analysed sections is not affected by diffusion through the grain-grain interfaces, which is usually many orders of magnitude faster than volume (lattice) diffusion. For this purpose, we took special care in the preparation of the experiments, such as the synthesis of large crystals, surface treatment of diffusion couples, high-resolution analysis of diffusion profiles, the study of the deconvolution effect etc. (see the chapter Experimental and analytical methods). However, our study also showed outlier data points indicating much faster diffusion.

As shown in Figure 4.3, data points S7766 and S5548 have a diffusion rates of ~ 4 orders of magnitude faster than other experiments under similar conditions. One of the most plausible reasons for such an increase in diffusion rate in a single experiment is the contribution of grain boundary diffusion for sample S5548. The effect of grain boundary diffusion contribution has also been analysed by Holzapfel (2004) in his thesis. He shows that Fe-Mg interdiffusion in perovskite is as slow as the Si self-diffusion from previous literature data. Additionally, he assumed that the grain boundary diffusion could be negligible for a grain size likely present in the lower mantle (~ 100 – 1,000 µm; Solomatov *et al.* (2002)). For example, he estimated an effective diffusion coefficient ~ 30 times larger than the D_V due to the contribution of the grain size of 10 µm. The effective diffusion coefficient is the weighted average of the volume diffusion coefficient and the grain boundary diffusion coefficient as a function of the grain size and the grain boundary width (see section 1.4.1 of the Introduction). Consequently, the correlation of grain size with diffusion rate could explain the increased diffusivity in our H5548 diffusion experiment. It is possible that the fast diffusion experiments were influenced by smaller grain sizes of the synthesised material (~ 1 µm) compared to the other diffusion experiments (~ 3 µm) (Appendix A, Table 4). Therefore, this study was carefully focused on volume diffusion by selecting grains with a minimum size of 2 µm to avoid grain boundary effects on the diffusion coefficient (section 2.2.2; Appendix A, Table 4). Otherwise the analytical data could be affected by the significant contribution of grain boundary or sub-grain boundary diffusion due to small grain sizes, thus showing higher diffusion coefficients. Therefore, it is essential to separate grain boundary contributions from volume diffusion.

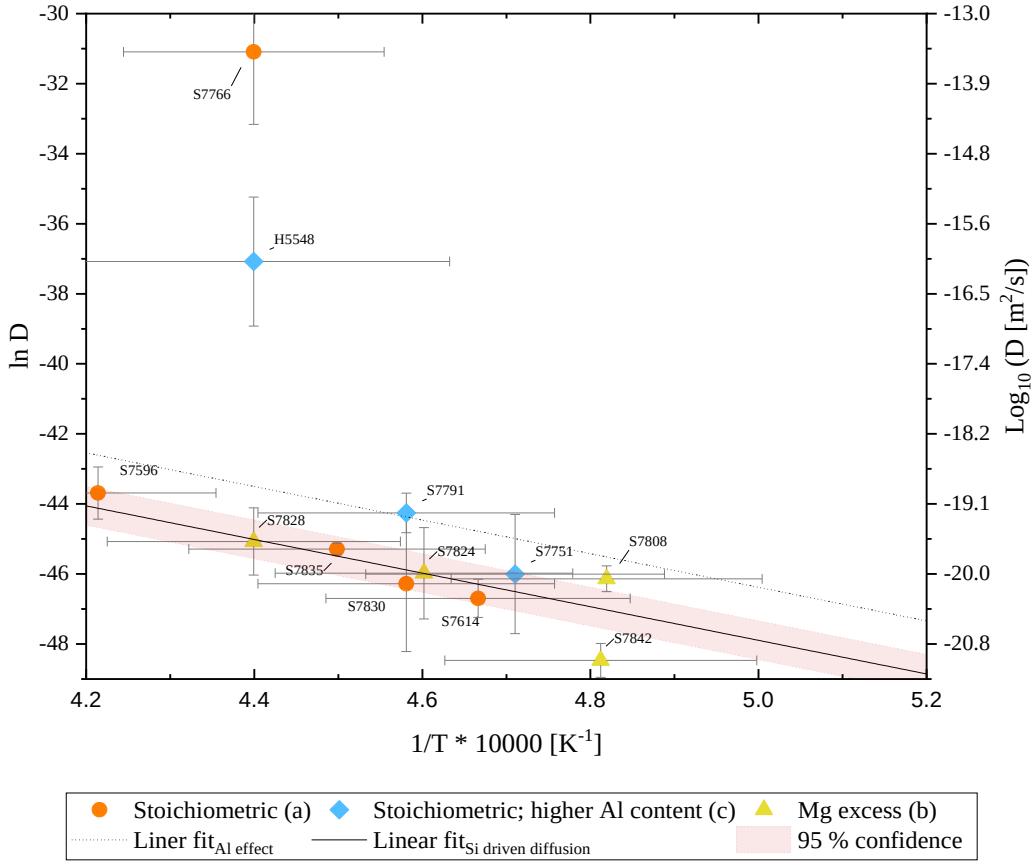

Figure 4.3: Comparison of all diffusion experiments. S7766 and H5548 are averaged convoluted diffusion coefficients and the other data points are averaged deconvoluted diffusion coefficients. It can be seen that S7766 and H5548 are outliers with up to 6 orders of magnitude faster diffusion rates, properly caused by the influence of grain boundary diffusion in these samples.

Yamazaki *et al*. (1996) have noted that the volume diffusion becomes dominant under Earth's lower mantle conditions, caused by grain sizes larger than a few microns. The experiments in this study are more sensitive to the lattice (volume) diffusion due to the TEM resolution and optimised synthesis conditions (ensuring large enough grain sizes). In a typical experimental setup, the grain size is smaller, and the grain boundary diffusion becomes relevant and could show ~ 4 orders of magnitude faster diffusion coefficients than for volume diffusion. A recent study by Fei *et al*. (2021) found a larger grain size of bridgmanite in the lower mantle than previously expected, making it even more critical to avoid grain boundary diffusion in analytical studies.

Comparison of other diffusing species in bridgmanite

One of the factors influencing diffusion is the type of diffusing species. Different species diffuse differently through the same crystallographic lattice under similar conditions. Figure 4.1 compares our data with previously reported data on the diffusion of other species in bridgmanite. As can be seen from the plot, diffusion coefficients of Al and Si from our data are at least 1.5 to 2 orders of magnitude lower than the diffusion coefficients of other diffusing species (Mg and Fe) shown in this figure. On the other hand, data for both compositions with Al content of 2.5 - 3 wt. % (stoichiometric and with Mg excess) are 2 orders of magnitude lower compared to Fe-Mg interdiffusion or Si self-diffusion in bridgmanite (Figures 4.1 + 4.4). However, two data points with increased Al content (5 wt. %) tend to be closer to Fe-Mg interdiffusion, suggesting a non-linear effect of Al concentration on Al-Si interdiffusion. This can imply that the higher Al content tend to create more cation vacancies in the Mg A-site in the mineral structure and might enhance Al diffusion as the same way as ferric iron, Fe^{3+} behaves in the faster Mg-Fe diffusion at high f_{O_2} conditions. The observation of this effect supports findings of Frost & Langenhorst (2002), who studied the effect of Al_2O_3 on Fe–Mg partitioning between magnesiowüstite and magnesium silicate perovskite. They suggest that with increasing Al^{3+} content (up to 10 wt. %), the charge-coupled substitution mechanism, and at lower Al contents, both OV and CC mechanisms take place. This is also in agreement with the results obtained by Huang *et al.* 2021, where charge-coupled substitution is dominant for trivalent cations (Fe^{3+} and Al^{3+}) and the oxygen vacancy component does not exceed 0.04 pfu for the studied bridgmanite crystals. As can be seen from Figure 3.23, the diffusion rates of the samples with higher Al content appear to be faster as presumably mainly driven by charge-coupled substitution. This observation seems to lead to the assumption that this is happening because the effect of the A-site becomes relevant and will make a difference to the diffusion rate (Figure 1.4). On the other hand, the difference in the diffusion coefficients could be due to the fact that the studied species are different: The difference between Al-Si diffusion and Mg-Fe diffusion (by Holzapfel *et al.*, 2005) in similar ATEM characterisations suggests that Si diffusion is the slowest in bridgmanite. Holzapfel *et al.* (2005) focused on Fe-Mg interdiffusion in bridgmanite under oxidizing and reducing conditions. They performed their experiments at 22 – 26 GPa up to 24 h on diffusion couples consisting of Fe-free polycrystalline perovskite, in contact with Fe alloy and Fe-bearing polycrystalline perovskite, under varied composition of the alloy and analysed them by TEM.

The Holzapfel *et al.* (2005) diffusion coefficients also show faster diffusion rates, which may be due to the different substitution mechanisms of the diffusiong species (Al and Si as opposed to Fe and Mg) and not caused by analytical errors. In addtion, the Fe-Mg diffusion rate depends on the oxidation state of Fe; under oxidizing conditions the diffusion rate becomes faster (Holzapfel *et al.* 2005). For this section, it can be concluded that the interdiffusion between Al and Si has the slowest diffusion rate in bridgmanite, confirming previous suggestions for Si (Reali *et al.* 2019 a). Another question that arises is the effect of the crystal structure on Al-Si interdiffusion in different minerals, which will be discussed in the following section.

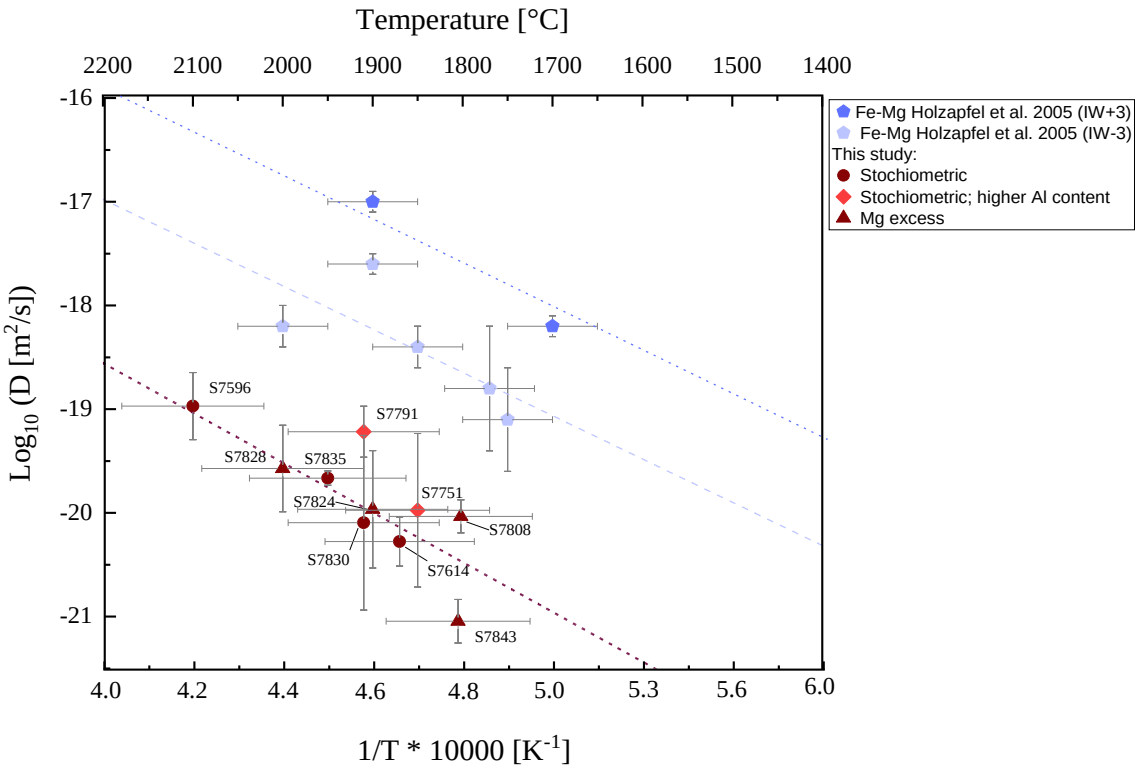

Figure 4.4: Arrhenius plot of all data points of the averaged deconvoluted diffusion coefficients. Data from this study are shown in dark red, except for the stoichiometric data with higher Al content (brighter red). Light blue and blue data points represent Fe-Mg interdiffusion in bridgmanite at different oxidation state.

4.2.2. Effect of mineral structure on diffusion

Here, the Al-Si interdiffusion coefficients are compared to Al-Si interdiffusion in garnets and other mantle minerals to demonstrate mineral structure differences. Then, different diffusion mechanisms in bridgmanite are compared to understand the difference in diffusion rates for self-diffusion and interdiffusion. Figure 4.5 shows Al-Si interdiffusion coefficients plotted vs temperature in logarithmic scale (Arrhenius plot) for bridgmanite from this study in comparison with data of Van Mierlo *et al*. (2013) and Nishi *et al.* (2013) reported for majorite. As one can see, the absolute values of diffusion coefficients for bridgmanite are 1.5 to 2 orders of magnitude lower than Al-Si interdiffusion coefficients reported for majoritic garnets at the corresponding conditions (P and T). Nishi *et al.* (2013) report that their results showed a diffusion coefficient up to 4 orders of magnitude slower than the Si self-diffusion coefficients in wadsleyite, ringwoodite and olivine. Van Mierlo *et al*. (2013), instead, shows similar results to the rates of silicon diffusion in wadsleyite and ringwoodite. Whereas both agree that their results are up to 7 orders of magnitude slower than Fe-Mg interdiffusion coefficients in wadsleyite at 15 GPa reported in other studies (Holzapfel *et al.*, 2009, Chakraborty 2010, Shimojuku 2009).

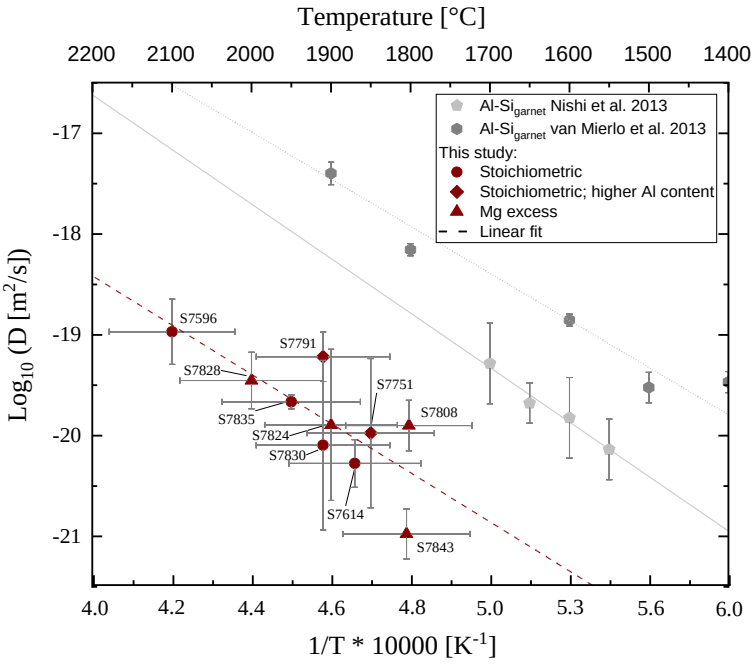

Figure 4.5: Arrhenius plot of all data points of the averaged deconvoluted diffusion coefficients. Al- Si interdiffusion data from this study are shown in dark red. The plot compares the diffusion results with data of majorite garnet at 17 GPa from Nishi et al. (2013) and at 15 GPa from Van Mierlo et al. (2013).

Furthermore, Van Mierlo *et al*. (2013) extrapolated their data to pressures at the top of the lower mantle. They showed that at 1,700 °C, Al-Si interdiffusion from their extrapolation is even slower than the silicon self-diffusion and Fe-Mg interdiffusion in silicate perovskite reported by Yamazaki *et al.* (2000) and Holzapfel *et al.* (2005) and shown in Figure 4.1 in the previous section. A further aspect of the effect of mineral structure on the diffusivity in bridgmanite is related to the 6-coordinated silicon in minerals which are compared in this study. So, for example, stishovite (Xu *et al.,* 2017) has 6-coordinated silicon as well as majorite (Nishi *et al.,* 2013; Van Mierlo *et al.,* 2013). This may suggest that Al-Si interdiffusion may depend on mineral structure, as these previous studies show similar diffusion rates or slower diffusion coefficients than other mantle minerals (Figure 4.1). Even Xu *et al.* (2011) mentioned that their Si and Mg diffusion in perovskite results showed a diffusion coefficient up to 5 orders of magnitude lower than the Si self-diffusion coefficients and Fe-Mg interdiffusion coefficients of other minerals such as in wadsleyite, ringwoodite and olivine. Some studies indicate Si (Yamazaki *et al.,* 2000), but others show that Mg (Holzapfel *et al.,* 2005) is the slowest diffusing species in bridgmanite. The diffusion coefficients in this study show that the Si diffusivity in bridgmanite should be slower at mantle conditions than expected, as seen in Figure 4.1. In the case of studies that do not agree with our results (Yamazaki *et al.,* 2000 and Xu *et al.,* 2011), it may be that there were critical issues with the SIMS measurements (see section 4.2.4. (“Effect of sample surface treatment and convolution”).

In a follow-up study on Si self-diffusion in pyrope-rich garnet, Shimojuku *et al.* (2014) observed that their data at 16 GPa plotted between those of Van Mierlo *et al.* (2013) and Nishi *et al.* (2013) at 17 GPa. They also concluded that Si diffusion seems to be the slowest in the major constituent elements in pyrope-rich garnets. In this work we show that Al-Si interdiffusion in bridgmanite is even slower. On the other hand, Xu *et al.,* 2017 find the slowest rate of Si diffusion in stishovite among all the minerals in the mantle. Both bridgmanite and stishovite have Si in octahedral coordination and Si in majoritic garnets and Pyp75Alm15Gr10 garnets (Van Mierlo *et al.,* 2013; Nishi *et al.,* 2013; Shimojuku *et al*., 2014) has both 6 - and 4 - coordinated silicon. This leads to the hypothesis that Si diffusion in structures with 6 - coordinated Si is slower than diffusion of Si in mixed or 4 - coordinated Si. Whether the diffusion of the same species (Si and Al) appears slower or faster may depend on the structures (their density and bonding properties) of the mineral.

4.2.3. Effect of Al^{3+} substitution and point defects on bridgmanite properties

As already introduced in section 1.3.2 Al^{3+} can substitute into bridgmanite by two different substitution mechanisms (Brodholt, 2000; Yamamoto *et al.,* 2003), including point defects such as oxygen vacancies, which will be discussed in the following section. Defects in mineral lattices that serve as short-circuit paths for diffusing species have a lower diffusion activation energy. Thus, point defects control the diffusive transport of elements and flux in the solid state. Point defects generally result from interstitials, antisties and vacancies and the substitution of trivalent cations (Navrotsky, 1999). The mechanism of vacancies is driven by the activation energy required to create and move a vacancy. Diffusion by this mechanism can occur by atoms moving into adjacent vacancies.

Looking at our data from an overall perspective, it is noticeable that no explicit assumption can be made about the Al^{3+} substitution mechanism (Figure 3.9). The samples tend to have oxygen vacancies in the MgO-enriched samples, and the stoichiometric and SiO_2-enriched samples tend to be close to the charge-coupled trend line. A literature search shows similarly that oxygen vacancies in the upper part of the lower mantle are much more abundant in perovskites than cation vacancies (Ammann *et al.,* 2009; Xu *et al.,* 2011; Grüninger *et al.,* 2019). With increasing pressure and aluminium content, the abundance of OVs decreases and CCs become dominant (Liu *et al.,* 2017 a; Liu *et al.,* 2017 b). It can be assumed that the defect substitutions of Al^{3+} into sixfold sites could dominate the uppermost lower mantle and could affect the mechanism of oxygen-vacancy substitution, which in turn affects the diffusivity in bridgmanite. If an oxygen-vacancy substitution primarily drives our samples according to the slowest diffusing species, Si, this could explain the slower diffusion as already mentioned in section 4.2.2. In other word, the Al,Si diffusion rate could be enhanced by CC substitution at higher pressure conditions, since OV substitution does not enhance it from our results of diffusion on Mg excess couples.

Moreover, the larger size of Al compared to Si and the potential for migration via the coupling of point defects to maintain local charge equilibrium (Cherniak & Watson, 2019) may lead to the higher activation energy for diffusion observed for Al compared to other species such as Mg, Fe or Si, discussed in section 4.2. The vacancies are different in Al-bearing and Al-free materials, which may affect differences in point defect coupling. This, in turn, can affect Si migration (diffusion rate) in crystals through activation enthalpies (Béjina & Jaoul, 1997) and

may be part of the explanation for the differences in diffusion rates from different silicate minerals which were compared in this study.

Hirsch & Shankland (1991) have also studied point defects in perovskites and found that fundamental differences in defect structure depend on various experimental factors such as the degree of equilibrium or thermodynamic conditions. This highlights the importance of comparing diffusion rates under the same experimental conditions. However, they did not consider the presence of aluminium in their theoretical calculations. Certainly, Ammann (2011) showed that impurities could play a crucial role in the diffusion rate. Therefore, the Al-Si interdiffusion studied here could be of great interest. Yamazaki *et al.* (1996) already discuss that volume diffusion dominates under lower mantle conditions caused by grain sizes larger than a few microns (Karato & Li, 1992). Still, they have not included aluminium in their study. After they showed that volume diffusion dominates the lower mantle Yamazaki *et al*. (2000) demonstrated a faster Si self-diffusion compared to our data. This suggests that Al may reduce the diffusion rate in bridgmanite. In summary, Al as an impurity significantly affects lower mantle diffusion rates. However, no meaningful conclusions about Al^{3+} substitution mechanisms in bridgmanites can be drawn from this study, as no significant effects on Al-Si diffusion are detectable, but Al in the A-site might enhance it ("high Al effect"). Thus, oxygen vacancies have no observable effects on Al-Si diffusion in the bridgmanites studied here, and further investigation is needed.

4.2.4. Effect of sample surface treatment and convolution

The presence of dislocations and stacking faults on the surface increases the diffusivity of the diffusing species. To concentrate only on volume diffusion, the sample surface has to be prepared to remove all defects. In their research, for example, Yamazaki *et al.* (1996) refrained from preparing the diffusion couples by chemically initiated polishing before using them. They polished polycrystalline samples with 0.25 µm diamond paste and coated them with ^{29}Si on the surface. This could have led to a fast diffusion track through dislocations and defects. After an annealing time of up to 50 h at 25 GPa, they analysed the samples by secondary-ion mass spectrometry (SIMS). To look more closely at the influence of the preparation method, the self-diffusion coefficients of Dobson *et al.* (2008) and Xu (2017) were considered in more detail. They also dealt with Si self-diffusion in perovskites but used another polishing method for sample preparation. After mechanical polishing with 1/4 mm diamond paste, they used chemical polishing with colloidal silica. This served to remove the defects and damages on the surface of the crystal lattice (Dobson *et al.*, 2008). It turns out that the surface preparation has a significant influence on the diffusion rate.

Xu *et al.* (2011) investigated the self-diffusion coefficients by sputtering ^{29}Si- and ^{25}Mg-enriched $MgSiO_3$ thin films onto the polished surfaces of oriented perovskite single crystals and analysed them by SIMS (see Dohmen *et al.* (2002) for details). Dobson *et al.* (2008) deposited ^{18}O and ^{29}Si films on perovskite, performed their experiments and analysed them in the same way as Xu *et al.* (2011) by depth profiling by SIMS. Both show faster diffusion rates which leads to the hypothesis that the analytical method could significantly affect the the evaluation of diffusivities on short diffusion profiles (convolution effect). In other words, SIMS might be insufficient for measuring diffusion profiles. But Xu *et al.* (2017) did surface roughness measurements and improved the SIMS measurement method. In that way, they reduced the uncertainties of diffusion coefficients caused by SIMS convolution effects to make reliable statements about the diffusion coefficient of slow diffusing species such as Si. After the surface treatment and deconvolution in their diffusion profiles they showed lower Si self-diffusion rates and higher activation energy in stishovite (Figure 4.1) than Yamazaki *et al.* (2000), Dobson *et al.* (2008) and Xu *et al.* (2011) in the same PT conditions, an advance in the SIMS method for trace element investigation. As one can see, since SIMS imaging has a lower resolution than TEM imaging by over two orders of magnitude (Eswara *et al.*, 2019), extreme caution with a surface treatment has to be considered. This can explain unusually fast diffusion rates in many older studies using SIMS analysis.

In conclusion, the diffusion data in Figures 4.1 + 4.2 need to be more consistent between them due to artifacts such as the surface preparation and issues with the analytical method. The roughness of the sample surface is the leading cause of the convolution effect. This discrepancy in diffusivity may be due to the fact that the convolution effect was not considered in their study where, as expected, the convolution effect is more significant because a smaller crater size (~50 × 50µm) gives a larger edge effect in their short diffusion profiles of a few hundred nanometres or less (Xu *et al.,* 2017). With further development, as done by Xu *et al.* (2017), the newer studies can be more meaningfully with our data and used for further discussion. This shows that both SIMS and TEM are reliable with proper deconvolution corrections and suitable for investigating Si diffusion in the lower mantle. For the reasons described above, the TEM was used instead of SIMS because of its much higher resolution in this study. Furthermore, the diffusion zone must be investigated laterally and not in-depth for diffusion pair experiments, which makes SIMS and other methods, such as Rutherford backscattering for trace element studies, not usable in this case (Holzapfel 2004).

4.3. **Effect of temperature**

All the experiments in this study were performed at 24 GPa, comparable to the other studies described in section 4.1. We assume the pressure effect to be negligible, while the temperature is one of the most significant factors influencing diffusivity. The Arrhenius plot is commonly used to compare data obtained at different temperatures and to make a prediction of diffusion coefficients at any temperature in the range of interest. As described in section 1.3.4, the Arrhenius plot of a thermally activated reaction describes the temperature dependence of the diffusion coefficients. The activation energy can be derived from the slope of the regression line of an Arrhenius plot and the pre-exponential factor D_0 from the intercept of this line with the y-axis, as mentioned in section 3.2.4. These two parameters are correlated.

As shown in Figure 4.1, taking into account the correlation and experimental uncertainties, it can be assumed that the activation energy of the previous studies has a similar error. We fixed the activation energy at 400 kJ/mol, derived from previous activation energy data for lower mantle minerals. This helps to compare our diffusion rates with literature data. An average pre-exponential diffusion coefficient D_0 for our data was calculated to be $D_{Al\text{-}Si} = 4.2 \pm 0.9 \times 10^{-11}$ m^2/s. The study of Yamazaki *et al.* (2000), shown in Figure 4.1, calculated a volume diffusion coefficient of $D_{Si} = 2.74 \times 10^{-10} \exp[-336$ kJ mol^{-1}/RT] m^2/s for Si self-diffusion. Xu *et al.* (2011) calculated a similar self-diffusion coefficient of $D_{Si} = 5.10 \times 10^{-11} \exp[-308 \pm 58$ kJ mol^{-1}/RT] m^2/s and $D_{Mg} = 4.99 \times 10^{-11} \exp[-305$ kJ mol^{-1}/RT] m^2/s. They also investigated the anisotropy of Si self-diffusion mainly along the c-axis in $MgSiO_3$ perovskite and found the diffusivity to be isotropic. At the same time, Holzapfel *et al.* (2005) determined a Fe-Mg volume diffusion coefficient under reducing conditions ($\Delta_{fO_2} \approx$ -2.7) of $D_{Fe,Mg} = 4.0$ (0.7) $\times 10^{-9} \exp[-414 \pm 62$ kJ mol^{-1}/ RT] m^2/s and under oxidising conditions (Ni-NiO buffer) $D_{Fe,Mg} = 7.9$ (1.4) $\times 10^{-8} \exp[-414 \pm 62$ kJ mol^{-1}/ RT] m^2/s experimentally in perovskite. Recent studies suggest that the activation enthalpies of Si and Mg self-diffusion in bridgmanite are 300 to 400 kJ/mol (Dobson *et al.*, 2008; Tsujino *et al.*, 2022; Xu *et al.*, 2011; Yamazaki *et al.*, 2000), including uncertainties such as the activation energies obtained in this and previous studies. This shows that the temperature effect are similar for most of the discussed results within their experimental uncertainties.

Despite the different reported activation energies (Table 4.1 and Figure 4.2), it can be seen from Figure 4.1 that all the data have a very similar temperature dependence, and the reported activation energies could only be used together with the pre-exponential factor to calculate the diffusion coefficient at temperatures in the range of interest and close to the experimental range. Extrapolation of diffusion coefficients to temperatures far from the experimental range must be done with extreme caution. Such diffusion data are needed for different rheological models of the mantle. In anticipation of the next section, the viscosity of bridgmanite in the lower mantle can be estimated qualitatively.

4.4. **Rheology of the lower mantle**

There are mainly two experimental approaches to obtaining deformation rate (strain rate) from the rheological properties (such as diffusivity, grain size and width of grain boundary): deformation experiments and diffusion experiments. Due to the lack of parameters, the following section looks at studies that have dealt with diffusion-controlled creep and the rheology of the Earth's lower mantle. The data from this study are used as input into the earlier results and models to estimate viscosity. Recent studies have again shown the importance of studying bridgmanite in terms of its physical properties.

The viscosity strongly depends on the grain size, assuming that diffusion creep prevails in the lower mantle (Elliott, 1973; Karato & Li, 1992; Glišovic *et al.*, 2015). Thus, for further discussion, the focus is on diffusion creep. The diffusion creep can be calculated using the D_{eff}, and the viscosity of the Earth's lower mantle can be estimated. Some assumptions must be made to calculate the effective diffusion coefficient D_{eff}, and data from the literature must be considered. Following Holzapfel *et al.* (2005), no experimental data on grain boundary diffusion is available for Al-Si interdiffusion, which is why the same assumptions are made for the grain boundary diffusion D_{gb} (negligible in the lower mantle) and the grain boundary width δ (1 nm) to estimate the effective diffusion coefficient. We assume that the volume diffusion ("Nabarro-Herring (NH) Creep") becomes dominant in the upper part of the lower mantle and that $D_{eff} \triangleq D_v$.

From the experimental point of view, the flow law can be obtained by measuring the strain rate and stress through deformation experiments. So, Tsujino *et al.* (2022) and Girard *et al.* (2016) showed from their experimentally determined strain rate data that bridgmanite dominates lower mantle rheology and controls the lower mantle viscosity. They experimentally investigated deformation in bridgmanite at a strain rate of 10^{-5} s^{-1}. They proposed a strain rate of $10^{-18} – 10^{-16}$ s^{-1} and stress magnitude of 2×10^4 to 3×10^5 Pa in the grain size–insensitive dislocation creep regime for the lower mantle. From the deformation data they obtained, they also proposed stress-independent diffusion creep mechanisms under the grain size of several millimetres of bridgmanite to realise the viscosity of 10^{21-22} Pa·s at the top of the lower mantle. It is still debated which creep mechanism is dominant in the Earth's mantle. Bridgmanite viscosity in both dislocation creep and diffusion creep regions strongly depends on the diffusion coefficient of Si and Mg. This is why our new diffusion data are an important contribution to further discussion.

Considering the absence of seismic anisotropy in the lower mantle, the small grain size of 1 – 10 mm (Solomatov *et al.*, 2002; Shimojuku *et al.*, 2009) and low stresses of ~ 10^5 Pa (Xu *et al.*, 2017; Tsujino *et al.*, 2022) lead to diffusion creep being the dominant creep mechanism through the lower mantle (Karato *et al.*, 1995) This enables consideration of the effect of the diffusion coefficient determined in this study on the mantle rheology.

$$\eta = {}^{\sigma}/_{\dot{\varepsilon}_{total}} \qquad (4.1)$$

Previous mantle viscosity η calculations show a viscosity of $10^{21–22}$ Pa · s (Ammann, 2011; Tsujino *et al.*, 2022). As mentioned in the introduction (section 1.5), Tsujino *et al.* (2022) tried to explain the observed viscosity by using deformation mechanism maps of bridgmanite. Therefore, e.g., Tsujino *et al.* (2022) used the total strain rate $\dot{\varepsilon}_{total}$ calculated as the sum of strain rates of diffusion creep ($\dot{\varepsilon}_{diff}$) and dislocation creep ($\dot{\varepsilon}_{dis}$). The $\dot{\varepsilon}_{diff}$ was calculated from previous diffusion data (Dobson *et al.*, 2008; Xu *et al.*, 2011; Yamazaki *et al.*, 2000) and the $\dot{\varepsilon}_{dis}$ was estimated by in situ stress and strain measurements of $MgSiO_3$ bridgmanite during uniaxial deformation. Following the same approach and assumptions for stress and strain rate as Tsujino *et al.* (2022) and taking our diffusion data into account (Figure 4.5), the viscosity of bridgmanite in the lower mantle could be 1 to 2 orders of magnitude higher than their estimations compared to using Si self diffusivity based on Yamazaki *et al.* (2000), and compared their results with Si self-diffusion data from Dobson *et al.* (2008) and Xu *et al.* (2011).

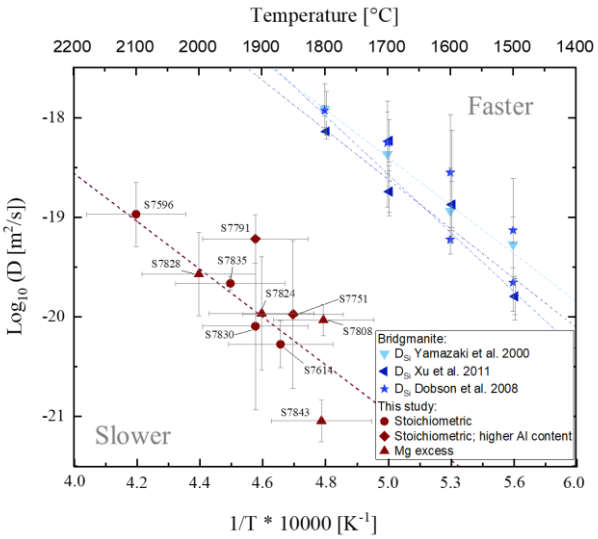

Figure 4.6: Direct comparison of diffusion data from previous studies used to calculate lower mantle viscosity models and the diffusion data from this study. Again, it can be seen that the linear relations between the data have a difference of 2 orders of magnitude.

4.5. **Potential geothermometer**

It is known from other minerals that the Al content can be important for geothermometry (Sasaki *et al.*, 1985; Hoff & Watson, 2018; Cherniak & Watson, 2019). Since the Al content is also known to influence the diffusion of other species and stishovite is present as a secondary phase in the samples here, the question arises whether the Al content in stishovite can be used to independently determine the temperature of the bridgmanite samples. In the data, significant variations are noticeable. Comparison with earlier data (Figure 4.6) shows that the samples generally contain ~ 0.5 to 1.5 wt% Al_2O_3 in stishovite.

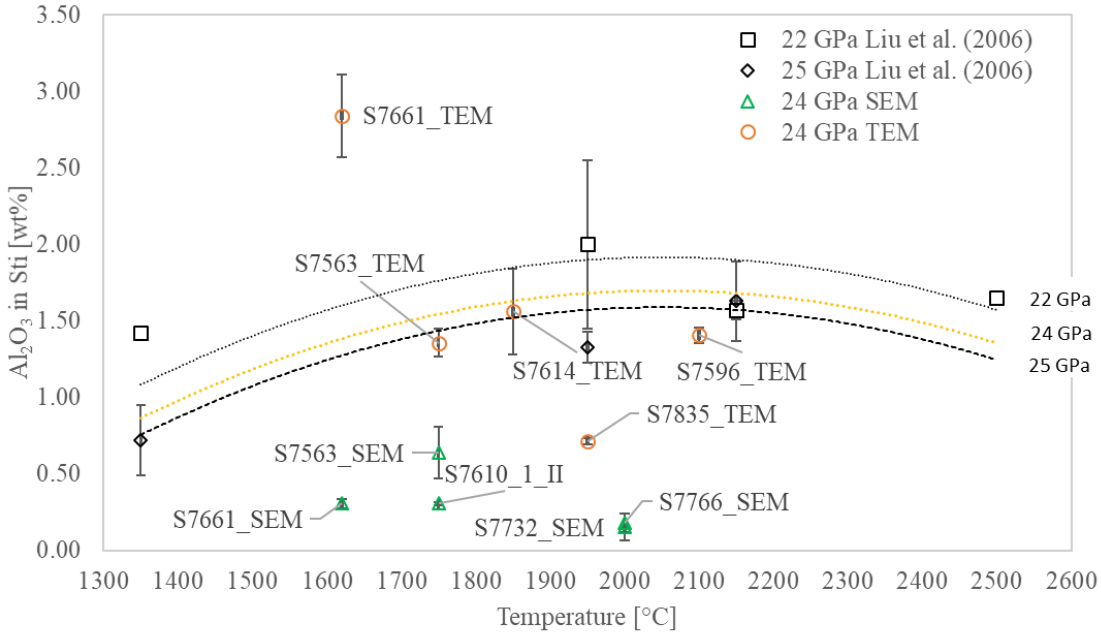

Figure 4.7: Effect of temperature on the Al_2O_3 content in Sti. The uncertainty in the temperature measurement is calculated by the analytical error. The Al_2O_3 content in Sti has been fitted compared to previous studies on anhydrous stishovite (Liu et al., 2006). The lines are drawn according to a calculated polynomial by Liu et al. (2006).

The lack of a strong correlation suggests that the data in the present study are not suitable for using the Al content in stishovite as a geothermometer. However, a slight correlation can be anticipated, which positively supports the calculated temperature of the data. Looking more closely at the aluminium content of the SEM samples, it is noticeable that the aluminium content is lower than the measured Al content in the same sample analysed by TEM. Based on the previous results, the Al content of the stishovite crystals would be expected to overlap with the Al content of the larger bridgmanite crystals and increase the Al content.

However, the SEM observation was carried out at 5 kV and a 30 µm aperture, which gives a lower number of counts per second and this results in too low an Al content because the signal to be received is too low.

This could be improved by a longer exposure time. Therefore, SEM observations could be carried out more carefully in the future based on these observations. This evaluation needs further data for a meaningful statement on the temperature dependence in Al content in stishovite. Since anhydrous stishovite can be used only poorly for temperature determination as seen in recently published work (Ishii *et al.*, 2022), only hydrous stishovite shows an increase in Al content with increasing temperature (Litasov *et al.*, 2007; Ishii *et al.*, 2022). In anhydrous stishovite, the Al content drops again with increasing temperature after a saddle point (Figure 4.6). In conclusion, it can be said that the determination of the Al content in stishovite was not useful in this study and more data are needed at higher temperatures. As can be seen from Figure 4.6, three of the TEM data agree with the Liu *et al.* (2006) polynomial. However, it can be hypothesised that if stishovite were a water carrier and allowed several ppm of water to be brought to the mantle-core interface, there would be an increased amount of water in the lower mantle than previously thought, raising the question of what (water) effect this would have on Al solubility in bridgmanite and how far this would change Al-Si interdiffusion in silicate minerals of the lower mantle.

5. Conclusion and Perspectives

This thesis investigated the Al-Si interdiffusion in $MgSiO_3$ Al-bearing bridgmanite under Earth's lower mantle conditions. The central questions for this research were as follows:

→ What is the Al-Si interdiffusion rate in aluminium-bearing bridgmanite as a function of temperature (diffusion activation energy) at PT conditions in the upper part of the lower mantle?

→ How does Al-Si interdiffusion influence the Earth's lower mantle rheology?

The investigation of Al-Si interdiffusion was one of several essential issues to constrain the Earth's mantle rheology and improve Earth's mantle modelling. The diffusivity determined in this study was found to be $D_{Al\text{-}Si} = 4.2 \pm 0.9 \times 10^{-11} \exp[-400\ [kJ\ mol^{-1}]/RT]\ m^2/s$ *at 24 GPa. The Al-Si volume diffusion is 1 – 2 orders of magnitude slower than expected and seems to be the slowest diffusing species. Since the slowest diffusing species controls the creep mechanism, involving the stress and strain rate, our data allow us to make new estimates of the Earth's lower mantle's viscosity and reconsider existing models based on bridgmanite-dominant rheology in the lower mantle.*

The following conclusions can be drawn and perspectives proposed:

(1) For the first time, Al-Si interdiffusion coefficients in bridgmanite have been determined experimentally on Al-bearing polycrystalline bridgmanite samples at 24 GPa and a temperature range of 1,750 to 2,100 °C, which corresponds to conditions in the Earth's lower mantle.

(2) We demonstrated the reliability of the TEM analytic technique for diffusion experiments with very short diffusion profiles (50 to 120 nm). The diffusion coefficients obtained in this study would result in a diffusion profile below the detection limit for techniques like SIMS, which was widely used in previous studies. Another possible technique, Rutherford backscattering, cannot be used in the case of diffusion pair experiments as the diffusion zone must be investigated laterally and cannot be examined as a function of depth.

(3) From the temperature dependence in Figure 3.23 it can be seen that data sets ***a*** (stoichiometric) and ***b*** (Mg excess) cannot be distinguished within the experimental error due to different amounts of oxygen vacancies, so ***a*** and ***b*** were fitted as one data set. In addition, it can be speculated that the diffusion rate at higher Al content (data set ***c***) is an

order of magnitude faster than data sets ***a*** and ***b***. The plot of data set ***c*** is systematically higher, although it has only two data points.

(4) The diffusion coefficients were significantly lower in bridgmanite samples compared to Si and Mg self-diffusion and Fe-Mg interdiffusion studied previously, challenging the analysis of previous experimental diffusion profiles, based on observations of the present work. The previous analytical results could have been partly influenced by grain boundary diffusion due to the resolution because, as showed in this work, even a minimal influence of grain boundary diffusion controls the evaluations on volume diffusion coefficients due to a faster path on diffusion. Furthermore, the data can be used for understanding Al^{3+} substitution in bridgmanite. For this, the samples would have to be reprocessed and chemically investigated more closely and in more detail.

(5) The pre-exponential diffusion coefficient for Al-Si interdiffusion fitted from our data was found to be $D_0 = 4.2 \pm 0.9 \times 10^{-11}$ m^2/s on the assumption of an activation energy (E_A = 400 kJ/mol). This value is 1 to 2 orders of magnitude lower compared to self-diffusion coefficients of Si and Mg in bridgmanite and 1 to 2 orders of magnitude lower than the D_0 for Al-Si interdiffusion in majorite garnet.

(6) The temperature dependence of Al-Si interdiffusion has been investigated and extrapolated in the temperature range of 1,400 to 2,100 °C. The slope of T dependence in the Arrhenius plot was fixed to be - 4.8 (E_A = 400 kJ/mol), which is similar within uncertainty to the slope of Si and Mg self-diffusion and Fe-Mg interdiffusion of bridgmanite (Dobson *et al.*, 2008; Xu *et al.*, 2011; Yamazaki *et al.*, 2000). This behaviour shows that the temperature effect is similar for most of the discussed results. So, in summary, although this study reports slower diffusion rates, the activation energies are the same as those in previous studies.

(7) This study investigates the effect of mineral structure and finds that Al-Si interdiffusion is the slowest diffusion rate in the lower mantle as long as the Si is in a 6-coordinated mineral structure. This observation suggests that this type of diffusion controls the rheology of the lower mantle via the relationship between strain rate and viscosity.

(8) Surface treatment before and after (in case of SIMS because of the diffusion-depth profiles from the surface of the recovered sample) the diffusion experiment significantly influences the diffusion rate and the proper operation of analytical measurement methods such as TEM and SIMS.

(9) Our data were compared with previous studies such as Tusjino *et al.* (2022). Their estimated strain rate and stress from deformation experiments support the observed viscosity using deformation mechanism maps of bridgmanite. Consequently, bridgmanite dominates the rheology of the lower mantle, which means that bridgmanite acts as a limiting factor by aggregating with ferropericlase to control the viscosity of the lower mantle. Our data show slower diffusion than those of Tsujino *et al.* (2022) used in their modelling. Taking our data into account will lead to a higher viscosity in the lower mantle model. This, in turn, affects the heat and material exchange between the Earth's core and mantle.

(10) The experimental and analytical success of this study opens the possibility of applying experimental techniques used in this study to determine the activation volume via the pressure dependence to further constrain the parameters for calculating mantle rheology and make significant progress in estimating the viscosity of the lower mantle as input to models like Mitrovica & Forte (2004), Ricard & Wuming (1991).

Acknowledgements

First of all, I would like to thank Nobuyoshi Miyajima for trusting me to manage the German Research Foundation (DFG) project and for supporting me with great enthusiasm throughout my PhD process. Without his dedication and sense of urgency, I would not have been able to complete this project so quickly. I would also like to thank him for teaching me the TEM, which gave me a deep insight into a unique and exciting analytical method.

I would also like to thank Catherine McCammon, who has been a neutral and diplomatic mentor, helping me to grow in the project and encouraging me with her always positive feedback. Her experience and commitment to scientific research have inspired and encouraged me to pursue an academic career.

I am grateful to Dan Frost for his insightful comments and suggestions throughout my studies and for inspiring me with his ideas.

I want to acknowledge Raphael Njul and Alexander Rother for the excellent sample preparation, Heinz Fischer, and Stefan Übelhack for the high-quality high-pressure assemblies and cubes, Detlef Krausse for his IT support and Ulrike Trenz for her aid with the chemical laboratory. Furthermore, I want to acknowledge Christine Kellner, my scientific assistant, for evaluating my data via SEM and for her support.

I am incredibly grateful to my officemate Doro Wiesner for her kind assistance and guidance during long SEM and FIB sessions. I am also thankful for her and Tiziana Boffa Ballaran open ear and lovely support through all the obstacles I have overcome during my PhD. I want to thank Petra Buchert, Janina Potzel and Anna Dinius for their invaluable administrative help.

I sincerely thank Dagmar Martin and the CoMento team at the University of Bayreuth for their support and the fruitful discussion about my PhD's scientific field.

I am most thankful to all my colleague and friends, Sumith Abeykoon, Alex Kurnosov, Serena Dominijanni, Miriam Horn-Schott and Matthias Schott, Anna Ayeh, Giulia Marras (from Rome), Alena Krupp and Caterina Melai. Thank you all for the times you helped and encouraged me and for all the unforgettable moments we shared.
A special thanks to my family and friends Anja Sattler and Lorena Straub for everything they have done for me and their endless support and care.

And finally, thank you, my little girl Lara-Sophie, for always giving me the strength to overcome difficult times. With your help and your constant efforts to make me work on my big dream, I have achieved everything I (we) wanted to achieve in the last few years.

Danke, mein Liebling!

List of Figures

Figure 1.1: Crystal structure of bridgmanite (Mg, Fe)SiO_3 (space group Pbnm, #62). Red spheres represent oxygen (O) atoms, orange spheres represent magnesium (Mg) or iron (Fe) atoms, and blue spheres correspond to silicon (Si) atoms. The two cation positions of bridgmanite can be seen: the dodecahedral A-site substitution of Mg and the octahedral B-site substitution of Si. Figure by Merkel (2023). 3

Figure 1.2: Schematic drawing of three types of diffusion paths in polycrystalline materials. Surface diffusion is the motion of atoms or molecules on the solid surface matter. Volume diffusion is diffusion through the crystal lattices and is also called lattice diffusion. Grain boundary diffusion is relatively faster than bulk diffusion along individual grain boundaries. This is due to the gradient, as less energy must be expended to diffuse along a grain boundary than through the crystal lattice. Figure by Zhang (2017). 7

Figure 1.3: Substitution mechanism in ternary systems. Sample compositions along the $MgSiO_3$ – $AlAlO_3$ join (blue dashed line) produce bridgmanite samples that fall along the CCS trend line. Sample compositions with Mg > Si result in bridgmanite compositions (red dashed line) between the CCS and OVS trend lines. Figure modified after Liu et al. (2019, Figure 1). 9

Figure 1.4: (a) Si cation number of Brg versus the Al per formula unit based on three oxygens at 25 – 27 GPa and 1,600 – 1,727 °C. The CCS and OVS lines indicate the trend expected for trivalent cation substitution by charge-coupled or oxygen vacancies substitution mechanisms. Different starting bulk compositions were studied: Mg > Si for the orange circles and Mg = Si for the green ones. The data comes from Navrotsky et al. (2003b); Kojitani et al. (2007); Liu et al. (2017 a), and Liu et al. (2019 a, b). (b) Mole fraction of $MgAlO_{2.5}$ (red) and $AlAlO_3$ (blue) versus the Al per formula unit at 27 GPa and 1,727 °C. The data come from Liu et al. (2019 a, b). The lines were calculated based on the thermodynamic models. Figures by Huang (2020). 10

Figure 1.5: Point defect species in crystals. Vacancy defects are lattice sites in a crystal that would otherwise be occupied by a regular atom or ion. Interstitial defects are atoms such as the ones the crystal is made of that sit 'in the gap' between the regular atoms. Impurity atoms (green) or ions (light grey) are often incorporated into a crystal. These are neither vacant sites nor regular atoms on an interstitial site. The diffusion of impurity atoms does not require vacancies. Here the atoms jump directly from one interstitial site to the next. Interstitial impurity atoms, therefore, often diffuse faster than substitutional atoms. 11

Figure 1.6: Scheme of (a) edge dislocation and (b) screw dislocation. (a) Edge dislocation: The Burger's vector b (the movement of the planes through any translation vector of the grid) is perpendicular to the dislocation line. (b) Screw dislocation: The Burger's vector b is parallel to the dislocation line. Figure by Oswald (2019). 12

Figure 1.7: The Arrhenius plot is obtained by the linear relationship of ln D versus inverse temperature. The line helps find the missing variables of the Arrhenius equation. The slope gives the activation energy divided by the gas constant R, and the extrapolation of the line back to the y-intercept yields the value for ln D_0. 14

Figure 1.8: Creep by a diffusion mechanism modified after Bhadeshia (2003). Grain boundaries are sinks and sources of vacancies. Vacancies move in the crystal lattice from regions with low tension σ to regions with higher tension. 18

Figure 1.9: A second range of the creeping stage: range of constant/minimal strain rate with a dynamic equilibrium of strain hardening and softening (overcoming obstacles due to increased temperatures). Creep rate is an exponential function of temperature T and depends on external stress σ via a power law (see Equation 1.15). Creep exponent modified after Bürgel et al. (1998). 19

Figure 1.10: The mantle can flow like a viscous fluid at the geological time scale. This is influenced by the creep mechanism, which involves the motion of the atoms between crystals and their defects. This work focuses on elemental diffusion at the nanometre scale. It could, in the future, contribute to the modelling of bulk diffusion in the lower mantle, allowing the consequences for different Earth models to be considered. 20

Figure 1.11: Viscosity models with depth from Amman (2011). Models were derived by inversion of geophysical data and involve different datasets, inversion techniques and observables: (1) (Hager & Richards, 1989), (2) (Forte & Mitrovica, 1996), (3) (Ricard & Wuming, 1991) (4) (Steinberger & Calderwood, 2001), (5) (McNamara et al., 2003) (6) (Mitrovica & Forte, 2004) and (7) (Forte & Mitrovica, 2001). 21

Figure 1.12: Calculated viscosity of perovskite in the lower mantle by Ammann (2011) based on his absolute diffusion results. The viscosity profile was calculated for the lower mantle using 100 % $MgSiO_3$ perovskites (curved) composition. Regarding upper bounds, he assumed the vacancy concentration $N_V = 2 \times 10^{-5} mm^{-1}$ for a grain size of 1 mm and for a grain size (G) of 0.1 mm a vacancy concentration of 2×10^{-7} mm^{-1}. The lower bound corresponds to $N_V = 2 \times 10^{-3}$ mm^{-1} (G = 1 mm) and $N_V = 2 \times 10^{-5}$ mm^{-1} (G = 0.1 mm), which is two orders of magnitude greater than the upper bound (for the same grain size). The geotherm was derived from Stacey (1995) and Stacey & Davis (2008). Superimposed

on his predicted viscosity profile is that obtained by Mitrovica & Forte (2004) from a join inversion of convection and glacial rebound data. 22

Figure 2.1: Synthesis of polycrystalline bridgmanite from pre-synthesized enstatite. The Brg diffusion couples for the interdiffusion experiments were synthesised from 1 – 5 mol % Al_2O_3-bearing $MgSiO_3$ enstatite at 24 GPa and 1,750 – 2,000 °C, using conventional multi-anvil apparatuses. See section 2.2.2. 28

Figure 2.2: Experimental conditions for 0, 3 and 5 mol % Al_2O_3 bridgmanite at MA high-pressure experiments. Blue star: 95 mol % $MgSiO_3$ + 5 mol % Al_2O_3 (En95Cor5) starting material; Yellow stars: En100 and En97Cor3 starting materials. Figure by Akaogi & Ito (1999). 29

Figure 2.3: Schematic setups/Cross-section of the 7/3 assembly types used for diffusion experiments and polycrystalline sample syntheses. The 7/3 assembly (a) has been used for most experiments. D-type thermocouples were inserted into all assemblies but mostly failed at reading the temperature at assembly method (b). (a) the right side shows the recovered sample after the S7791 run. (c) shows the same layout as (a) except for the fused Si capillaries in the heater to isolate the TC from the heater. 30

Figure 2.4: Power-temperature correlation calculated via consistently stable and readable temperatures through the TC of 16 multi-anvil experiments from this study and 7 multi-anvil experiments from Greta Rustioni (pers. comm.) at the same PT conditions and assembly size. The red fitting curve of the second- order polynomial equation was calculated by least-squares fitting ($y = 0.0071\ x^2 + 2.226\ x + 44.803$). 32

Figure 2.5: Drawing of a diffusion experiment. The bridgmanite sample after synthesis is shown on the left. The sample was cut into three pieces and each piece was polished with colloidal silica. In the middle, the shapes of cylinders with a diameter of 250 µm and a height of 250 µm are indicated for further processing. Two cylinders can be cut from a sample disk. One of these cylinders was inserted into the experimental setup on the right. In this case it was the Al-free bridgmanite sample. The same procedure was followed for the Al-bearing bridgmanite samples. 34

Figure 2.6: Photo of the Philips X'Pert powder diffractometer located in BGI Bayreuth. Equipment with a high-intensity ceramic sealed tube (3 kW) characterised the glass and orthopyroxene starting materials using an energy-dispersive system. 35

Figure 2.7: To maximally amplify each other (interfere constructively), two waves must be in the same phase. In the case of reflection from a thin crystal lattice with lattice spacing d, this is only the case for two waves arriving in the same phase if the additional distance l that a wave travels because it is reflected only at the second lattice plane is a multiple of the wavelength λ. The difference in path length l between the two waves depends on the angle of incidence θ of the wave and the distance d of the lattice planes. The incident and scattered X-rays in Bragg condition reflected from the plane (hkl) with d spacing d_{hkl} at a scattering angle of θ. This image has been modified from Putnis (1992).....36
Figure 2.8: Powder diffraction pattern obtained from the different starting materials. Quartz and orthoenstatite are the identified phases by CrystalDiffrac 6. 37
Figure 2.9: Powder diffraction pattern collected by Bruker. The pattern shows the En100 endmember is composed of clino- and orthoenstatite.....38
Figure 2.10: Micro X-ray diffraction of Pyrope. Phase identification was made via diffract.eva and compared with the diffraction pattern from the COD database. 39
Figure 2.11: Left: Raman spectrum of bridgmanite sample collected from Pos1 (black), Pos2 (red) and Pos3 (blue). Right: Optical image of the collected sample. For all images applies: Pos1 –> Al-free part of the sample. Pos2 –> Al rich part of the sample. Pos3 –> Central position of the sample. Data were compared with data from Liu et al. (1995). .41
Figure 2.12: Illustration of the phenomena that occur from the interaction of highly energetic electrons with matter. Various types of signals are generated as a result of electron–matter interactions. Also depicted is the pear shape interaction volume, which is typically observed in this type of interaction. Figure by ThermoFisher Scientific, (2022). 43
Figure 2.13: SEM images of the Al-free bridgmanite (Brg) sample S7381. (a) and (c) are orientated contrast images of the left-sided sample. (b) and (d) are orientated contrast images of the right-sided sample. The top-middle inset is an overview SE image. Orientated contrast images were made to estimate the grain sizes in the samples. 44
Figure 2.14: Schematic drawing of the commonly found dual beam FIB-SEM instrument. (a) FIB/ SEMs combine an SEM and a FIB in a single device and are often equipped with multiple detectors incl., SE, BSE, EDX, EBSD and in-lens detectors as well as a gas injection system. (b) shows the milling process with the Ga^+ beam. Inspired by Rigort & Plitzko, (2015).....45
Figure 2.15: Scanning electron microscopy images showing the cutting process on recovered MA samples in the FIB. (a) SE image showing trenches before cutting the lamella. (b) Cut off of the lamella and transfer procedure using a needle micromanipulator. (c)

Untreated lamella fixed to the copper grid. (d) Ga^+ beam image showing final lamella before “ion shower”. 47
Figure 2.16: Photograph of a transmission electron microscope Titan G2 at BGI with associated sketch modified by © wikipedia.com/Gringer. 49
Figure 2.17: Physical relation between the distance to the object S, the size of the object y and the angle of vision σ to see an object in focus and its entirety. Modified after Thomas & Gemming (2013)..... 50
Figure 2.18: Drawing showing how to adjust the objective aperture and lens to produce a BF image (a), a displaced-aperture DF image (b) and a centred dark-field image (c) where the diffracted beam emerges on the optical axis by tilting the incident beam. Figure modified after Williams & Carter (2009), p. 156. 52
Figure 2.19: Bright field image of sample S7808_L2 with dislocations and bending contours in bridgmanite crystals. Recorded in TEM mode on the Titan G2 at the BGI. 53
Figure 2.20: (a) Bright field and (b) Dark field of the Al bearing enstatite (En) sample B1288 with stacking faults or twin lamellae (red arrow) and dislocations (yellow arrow). 54
Figure 2.21: (a) Inverse diffraction pattern of the crystal on the right side in the bright field image. The central spot, marked by the yellow arrow, represents the direct beam. The crystal in figure (b) is centred under the beam and marked by a retractable arrow (beam stopper) on the TEM. 55
Figure 2.22: EDX-map of the pyrope starting material. Green boxes show the position of the spectra from the chemical map, displaying the thin part of the TEM sample (right side) to the thick part of the TEM sample (reddish left side). 56
Figure 2.23: Scheme of step-by-step evaluation of a diffusion experiment. In SEM image (a), the diffusion interface is shown as a dashed white line. The black bar represents the sampling position of the FIB sample. The HAADF STEM image (b) shows an overview of a diffusion lamella with the diffusion interface indicated as a white dashed line and the map position in black. In image (c), the EDX map is superimposed on the HAADF image of the sample position. It also shows how the line scan is aligned in the sample (yellow). The last image (d) shows the element concentration of each spectrum (red dots) of the line scan evaluation. It shows the diffusion profile for this sample in an Excel graph. . 59
Figure 2.24: Hypermap with 40 spectra to measure the diffusion coefficient manually. For this purpose, individual rectangles of approximately the same size are stretched in a line. Boxes are used instead of points to increase the information density and to generate a representative result. 60

Figure 2.25: QMap of the element Al in atomic percentages. Magnification 20 kx. Line scan covered the whole map height to generate high information depth. 61
Figure 2.26: The diffusion profile of sample S7835 is fitted by the diffusion Equation (2.5) in an Excel spreadsheet. Cation diffusion of aluminium occurred between endmember bridgmanite and 3 mol % Al_2O_3 bridgmanite at 24 GPa and 1808 °C for 21 h. The black points represent the measured data points. The blue dashed line shows the data calculation by the Crank equation implemented by the Solver function in Excel. 62
Figure 2.27: Diffusion profiles of $Si^{4+} + Mg^{2+} = 2Al^{3+}$. (a) shows the TEM-EDXX map of S7835. The yellowish part is Al-bearing diffusion couple; the bluish part shows the endmember En100. The yellow line with the rectangle represents the line scan area and includes all spectra data in this rectangle. The HAADF images show the map location marked in red. (b) shows sigmoidal diffusion profiles calculated by the PACE software (Jollands, 2020) with FWHM = 26.4 nm and the diffusion coefficient of its profiles. Experimental data: En97Cor3, 24 GPa, 1,808 °C for 21 annealing hours. Both lines coincide within the line thickness and can hardly be distinguished in this plot. 63
Figure 2.28: Cross-section of an irradiated TEM sample and visualizes beam broadening. With the electron density distribution and hatched volume around the primary beam in the way proposed by (Van Cappellen & Schmitz, 1992) to define the Spatial resolution of EDXS in the section with z as defining coordinate of the distance from the foils top surface in a direction parallel to the incident beam. The dark grey box contains 50 % of X-ray intensity if q = 2.35 and intersects with the hatched volume at a depth κt. 64
Figure 2.29: Procedure for FWHM determination. First: find a mechanical interface, like the Sti-Brg interface in (a). Second: Determine the beam size from a Gaussian convoluted profile using PACE-GD (b), showing the Si concentration profile with the corresponding sigma and FWHM values, which are extracted the beam size from a Gaussian convoluted profile and used for the third step). Third: Apply to deconvoluted diffusion profiles with calculated diffusion coefficient (c). In this case, S7835_L1 was annealed at 1,808 °C for 21 h. 66

Figure 3.1: Determination of the k-factors $k_{Mg,Si}$, $k_{Al,Si}$ and $k_{O,Si}$ by using a standard of synthetic pyrope. Calculating by 69
Figure 3.2: Typical EDX spectrum of the stoichiometric standard pyrope sample. 70

Figure 3.3: EDX spectra were measured in the green squares for the EDX analysis to test the k-factors in the B1288 sample. 71
Figure 3.4: Images and graphs intended to show the influence of the amorphous layer/grain boundary effect. This amorphous grain boundary layer has the same width (~ 50 nm) as the one at the diffusion interface of the same sample (white dashed line). (a) shows the EDX map of the sample S7843 and the HAADF image. The yellow box indicates the line scan perpendicular to the grain boundary between Brg and Sti, and the red box shows the EDX map position in the sample. (b) and (c) display the Si and Mg concentration profiles along the line scan. The PACE software calculated the sigma values and FWHM. The FWHM value gave the diameter at half the height of the intensity distribution. 74
Figure 3.5: Calculated FWHM values related to the sample thickness and determined by the same method as the diffusion profiles. The individual data points are highly scattered and therefore, not uniformly correlated (blue regression line). Therefore, two regression lines were constructed to cover the scattering data points' upper and lower limits. 75
Figure 3.6: Optical microscope image of sample S7761b. Yellow arrows indicate stishovite crystals with a darkish margin. The glass spacers are used to polish the sample evenly during the polishing process and provide stability during polishing. The sample is already 250 µm thick after cutting and is divided into two 250 µm diameter disks after the polishing process. 76
Figure 3.7: Bright-field TEM image of a surface sample. The black part is the Pt protective deposition on top. Directly below the protective film, the amorphous layer of carbon evaporation deposition can be seen. Underneath are crystalline bridgmanite crystals separated by a visible amorphous grain boundary. The radiation of the electron beam forms this amorphous grain boundary. No defects or dislocations are visible..... 77
Figure 3.8: Example diffusion profile, divided into three parts. The blue-shaded part represents the Al-bearing bridgmanite before the diffusion experiment. The yellow shaded area shows the actual diffusion profile. The green shaded area corresponds to the Al-free endmember before the diffusion experiment. For the ternary diagram, all data of the diffusion profile were converted to an Al content ≙ 0 of the Al-free endmember. 78
Figure 3.9: Ternary diagram of bridgmanite in the Mg-Al-Si system (at. %) with the separated data of each part in the diffusion profile. CCS: charge-coupled substitution line. OVS: oxygen vacancy substitution line. Composition data are from TEM analysis with the different starting materials. Full symbols relate to data from the diffusion experiment (shown in yellow in Figure 3.8). Symbols with a half-filled upper part represent the Al-

bearing bridgmanite samples (blue in Figure 3.8) and symbols with half-filled lower part represents the Al-free endmember (green in Figure 3.8). 79
Figure 3.10: Final ternary diagram including estimated uncertainties for four data points. These four data points serve as examples to provide a rough estimation of uncertainties. CCS: charge-coupled substitution line. OVS: oxygen vacancy substitution line. The stoichiometric samples are approximately on the CCS line considering the large uncertainties. Additional data points from the SEM analysis were added to this diagram (S7766 + H5548), indicated by the open hexagon shape. The large uncertainties are caused by the high analytical error of the absolute chemical values from the EDX analysis and do not apply to the relative determination of the Al concentration evaluation. 81
Figure 3.11: SE view of S7828 with associated chemical analysis of the lower sample area. Darker areas can be seen on the left-hand side. These areas were analysed in an EDX measurement to determine the chemical composition of this sample. As can be seen, sample S7828 contains Ag rich impurities which are removed during further sample preparation. In addition, two spectra were carried out to determine the chemical composition of the surrounding material. As expected, it was bridgmanite and the sample could be used for further work. 83
Figure 3.12: Detailed SE image of S7614 to estimate the grain size and wt. % of the secondary phase stishovite. It can be seen that the beam damage has already partially amorphized the grain boundaries and crystal grains, causing them to appear elevated in the image. This happens when radiation is too long and too strong. Since stishovite is more resistant to the beam, the grains show a clear relief. 84
Figure 3.13: Process during SEM observation of diffusion experiment S7828. (a) shows an overview image. This is enlarged as (b) and (c) show. (b) offers a more detailed overview image and provides an overview of the diffusion interface. (c) is a detailed image of the interface of the two diffusion couples and is used to get an impression of the contact between the two samples and to see if decompression cracks have developed. 85
Figure 3.14: SEM image in SE mode at the lowest possible magnification (S7808). The view is through the aperture. The intact sample with heater, filling material (MgO), thermocouple and the Pt case with the sample in the centre can be seen. 86
Figure 3.15: Overview of the S7808 sample. Visible are the diffusion interface and Pt surface impurities in the sample, which were created during polishing. In addition, bridgmanite mineral grains are visible in the enlarged image due to the longer exposure time. The

enlarged detail image of S7808 shows the perfect placement for a FIB lamella on the right. 86
Figure 3.16: Superimposed chemical evaluation of the Al content in sample S7808 for the line scan (yellow), also shown in green in Figure 3.15. The relative Al concentration profile is shown in red. 87
Figure 3.17: (a) HAADF image in which the freshly created EDX map (in the image (b)) is shown as a green box. An EDX analysis has already been carried out, indicated by the measurement spot in the upper middle area (orange box) in the image (a). Cracked carbon deposits cause such measurement spots. (b) QuantMap with line scan of sample S7835. The line scan is perpendicular to the diffusion interface (white dashed line) and is shorter than the map height because the crystal boundary is convex. 88
Figure 3.18: Ideal diffusion profile with many data points along the diffusion path (S7835). The data points represent the measured relative aluminium concentration. The dark line shows the data calculation by the Crank equation implemented by the Solver function in Excel. 89
Figure 3.19: Two spectra measured for 0-60 sec and 60-120 sec, respectively, in the same sample. The green spectrum represents an optimal spectrum of the stoichiometric sample. The black spectrum indicates a light Mg-loss. 90
Figure 3.20: The relationship between the diffusion coefficients and the temperature read during the experiment (Temperature T_{exp}) and the temperature calculated from the power-temperature relationship (Temperature T_{calc}). a) shows the diffusion coefficient (Excel $\log_{10}(D)$) versus the temperature read from the working TC or estimated temperature (from previous experiments at same PT conditions). The black dot indicates the 5 experiments that did not have a fully functional thermocouple and where the temperature was estimated. b) shows the diffusion coefficient vs. the calculated temperature from 23 successfully performed experiments with a fully functional thermocouple. 97
Figure 3.21: Correlation between diffusion coefficients and temperature. To do this, all four calculated diffusion coefficients were plotted against temperature. The largest markers represent the convolute diffusion coefficients calculated using the Crank equation and the solver function of Excel. The smaller markers represent the deconvoluted diffusion coefficients determined using the software PACE, considering the different Gaussian beam widths during the chemical analysis using the STEM. These deconvoluted diffusion coefficients have been averaged for simplicity and are shown as bright small markers. 99

Figure 3.22: Comparison of the deconvoluted diffusion coefficient and aluminium content. Diffusion coefficients were calculated from deconvoluted average data shown in Table 3-6. 100

Figure 3.23: Comparison of diffusion coefficients and temperature as a function of chemical composition. The slope was fixed at - 4.8, corresponding to E_A=400 kJ/mol. No clear statement can be made about the differences due to chemistry. Data points S7596 and S7808 were excluded from the fit as the experiments were performed at the lowest temperature and times of 1 h and 3 h, respectively, making them unreliable as equilibrium was most likely not reached. Experiment S7842 was included in the fit as the diffusion time was increased to 21 hours for the lowest temperature. The dashed linear regression (Al effect) was calculated from the blue data set with the same slope as for the other linear regression (Si driven diffusion). It is assumed that an increased Al content influences the diffusion behaviour in bridgmanite and therefore the data with increased Al content are considered separately in this plot. 102

Figure 3.24: Overview of the whole capsule of diffusion experiments S7766 and H5548. The capsule from S7766 (a) no longer has a rectangular shape and looks pitted. This is unusual compared to the other experiments. Compared to this, the capsule from diffusion experiment H5548 (b) indicates a typical shape. In this SE image, the whole experiment setup is shown, with TC, heater and MgO spacers. 104

Figure 3.25: Overview images of diffusion experiments S7766 (a) and H5548 (b). Both samples look partially melted. In sample S7766, the original diffusion couples are no longer visible. In sample H5548, the diffusion interface can still be guessed at, marked here by the white dashed line. 105

Figure 3.26: Parts of the TEM lamella from samples S7766 and H5548 with associated diffraction pattern. This shows that the bridgmanite sample is crystalline with ~ 5 – 10 times bigger crystal sizes than in the other diffusion experiments. 105

Figure 3.27: Optical microscope image of S7766. It suggests that the sample lies tilted in the Pt capsule and was polished at an angle, which is why the diffusion profile became longer. Because En100 measured in the EDX is on the far-left edge. This sample was ground to 5/8 to expose the diffusion pair fully. The dark rectangular region in the sample represents the FIB sample. This was taken on the side containing aluminium, as it was initially thought that the diffusion interface would be in the middle of the diffusion pair, as in all other diffusion experiments. It was decided not to take another sample because the Al profile was longer than the length of a FIB lamella. 106

Figure 3.28: Example of a chemical analysis of sample S7766 along the whole sample using a line scan. The upper image shows the SE image together with the line scan. The lower graph shows the Al profile in counts per second vs distance. A clear Al gradient can be seen. The peaks correspond to places where the line scan was placed over stishovite (SiO_2) or corundum (Al_2O_3) and thus contains either a little or a lot of Al..... 107

Figure 3.29: (a) Overview image of the EDX analysis of experiment S7766. Line scans (white lines) perpendicular to the grain boundary were measured to assess the Al content along the grain boundary. A gradient can be seen from the interior of the mineral grain to the mineral boundary. Additionally, maps (white and red boxes) were taken for the same purpose. (b) Enlargement to assess the SEM resolution. Each point in the line scan and the map has measured a spectrum. This corresponds to a resolution of 0.7 µm (10 µm = 14 spectra) for the line scan and 0.55 µm (10 µm = 18 spectra) for the map in the picture above left. 108

Figure 3.30: Line scans 1 and 2 marked in yellow corresponding to the white lines 2 and 3 in Figure 3.29 of sample S7766. Underneath the SE images, the element concentrations can be seen for oxygen (green), magnesium (blue), silicon (yellow) and aluminium (red). 109

Figure 3.31: Al content measurements of stishovite and bridgmanite in S7766. Individual spectra, as well as maps in different areas of the sample are indicated by crosses and boxes. Only the stishovite grains were used for evaluation. 110

Figure 3.32: Plot of Al content in the stishovite grains against the calculated temperature. Data were collected with TEM and SEM often in the same samples. It is noticeable that the analytical data for the same samples are sometimes different..... 111

Figure 4.1: Overview of the data that were compared in the discussion. The Arrhenius plot includes all data points of the averaged deconvoluted diffusion coefficients and shows the Al-Si interdiffusion data from this study in dark red at 24 GPa. The blue scale coloured data points represent all diffusion data from bridgmanite studies (excluding our data) at 25 GPa, and greyscale indicates Mg and Si self-diffusion coefficients in majoritic garnet from previous studies at 15 and 17 GPa. The red line shows Si self-diffusion in stishovite at 25 GPa. The lines of corresponding colours represent the linear fits of the literature data, in order to highlight the difference at any temperature in the range of interest... 115

Figure 4.2: Plot (log D_0 vs E_A) for atomic diffusion in lower mantle silicate minerals including bridgmanite (Brg), stishovite (Sti) and majoritic garnet (Maj). The diffusion data from this study are compared with previously published data in the context of their analytical methods such as TEM and SIMS. Majoritic garnet (dark red) was experimentally investigated at 15 and 17 GPa and Sti and Brg at 24 and 25 GPa. It is assumed that an increased Al content influences the diffusion behaviour in bridgmanite and therefore the data with increased Al content are denoted as "Al effect in Brg" on the plot. Details on determination of D_0 for dataset with increased Al content are given in 3.2.4. 117

Figure 4.3: Comparison of all diffusion experiments. S7766 and H5548 are averaged convoluted diffusion coefficients and the other data points are averaged deconvoluted diffusion coefficients. It can be seen that S7766 and H5548 are outliers with up to 6 orders of magnitude faster diffusion rates, properly caused by the influence of grain boundary diffusion in these samples. 119

Figure 4.4: Arrhenius plot of all data points of the averaged deconvoluted diffusion coefficients. Data from this study are shown in dark red, except for the stoichiometric data with higher Al content (brighter red). Light blue and blue data points represent Fe-Mg interdiffusion in bridgmanite at different oxidation state. 121

Figure 4.5: Arrhenius plot of all data points of the averaged deconvoluted diffusion coefficients. Al- Si interdiffusion data from this study are shown in dark red. The plot compares the diffusion results with data of majorite garnet at 17 GPa from Nishi et al. (2013) and at 15 GPa from Van Mierlo et al. (2013). 122

Figure 4.6: Direct comparison of diffusion data from previous studies used to calculate lower mantle viscosity models and the diffusion data from this study. Again, it can be seen that the linear relations between the data have a difference of 2 orders of magnitude. 131

Figure 4.7: Effect of temperature on the Al_2O_3 content in Sti. The uncertainty in the temperature measurement is calculated by the analytical error. The Al_2O_3 content in Sti has been fitted compared to previous studies on anhydrous stishovite (Liu et al., 2006). The lines are drawn according to a calculated polynomial by Liu et al. (2006). 132

List of Tables

Table 2-1: Chemical compositions of the diffusion couples before the experiment, analysed by TEM and calculated from the absolute element concentrations. The detailed data are given in Appendix A, Table 3. 27

Table 2-2: Overview of the pre-synthesis conditions, including the experimental conditions and source material pyrope (Prp), enstatite (En) and corundum (Cor) in different mixture volumes. For these experiments the thermocouple (TC) worked in every synthesis. 33

Table 2-3: Multi-anvil diffusion experiments in 7/3 assemblies at 24 GPa. Listed with experimental conditions and source material pyrope (Prp), enstatite (En), brownmillerite (Brm) and corundum (Cor) in different mixture volumes. The thermocouple (TC) did not work in every diffusion experiment. TC worked? – Yes "y", no "n" or worked partly "y/n". 33

Table 3-1 Summary of successful diffusion experiments in 7/3 assembly at 24 GPa. The table indicates if the temperature measurement via the TC worked, what experimental temperature was reached or estimated, and what power was applied. Additionally, the calculated temperature is shown derived from the temperature-power relation. The last column shows the annealing time. 68

Table 3-2: Summary of the k-factors for Mg, Al, O and their mean values determined on standards, using the FEI Titan G2, BGI, operating at 200 kV, t = 0. 72

Table 3-3: Chemical analysis of B1288 corrected by the previously calculated k-factors of the known sample pyrope. 72

Table 3-4: Diffusion coefficients calculated by the Crank equation in Excel from the raw data from the EDX Maps. 91

Table 3-5: Deconvoluted diffusion coefficients calculated by the Crank equation in PACE from the raw data from the EDX Maps. Several estimated coefficients per sample were summarised to calculate the diffusion coefficients, and a standard deviation of the individual results was calculated. 93

Table 3-6: Summary table of all diffusion experiments and associated results of convoluted diffusion coefficients (Excel), deconvoluted diffusion coefficients calculated by the PACE software, the average of the deconvoluted PACE diffusion coefficients (deconvoluted diffusion coef.) and further analytical results like the Mg/Si ratio and the oxygen vacancy

(OV) and charge – couple (CC) substitution data calculated from the absolute data from the EDX measurements at the STEM. 94

Table 4-1: Comparison of pre-exponential factors and activation energies from this study and previous studies of different mantle minerals at comparable pressures. 114

List of References

Akaogi, M. (2022). High-Pressure Silicates and Oxides: Phase Transition and Thermodynamics. Springer Nature.

Akaogi, M., & Ito, E. (1999). Calorimetric study on majorite–perovskite transition in the system $Mg_4Si_4O_{12}$–$Mg_3Al_2Si_3O_{12}$: transition boundaries with positive pressure–temperature slopes. Physics of the Earth and Planetary Interiors, 114(3-4), 129-140.

Ammann, M. W. (2011). Diffusion in minerals of the Earth's lower mantle: constraining rheology from first principles (Doctoral dissertation, UCL (University College London)).

Ammann, M. W., Brodholt, J. P., & Dobson, D. P. (2009). DFT study of migration enthalpies in $MgSiO_3$ perovskite. Physics and Chemistry of Minerals, 36(3), 151-158.

Andrault, D., Bolfan-Casanova, N., Bouhifd, M. A., Guignot, N., & Kawamoto, T. (2007). The role of Al-defects on the equation of state of Al–(Mg, Fe) SiO_3 perovskite. Earth and Planetary Science Letters, 263(3-4), 167-179.

Becerro, A. I., McCammon, C., Langenhorst, F., Seifert, F., & Angel, R. (1999). Oxygen vacancy ordering in $CaTiO_3$–$CaFeO_{2.5}$ perovskites: From isolated defects to infinite sheets. Phase Transitions, 69(1), 133-146.

Bejina, F., & Jaoul, O. (1997). Silicon diffusion in silicate minerals. Earth and Planetary Science Letters, 153(3-4), 229-238.

Bhadeshia, H. K. D. H. (2003). Mechanisms and models for creep deformation and rupture. In Milne, I., Ritchie, R. O., & Karihaloo, B. L. (Eds.), Comprehensive structural integrity: Cyclic loading and fatigue (Vol. 4, 1-23). Elsevier.

Borg, R. J., & Dienes, G. J. (1988). III–Mechanisms of Diffusion. An Introduction to Solid State Diffusion, 53-77. Elsevier.

Brassart, L., & Delannay, F. (2019). Bounds for shear viscosity in Nabarro–Herring–Coble creep. Mechanics of Materials, 137, 103106.

Brodholt, J. P. (2000). Pressure-induced changes in the compression mechanism of aluminous perovskite in the Earth's mantle. Nature, 407(6804), 620-622.

Bunge, H. P., Richards, M. A., & Baumgardner, J. R. (1996). Effect of depth-dependent viscosity on the planform of mantle convection. Nature, 379(6564), 436-438.

Bürgel, R., Bürgel, R., Maier, H. J., & Niendorf, T. (1998). Handbuch Hochtemperatur-Werkstofftechnik. Wiesbaden: Vieweg+ Teubner Verlag.

Chadwick, A. V., & Terenzi, M. (2013). Defects in Solids: Modern Techniques. Springer Science & Business Media.

Chakraborty, S. (1997). Rates and mechanisms of Fe-Mg interdiffusion in olivine at 980°–1300°C. Journal of Geophysical Research: Solid Earth, 102(B6), 12317-12331.

Chakraborty, S. (2008). Diffusion in solid silicates: a tool to track timescales of processes comes of age. Annual review of Earth and planetary sciences, 36(1), 153-190.

Chakraborty, S. (2010). Diffusion coefficients in olivine, wadsleyite and ringwoodite. Reviews in Mineralogy and Geochemistry, 72(1), 603-639.

Chateigner, D., Chen, X., Ciriotti, M., Downs, R. T., Gražulis, S., Kaminsky, W., Le Bail, A., Lutterotti, L., Matsushita, Y., Merkys, A., Moeck, P., Murray-Rust, P., Quirós Olozábal, M., Rajan, H., Baitkus, A. & Yokochi, A. F. T. (2014). Open-access collection of crystal structures of organic, inorganic, metal-organic compounds and minerals, excluding biopolymers. Crystallography Open Database. Retrieved January 16, 2023, from http://www.crystallography.net/cod/

Cherniak, D. J., & Watson, E. B. (2019). Al and Si diffusion in rutile. American Mineralogist: Journal of Earth and Planetary Materials, 104(11), 1638-1649.

Cliff, G., & Lorimer, G. W. (1975). The quantitative analysis of thin specimens. Journal of Microscopy, 103(2), 203-207.

Coble, R.L. (1963). A Model for Boundary Diffusion Controlled Creep in Polycrystalline Materials. Journal of Applied Physics 34(6), 1679-1682.

Cocks, A. C. F. (1996). Variational principles, numerical schemes and bounding theorems for deformation by Nabarro-Herring creep. Journal of the Mechanics and Physics of Solids, 44(9), 1429-1452.

Costa, F., & Chakraborty, S. (2008). The effect of water on Si and O diffusion rates in olivine and implications for transport properties and processes in the upper mantle. Physics of the Earth and Planetary Interiors, 166(1-2), 11-29.

Crank, J., & Gupta, R. S. (1975). Isotherm migration method in two dimensions. International Journal of Heat and Mass Transfer, 18(9), 1101-1107.

De Graef, M. (2003). Introduction to conventional transmission electron microscopy. Cambridge university press.

Dobson, D. P., Dohmen, R., & Wiedenbeck, M. (2008). Self-diffusion of oxygen and silicon in $MgSiO_3$ perovskite. Earth and Planetary Science Letters, 270(1-2), 125-129.

Dohmen, R., Chakraborty, S., & Becker, H. W. (2002). Si and O diffusion in olivine and implications for characterizing plastic flow in the mantle. Geophysical research letters, 29(21), 26-1.

Elliott, D. (1973). Diffusion flow laws in metamorphic rocks. Geological Society of America Bulletin, 84(8), 2645-2664.

Eswara, S., Pshenova, A., Yedra, L., Hoang, Q. H., Lovric, J., Philipp, P., & Wirtz, T. (2019). Correlative microscopy combining transmission electron microscopy and secondary ion mass spectrometry: A general review on the state-of-the-art, recent developments, and prospects. Applied Physics Reviews, 6(2), 021312.

Farber, D. L., Williams, Q., & Ryerson, F. J. (2000). Divalent cation diffusion in Mg_2SiO_4 spinel (ringwoodite), β phase (wadsleyite), and olivine: Implications for the electrical conductivity of the mantle. Journal of Geophysical Research, 105(B1), 513-529.

Fei, H., Faul, U., & Katsura, T. (2021). The grain growth kinetics of bridgmanite at the topmost lower mantle. Earth and Planetary Science Letters, 561, 116820.

Fick, A. (1855a). V. On liquid diffusion. The London, Edinburgh, and Dublin Philosophical Magazine and Journal of Science, 10(63), 30-39.

Fick, A. (1855b). Über Diffusion. Annalen der Physik, 170(1), 59-86.

Forte, A. M., & Mitrovica, J. X. (1996). New inferences of mantle viscosity from joint inversion of long-wavelength mantle convection and post-glacial rebound data. Geophysical Research Letters, 23(10), 1147-1150.

Forte, A. M., & Mitrovica, J. X. (2001). Deep-mantle high-viscosity flow and thermochemical structure inferred from seismic and geodynamic data. Nature, 410(6832), 1049-1056.

Frost, H. J., & Ashby, M. F. (1982). Deformation-mechanism maps: the plasticity and creep of metals and ceramics. Oxford: Pergamon Press.

Frost, D. J., & Langenhorst, F. (2002). The effect of Al2O3 on Fe–Mg partitioning between magnesiowüstite and magnesium silicate perovskite. *Earth and Planetary Science Letters*, *199*(1-2), 227-241.

Gillet, P., Daniel, I., Guyot, F., Matas, J., & Chervin, J. C. (2000). A thermodynamic model for $MgSiO_3$-perovskite derived from pressure, temperature and volume dependence of the Raman mode frequencies. Physics of the Earth and Planetary Interiors, 117(1-4), 361-384.

Girard, J., Amulele, G., Farla, R., Mohiuddin, A., & Karato, S. I. (2016). Shear deformation of bridgmanite and magnesiowüstite aggregates at lower mantle conditions. Science, 351(6269), 144-147.

Glazer, A. M. (1972). The classification of tilted octahedra in perovskites. Acta Crystallographica Section B: Structural Crystallography and Crystal Chemistry, 28(11), 3384-3392.

Glišović, P., Forte, A. M., & Ammann, M. W. (2015). Variations in grain size and viscosity based on vacancy diffusion in minerals, seismic tomography, and geodynamically inferred mantle rheology. Geophysical Research Letters, 42(15), 6278-6286.

Goldstein, J. I., Newbury, D. E., Michael, J. R., Ritchie, N. W., Scott, J. H. J., & Joy, D. C. (2018). Scanning Electron Microscopy and X-Ray Microanalysis. Springer, New York, NY.

Grüninger, H., Liu, Z., Siegel, R., Boffa Ballaran, T., Katsura, T., Senker, J., & Frost, D. J. (2019). Oxygen vacancy ordering in aluminous bridgmanite in the Earth's lower mantle. Geophysical Research Letters, 46(15), 8731-8740.

Hager, B. H., & Richards, M. A. (1989). Long-wavelength variations in Earth's geoid: physical models and dynamical implications. Philosophical Transactions of the Royal Society of London. Series A, Mathematical and Physical Sciences, 328(1599), 309-327.

Hazen, R. M., & Finger, L. W. (1978). Crystal structures and compressibilities of pyrope and grossular to 60 kbar. American Mineralogist, 63(3-4), 297-303.

Hemley, R. J., & Cohen, R. E. (1992). Silicate perovskite. Annual Review of Earth and Planetary Sciences, 20, 553.

Herring, C. (1950). Diffusional Viscosity of a Polycrystalline Solid. Journal of Applied Physics, 21(5), 437-445.

Herzig, C., & Mishin, Y. (2005). Grain boundary diffusion in metals. In Diffusion in condensed matter (pp. 337-366). Springer, Berlin, Heidelberg.

Hirsch, L. M., & Shankland, T. J. (1991). Point defects in (Mg, Fe) SiO_3 perovskite. Geophysical Research Letters, 18(7), 1305-1308.

Hirth, J. P., Lothe, J., & Mura, T. (1983). Theory of dislocations. Journal of Applied Mechanics, 50(2), 476.

Hoff, C. M., & Watson, E. B. (2018). Aluminium in rutile as a recorder of temperature and pressure. In VM Goldschmidt Conference.

Höink, T., Lenardic, A., & Richards, M. (2012). Depth-dependent viscosity and mantle stress amplification: implications for the role of the asthenosphere in maintaining plate tectonics. Geophysical Journal International, 191(1), 30-41.

Holzapfel, C. (2004). Fe-Mg interdiffusion at high pressures in mineral phases relevant for the Earth s mantle (Doctoral dissertation, Universität zu Köln).

Holzapfel, C., Chakraborty, S., Rubie, D. C., & Frost, D. J. (2009). Fe–Mg interdiffusion in wadsleyite: the role of pressure, temperature and composition and the magnitude of jump in diffusion rates at the 410 km discontinuity. Physics of the Earth and Planetary Interiors, 172(1-2), 28-33.

Holzapfel, C., Rubie, D. C., Frost, D. J., & Langenhorst, F. (2005). Fe-Mg interdiffusion in (Mg, Fe) SiO_3 perovskite and lower mantle reequilibration. Science, 309(5741), 1707-1710.

Horiuchi, H., Ito, E., & Weidner, D. J. (1987). Perovskite-type $MgSiO_3$; single-crystal X-ray diffraction study. American Mineralogist, 72(3-4), 357-360.

Howard, C. J., & Stokes, H. T. (1998). Group-theoretical analysis of octahedral tilting in perovskites. Acta Crystallographica Section B: Structural Science, 54(6), 782-789.

Howard, C. J., & Stokes, H. T. (2005). Structures and phase transitions in perovskites–a group-theoretical approach. Acta Crystallographica Section A: Foundations of Crystallography, 61(1), 93-111.

Huang, R. (2020). Bridgmanite crystal chemistry and iron content in the Earth′s lower mantle. Universitaet Bayreuth (Germany).

Huang, R., Boffa Ballaran, T., McCammon, C. A., Miyajima, N., & Frost, D. J. (2021). The Effect of Fe-Al Substitution on the Crystal Structure of MgSiO3 Bridgmanite. *Journal of Geophysical Research: Solid Earth*, *126*(9), e2021JB021936.

Hull, D., & Bacon, D. J. (2011). Introduction to dislocations (Vol. 37). Elsevier.

Imamura, M. (2018). Experimental study on rheological properties of mantle minerals: Implication for subducting slab and the lower mantle (Doctoral dissertation, Kyushu University).

Irifune, T. (1994). Absence of an aluminous phase in the upper part of the Earth's lower mantle. Nature, 370(6485), 131-133.

Ishii, T., Criniti, G., Ohtani, E., Purevjav, N., Fei, H., Katsura, T., & Mao, H. K. (2022). Superhydrous aluminous silica phases as major water hosts in high-temperature lower mantle. Proceedings of the National Academy of Sciences, 119(44), e2211243119.

Ito, E., & Matsui, Y. (1978). Synthesis and crystal-chemical characterization of $MgSiO_3$ perovskite. Earth and Planetary Science Letters, 38(2), 443-450.

Ito, E., Takahashi, E., & Matsui, Y. (1984). The mineralogy and chemistry of the lower mantle: an implication of the ultrahigh-pressure phase relations in the system $MgOFeOSiO_2$. Earth and Planetary Science Letters, 67(2), 238-248.

Joesten, R. (1991). Grain-boundary diffusion kinetics in silicate and oxide minerals. In Diffusion, atomic ordering, and mass transport (pp. 345-395). Springer, New York, NY.

Jollands, M. C. (2020). Assessing analytical convolution effects in diffusion studies: Applications to experimental and natural diffusion profiles. PloS one, 15(11), e0241788.

Kanzaki, M. (2021). Institute for Planetary Minerals. Okayama University. Retrieved January 16, 2023, from https://www.misasa.okayama-u.ac.jp/eng/

Karato, S. I., & Li, P. (1992). Diffusion creep in perovskite: implications for the rheology of the lower mantle. Science, 255(5049), 1238-1240.

Karato, S. I., Zhang, S., & Wenk, H. R. (1995). Superplasticity in Earth's lower mantle: evidence from seismic anisotropy and rock physics. Science, 270(5235), 458-461.

Karato, S. I., & Wu, P. (1993). Rheology of the upper mantle: A synthesis. Science, 260(5109), 771-778.

Karki, B. B., Wentzcovitch, R. M., De Gironcoli, S., & Baroni, S. (2000). Ab initio lattice dynamics of MgSiO 3 perovskite at high pressure. *Physical Review B*, *62*(22), 14750.

Kirby, S. H., & Raleigh, C. B. (1973). Mechanisms of high-temperature, solid-state flow in minerals and ceramics and their bearing on the creep behavior of the mantle. Tectonophysics, 19(2), 165-194.

Kohlstedt, D. L. (2006). The role of water in high-temperature rock deformation. Reviews in Mineralogy and Geochemistry, 62(1), 377-396.

Kojitani, H., Katsura, T., & Akaogi, M. (2007). Aluminium substitution mechanisms in perovskite-type $MgSiO_3$: an investigation by Rietveld analysis. Physics and Chemistry of Minerals, 34(4), 257-267.

Kraych, A., Carrez, P., & Cordier, P. (2016). On dislocation glide in $MgSiO_3$ bridgmanite at high-pressure and high-temperature. Earth and Planetary Science Letters, 452, 60-68.

Kraych, A., Carrez, P., Hirel, P., Clouet, E., & Cordier, P. (2016). Peierls potential and kink-pair mechanism in high-pressure $MgSiO_3$ perovskite: an atomic scale study. Physical Review B, 93(1), 014103.

Kröger, F. A., & Vink, H. J. (1956). Relations between the concentrations of imperfections in crystalline solids. In Solid state physics (Vol. 3, pp. 307-435). Academic Press.

Kubo, A., & Akaogi, M. (2000). Post-garnet transitions in the system $Mg_4Si_4O_{12}$–$Mg_3Al_2Si_3O_{12}$ up to 28 GPa: phase relations of garnet, ilmenite and perovskite. Physics of the Earth and Planetary Interiors, 121(1-2), 85-102.

Lane, D. L., & Ganguly, J. (1980). Al_2O_3 solubility in orthopyroxene in the system MgO-$Al2O_3$-SiO_2: A reevaluation, and mantle geotherm. Journal of Geophysical Research: Solid Earth, 85(B12), 6963-6972.

Lauterbach, S., McCammon, C. A., Van Aken, P., Langenhorst, F., & Seifert, F. (2000). Mössbauer and ELNES spectroscopy of (Mg, Fe)(Si, Al)O_3 perovskite: a highly oxidised component of the lower mantle. Contributions to Mineralogy and Petrology, 138(1), 17-26.

Lay, T., Hernlund, J., & Buffett, B. A. (2008). Core–mantle boundary heat flow. Nature geoscience, 1(1), 25-32.

Litasov, K. D., Kagi, H., Shatskiy, A., Ohtani, E., Lakshtanov, D. L., Bass, J. D., & Ito, E. (2007). High hydrogen solubility in Al-rich stishovite and water transport in the lower mantle. Earth and Planetary Science Letters, 262(3-4), 620-634.

Liu, L. G., Mernagh, T. P., & Irifune, T. (1995). Raman spectra of $MgSiO_3$· 10% Al_2O_3-perovskite at various pressures and temperatures. Physics and Chemistry of Minerals, 22(8), 511-516.

Liu, X., Nishiyama, N., Sanehira, T., Inoue, T., Higo, Y., & Sakamoto, S. (2006). Decomposition of kyanite and solubility of Al_2O_3 in stishovite at high pressure and high temperature conditions. Physics and Chemistry of Minerals, 33(10), 711-721.

Liu, Z., Akaogi, M., & Katsura, T. (2019 a). Increase of the oxygen vacancy component in bridgmanite with temperature. Earth and Planetary Science Letters, 505, 141-151.

Liu, Z., Boffa Ballaran, T., Huang, R., Frost, D. J., & Katsura, T. (2019 b). Strong correlation of oxygen vacancies in bridgmanite with Mg/Si ratio. Earth and Planetary Science Letters, 523, 115697.

Liu, Z., Ishii, T., & Katsura, T. (2017 a). Rapid decrease of $MgAlO_{2.5}$ component in bridgmanite with pressure. Geochemical Perspectives Letters, 5, 12-18.

Liu, Z., Nishi, M., Ishii, T., Fei, H., Miyajima, N., Boffa Ballaran, T., Ohfuji, H., Sakai, T., Wang, L., Shcheka, S., Arimoto, T., Tange, Y., Higo, Y., Irifune, T., & Katsura, T. (2017 b). Phase relations in the system $MgSiO_3$-Al_2O_3 up to 2300 K at lower mantle pressures. Journal of Geophysical Research: Solid Earth, 122(10), 7775-7788.

Lowry, R. K., Henderson, P., & Nolan, J. (1982). Tracer diffusion of some alkali, alkaline-earth and transition element ions in a basaltic and an andesitic melt, and the implications concerning melt structure. Contributions to Mineralogy and Petrology, 80, 254-261.

Marquardt, H., & Miyagi, L. (2015). Slab stagnation in the shallow lower mantle linked to an increase in mantle viscosity. Nature Geoscience, 8(4), 311-314.

Maruyama, G., & Hiraga, T. (2017). Grain-to multiple-grain-scale deformation processes during diffusion creep of forsterite+ diopside aggregate: 1. Direct observations. Journal of Geophysical Research: Solid Earth, 122(8), 5890-5915.

Massa, W. (2015). Röntgenbeugung. In Kristallstrukturbestimmung (pp. 13-28). Wiesbaden: Springer Spektrum.

Maurice, M., Tosi, N., Samuel, H., Plesa, A. C., Hüttig, C., & Breuer, D. (2017). Onset of solid-state mantle convection and mixing during magma ocean solidification. Journal of Geophysical Research: Planets, 122(3), 577-598.

McCammon, C. (1997). Perovskite as a possible sink for ferric iron in the lower mantle. Nature, 387(6634), 694-696.

McNamara, A. K., van Keken, P. E., & Karato, S. I. (2003). Development of finite strain in the convecting lower mantle and its implications for seismic anisotropy. Journal of Geophysical Research: Solid Earth, 108(B5).

Mehrer, H. (2005). Diffusion: Introduction and case studies in metals and binary alloys. In Diffusion in Condensed Matter (pp. 3-63). Springer, Berlin, Heidelberg.

Meißner, E., Sharp, T. G., & Chakraborty, S. (1998). Quantitative measurement of short compositional profiles using analytical transmission electron microscopy. *American Mineralogist*, *83*(5-6), 546-552.

Meißner, E. (2000). Messung von kurzen Konzentrationsprofilen mit Hilfe der analytischen Transmissionselektronenmikroskopie (TEM-EDX) am Beispiel der Bestimmung von Diffusionskoeffizienten für die Mg-Fe-Interdiffusion in Olivin (Doctoral dissertation, Universität Bayreuth, Fakultät für Biologie, Chemie und Geowissenschaften).

Merkel, S. (2023). Bridgmanite, Viewed Down [010] in the Pbnm Setting. Scientific Illustrations -- Slip systems for the lower mantle. Retrieved January 16, 2023, from http://merkel.texture.rocks/Illustrations/montrerimage.php?lang=en&gal=1&im=0&index=3

Mitrovica, J. X., & Forte, A. M. (2004). A new inference of mantle viscosity based upon joint inversion of convection and glacial isostatic adjustment data. Earth and Planetary Science Letters, 225(1-2), 177-189.

Miyajima, N., Holzapfel, C., Asahara, Y., Dubrovinsky, L., Frost, D. J., Rubie, D. C., Drechsler, M., Niwa, K., Ichihara, M., & Yagi, T. (2010). Combining FIB milling and conventional Argon ion milling techniques to prepare high-quality site-specific TEM samples for quantitative EELS analysis of oxygen in molten iron. Journal of Microscopy, 238(3), 200-209.

Morimoto, N., & Koto, K. (1969). The crystal structure of orthoenstatite. Zeitschrift für Kristallographie, 129(1-4), 65-83.

Murakami, M., Hirose, K., Sata, N., & Ohishi, Y. (2005). Post-perovskite phase transition and mineral chemistry in the pyrolitic lowermost mantle. Geophysical Research Letters, 32(3).

Nabarro, F. R. N. (1948). Report of a Conference on the Strength of Solids. The Physical Society, London, 75, 590.

Nabarro, F. R. N. (1967). Steady-state diffusional creep. Philosophical Magazine, 16(140), 231-237.

Nakakoji, T., Hiraga, T., Nagao, H., Ito, S., & Kano, M. (2018). Diffusion creep and grain growth in forsterite +20 vol% enstatite aggregates: 1. High-resolution experiments and their data analysis. Journal of Geophysical Research: Solid Earth, 123(11), 9486-9512.

Navrotsky, A. (1999). A lesson from ceramics. Science, 284(5421), 1788-1789.

Navrotsky, A., Schoenitz, M., Kojitani, H., Xu, H., Zhang, J., Weidner, D. J., & Jeanloz, R. (2003). Aluminum in magnesium silicate perovskite: Formation, structure, and energetics of magnesium-rich defect solid solutions. Journal of Geophysical Research: Solid Earth, 108(B7).

Newbury, D. E., & Ritchie, N. W. (2013). Is scanning electron microscopy/energy dispersive X-ray spectrometry (SEM/EDS) quantitative?. Scanning, 35(3), 141-168.

Nishi, M., Kubo, T., Ohfuji, H., Kato, T., Nishihara, Y., & Irifune, T. (2013). Slow Si–Al interdiffusion in garnet and stagnation of subducting slabs. Earth and Planetary Science Letters, 361, 44-49.

Nye, J. F. (1985). Physical properties of crystals: their representation by tensors and matrices. Oxford university press.

Okamoto, A., & Hiraga, T. (2022). A common diffusional mechanism for creep and grain growth in polymineralic rocks: Experiments. Journal of Geophysical Research: Solid Earth, 127(9), e2022JB024638.

Oswald, P. (2019). Dynamics of Dislocations in Smectic A Liquid Crystals Doped with Nanoparticles. Crystals, 9(8), 400.

Overwijk, M. H. F., Van den Heuvel, F. C., & Bulle-Lieuwma, C. W. T. (1993). Novel scheme for the preparation of transmission electron microscopy specimens with a focused ion beam. Journal of Vacuum Science & Technology B: Microelectronics and Nanometer Structures Processing, Measurement, and Phenomena, 11(6), 2021-2024.

Panero, W. R., Akber-Knutson, S., & Stixrude, L. (2006). Al_2O_3 incorporation in $MgSiO_3$ perovskite and ilmenite. Earth and Planetary Science Letters, 252(1-2), 152-161.

Poirier, J. P. (1985). Creep of crystals: high-temperature deformation processes in metals, ceramics and minerals. Cambridge University Press.

Poirier, J. P., & Liebermann, R. C. (1984). On the activation volume for creep and its variation with depth in the Earth's lower mantle. Physics of the earth and planetary interiors, 35(4), 283-293.

Prior, D. J., Boyle, A. P., Brenker, F., Cheadle, M. C., Day, A., Lopez, G., Peruzzo, L., Potts, G. J., Reddy, S., Spiess, R., Timms, N. E., Trimby, P., Wheeler, J., & Zetterstrom, L. (1999). The application of electron backscatter diffraction and orientation contrast imaging in the SEM to textural problems in rocks. American Mineralogist, 84(11-12), 1741-1759.

Prior, D. J., Trimby, P. W., Weber, U. D., & Dingley, D. J. (1996). Orientation contrast imaging of microstructures in rocks using forescatter detectors in the scanning electron microscope. Mineralogical Magazine, 60(403), 859-869.

Putnis, A. (1992). An Introduction to Mineral Sciences. Cambridge University Press.

Reali, R., Jackson, J. M., Van Orman, J., Bower, D. J., Carrez, P., & Cordier, P. (2019 a). Modeling viscosity of (Mg,Fe)O at lowermost mantle conditions. Physics of the earth and planetary interiors, 287, 65-75.

Reali, R., Van Orman, J. A., Pigott, J. S., Jackson, J. M., Boioli, F., Carrez, P., & Cordier, P. (2019 b). The role of diffusion-driven pure climb creep on the rheology of bridgmanite under lower mantle conditions. Scientific reports, 9(1), 1-9.

Reed, S. J. B. (2005). Electron microprobe analysis and scanning electron microscopy in geology. Cambridge University Press.

Ricard, Y., & Wuming, B. (1991). Inferring the viscosity and the 3-D density structure of the mantle from geoid, topography and plate velocities. Geophysical Journal International, 105(3), 561-571.

Richmond, N. C., & Brodholt, J. P. (1998). Calculated role of aluminium in the incorporation of ferric iron into magnesium silicate perovskite. American Mineralogist, 83(9-10), 947-951.

Rigort, A., & Plitzko, J. M. (2015). Cryo-focused-ion-beam applications in structural biology. Archives of Biochemistry and Biophysics, 581, 122-130.

Ringwood, A. E. (1991). Phase transformations and their bearing on the constitution and dynamics of the mantle. Geochimica et Cosmochimica Acta, 55(8), 2083-2110.

RRUFF (2016). Database of Raman spectroscopy, X-ray diffraction and chemistry of minerals. Retrieved January 16, 2023, from https://rruff.info/

Rudolph, M. L., Lekić, V., & Lithgow-Bertelloni, C. (2015). Viscosity jump in Earth's mid-mantle. Science, 350(6266), 1349-1352.

Sasaki, J., Peterson, N. L., & Hoshino, K. (1985). Tracer impurity diffusion in single-crystal rutile (TiO_2−x). Journal of Physics and Chemistry of Solids, 46(11), 1267-1283.

Schmalzried, H., & Frick, T. (1995). Internal Solid State Reaction: Formation of Perovskite in NiO-Matrix. Berichte der Bunsengesellschaft für physikalische Chemie, 99(7), 914-919.

Shimojuku, A., Kubo, T., Kato, T., Yoshino, T., Nishi, M., Nakamura, T., .Okazaki, R., & Kakazu, Y. (2014). Effects of pressure and temperature on the silicon diffusivity of pyrope-rich garnet. Physics of the Earth and Planetary Interiors, 226, 28-38.

Shimojuku, A., Kubo, T., Ohtani, E., Nakamura, T., Okazaki, R., Dohmen, R., & Chakraborty, S. (2009). Si and O diffusion in (Mg, Fe) $2SiO_4$ wadsleyite and ringwoodite and its implications for the rheology of the mantle transition zone. Earth and Planetary Science Letters, 1(284), 103-112.

Solomatov, V. (2007). Magma oceans and primordial mantle differentiation. Evolution of the Earth, 9, 91-119.

Solomatov, V. S., El-Khozondar, R., & Tikare, V. (2002). Grain size in the lower mantle: constraints from numerical modeling of grain growth in two-phase systems. Physics of the Earth and planetary interiors, 129(3-4), 265-282.

Solomatov, V. S., & Reese, C. C. (2008). Grain size variations in the Earth's mantle and the evolution of primordial chemical heterogeneities. Journal of Geophysical Research: Solid Earth, 113(B7).

Stacey, F. D. (1995). Theory of thermal and elastic properties of the lower mantle and core. Physics of the Earth and Planetary Interiors, 89(3-4), 219-245.

Stacey, F. D., & Davis, P. M. (2004). High pressure equations of state with applications to the lower mantle and core. Physics of the Earth and Planetary interiors, 142(3-4), 137-184.

Stacey, F. D., & Davis, P. M. (2008). Physics of the Earth. Cambridge University Press.

Stebbins, J. F., Kroeker, S., & Andrault, D. (2001). The mechanism of solution of aluminum oxide in $MgSiO_3$ perovskite. Geophysical Research Letters, 28(4), 615-618.

Steinberger, B., & Calderwood, A. R. (2000). Mineral physics constraints on viscous flow models of mantle flow. In AGU 2000 Fall Meeting (San Francisco, USA 2000).

Stixrude, L., & Lithgow-Bertelloni, C. (2011). Thermodynamics of mantle minerals-II. Phase equilibria. Geophysical Journal International, 184(3), 1180-1213.

Stixrude, L., & Lithgow-Bertelloni, C. (2012). Geophysics of chemical heterogeneity in the mantle. Annual Review of Earth and Planetary Sciences, 40, 569-595.

Stocker, R. L., & Ashby, M. F. (1973). On the rheology of the upper mantle. Reviews of Geophysics, 11(2), 391-426.

Tackley, P. J. (1996). On the ability of phase transitions and viscosity layering to induce long wavelength heterogeneity in the mantle. Geophysical Research Letters, 23(15), 1985-1988.

ThermoFisher Scientific (2022). Material Science. Retrieved January 17, 2023, from https://www.thermofisher.com/de/de/home/materials-science/learning-center/applications/sem-electrons.html

Thomas, J., & Gemming, T. (2013). Analytische Transmissionselektronenmikroskopie: Eine Einführung für den Praktiker. Wien: Springer Verlag.

Tschauner, O., Ma, C., Beckett, J. R., Prescher, C., Prakapenka, V. B., & Rossman, G. R. (2014). Discovery of bridgmanite, the most abundant mineral in Earth, in a shocked meteorite. Science, 346(6213), 1100-1102.

Tsujino, N., Yamazaki, D., Nishihara, Y., Yoshino, T., Higo, Y., & Tange, Y. (2022). Viscosity of bridgmanite determined by in situ stress and strain measurements in uniaxial deformation experiments. Science advances, 8(13), eabm1821.

Van Cappellen, E. (1990). The parameterless correction method in X-ray microanalysis. Microscopy Microanalysis Microstructures, 1(1), 1-22.

Van Cappellen, E., & Doukhan, J. C. (1994). Quantitative transmission X-ray microanalysis of ionic compounds. Ultramicroscopy, 53(4), 343-349.

Van Cappellen, E., & Schmitz, A. (1992). A simple spot-size versus pixel-size criterion for X-ray microanalysis of thin foils. Ultramicroscopy, 41(1-3), 193-199.

Van Mierlo, W. L., Langenhorst, F., Frost, D. J., & Rubie, D. C. (2013). Stagnation of subducting slabs in the transition zone due to slow diffusion in majoritic garnet. Nature Geoscience, 6(5), 400-403.

Waldo, R. A., Militello, M. C., & Gaarenstroom, S. W. (1993). Quantitative thin-film analysis with an energy-dispersive x-ray detector. Surface and interface analysis, 20(2), 111-114.

Walter, M. J., Kubo, A., Yoshino, T., Brodholt, J., Koga, K. T., & Ohishi, Y. (2004). Phase relations and equation-of-state of aluminous Mg-silicate perovskite and implications for Earth's lower mantle. Earth and Planetary Science Letters, 222(2), 501-516.

Walter, M. J., Trønnes, R. G., Armstrong, L. S., Lord, O. T., Caldwell, W. A., & Clark, S. M. (2006). Subsolidus phase relations and perovskite compressibility in the system $MgO–AlO_{1.5}–SiO_2$ with implications for Earth's lower mantle. Earth and Planetary Science Letters, 248(1-2), 77-89.

Weertman, J. (1968). Diffusion law for the dispersion of hard particles in an ice matrix that undergoes simple shear deformation. Journal of Glaciology, 7(50), 161-165.

Wentzcovitch, R. M., Karki, B. B., Cococcioni, M., & De Gironcoli, S. (2004). Thermoelastic Properties of $MgSiO_3$-Perovskite: Insights on the Nature of the Earth's Lower Mantle. Physical Review Letters, 92(1), 018501.

Williams, D. B., & Carter, C. B. (2009). Transmission electron microscopy: Basic diffraction, imaging, and spectrometry. Springer Verlag.

Williams, D. B., Michael, J. R., Goldstein, J. I., & Romig Jr, A. D. (1992). Definition of the spatial resolution of X-ray microanalysis in thin foils. Ultramicroscopy, 47(1-3), 121-132.

Wirth, R. (2004). Focused Ion Beam (FIB) A novel technology for advanced application of micro-and nanoanalysis in geosciences and applied mineralogy. European Journal of Mineralogy, 16(6), 863-876.

Wright, K., & Price, G. D. (1993). Computer simulation of defects and diffusion in perovskites. Journal of Geophysical Research: Solid Earth, 98(B12), 22245-22253.

Xu, F. (2017). Experimental study on rheology of deep mantle minerals. Okayama University.

Xu, F., Yamazaki, D., Sakamoto, N., Sun, W., Fei, H., & Yurimoto, H. (2017). Silicon and oxygen self-diffusion in stishovite: Implications for stability of SiO_2-rich seismic reflectors in the mid-mantle. Earth and Planetary Science Letters, 459, 332-339.

Xu, J., Yamazaki, D., Katsura, T., Wu, X., Remmert, P., Yurimoto, H., & Chakraborty, S. (2011). Silicon and magnesium diffusion in a single crystal of $MgSiO_3$ perovskite. Journal of Geophysical Research: Solid Earth, 116(B12).

Yamamoto, T., Yuen, D. A., & Ebisuzaki, T. (2003). Substitution mechanism of Al ions in $MgSiO_3$ perovskite under high pressure conditions from first-principles calculations. Earth and Planetary Science Letters, 206(3-4), 617-625.

Yamazaki, D., Kato, T., Ohtani, E., & Toriumi, M. (1996). Grain growth rates of $MgSiO_3$ perovskite and periclase under lower mantle conditions. Science, 274(5295), 2052-2054.

Yamazaki, D., Kato, T., Yurimoto, H., Ohtani, E., & Toriumi, M. (2000). Silicon self-diffusion in $MgSiO_3$ perovskite at 25 GPa. Physics of the Earth and Planetary Interiors, 119(3-4), 299-309.

Yoshino, T., Kamada, S., Zhao, C., Ohtani, E., & Hirao, N. (2016). Electrical conductivity model of Al-bearing bridgmanite with implications for the electrical structure of the Earth's lower mantle. Earth and Planetary Science Letters, 434, 208-219.

Zhang, B. (2017). An overview of Fe–Mg interdiffusion in mantle minerals. Surveys in Geophysics, 38(4), 727-755.

1: Summary of all successful synthesis experiments with starting material, experimental conditions, and material.

Name	Material	Press	Assembly	TC	P [GPa]	T [°C]	Heating – time [h]
H5562	En100	Hymak	7/3	y	24	1800	17
S7381	En100	Sumitomo	7/3	n	24	1750	4
S7596	En100	Sumitomo	7/3	n	24	1750	3.5
S7664	En100	Sumitomo	7/3	n	24	1750	4
S7726	En100	Sumitomo	7/3	n	23	1750	1
S7795	En100	Sumitomo	7/3	y	23	1850	4
S7833	En100	Sumitomo	7/3	y	24	1800	17
S7563	En97Cor3	Sumitomo	7/3	n	>24	1750	4
S7610a	En97Cor3	Sumitomo	7/3	n	24	1750	4
S7661	En97Cor3	Sumitomo	7/3	y	24	1750	4
S7732	En97Cor3	Sumitomo	7/3	n	24	2000	4
S7791	En97Cor3	Sumitomo	7/3	n	24	1750	4
S7828	En97Cor3	Sumitomo	7/3	y	24	1800	4
S7833	En97Cor3	Sumitomo	7/3	y	24	1800	17
S7843	En97Cor3	Sumitomo	7/3	y	24	1808	21
S7450	En95Cor5	Sumitomo	7/3	y	24	1750	3.5
H5562	En95Brm5	Hymak	7/3	y	24	1800	17
S7610b	En95Brm5	Sumitomo	7/3	n	24	1750	4
S7727	En95Brm5	Sumitomo	7/3	y	24	1750	4
S7800	En95Brm5	Sumitomo	7/3	n	24	1800	4
S7824	En95Brm5	Sumitomo	7/3	y/n	24	1800	6
S7830	En95Brm5	Sumitomo	7/3	y	24	1800	21
S7614	En90Brm10	Sumitomo	7/3	y	24	1750	7
S7661	En90Brm10	Sumitomo	7/3	y	24	1750	4
S7722	En90Brm10	Sumitomo	7/3	y	24	1750	4

* The TC was working at the beginning of the experiment. It broke during the test run.

2: Diffusion coefficients for every single experiment and the average values used in the final calculations.

#	Excell log10(D)	average	StdDev	PACE log10(D) (FWHM=26.4)	average	StdDev	PACE log10(D) (FWHM=10)	average	StdDev	thickness
S7596_L1_Map1	-19.84			-19.50			-19.33			0.14
S7596_L1_Map2	-19.13			-18.62			-18.59			0.14
S7596_L1_Map3	-19.44	-19.46	0.29	-18.97	-19.01	0.35	-18.92	-18.93	0.30	0.13
S7596_L2_Map1	-19.69			-19.27			-19.16			0.08
S7596_L2_Map2	-19.53			-19.07			-19.00			0.08
S7596_L2_Map3	-19.14			-18.63			-18.60			0.13
S7614_L1_Map1	-20.12			-20.29			-20.13			0.31
S7614_L1_Map2	-20.11	-20.09	0.29	-20.27	-20.38	0.30	-20.12	-20.18	0.18	0.18
S7614_L1_Map3	-20.41			-20.81			-20.43			0.11
S7614_L1_Map4	-19.71			-20.14			-20.02			0.38
S7751_L1_Map1	-20.19			-20.37			-20.21			0.23
S7751_L1_Map2	-19.99	-20.38	0.45	-20.64	-20.05	10.04	-20.37	-19.90	9.97	0.24
S7751_L2_Map1	-20.30			-19.13			-19.13			0.22
S7751_L2_Map3	-21.04			*			(-21.08)*			0.18
S7791_L1_Map1	-19.01			-19.19			-19.02			0.17
S7791_L2_Map1	-19.80			*			-19.87			0.22
S7791_L2_Map2	-19.22	-19.19	0.36	*	-19.14	10.49	-19.64	-19.29	0.45	0.23
S7791_L2_Map3	-18.98			-19.14			-18.98			0.25
S7791_L2_Map4	-18.94			-19.1			-18.95			0.21
S7808_L1_Map1	-19.80			-19.99			-19.81			0.20
S7808_L1_Map2	-19.87	-19.63	0.35	-20.1	-20.17	0.22	-19.88	-19.90	0.10	0.17
S7808_L2_Map1	-19.23			-20.41			-20.01			0.23
S7824_L1_Map1	-20.50	-19.75	1.06	(-21.5)*	-19.80	14.00	-20.53	-20.13	0.57	0.08
S7824_L2_Map1	-19.00			-19.8			-19.73			0.15
S7828_L1_Map2	-19.08			-19.11			-19.09			0.23
S7828_L2_Map1	-19.67	-19.22	0.40	-19.77	-19.61	0.45	-19.68	-19.53	0.39	0.20
S7828_L2_Map2	-18.90			-19.96			-19.82			0.17
S7830_L1_Map1	-20.60	-20.04	0.78	-20.77	-20.14	0.89	-20.61	-20.05	0.79	0.16
S7830_L1_Map2	-19.49			-19.51			-19.49			0.08
S7835_L1_Map1	-19.57			-19.59			-19.58			0.38
S7835_L1_Map2	-19.02	-19.43	0.36	-19.71	-19.67	0.07	-19.7	-19.66	0.07	0.25
S7835_L2_Map4	-19.69			-19.71			-19.7			0.28
S7843_L1_Map1	-20.96			-21.56			-20.98			0.12
S7843_L1_Map2	-20.72	-20.84	0.12	-20.97	-21.24	0.30	-20.74	-20.85	0.12	0.10
S7843_L2_Map1	-20.84			-21.18			-20.84			0.08

* Omitted values from the calculation

3: Analytical data from the Al bearing bridgmanite. Used for Table 2-1. Experiments were made at 24 GPa and between 1750 and 2000 °C for annealing hours from 3 to 21hours

#	wt%				Molecular formula				mol %			at %			
Sample	MgO	Al_2O_3	SiO_2	total	Mg	Al	Si	O	Mg/Si	OV	CC	O	Mg	Al	Si
S7596_I	38.8	2.9	55.8	97.5	0.99	0.06	0.95	2.91	1.03	3.3	1.3	60.0	18.9	1.1	18.2
S7596_I	38.6	3.4	57.0	99.0	0.98	0.07	0.97	2.96	1.01	0.8	2.9	60.2	19.1	1.3	18.9
S7614_I	39.5	2.7	56.7	98.9	1.01	0.05	0.97	2.95	1.04	3.8	0.7	61.0	19.8	1.1	19.1
S7614_I	38.5	3.1	54.8	96.4	0.98	0.06	0.94	2.87	1.05	4.5	0.9	61.6	19.0	1.2	18.2
S7830	38.7	3.0	55.3	97.0	0.99	0.06	0.94	2.89	1.04	4.2	0.9	61.1	19.1	1.2	18.3
S7830	38.7	2.3	56.6	97.7	0.99	0.05	0.97	2.91	1.02	1.9	1.4	61.0	19.2	0.9	18.8
S7835	38.0	3.4	58.3	99.7	0.97	0.07	1.00	2.98	0.97	-2.9	4.8	60.2	18.9	1.3	19.5
S7835	37.1	3.6	57.3	98.0	0.94	0.07	0.98	2.93	0.96	-3.6	5.4	60.5	18.2	1.4	18.9
	0.7	0.4	1.1	1.1	0.02	0.01	0.02	0.04	0.03	3.2	1.9	0.6	0.5	0.2	0.5
	38.5	3.0	56.5	98.0	0.98	0.06	0.96	2.92	1.02	1.5	2.3	60.7	19.0	1.2	18.7
S7751_Map1_L1a	40.2	1.1	61.0	102.3	1.02	0.02	1.04	3.06	0.98	-1.8	2.0	60.8	20.8	0.5	21.2
S77551_Map2_L1	37.7	5.8	56.2	99.8	0.96	0.12	0.96	2.98	1.00	0.0	5.7	60.5	18.9	2.3	18.9
S7751_Map3_L2	37.5	5.7	55.2	98.5	0.96	0.11	0.94	2.94	1.01	1.3	5.0	60.7	18.6	2.2	18.4
S7751_Map2_L2	37.8	5.8	55.2	98.8	0.96	0.12	0.94	2.95	1.02	2.0	4.8	60.5	18.8	2.3	18.4
S7791_Map1_L1	37.7	5.9	55.4	99.0	0.96	0.12	0.95	2.95	1.02	1.4	5.2	60.4	18.8	2.3	18.5
S7791_Map3_L3	38.0	5.9	56.3	100.2	0.97	0.12	0.96	2.99	1.01	0.5	5.6	59.9	18.9	2.3	18.8
	1.0	1.9	2.2	1.4	0.03	0.04	0.04	0.05	0.01	1.3	1.4	0.3	0.8	0.8	1.1
	38.2	5.1	56.6	99.8	0.97	0.10	0.97	2.98	1.01	0.6	4.7	60.5	19.1	2.0	19.0
S7808	39.2	2.6	56.6	98.3	1.00	0.05	0.97	2.93	1.03	3.0	1.1	60.7	19.4	1.0	18.8
S7808	39.1	2.7	57.0	98.7	0.99	0.05	0.97	2.94	1.02	2.1	1.6	60.6	19.4	1.1	19.0
S7824	39.1	2.7	57.0	98.7	0.99	0.05	0.97	2.94	1.02	2.2	1.6	60.6	19.4	1.1	19.0
S7824	38.9	2.7	57.0	98.6	0.99	0.05	0.97	2.94	1.02	1.7	1.8	60.6	19.3	1.0	19.0
S7828	38.9	2.6	57.2	98.7	0.99	0.05	0.98	2.94	1.02	1.5	1.8	60.6	19.3	1.0	19.1
S7843	39.2	2.7	56.0	97.9	1.00	0.06	0.96	2.91	1.04	4.1	0.7	60.5	19.3	1.1	18.5
S7843	39.1	2.6	57.7	99.4	0.99	0.05	0.98	2.97	1.01	0.9	2.2	60.3	19.4	1.0	19.3
S7843_L2	39.5	2.8	56.1	98.4	1.01	0.06	0.96	2.93	1.05	4.9	0.4	60.6	19.6	1.1	18.7
	0.2	0.1	0.6	0.4	0.00	0.00	0.01	0.02	0.01	1.4	0.6	0.1	0.1	0.0	0.2
	39.1	2.7	56.8	98.6	1.00	0.05	0.97	2.94	1.03	2.6	1.4	60.5	19.4	1.0	18.9

4: Rough grain size estimation on SEM and TEM overview images. It is important to note that the grain sizes have only been calculated from sections of the corresponding samples.

	Synthesis				Diffusion experiments	
	Al free	grain size [µm]	Al rich	grain size [µm]	**Sample name**	grain size [µm]
Stoichiometric	S7381_a	8 (2)	S7563_2	3(1)	**S7596**	4 (1)
	S7596_a	7 (3)	S7563_1	3 (1)	**S7614**	4 (2)
	S7795_I	8 (2)	S7732_I	4 (1)	**S7830**	4 (2)
	S7795_II	8 (2)	S7732_II	4 (1)	**S7835**	5 (1)
	S7726_II	5 (2)	S7610_II	3 (2)	**S7766°**	15 (2)
Stoichiometric; higher Al content	S7664_a	6 (1)	S7722	1.0 (5)	**S7751**	1 (1)
	S7664_b	6 (1)	S7722	1.0 (5)	**S7791**	2 (1)
	S7664b2_II	7 (2)	S7722_II	1.0 (5)	**H5548°**	10 (2)
Mg excess	S7664b1_II	7 (2)	S7800_I	2 (1)	**S7808**	3 (1)
	S7664b2_I	7 (2)	S7800_II	2 (1)	**S7824**	2 (1)
	S7726_III	4 (2)	S7824_I	2 (1)	**S7828**	2 (1)
	H5562_I	9 (1)	S7830_I	2 (1)	**S7843**	3 (1)

° Fast diffusion experiment

5: Summary table of EDX map size calculation with name, height (y) and width (z) & pixel density

#	x	y	mag	time	pixel size [nm]	pixel size [µm]	pixel/µm²
S7664_Map1	368	284	10000	1800	7	0.007	2132897959
S7596_Map1	530	280	5000	3600	11	0.011	1226446281
S7596_Map2	748	349	14000	3600	5	0.005	10442080000
S7614_Map1	292	749	14000	3600	5	0.005	8748320000
S7614_Map2	630	730	28500	3600	3	0.003	51100000000
S7610_Map2	700	500	10000	3600	7	0.007	7142857143
S7610_Map3	400	440	10000	3600	7	0.007	3591836735
S7610_Map1	750	750	14000	3600	5	0.005	22500000000
S7596_L2_Map1	710	470	28500	3600	3	0.003	37077777778
S7751_Map1	686	324	20000	3600	4	0.004	13891500000
S7751_Map2	686	324	20000	3600	4	0.004	13891500000
S7751_Map3	353	376	14000	3600	5	0.005	5309120000
S7791_Map1	480	250	14000	3600	5	0.005	4800000000
S7791__L3_Map4	430	420	28500	3600	3	0.003	20066666667
S7828_Map1	700	450	10000	3600	7	0.007	6428571429
S7843_Map2	601	486	40000	4900	2	0.002	73021500000
S7661_Map1	686	367	28500	5400	3	0.003	27973555556
S7596_Map2	800	520	40000	7200	2	0.002	104000000000
S7596_Map3	768	768	40000	7200	2	0.002	147456000000
S7596_L2_Map2	800	422	20000	7200	4	0.004	21100000000
S7596_L2_Map3	850	360	20000	7200	4	0.004	19125000000
S7614_I_Map3	903	608	40000	7200	2	0.002	137256000000
S7614_I_Map4	903	608	40000	7200	2	0.002	137256000000
S7791__L3_Map1	400	450	28500	7200	3	0.003	20000000000
S7791__L3_Map2	340	370	20000	7200	4	0.004	7862500000
S7791__L3_Map3	444	666	28500	7200	3	0.003	32856000000
S7808_Map1	370	350	20000	7200	4	0.004	8093750000
S7808_Map2	400	644	20000	7200	4	0.004	16100000000
S7824_Map1	700	500	28500	7200	3	0.003	38888888889
S7824_L2_Map1	600	700	20000	7200	4	0.004	26250000000
S7828_Map2	700	450	10000	7200	7	0.007	6428571429
S7830_L1_Map1	832	392	14000	7200	5	0.005	13045760000
S7830_L1_Map2	600	400	14000	7200	5	0.005	9600000000
S7835_Map1	660	500	10000	7200	7	0.007	6734693878
S7835_Map2	412	373	20000	7200	4	0.004	9604750000
S7843_Map1	700	600	20000	7200	4	0.004	26250000000
S7614_II_Map1	555	775	20000		4	0.004	26882812500
S7614_II_Map2	819	669	20000		4	0.004	34244437500

6: Table of diffusion experiments which were used for the final result evaluation and its associated results of convoluted diffusion coefficients (Excel), deconvoluted diffusion coefficients calculated by the PACE software, the average of the deconvoluted PACE diffusion coefficients (deconvoluted diffusion coef.) and further analytical results like the Mg/Si ration and the oxygen vacancy (OV) and charge – couple (CC) substitution data calculated from the absolute data from the EDX measurements at the STEM.

Starting material	Al free	Al rich	**Sample name**	TC	T_{exp} [°C]	P [W]	T_{calc} [°C]	±σ	Heating [h]	FIB Samples	TEM EDX maps	Sample thickness	Excel $log_{10}(D)$	Avg.	StdDev	PACE $log_{10}(D)$ (FWHM=26.4)	Avg.	StdDev	PACE $log_{10}(D)$ (FWHM=10)	Avg.	StdDev	**Deconv. diffusion coef.**	**StdDev**	Mg/Si	Avg.	StdDev	OV (diff. profile)	Avg.	StdDev	CC (diff. profile)	Avg.	StdDev
Stoichiometric	S7381_a	S7563_2	**S7596**	n	1,750	340	2,100	79	3.5	#1442	S7596_L1_Map1	0.14	-19.84	-19.46	0.29	-19.50	-19.01	0.35	-19.33	-18.93	0.30	**-18.97**	**0.32**	1.03	1.02	0.01	2.59	1.62	0.79	0.52	1.28	0.53
											S7596_L1_Map2	0.14	-19.13			-18.62			-18.59					1.02			0.76			1.42		
											S7596_L1_Map3	0.13	-19.44			-18.97			-18.92					1.02			1.69			1.24		
										#1464	S7596_L2_Map1	0.08	-19.69			-19.27			-19.16					1.01			0.70			1.85		
											S7596_L2_Map2	0.08	-19.53			-19.07			-19.00					1.02			2.38			1.35		
											S7596_L2_Map3	0.13	-19.14			-18.63			-18.60					1.02			1.48			0.51		
	S7596_a	S7563_1	**S7614**	y	1,750	370	1,870	83	7	#1459	S7614_L1_Map1	0.31	-20.12	-20.09	0.29	-20.29	-20.38	0.30	-20.13	-20.18	0.18	**-20.28**	**0.24**	1.04	1.03	0.02	0.00	1.56	1.68	4.80	1.92	2.10
											S7614_L1_Map2	0.18	-20.11			-20.27			-20.12					1.01			1.11			0.95		
											S7614_L1_Map3	0.11	-20.41			-20.81			-20.43					1.04			3.57			0.00		
											S7614_L1_Map4	0.38	-19.71			-20.14			-20.02					1			0.00			1.32		
	S7795_I	S7732_I	**S7830**	y	1,808	381	1,910	84	21	#1571	S7830_L1_Map1	0.16	-20.60	-20.04	0.78	-20.77	-20.14	0.89	-20.61	-20.05	0.79	**-20.10**	**0.84**	1.03	1.02	0.01	1.68	1.04	0.91	0.59	0.83	0.33
											S7830_L1_Map2	0.08	-19.49			-19.51			-19.49					1.01			0.40			1.06		
	S7795_II	S7732_II	**S7835**	y	1,808	387	1,950	87	21	#1574	S7835_L1_Map1	0.38	-19.57	-19.43	0.36	-19.59	-19.67	0.07	-19.58	-19.66	0.07	**-19.67**	**0.07**	0.97	0.97	0.01	0.00	0.00	0.00	3.91	3.75	0.68
											S7835_L1_Map2	0.25	-19.02			-19.71			-19.70					0.96			0.00			4.34		
										#1585	S7835_L2_Map4	0.28	-19.69			-19.71			-19.70					0.98			0.00			3.01		
Stoichiometric higher Al content	S7664_a	S7722	**S7751**	n	1,750	370	1,850	80	8	#1520	S7751_L1_Map1	0.23	-20.19	-20.38	0.45	-20.37	-20.05	0.81	-20.21	-19.90	0.67	**-19.98**	**0.74**	0.98	1.00	0.02	0.00	0.56	1.11	4.00	2.86	0.83
											S7751_L1_Map2	0.24	-19.99			-20.64			-20.37					1			0.00			2.33		
										#1532	S7751_L2_Map1	0.22	-20.30			-19.13			-19.13					1.02			0.00			2.93		
											S7751_L2_Map3	0.18	-21.04			*			(-21.08)*					1.01			2.22			2.17		
	S7664_b	S7722	**S7791**	n	1,750	380	1,910	84	0.5	#1552	S7791_L1_Map1	0.17	-19.01	-19.19	0.36	-19.19	-19.14	0.05	-19.02	-19.29	0.45	**-19.22**	**0.25**	1.01	1.00	0.01	0.00	0.00	0.00	4.60	2.93	1.41
											S7791_L2_Map1	0.22	-19.80			*			-19.87					1.01			0.00			1.69		
										#1560	S7791_L2_Map2	0.23	-19.22			*			-19.64					0.99			0.00			2.51		
											S7791_L2_Map3	0.25	-18.98			-19.14			-18.98					1.00			0.00			4.44		
											S7791_L2_Map4	0.21	-18.94			-19.10			-18.95					1.00			0.00			1.81		
	S7664b2_II	S7722_II	**H5548°**	y/n	1,750	605	1,900	170	4	#1567	H5548_L1_Map3	0.12	-16.08	-15.37	0.95	-16.08	-15.44	0.84	-16.08	-15.33	1.02	**-15.38**	**0.93**	1.01	1.00	0.02	1.69	1.50	1.41	1.29	2.01	2.46
										SEM	H5548_SEM	0.13	-14.29			-14.49			-14.16					0.98			2.80			0.00		
											H5548_SEM	0.13	-15.74			-15.74			-15.74					1.01			0.00			4.75		
Mg excess	S7664b1_II	S7800_I	**S7808**	n	1,800	350	1,802	79.5	3	#1563	S7808_L1_Map1	0.20	-19.80	-19.63	0.35	-19.99	-20.17	0.22	-19.81	-19.90	0.10	**-20.03**	**0.16**	1.03	1.03	0.01	3.41	2.81	0.25	1.06	0.37	0.60
											S7808_L1_Map2	0.17	-19.87			-20.10			-19.88					1.03			2.63			0.06		
										SEM	S7808_SEM	0.23	-19.23			-20.41			-20.01					1.02			2.99			0.00		
	S7664b2_I	S7800_II	**S7824**	y/n	1,800	363	1,900	83.5	6	#1564	S7824_L1_Map1	0.08	-20.50	-19.75	1.06	(-21.5)*	-19.80	*	-20.53	-20.13	0.57	**-19.97**	**0.57**	1.02	1.02	0.01	2.36	2.06	0.42	0.00	0.79	1.11
										#1565	S7824_L2_Map1	0.15	-19.00			-19.80			-19.73					1.01			1.76			1.57		
	S7726_III	S7824_I	**S7828**	y	1,750	395	2,000	90	4	#1568	S7828_L1_Map2	0.23	-19.08	-19.22	0.40	-19.11	-19.61	0.45	-19.09	-19.53	0.39	**-19.57**	**0.42**	1.01	1.01	0.01	1.03	1.17	0.61	0.93	0.74	0.37
										#1570	S7828_L2_Map1	0.20	-19.67			-19.77			-19.68					1.01			0.65			0.31		
											S7828_L2_Map2	0.17	-18.90			-19.96			-19.82					1.02			1.84			0.97		
	H5562_I	S7830_I	**S7843**	y	1,800	361	1,805	80	21	#1576	S7843_L1_Map1	0.12	-20.96	-20.84	0.12	-21.56	-21.24	0.30	-20.98	-20.85	0.12	**-21.05**	**0.21**	1.04	1.03	0.02	3.37	2.62	1.32	0.00	0.55	0.96
											S7843_L1_Map2	0.10	-20.72			-20.97			-20.74					1.01			1.09			1.66		
										#1578	S7843_L2_Map1	0.08	-20.84			-21.18			-20.84					1.04			3.39			0.00		

* Can´t be measured
° Fast diffusion experiment

Appendix B: Figures

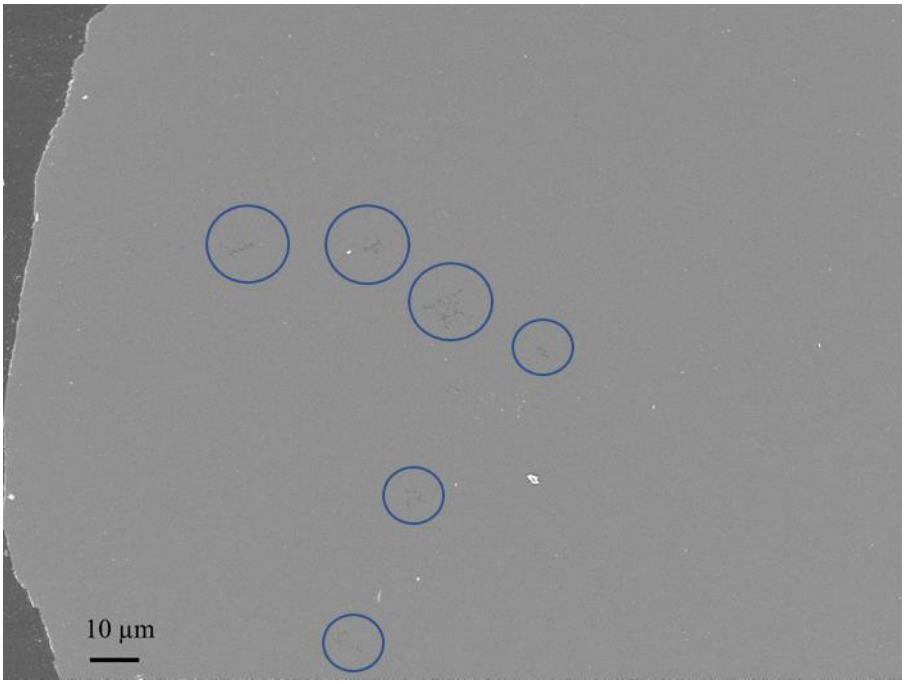

1: SE overview image of S7800 with clearly visible darker mineral grains in the sample (blue circle).

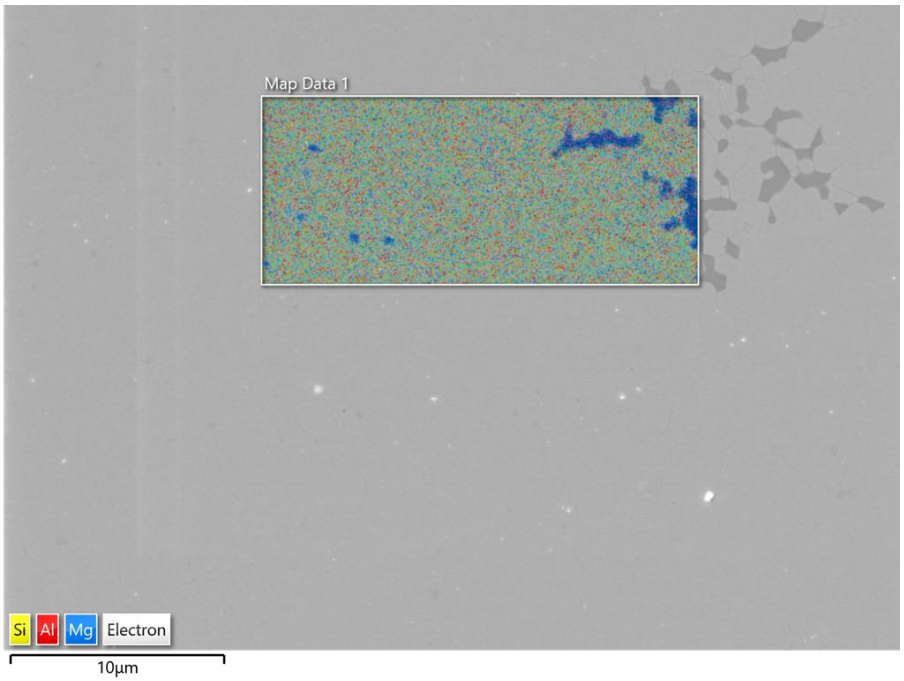

2: SEM SE image at 5 kV of sample S7800 superimposed by an EDX map created in FE-SEM with a pyrope-standard calibration showing coexisting periclase grains (blue) in the Mg excess sample and Mg/Si = 1.02(1) in the bridgmanite grains (greenish).

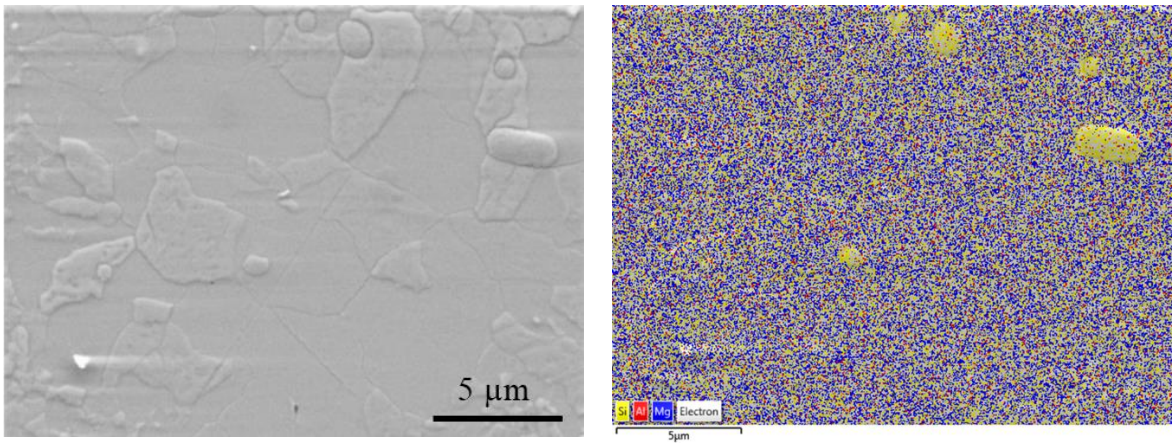

3: SE image at 5 kV of the stoichiometric sample S7610 and EDX map of the element concentration. In violet the bridgmanite grains and in yellow the stishovite grains.

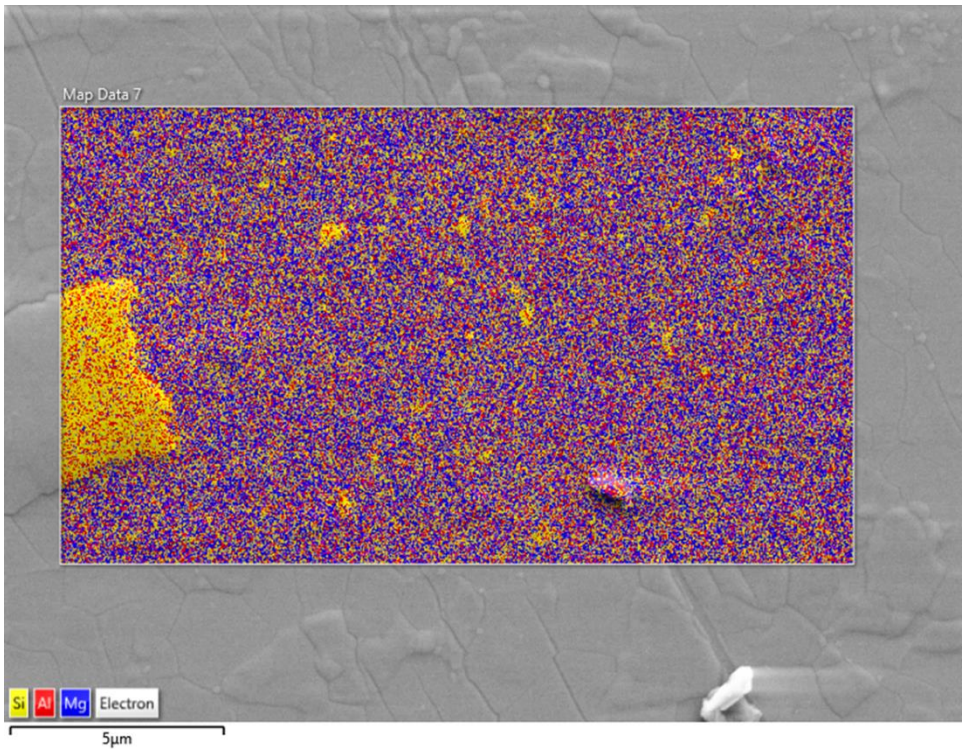

4: SE image at 5 kV of stoichiometric sample S7614 with higher Al content and superimposed by EDX map of sample S7614. In violet the bridgmanite grains and in yellow the stishovite grains.

(Eidesstattliche) Versicherungen und Erklärungen

(§ 9 Satz 2 Nr. 3 PromO BayNAT)

Hiermit versichere ich eidesstattlich, dass ich die Arbeit selbstständig verfasst und keine anderen als die von mir angegebenen Quellen und Hilfsmittel benutzt habe (vgl. Art. 64 Abs. 1 Satz 6 BayHSchG).

(§ 9 Satz 2 Nr. 3 PromO BayNAT)

Hiermit erkläre ich, dass ich die Dissertation nicht bereits zur Erlangung eines akademischen Grades eingereicht habe und dass ich nicht bereits diese oder eine gleichartige Doktorprüfung endgültig nicht bestanden habe.

(§ 9 Satz 2 Nr. 4 PromO BayNAT)

Hiermit erkläre ich, dass ich Hilfe von gewerblichen Promotionsberatern bzw. -vermittlern oder ähnlichen Dienstleistern weder bisher in Anspruch genommen habe noch künftig in Anspruch nehmen werde.

(§ 9 Satz 2 Nr. 7 PromO BayNAT)

Hiermit erkläre ich mein Einverständnis, dass die elektronische Fassung meiner Dissertation unter Wahrung meiner Urheberrechte und des Datenschutzes einer gesonderten Überprüfung unterzogen werden kann.

(§ 9 Satz 2 Nr. 8 PromO BayNAT)

Hiermit erkläre ich mein Einverständnis, dass bei Verdacht wissenschaftlichen Fehlverhaltens Ermittlungen durch universitätsinterne Organe der wissenschaftlichen Selbstkontrolle stattfinden können.

…….

Ort, Datum, Unterschrift